



UNIVERSITÀ DEGLI STUDI DI TRIESTE

XXII Ph.D CYCLE
(I CYCLE OF THE Ph.D. SCHOOLS) IN
Chemical and Pharmaceutical Sciences and Technologies

Scientific-disciplinary field
ING-IND/24: Principles of Chemical Engineering

BIOMATERIALS FOR BIOTECHNOLOGICAL APPLICATIONS: SYNTHESIS AND ACTIVITY EVALUATION

Ph.D. student

Danilo PERIN

Ph.D. School Director
Prof. Enzo ALESSIO

Supervisor
Prof. Mario GRASSI
Università degli Studi di Trieste

Assistant supervisors
Prof. Gabriele GRASSI
Università degli Studi di Trieste

Dott. Erminio MURANO
Istituto di Ricerca Protos - Trieste

*“La teoria è quando si sa tutto e niente funziona.
La pratica è quando tutto funziona e nessuno sa il perché.
In questo caso, abbiamo messo insieme la teoria e la pratica:
niente funziona... e nessuno sa il perché!”
(Albert Einstein)*

*A Sara,
Franca
e Roberto*

1 – INTRODUCTION	1
1.1 – Definition of biomaterials	1
1.2 – Biomaterials in tissue engineering	1
1.3 – Biomaterials for controlled drug delivery systems	4
1.4 – Biomaterials for delivery of nucleic acids and derivatives	5
1.5 – Aim of the Thesis	6
1.5.1 – The medical need: in-stent restenosis	7
1.5.2 – Experimental plan	9
1.5.2.1 – The cryoporometric analysis	9
1.5.2.2 – Rheological analysis	9
1.5.2.3 – Low field NMR analysis	10
1.5.2.4 – <i>In vivo</i> experiments	10
References	10
2 – NUCLEIC ACID BASED DRUGS (NABDS)	13
2.1 – Introduction	13
2.2 – Mechanism of action and therapeutic applications	13
2.2.1 – Decoy Oligodeoxynucleotides	14
2.2.2 – Triplex forming oligonucleotides	15
2.2.3 – Ribozymes	16
2.2.4 – DNAzymes	17
2.2.5 – SiRNA	19
2.2.6 – Antisense oligonucleotide	23
2.2.7 – Aptamers	24
2.3 – NABD delivery strategies	25
2.3.1 – NABD chemical modifications	26
2.3.1.1 – Modification involving phosphate moiety	27
2.3.1.2 – Modification involving sugar moiety	28
2.3.1.3 – Deep modification of the chemical structure	30
2.3.1.4 – Oligoconjugates	30
2.3.2 – Synthetic vector for NABDs release	31
2.3.2.1 – Liposomes	31
2.3.2.2 – Mesoporous silica nanoparticles	35
2.3.2.3 – Polymeric micelles and capsules	37
2.3.2.4 – Polyplexes	38
2.3.2.5 – Dendrimers	40

2.3.2.6 – Cyclodextrins	42
2.3.2.7 – Microbubbles	43
2.3.2.8 – Matrices for NABDs delivery	44
2.3.2.9 – Other delivery strategies	45
2.3.3 – Viral vector NABDs delivery systems	47
2.3.4 – Join approaches: chemo-virus, Chimerical virus and synthetic virus-like systems	50
References	52
3 – POLYMERIC DRUG DELIVERY SYSTEMS	67
3.1 – Polymer in drug delivery systems (DDS)	67
3.1.1 – Matrices	68
3.1.2 – Reservoir systems	69
3.1.3 – Bioerodible systems	69
3.1.4 – Pendant chain systems	70
3.2 – Gels	70
3.3 – Hydrogels	71
3.3.1 – Overview on hydrogel systems	71
3.4.2 – Alginates	73
3.4.3 – Pluronics TM	78
3.4.3.1 – General aspect of the Pluronic TM polymers	78
3.4.3.2 – Pluronics TM micellation in water solution	80
3.4.3.3 – Pluronics TM gelation	82
3.4.4 – Dextran based interpenetrating networks (IPNs)	84
3.4.5 – Polyethylene glycol (PEG) and benzofulvene derivates	86
2.3.5.1 – Polyethylene glycol (PEG) derivates	86
2.3.5.2 – Benzofulvene derivates	86
2.3.5.3 – Poly-1a and poly-1b properties	88
References	88
4 – TECHNIQUES FOR HYDROGELS AND ZEOLITE STRUCTURAL CHARACTERIZATION	93
4.1 – Nuclear magnetic resonance (NMR) spectroscopy	93
4.1.1 – NMR principles	94
4.1.1.1 – Quantum mechanics model for an isolated nucleus	94
4.1.1.2 – Energy absorption mechanism: the resonance	97
4.1.1.3 – Macroscopic magnetization	98
4.1.2 – The NMR experiment	99
4.1.3 – Low field NMR	104

4.1.3.1 – Introduction to the low field NMR	104
4.1.3.2 – T_2 measurements and analysis in low field NMR	105
4.2 – Rheological characterization	107
4.2.1 – The parallel plates measuring system geometry	108
4.2.2 – Stress sweep tests	109
4.2.3 – Gap determination: short stress sweep tests	110
4.2.4 – Frequency sweep tests	111
4.2.5 – Correlation models	111
4.3 – Crosslink density	113
4.4 – Pores diameter distribution	116
4.5 – Cryoporometry	118
4.5.1 – Introduction	118
4.5.2 – Determinations of the pores size distribution	119
4.5.2.1 – Nanopores volume (V_p) distribution as function of the pore radius R_p	119
4.5.2.2 – Nanocrystal volume (V_f) distribution as function of pore radius R_p	123
4.5.2.3 – Pore size distribution as function of the nanocrystal melting temperature T	125
4.5.4 – Evaluation of the non-freezable water layer thickness (β)	127
4.5.5 – Evaluation of the melting temperature distribution as function of the pore radius (dT/dR_p)	129
4.5.5.1 – Pore geometry and physical conditions	129
4.5.5.2 – Cylindrical pores geometry with an excess of water	130
4.5.5.3 – Cylindrical pores geometry without excess of water	132
4.5.5.4 – Spherical pores geometry	134
4.5.5.5 – Numerical determination of β and dT/dR_p	135
4.6 – Gas porosimetry	140
4.6.1 – Theoretical considerations	140
4.6.2 – Experimental considerations: the BET method	142
References	143
5 – MATERIALS AND METHODS	145
5.1 – Sample preparation	145
5.1.1 – Alginate hydrogels	145
5.1.2 – Pluronic TM hydrogel	146
5.1.3 – Dextran methacrylate hydrogels	146
5.1.3.1 – Synthesis of dextran methacrylate polymers	146
5.1.3.2 – Hydrogels preparation	147
5.1.4 – Hydrogel derived from benzofulvene: the poly-1b	147
5.1.4.1 – Step 1: synthesis of MOEG	147

5.1.4.2 – Step 2: synthesis of <i>2b</i>	147
5.1.4.3 – Step 3: synthesis of <i>3b</i>	147
5.1.4.4 – Step 4: synthesis of <i>1b</i>	148
5.1.4.5 – Step 5: <i>1b</i> self polymerization	148
5.1.5 – Pluronic™-alginate hydrogels	148
5.1.6 – Alginate-dextran methacrylate hydrogels	149
5.1.7 – Zeolites samples preparation	150
5.2 – Nucleic acid molecules	150
5.3 – Liposomes physical characterization	151
5.3.1 – Liposome-nucleic acid complexes preparation	151
5.3.2 – Liposomes particle size	151
5.3.3 – Zeta potential evaluation	152
5.4 – In vivo studies	152
5.4.1 – Cell culture	152
5.4.2 – Uptake studies	152
5.4.3 – Release studies of FITC-NAM-R/Cellfectin™ complexes	153
5.4.4 – Statistical analysis	153
References	153
6 – RESULTS AND DISCUSSIONS	155
6.1 – Introduction	155
6.2 – Zeolites Gas porosimetry and Cryoporometry studies	155
6.3 – Alginate based hydrogels	159
6.3.1 – 1% alginate hydrogels	159
6.3.1.1 – Macroscopic properties characterizations by Rheology	159
6.3.1.2 – Microscopic characterizations by low field NMR	161
6.3.2 – 2% alginate hydrogels	165
6.3.2.1 – Macroscopic properties characterizations by rheological studies	165
6.3.2.2 – Microscopic characterizations by low field NMR	167
6.3.2.3 – Cryoporometry structural properties studies on 2% copper alginate	171
6.3.3 – 3% alginate hydrogels	173
6.3.3.1 – Macroscopic characterizations by rheological studies	173
6.3.3.2 – Characterizations by low field NMR	174
6.3.4 – Concentration effects on alginates hydrogels pores size distribution	176
6.4 – Pluronic™ F127 18% hydrogel system	178
6.4.1 – Relaxation time (T_2) measurements by CPMG sequence	178
6.5 – Dextran methacrylate hydrogel based systems	182

6.5.1 – Macroscopic characterizations by rheological studies	182
6.5.2 – Cryoporometry structural properties studies	183
6.6 – Poly-1b hydrogel system	184
6.6.1 – Macroscopic properties characterizations by rheological studies	185
6.6.2 – Microscopic characterizations by low field NMR	185
6.6.3 – Pores size distribution studies	187
6.7 – Polymeric blends	189
6.7.1 – Pluronic™-alginate hydrogel system	189
6.7.1.1 – Structural analysis by NMR-rheology	189
6.7.1.2 – Structural analysis by Cryoporometry	191
6.7.2 – Alginate-dextran methacrylate hydrogel systems	192
6.7.2.1 – Macroscopic characterizations by rheological studies	192
6.7.2.2 – Characterization by low field NMR	193
6.7.2.3 – Pores size distribution studies	195
6.8 – Biological evaluation of Pluronic™-alginate system for NABDs delivery	196
6.8.1 – Introduction	196
6.8.2 – Choice of liposomes	196
6.8.3 – Characterization of liposomes particle size	197
6.8.4 – Zeta potential determination	199
6.8.5 – Rheological characterization	200
6.8.6 – Release and uptake studies from the Pluronic™-alginate blend	203
6.8.7 – Polyplexes transfection experiments	205
References	207
7 – CONCLUSIONS	209
7.1 – Systems characterization	209
7.2 – Cryoporometry studies	212
7.3 – Biological evaluations	213
SYMBOLS AND ABBREVIATIONS	215
ACKNOWLEDGEMENTS/RINGRAZIAMENTI	225

1 – Introduction

1.1 – Definition of biomaterials

The term biomaterial can be used to indicate a living biological material such as tissues, or a material that mimics the structure and the function of living biological materials.

According to the Clemson Advisory Board for Biomaterials, “a biomaterials is a systematically, pharmacologically inert substance designed for implantation or interaction in a living system” [1]. More recently, a biomaterial was defined as any non-living material used in a medical device that interact with biological systems [2]. Many different applications involve the use of biomaterials. The most important fall in the pharmacological applications (tablets and capsules coating, component of the transdermal patch), in the controlled drug release field [3-5], in extracorporeal devices such as contact lens, emodialysis devices, cardiopulmonary bypass oxygenators. Finally, biomaterials are fundamental components of any artificial prostheses (i.e.. skeletal, vascular, pacemaker etc.) [6-7].

The development of biomaterials has followed a long evolutionary process. Many biomaterials, at the beginning, were not intended for today's applications but they were used in other fields. Their entry into the biomedical field was initially due for the production of vascular prostheses that derived from textile industry applications.

1.2 – Biomaterials in tissue engineering

Tissue engineering is a discipline that investigates the structural-functional relationships of healthy or diseased tissues of the body in an attempt to restore, maintain or improve the functionality of living tissues. In order to achieve these targets, the experience and expertise in four disciplines must be combine: biology, chemistry, medicine and bioengineering. Biology deals the interaction of cells and biomaterials while medicine deals the clinical use of biomaterials and their interaction with the host organism. Chemistry studies and design properties while bio-engineering deals with the micro and macro characterization of biomaterials [8]. Indeed, material micro and

macro properties are fundamental for cell growth, an important requisite for achieving a spatial organization similar to that in native tissues [8-10].

In the development history of biomaterials, there are three distinct generations that have evolved over time. [8-10]. The 1st generation biomaterials were able to restore functionality of damaged tissue by their specific physical properties even they did not interact with the biological tissues. Members of this category are silicon, very high molecular weight poly-ethylene, tantalum oxide, titanium, zirconium and alumina. Several studies have shown that the use of inert materials has not led to satisfactory results as they do not yield to a full functional tissue [8-10].

The 2nd generation biomaterials have been developed since the 80s and consists in bioactive materials able to promote interaction with biological tissue, this allowing cells growth on the material surface. This category includes materials such as high density hydroxyapatite and bioglass, which are currently widely used in orthopedic and odontoiatric surgery. In order to improve protein absorption and cellular adhesion by modification of the surface properties several physical and chemical surface treatments can be adopted. In some studies, peptide sequences were inserted into polymeric structures and in this field, promising results were obtained immobilizing in the matrices short amino acid sequences responsible for cell adhesion [11-13]. The 2nd generation biomaterials include also the reasonable materials, systems which undergo a progressive dissolution within the biological system, without any rejection or toxic effects. In this case the interface problems between host tissue and the biomaterial are outdated since the biomaterial is gradually eroded and replaced by host tissue and it finally disappears. Degradation can be modulated by a different composition of the implanted system. A typical example of bio-absorbable material is given by the common sutures thread made by poly(lactic acid) (PLA) and poly(glycolic acid) (PGA).

The limit of the 1st and 2nd generation biomaterials resides in he impossibility of responding to changes in physiological and biological stimuli in a dynamic way. Indeed, an ideal biomaterial, in oreder to promote cells growth and differentiation in an appropriate three-dimensional environment, does not have to merely work as a mechanical support, but it must interact continuously and dynamically with the supported cells. In order to realize these types of materials, it is necessary to imprint in the materials all the biological and biophysical signals that direct cells growing, migration and differentiation. This 3th generation biomaterials are both *bioactive* and *bioerodible* [8, 14-16]. These biomaterials must be able to interact with the cells (supporting the growth and production of extracellular matrix components) and with the environment in which they are implanted. Simultaneously, the biomaterial, once implanted must be degraded leaving space for the growth of other structures, such as blood vessels, ensuring the full integration of the engineered tissue. The growth of tissue in a biomaterial scaffold is strongly influenced by the vascularization of

the scaffold. Indeed, an adequate supply of oxygen, nutrients, growth factors, etc., to the cells inside the scaffold [2, 17].

	Year	Goal	Characteristics
1st generation	1950'<	Biostability	Non immunogenicity
2nd generation	1980'<	Bioactivity	A controlled interaction with the pharmacological environment
3th generation	2000'<	Full functional tissue regeneration	Bioactive, biodegradable, able to induce a specific cellular response such as proliferation, differentiation, protein production, etc.

Tab. 1.1: characteristics and requirements of biomaterials for tissue engineering.

The biomaterials used in tissue engineering include natural, synthetic and semi-synthetic materials. The natural materials tend to be replaced by synthetic materials because they can be designed with appropriate and reproducible mechanical and structural properties depending on the considered applications. A scaffold must possess some essential characteristics for practical applications:

- Biocompatibility (it must induce immune or inflammatory response) [3]
- Biodegradability [18]
- A particular three-dimensional structure in order to promote cells proliferation and biosynthesis (formation of new tissue) [5]
- A suitable porosity and pores interconnection to ensure cells migration, tissue invasion, diffusion of nutrients and removal of metabolic wastes [5]
- Proper pores size. The ideal pores size depends on the tissue to regenerate: for soft tissue the optimal size is between 20 and 125 μm [6], for hard tissue it is from 150 to 400 μm and for liver tissue between 45 and 150 μm [7]
- A proper surface area in terms of extension and chemical composition. High ratio of internal surface area on scaffolding volume is important for the cell adhesion and migration [6]
- Appropriate mechanical properties because the biomaterial must provide a mechanical support for growing tissue [5].

Although some scaffolds have been successfully applied to regenerative medicine, there are several limitations that restrict their application fields [6]. A strategy for the vascular engineering is to seed endothelial cells on a biodegradable scaffold. The possibility to modulate the mechanical properties of the material and stimulate cells growth and differentiation allows to remodel the engineered constructs into mature and functional tissue [19-20]. In this sense synthetic

biodegradable polymers represent a support structure for cells that may facilitate the formation of new tissues.

On the basis of the prerequisites listed, the scientific and technological challenge in the scaffolds design for tissue engineering, consists in the development of materials with a proper, well defined structural (i.e. spatial form, strength, density, porosity) and microstructural (i.e. size, density of crosslinking) characteristics. One of the key aspects in the implementation of suitable platforms for regenerative medicine applications is the control of crosslinking degree as well as the pores size and shape [19-26].

1.3 – Biomaterials for controlled drug delivery systems

Controlled drug delivery systems can be used in the field of contraception, ophthalmology, thrombosis prevention, odontoiatric field, in the fight against cancer, in the fight against alcoholism and in the treatment and cure of diabetes. In the design of controlled release systems, the target is getting the correct release kinetic. This is a particularly difficult achievement because it can depend on variables such as body temperature (normal state or fever), medium concentration in which the drug is dispersed, the type of administration system (tablets, capsules, patches) and its geometric configuration [27].

The evaluation of active agent release kinetics implies the execution of *in vivo* test that represent the final and most important verification of delivery system effectiveness and reliability. In a traditional pharmaceutical system, the dissolution and drug absorption are inhomogeneous and the drug delivery is rapid, uncontrolled and depends only on drug nature, in particular on its water solubility. The drug concentration profile, in general, has a maximum followed by a quite rapid monotonous decay due to natural metabolic processes (*Fig. 1.1a_i*) [27]. As represented in the figure, the blood concentration of a drug depends only on the dose included in the release systems (a_i) and, moreover, the maximum concentration is achieved after the same time from administration, independently from the dose. Notably, after the maximum, the concentration curves are parallel, confirming that, in traditional systems, the absorption of the active agents depends only on the organism absorption capacity in the release site. Dose increasing only increase the time required to achieve a specified reduction in concentration [27].

For each active agent there are two fundamental concentration limits: the lower limit, commonly called therapeutic limit, below which the drug is too dilute to obtain the expected benefits, and an upper limit or toxicity, above which the benefits are much lower than the negative effects. Therefore, any pharmaceutical system must be administered in a proper manner and with

the right dose in order to avoid that drug concentration, at any time, exit from the range between the therapeutic and toxicity limits [27-28].

If, rather than a single dose administration, a multiple repeated dose is considered, the situation may be not better. Indeed, curve *b* of *figure 1.1* shows that, even if only after three administrations drug concentration exceeds the therapeutic limits, the fourth administration exceeds the toxicity limit [28].

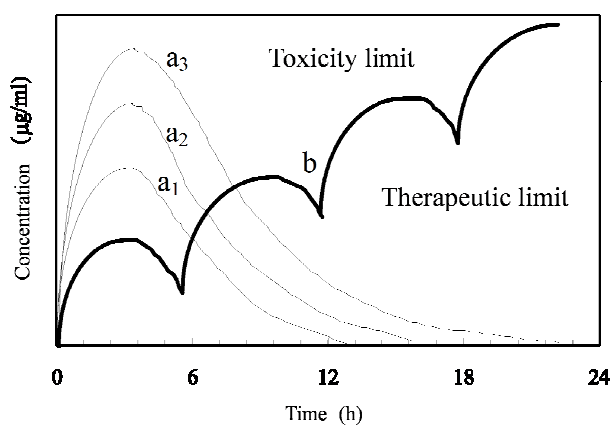


Fig. 1.1: typical drug concentration profiles over time in blood or in tissues after the administration of single doses (a_i) or multiple repeated doses every 6 hours (*b*).

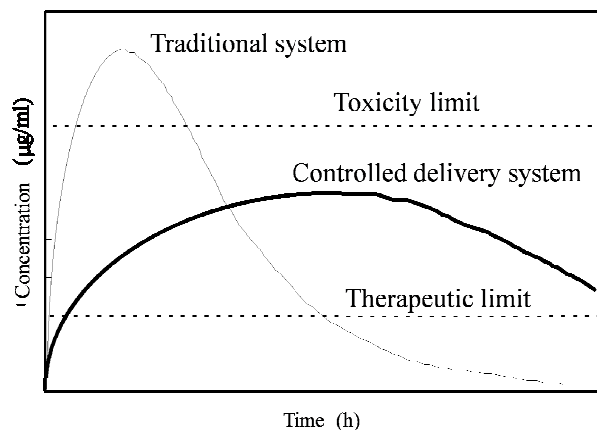


Fig. 1.2: comparison of drug concentration profiles over the time between traditional release systems and controlled delivery systems.

The goal of every controlled release system is to maintain the concentration of the drug to a targeted level for a period of time as long as possible. This can be achieved if, at an early stage, the concentration quickly reaches the effective level and then, the release rate is enough to balance the removal rate that depends on drug metabolism. *Figure 1.2*, compares the drug concentration profile due to a traditional release system and that competing to controlled release system [28].

1.4 – Biomaterials for delivery of nucleic acids and derivatives

Among the different applications of controlled drug delivery systems, one of the most interesting regards the release of nucleic acids and their derivatives. These molecules, defined as “nucleic acid base drugs” (NABDs), allow highly targeted cellular metabolism modifications. As it will be explained in subsequent sections, NABDs may find applications in many different diseases treatments: from cancer to eye disease, from vascular problems to the treatment of metabolic diseases, going from time to time to selectively shutdown or turn on the cellular pathways. Because the wide range of possible therapeutic applications, more and more private companies and public research laboratories invest in this sector and the most interesting examples concern the class of NABDs constituted by small interfering RNA (siRNA) [29].

Unfortunately, the clinical use of NABDs is still rather limited mainly because of problems related to their delivery. Indeed, in physiological environment, these molecules are particularly labile and present a limited cellular internalization [30]. Controlled delivery systems based on biomaterials, can solve these problems yielding to effective therapeutic action of NABDs. The role of controlled delivery systems is explicated at different levels [30-31]:

- Protect the active molecule from the degradation in physiological environment
- Tune the release kinetics
- Allow to get a targeted delivery with respect to delivery site and cells type
- Avoid the active molecule dispersion far from the target site
- Increase cellular internalization
- Increase the intracellular efficiency (i.e. endosomal escape, nuclear localization)

Controlled release systems based on polymeric biomaterials (synthetic or natural, variously modified and/or in combination) and in particular the hydrogel systems, have the potentiality to accomplish the mentioned requirements as well as the need for a biocompatible and biodegradable system. Indeed, the characteristics of polymer hydrogel can be adapted to modulate NABDs delivery as desired by acting, for example, on mesh size, swelling properties and mechanical strength [32].

Notably, many gels and hydrogel systems present a three-dimensional structure and mechanical properties attractive for applications in tissue engineering. In that sense, the hydrogel represent a meeting point within the 3rd generation of biomaterials used for tissue engineering and those used in systems for controlled drug delivery [3].

In subsequent chapters it will be discussed, the state of the art on NABDs and their possible applications and the release approaches. Particular emphasis will be devoted on NABDs complex consisting of siRNA and liposomes, the class of NABDs probably more widespread, and release systems based on polymer hydrogel, the subject of this work.

1.5 – Aim of the Thesis

The purpose of this research project concerns the characterization of biomaterials for biotechnological applications and evaluation of their activities. In particular, because of the great therapeutics and commercial interest and the delivery problems that are largely unresolved, the attention is focused on the study of new delivery systems for siRNA. Indeed they proved to be useful for what concerns the in-stent restenosis, pathology implying the re-occlusion of the artery due to the iper-proliferation of smooth muscle cells induced by the presence of the stent, a metal

prosthesis that is applied to avoid the elastic recoil of the artery wall after balloon angioplasty. In this system, the siRNA should act as an anti-proliferative on smooth muscle cells without interfering with endothelial cells.

The adopted approach consists in a stabilization of siRNA *in vivo* achieved by the complexation with liposomes that act as carrier and facilitator for cellular up-take. The control of the release kinetics is delegated to the physical and structural properties of a properly designed polymeric network (hydrogel) where the siRNA-liposome construct is embedded.

In order to design an appropriate delivery system it is crucial a precise structural and dimensional characterization of polymeric mesh. This purpose was achieved by the use of various techniques such as Rheology, low field NMR and Cryoporometry. Rheology allows the evaluation of the macroscopic mechanical properties of the system under investigation (Young's and shear modulus for example). Low field NMR, instead, allows to evaluate the microscopic properties and, coupled to the rheology, provides an estimation of the polymeric mesh size distribution. Cryoporometry is another method to assess the mesh size distribution. Finally, the selected delivery system is tested *in vivo* models of smooth muscle and endothelial cells in culture.

1.5.1 – *The medical needing: in-stent restenosis*

The in-stent restenosis is a pathology occurring in blood vessels, normally large arteries that have the tendency to re-occlude after an angioplasty treatment and application of a stent [33]. The angioplasty is a medical technique that restores the blood flow in narrowed or obstructed arteries, typically as a result of atherosclerosis plaques. The procedure consists in passing in the narrowed vessel area an empty and collapsed balloon catheter on a guide wire. Then, the balloon is inflated to a fixed size using pressures 75 to 500 times the normal blood pressure. The balloon crushes the atherosclerosis deposits opening the blood vessel improving flow. After the treatment, the balloon is deflated and withdrawn (*Fig. 1.3*). During this procedure, metallic stent prosthesis is applied by the balloon expansion to the artery wall in order to avoid the elastic recoil of the vessel [34]. Unfortunately, in more than 30% of patients who undergone balloon angioplasty, an uncontrolled proliferation of the smooth muscle cells can result after 3-6 month from the treatment, in a re-occlusion of the vessel (*Fig. 1.4*) [33].

Restenosis is triggered by the damage caused to the endothelial cells layer by the angioplasty treatment and by the presence of the stent perceived as a foreign body. The vessel responds to those conditions by physiological mechanisms to repair the damage. In a first stage that occurs immediately after tissue trauma, a blood clot forms at the site of damage accompanied by an inflammatory immune response. In a second stage, the permanent inflammatory state results in a

proliferation of the intimal smooth muscle cells (neointimal hyperplasia) causing a reduction of the vessel lumen (*Fig. 1.4*). Restenosis is treated by another angioplasty on the previous one or, in serious case, by the local tissue growth inhibition with radiation [33-34].

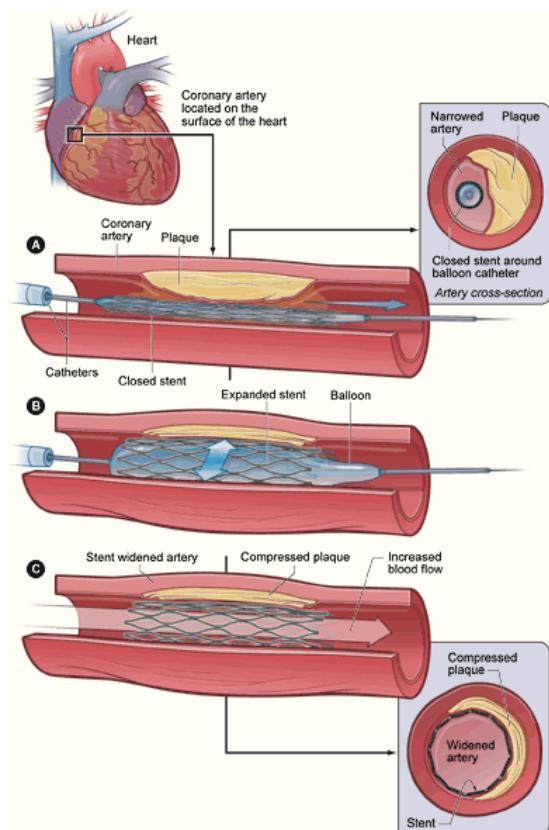


Fig. 1.3: balloon angioplasty procedure. **A** The balloon catheter is guided in the narrowed vessel area. **B** balloon expansion crushes the atherosclerosis deposits and implants a stent. **C** the stent maintains open the blood vessel.

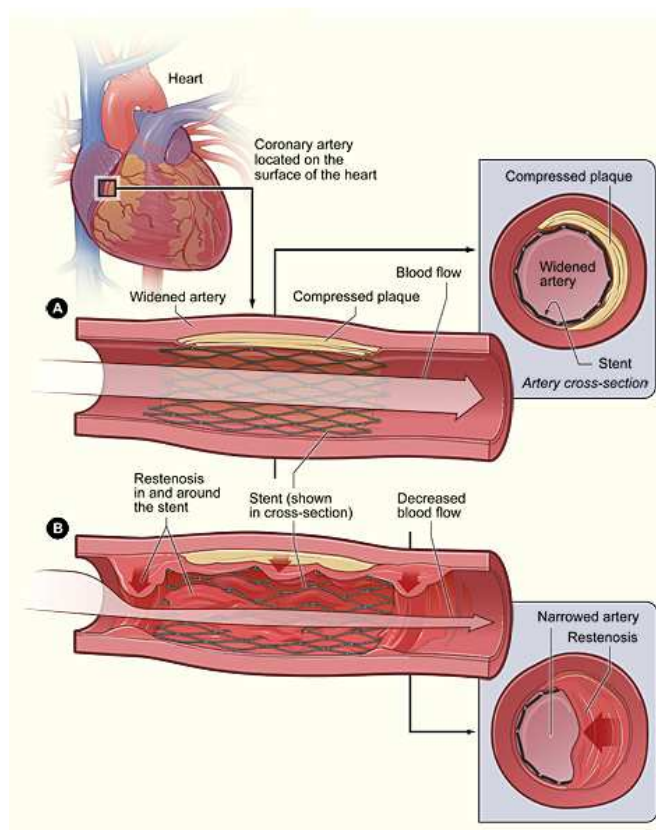


Fig. 1.4: restenosis process. **A** The freshly angioplasty treated vessel with a stent implant. **B** The neointimal hyperplasia caused by inflammatory response results in the vessel re-occlusion.

Currently, the medical treatments are directed to the prevention of restenosis by the administration of anti-platelet drugs and the design of active stent coated by antiproliferative drugs [34]. Our approach consists in the selection, by precise characterization, of a polymeric system useful for the *in vivo* application as stent coating. The polymeric coating is going to explicate a double action. On one side it covers all the damage area preventing the contact with the blood flow and limiting the inflammatory response. On the other side, it is going to release antiproliferative siRNA complex to prevent the neointimal hyperplasia [35]. The siRNA, selected from previous studies, target against the mRNA of cyclin E1, a key protein in the regulation of cell proliferation [36]

1.5.2 – Experimental plan

The experimental plan has been drawn taking into account the final objective or the research project: the realization of a delivery system for siRNA. The attention has been focused on polymeric hydrogels, whose biocompatibility and biodegradability is well known [3]. The considered polymers are:

- Alginate (polymeric concentration 1% - 2% - 3%), crosslinked by Ca^{2+} or Cu^{2+} water solution
- Pluronic™ F127 18% in water
- Dextran 5% or 30% methacrylate (respectively D40MA5 and D500MA30; polymeric concentration 5%) crosslinked by UV
- Gel systems derived from benzofulvene

The first step was the characterization of the above listed systems as individual components and polymeric blends have been analyzed:

- Pluronic™-alginate hydrogels respectively at 18% and 2% in water
- Dextran methacrylate-alginate respectively at 5% and 2% in water (D40MA5 or D500MA30)

1.5.2.1 – The cryoporometric analysis

The first step was the evaluation of the Cryoporometric technique as method for measurement of the pores size distribution. To do this, zeolites (Si60 and Si100), highly porous crystalline systems, have been taken as model. The results obtained through cryoporometric analysis were compared with those from gas porosimetric analysis. Once verified the reliability of the technique on the zeolites, the cryoporometric analysis was applied on non-standard systems such as hydrogels and compared with data from other methodologies.

1.5.2.2 – Rheological analysis

Rheological tests of stress sweep and frequency sweep allowed the determination of mechanical properties by measuring the storage (G') and loss (G'') modulus. Based on this characterization it was possible to get the crosslink density ρ_x and mean mesh size φ , important parameters for the evaluation of the polymeric networks as delivery systems.

1.5.2.3 – Low field NMR analysis

The low field NMR measurements allow assessing the behavior of water within the hydrogel systems and, coupled with the rheological results, allow to obtain the mesh size distribution of the polymeric network.

1.5.2.4 – *In vivo* experiments

In vivo tests represent the final step of the experimental process. The polymeric system's ability to carry and delivery the liposome-siRNA complexes, was tested in culture models of smooth muscle cells and endothelial cells.

References

1. Park, G.B., *Biomaterials science and engineering*. 1984, New York: Plenum Press.
2. Gurland, B.J., et al., *Impairment of communication and adaptive functioning in community-residing elders with advanced dementia: assessment methods*. Alzheimer Dis Assoc Disord, 1994. **8 Suppl 1**: p. S230-41.
3. Drury, J.L. and D.J. Mooney, *Hydrogels for tissue engineering: scaffold design variables and applications* Biomaterials, 2003. **24**(24): p. 4337-51
4. Schoenmakers, R.G., et al., *The effect of the linker on the hydrolysis rate of drug-linked ester bonds*. J Control Release, 2004. **95**(2): p. 291-300.
5. Tabata, Y., et al., *Vascularization into a porous sponge by sustained release of basic fibroblast growth factor*. J Biomater Sci Polym Ed, 1999. **10**(9): p. 957-68.
6. Ratner, B.D., *New ideas in biomaterials science--a path to engineered biomaterials*. J Biomed Mater Res, 1993. **27**(7): p. 837-50.
7. Peppas, N.A., *A model of dissolution-controlled solute release from porous drug delivery polymeric systems*. J Biomed Mater Res, 1983. **17**(6): p. 1079-87.
8. Hench, L.L. and J.M. Polak, *Third-generation biomedical materials*. Science, 2002. **295**(5557): p. 1014-7.
9. Hubbell, J.A., *Biomaterials in tissue engineering*. Biotechnology (N Y), 1995. **13**(6): p. 565-76.
10. Peppas, N.A. and R. Langer, *New challenges in biomaterials*. Science, 1994. **263**(5154): p. 1715-20.
11. West, J.L. and J.A. Hubbell, *Comparison of covalently and physically cross-linked polyethylene glycol-based hydrogels for the prevention of postoperative adhesions in a rat model*. Biomaterials, 1995. **16**(15): p. 1153-6.
12. Pratt, A.B., et al., *Synthetic extracellular matrices for in situ tissue engineering*. Biotechnol Bioeng, 2004. **86**(1): p. 27-36.
13. Hirashima, M., et al., *Maturation of embryonic stem cells into endothelial cells in an in vitro model of vasculogenesis*. Blood, 1999. **93**(4): p. 1253-63.
14. Sittinger, M., et al., *Tissue engineering and autologous transplant formation: practical approaches with resorbable biomaterials and new cell culture techniques*. Biomaterials, 1996. **17**(3): p. 237-42.
15. Vacanti, J.P. and R. Langer, *Tissue engineering: the design and fabrication of living replacement devices for surgical reconstruction and transplantation*. Lancet, 1999. **354 Suppl 1**: p. SI32-4.

16. Xue, L. and H.P. Greisler, *Biomaterials in the development and future of vascular grafts*. J Vasc Surg, 2003. **37**(2): p. 472-80.
17. Ribatti, D., et al., *The chick embryo chorioallantoic membrane as a model for in vivo research on angiogenesis*. Int J Dev Biol, 1996. **40**(6): p. 1189-97.
18. Wu, X., et al., *Tissue-engineered microvessels on three-dimensional biodegradable scaffolds using human endothelial progenitor cells*. Am J Physiol Heart Circ Physiol, 2004. **287**(2): p. H480-7.
19. Schugens, C., et al., *Polylactide macroporous biodegradable implants for cell transplantation. II. Preparation of polylactide foams by liquid-liquid phase separation*. J Biomed Mater Res, 1996. **30**(4): p. 449-61.
20. Schugens, C., et al., *Biodegradable and macroporous polylactide implants for cell transplantation: I. Preparation of macroporous polylactide supports by solid-liquid phase separation*. Polymer, 1996. **97**(6): p. 1027-1038.
21. Leong, K.F., C.M. Cheah, and C.K. Chua, *Solid freeform fabrication of three-dimensional scaffolds for engineering replacement tissues and organs*. Biomaterials, 2003. **24**(13): p. 2363-78.
22. Chen, G., T. Ushida, and T. Tateishi, *Scaffold Design for Tissue Engineering*. Macromolecular Bioscience, 2002. **2**(2): p. 67-77.
23. Doshi, J. and D.H. Reneker, *Electrospinning process and applications of electrospun fibers*. Macromolecular Bioscience, 1995. **35**(2-3): p. 151-60.
24. *Synthetic biodegradable polymer scaffolds* ed. A. Atala and D.J. Mooney. 1997, Boston: Birkhauser.
25. Mikos, A.G. and J.F. Temenoff, *Formation of highly porous biodegradable scaffolds for tissue engineering*. Electronic J. Biotech, 2000. **3**(2): p. 115-19.
26. Landers, R., et al., *Fabrication of soft tissue engineering scaffolds by means of rapid prototyping techniques* J Mater Sci, 2002. **37**(15): p. 3107-3116.
27. Langer, R.S. and D.L. Wise, *Medical applications of controlled release*. Vol. 1. 1984, Boca Raton FL: CRC Press.
28. Kim, C.H., *Controlled release dosage form design*. 2000, Boca Raton FL: CRC Press.
29. *RNA interfering technology*, ed. K. Apasani. 2005, Cambridge UK: Cambridge University Press.
30. Lu, P.Y. and M.C. Woodle, *Delivery small interfering RNA for novel therapeutics*, in *Drug delivery systems*, K.K. Jain, Editor. 2008, Humana Press: Totowas NJ.
31. *Antisense drug technology: principles strategies and applications*. 2nd ed, ed. S.T. Crooke. 2008, Boca raton: CRC Press.
32. *RNAi*, ed. M. Latterich. 2008, New York: Taylor & Francis.
33. *Coronary restenosis: from genetics to therapeutics* ed. G.Z. Feuerstein. 1997, New York: Marcel Dekeer.
34. *Restenosis: a guide to therapy*, ed. D.P. Faxon. 2001, London: Martin Dunitz.
35. Bhargawa, B., et al., *New approaches to preventing restenosis*. British Med J, 2003. **327**: p. 274-9.
36. Grassi, G., et al., *Temperature-sensitive hydrogels: potential therapeutic applications*. American J Drug Del, 2005. **3**: p. 239-51.

2 – Nucleic Acid Based Drugs (NABDs)

2.1 – Introduction

A novel and emergent class of molecules with potential therapeutic value is represented by the so called “*nucleic acid based drugs*” (NABDs). These molecules includes ribozymes, DNazymes, small interfering RNAs (siRNAs), antisense oligonucleotides (ASOs), decoy oligodeoxynucleotides (decoy ODN), aptamers and triplex forming oligonucleotides (TFOs). The biological activity of these molecules is based on different mechanisms but, all of them, have in common the ability to recognize, in a sequence-specific way, a particular target that can be a nucleic acid or a protein. Based on its action mechanism, the NABD is able to induce the digestion of an RNA, the transcriptional inhibition of a DNA sequence or the activity alteration of a target protein. As NABDs can be engineered to hit virtually any cellular target, in principle, is possible to specifically down-modulate, indirectly or directly, the functions of proteins which have undesired effect on the cell. The NABDs can thus find application in several human diseases including cancer and cardiovascular diseases.

In vitro, NABDs molecules, show high biological efficacy but unfortunately, *in vivo*, they tend to have considerably lower effects. This is mainly due to the fact that NABD application *in vivo* is hampered by the lack of optimal delivery systems so, despite the potential therapeutic value, their practical use in clinic still very limited. In order to improve the NABDs delivery, several strategies was used that include improvements in the amount of molecules delivered, stability and permanence of the molecules in the diseased tissue, cell/tissue specific delivery systems, NABDs chemical modifications, development of synthetic vectors.

2.2 – Mechanism of action and therapeutic applications

NABDs can be specifically directed against nucleic acid/protein targets thus inhibiting their biological functions through different mechanisms (*Fig. 2.1*). Decoy ODNs can bind transcription factors (TF) inhibiting the functions, TFOs instead, bind double stranded DNA whereas Ribozymes,

DNAzymes, siRNA and ASOs are able to bind and induce the cleavage a given specific mRNA. Finally, Aptamers can bind to proteins, carbohydrates, metal ion and small chemicals.

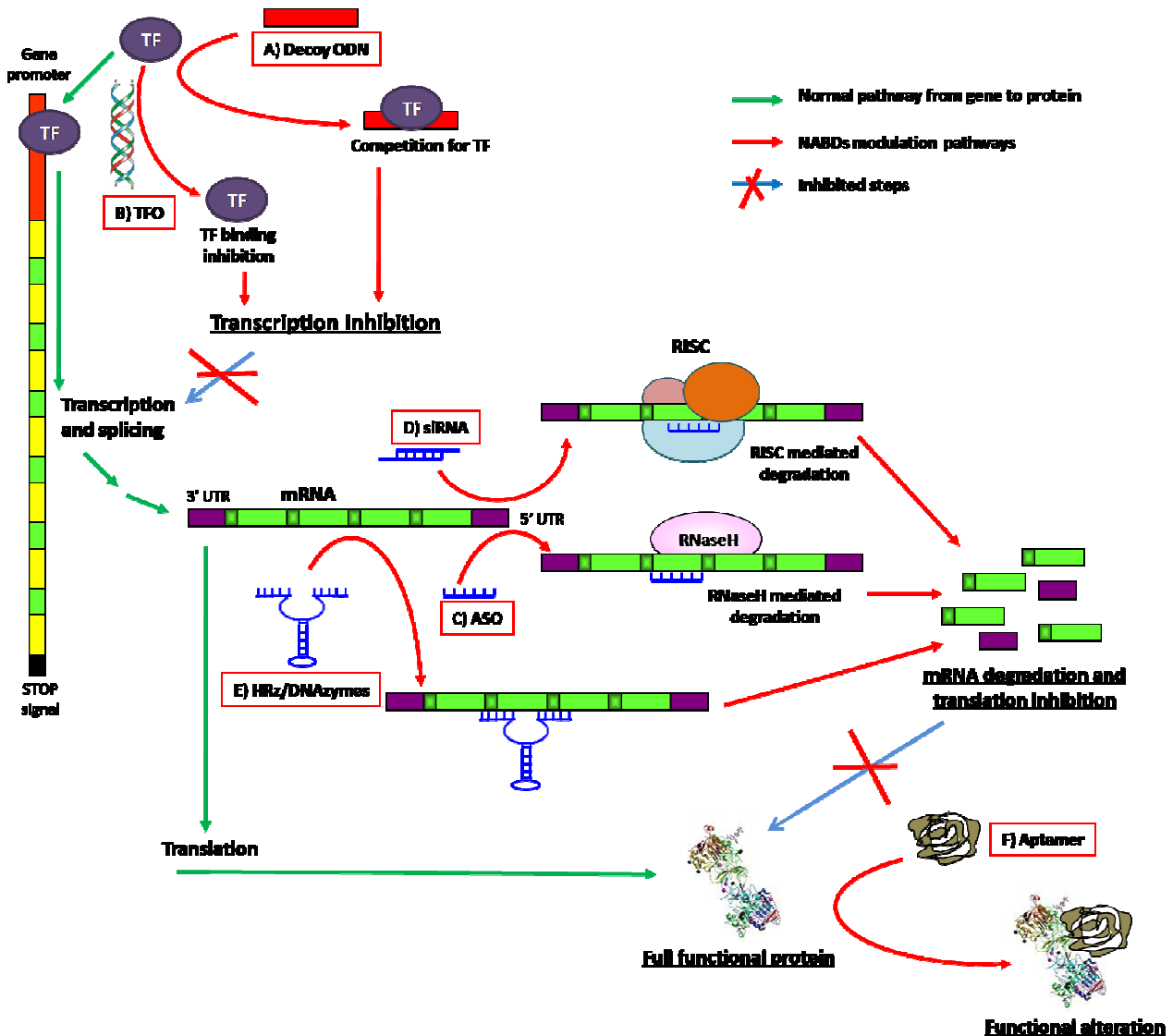


Fig. 2.1: silencing pathways. **A)** Double stranded decoy oligodeoxynucleotides (decoy ODNs) sequester transcription factors (TF) thus down-modulating gene transcription. **B)** Triple-forming oligodeoxynucleotides (TFOs) interact with a polypurine/pyrimidine region of dsDNA blocking transcription. **C)** Antisense oligodeoxynucleotides (ASOs) bind to a complementary target sequence blocking translation and/or inducing mRNA degradation via RNase-H activation. **D)** SiRNA induces target mRNA degradation guiding the catalytic protein complex RISC to an mRNA region complementary to the siRNA antisense strand. **E)** Hammerhead ribozymes (HRzs) and a DNAzymes promote mRNA cleavage thus inducing its degradation. **F)** Aptamers alter protein activity by binding to the protein itself.

2.2.1 – Decoy Oligodeoxynucleotides

Decoy oligodeoxynucleotides (ODNs) are short, double-stranded DNA molecules which can be designed to contain binding sequence for a variety of TFs. They work as a competitor for a specific TF reducing the factor available for the binding with the gene promoter regions reducing the transcription activity of the related genes [1].

Decoy ODNs technology have been successfully targeted to E2F and NF- κ B factors in order to prevent myocardial infarction [2], vein graft [3], inflammation [4] and restenosis following angioplasty [5-6]. Due to the involvement of NF- κ B in inflammatory pathways, studies have been performed also to down-modulate its biological effect in inflammatory diseases such as asthma, chronic obstructive pulmonary disease [7] and cystic fibrosis [8]. Another application of decoys consists of the targeting of the activator protein-1 (AP-1), a major transcription factor that up-regulates genes involved in immune and pro-inflammatory responses [9-10].

In case of tumour disease, E2F decoy ODN was successfully used to inhibit the proliferation of primary tumour cultured cells U2OS and C33A [11]. Moreover, a specific decoy ODN targeting NF- κ B factor resulted in a significant reduction in the expansion of glioblastoma cell line [12].

Recent studies have shown that decoy ODN targeting STAT3, a transcriptional factor that acts on several genes under stimulation by cytokines and growth factors, is amenable to suppress the growth of hepatocellular carcinoma [13] and glioma cells [14].

2.2.2 – Triplex forming oligonucleotides

Triplex forming oligonucleotides (TFOs) are short DNA molecules 15-30 nucleotides long which can bind sequence-specifically to segments of duplex DNA to constitute a triple helical structure. Felsenfeld et al. [15] first reported in 1957 the ability of nucleic acids to form triple helices. These structures are formed by the interaction of a polypurine or polypyrimidine TFO with the major groove of a homopurine: homopyrimidine DNA sequences which are over-represented in eukaryotic genomes, especially in human promoter regions [16]. The two types of hydrogen bonds between the third strand and the duplex are called Hoogsteen or “reverse” Hoogsteen. Three triple helix structural motives, different for orientation and base composition of the third strand, have been characterized [17] (*Fig. 2.2*).

TFOs can be used to alter gene expression by affecting DNA replication and RNA transcription [18-19]. Furthermore, inhibition of gene transcription can be obtained by preventing transcription factor binding to promoters [20-21] due to triple helix formation. Finally, triple helix can block transcription elongation [22].

Nowadays TFOs has been applied mainly as a tool for research in mutational correction studies *in vitro* [23-24] because the triplex stability in living cells is too low. Despite this, studies reporting TFO-mediated down-regulation for a variety of endogenous genes (c-myc, bcl-2, HER2/neu, bcr-abl, mdr1, TNF- α , MCP-1, GMF/CSF and ICAM-1) have been described. In particular, TFO is able to form a stable triple helix with a sequence in the α 1(I)-collagen gene promoter [25] with a potential role as anti-fibrosis.

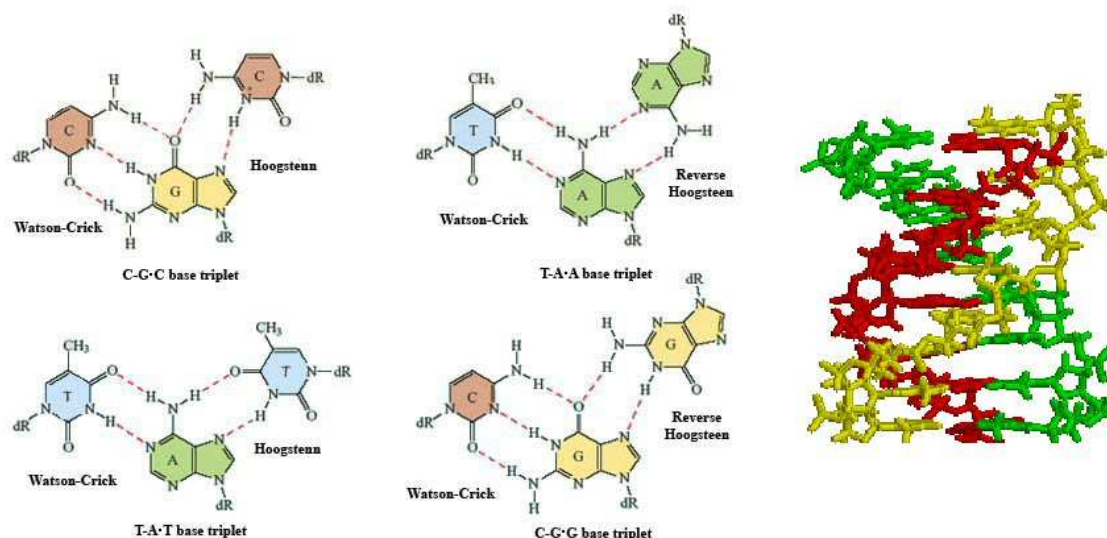


Fig. 2.2: triplex forming oligonucleotides hydrogen bonds. Representation of the two types of hydrogen bond present in a DNA triplex, on the left the Hoogsteen conformation, formed by cytosine and guanine in Watson-Crick conformation linked to a cytosine (C-G•C base triplet) or thymine and adenine in Watson-Crick conformation linked to a thymine (T-A•T base triplet). In the center the reverse Hoogsteen conformation, formed by thymine and adenine in Watson-Crick conformation linked to an adenine (A-T•A base triplet) or cytosine and guanine in Watson-Crick conformation linked to a guanine (C-G•C base triplet). On the right the DNA triple helix tridimensional structure.

2.2.3 – Ribozymes

Ribozymes are ribonucleic acid molecules which are able to display catalytic activity. Five classes of ribozymes have been described based on their sequences which includes the *Tetrahymena group I intron*, *RNase-P*, the *hairpin ribozyme*, the *hepatitis delta virus ribozyme* and the *hammerhead ribozymes* (HRzs) that are the best understood subcategory of all ribozymes and thereby the most commonly used form. HRzs have an enzymatic kinetics Mg^{2+} dependent [26-27] and, originally was isolated from viroid RNA [28-29] as a *cis*-acting molecule, with the ribozyme and the substrate on the same molecule. However, *trans*-acting HRzs which can cut a separate RNA molecule [30] can be designed.

Typical *Trans*-acting HRz is represented in *Fig. 2.3A*, containing less than 40 nucleotides, consists of: two binding arms that can be designed for the specific recognizing of virtually any target RNA [30], a catalytically active core represented by two stretches of highly conserved sequences [31] and a cleavage site within the target RNA which is composed of the tri-nucleotide triplet NUH where N represents any nucleotide and H represents in most of the case A, C, or U but also G is possible [32]. Unfortunately, not all RNA sequences can be targeted efficiently due to RNA folding which can severely impair HRzs action [33-34] and thus several experimental studies are usually required to identify HRzs that are suitable for gene product depletion.

How ether, HRzs have been extensively used to study their potential to prevent the expression of tumour-related genes. Some successfully targeted in order to obtain anti-tumour effects including bcr-abl, c-erb-2, h-ras, k-ras, n-ras, c-myc, vegf-a, tel-aml1 and very recently, κ B kinase (IKK), the major activator of NF- κ B which is responsible for the metastatic potential of melanoma cells [33, 35-40].

Another potential target considered to prevent tumour spreading is represented by the angiogenic process. HRzs targeted against vascular endothelial growth factor (VEGF), the principle angiogenic factor tumour-linked [41], was successfully down-regulated human hepatocellular carcinoma [42] and glioma cells [43]. Moreover, is actually under phase II trial in patients with advanced malignancy, an HRz (Angiozyme) directed against Flt-1, the human VEGF receptor [44]. Other anti-angiogenic target are represented by pleiotrophin, the cytokine hepatocyte growth factor/scatter factor with its receptor cMET and the fibroblast growth factor-binding protein [33].

Promising results in the development of potential cancer therapies have been obtained in several others studies *in vitro* or in animal models using HRzs. Anti c-fos proto-oncogene [45-46] and anti multidrug-resistance gene (MDR) [47-49] HRzs have shown to restore the sensitivity to chemotherapeutic agents in drugs resistance cancer. Anti survivin [50] and anti telomerase HRzs increased apoptosis rate and inhibited cell growth [51-56].

HRzs therapeutic potential is not limited to cancers, it covers other human pathological conditions such as those related to the cardiovascular system. In this regard, the excessive proliferation of vascular smooth muscle cells (VSMCs) represents an hallmark of many vascular pathologies such as vein graft occlusion, coronary by-pass surgery, in-stent restenosis, atherosclerosis and hypertension [57]. Many proteins responsible for excessive VSMC proliferation such as PDGF-A, TGF β -1, PCNA, transcription factor E2F1 and cyclin E has been targeted by HRzs [33, 58-60]. E2F1, PCNA, Ki-67 antigen and bcl-2 have been considered as HRz targets for other non tumour pathologies include glomerulonephritis, rheumatoid arthritis, proliferative vitreoretinopathy [33].

2.2.4 – DNAzymes

DNAzymes are DNA molecules which, in contrast to HRzs, do not occur naturally but were instead developed *in vitro* through a multi step process known as SELEX technique [61]. Based on this technique, different types of DNAzyme able to catalyzes several chemical reactions have been identified [62]. Our interest regarding, in particular, DNAzyme able to induce the catalytic cleavage of an RNA molecule due their therapeutic potential and a typical example is showed in *figure 2.3B*

called DNAzyme 10-23. The activity kinetics is similar to the HRZs with a catalytic core that perform the cleavage, flanked by two binding arms for the recognizing of target RNA [63-64].

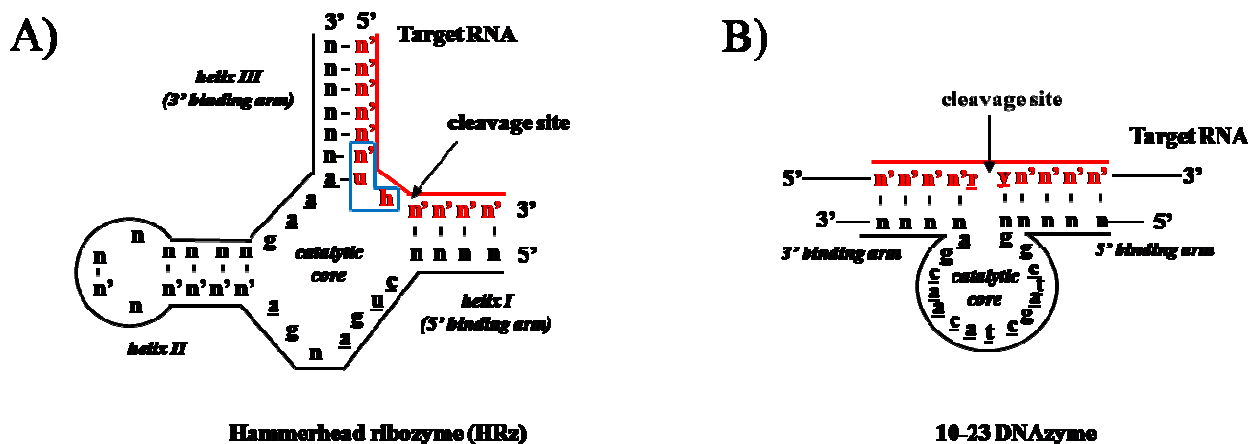


Fig. 2.3: Hammerhead and DNAzyme 10-23 structure. A) The two dimensional structure of a hammerhead ribozyme consists of three double helices numbered I, II, and III and a conserved catalytic active core (underlined); a triplet cleavage site (boxed) within the target RNA (in red), is cleaved upon ribozyme binding after the third nucleotide; the triplet is composed of the tri-nucleotide “nuh” where “n” represents any nucleotide and “h” represents “a, c, or u” (but hammerhead ribozymes which can cleave triplets ending with “g” have been also described). B) DNAzyme 10-23 two dimensional structure consists of a conserved catalytic domain (underlined) and two recognition binding arms; target RNA cleavage occurs between an unpaired purine (a, g - underlined) and a paired pyrimidine (u, c - underlined). r = purine; y = pyrimidine; n = any nucleotide; n' = a nucleotide complementary to “n”.

One of the earliest demonstrations of *in vivo* activity of 10-23 DNAzymes was in the field of chronic myelogenous leukaemia (CML), a condition caused by different possible translocations in chromosome 22. In particular, the L6 translocation, derived from the attachment of bcr exon 2 with abl exon 2 (b2a2) was considered as it contains a target site for the 10-23 DNAzyme. Notably, it was not possible to use an HRz as no ribozyme cleavage site at b2a2 junction exists. In different studies on cultured cells lines from CML patients, 10-23 DNAzyme reduced the pathological transcript, inhibit the growth and increased CML apoptosis [65-66].

As for HRzs, 10-23 DNAzymes was used to inhibit the neo-vessel formation in tumours targeting the platelet-type 12-lipoxygenase (12-LOX), known to play an important role in angiogenesis [67].

Others amenable targets for DNAzyme in order to reduce the tumour growth and induce apoptosis, are the oncogene c-jun and the Aurora kinase. C-jun is up-regulated in a variety of cancers and DNAzyme down modulation is proved to be able to reduce the growth and metastasis of pre-established osteosarcoma tumours [68]. Aurora kinase is also involved in the malignant progression of many types of cancer including prostate cancer and specific DNAzyme inhibition is able to strongly reduce its expression suppressing cell growth, inducing cell apoptosis and attenuating cell migration as demonstrated in prostate cancer cell line PC3 and DZ2 [69].

DNAzyme down-modulation has been also investigated in hyper-proliferative non tumour pathologies such as ocular neovascularisation, acute inflammation, rheumatoid arthritis [70]. In the cardiovascular field, DNAzymes targeted against the early growth response (*egr-1*) mRNA, the proto-oncogene *c-jun* and matrix metalloproteinase-2 mRNAs, have been considered in the case of in-stent restenosis and acute myocardial infarction (AMI) [71].

Other biological targets that have been successfully down-modulated by various 10-23 DNAzyme variants include viral RNAs such as human papilloma virus E6 mRNA, HIV-1 HXB2 RNA, HIV-1 gag RNA and HIV-1 TAT/Rev RNA and very recently HCV [72]; among messenger RNAs, *c-myc*, Huntingtin, protein kinase C α , integrins, laminins, vascular endothelial growth factor receptor 2 and vanilloid receptor subtype 1 have been considered [73].

2.2.5 – SiRNA

The mechanism of RNA interfering (RNAi) was first discovered in late 1990's in plant [74]. The same phenomena was observed in *C. Elegans* where the injection of double-stranded RNA molecules (dsRNA) induced the sequence-specific destruction of the target mRNA. The fact that only a few molecules were required to reduce the population of the target mRNA indicated the extremely potent mechanism of action [75].

The RNAi pathways are based on the function of two types of short RNA molecules: the micro RNAs (miRNAs) and the small interfering RNAs (siRNAs). The miRNAs are formed in the nucleus by the cleavage of an initial long precursor by specific RNase-III-type endonucleases called *Drosha*. The fragments originated by *Drosha*, form double strand RNA (dsRNA) hairpins with 2 nucleotides overhanging at 3' end and a phosphate at 5'end. In the cytoplasm, a second RNase-III-type endonucleases called *Dicer*, process the dsRNA in order to produce a 21-25 bp double strand siRNA. *Dicer* can also process dsRNA originated by RNA viruses and artificially introduced dsRNAs as demonstrated on cultured cell [76]. The siRNA is then embedded into a RISC (RNA interfering silencing complex), a protein complex where the siRNA strand complementary to the target RNA is retained [77]. The RISC complex is the final actuator of the silencing process using the short single stranded RNA as a template to recognize and cleavage the specific target mRNA [78] (*Fig. 2.4*). siRNAs can be easily predicted and produced for research purpose for virtually any target mRNA [79].

The possibility to use artificial siRNA to activate the specific silencing and the relatively stable and persists action, make the RNAi a powerful tool for the study of gene function and the therapeutic silencing of disease-related genes and human pathogens. In the field of tumour pathologies several potential applications have been investigated and many cellular mRNAs have

been targeted by siRNA. Oncogenes are the main attractive target for establishing a therapy; an example is the silencing of the *bcl-abl*, a fusion gene generated by a translocation in leukaemia. In experiments performed on leukaemia cell line, siRNA specific against *bcl-abl* is able to suppress the fusion protein without affecting the wild-type genes expression resulting in a concomitant increase in apoptosis and an inhibition of cell proliferation [80]. Other successfully targeted oncogenes, are: *runx1-cbfa2t1*, mutated forms of *p53* and the *ras* gene family [81]. Always in the field of tumour pathologies, other targets considered to be of potential therapeutic value are mediators of tumour neo-angiogenesis [82], protein kinases which are involved in many cancer biological processes [83], anti-apoptosis mediators [84] and genes conferring drug resistance such as the *mdr-1* gene which codifies the drug-efflux membrane pump P-glycoprotein [85].

Whereas the use of siRNAs in the cardiovascular field is still in its infancy, many promising investigations have been performed [86]. In this regard, siRNAs directed against relevant cell cycle promoting genes such as cyclin E1, cyclin E2 and the transcription factors E2F1 and serum responsive factor (SRF) have been developed [87]. The data suggest that these are amenable targets to down-modulate the excessive VSMC growth, an event implicated in the pathogenesis of different hyper-proliferative vascular diseases such as vein graft occlusion, coronary by-pass surgery, in-stent restenosis (ISR), atherosclerosis and hypertension [57].

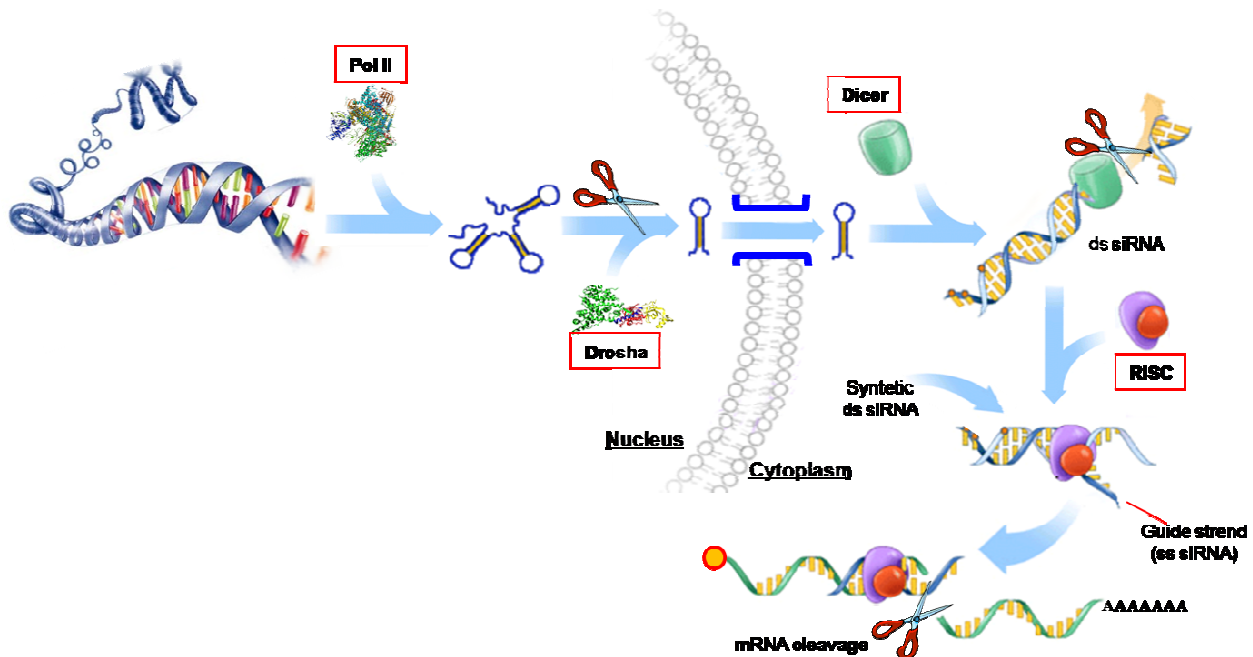


Fig. 2.4: mechanisms of RNA interference. Endogenous siRNAs are generated from transcription by Polymerase type II (Pol II) of RNA precursors. The precursors are processed by the enzyme Drosha in short RNA hairpins that translocate to the cytoplasm where encounter the enzyme Dicer. Following Dicer action, the siRNA is incorporated into the RISC complex (exogenous synthetic siRNA are directly incorporated into RISC) where the antisense strand guides the catalytic protein complex to the complementary region on the target mRNA; after recognition, the target RNA is cut and degraded.

Company Name	Molecule/Pipeline	Target	Clinical Phase	Country
Opko Health, Inc.	Bevasiranib sodium	Age-related Macular Degeneration (AMD)	Phase III discontinued	USA
		Diabetic Neuropathy	Phase II	
Alnylam Pharmaceuticals, Inc. (23 molecules in preclinical studies)	PF-4523655	Hypoxia-inducible gene RTP801.	Phase II	USA
	ALN-RSV01 Nasal	RSV nucleocapsid 'N' gene (viral infection)	Phase II	
	ApoB SNALP	(lipid disorders)	Phase I	
	ALN-VSP01		Phase I	
	CALAA01	Anti-cancer targeting the M2 subunit of RRM2	Phase I	
	Alnylam/CFFT Cystic Fibrosis Program	Cystic Fibrosis	Preclinical	
AlphaGEN Company, Ltd .	Hypoxia-inducible factors Inhibitors	Control factor for HIF (hypoxia-inducible factor)	Research	Japan
	siRNA Viral Infection Treatment Program	Viral infection target foreign (non-human) gene sequences	Research	
Benitec Ltd.	HIV RNAi Program	Long-term inhibition of HIV replication	Phase I	Australia
	Diabetes/Obesity RNAi Program	Based on the partial, tissue-specific ablation of c-Cbl gene	Preclinical	
Biomics Biotechnologies Co., Ltd.	AMD Program, Biomics	Data not available	Preclinical	China
Cequent Pharmaceuticals, Inc.	CEQ501	Inherited bowel tumor	Preclinical	USA
	Cequent / Novartis IBD Program	Inflammatory Bowel Disease (IBD)	Preclinical	
Dicerna Pharmaceuticals, Inc.	DsiRNAs Program	Rheumatoid Arthritis	Preclinical	USA
	Virology Program	Hepatitis C	Preclinical	
	Oncology Program	Solid tumors	Preclinical	
Genesis Research & Development, Corp.	Genesis RNAi Program	Allergy	Preclinical	New Zealand
Intradigm, Corp. (8 molecules in research studies)	ICS-283	Multiple VEGF pathway genes.	Preclinical	USA
	SARS siRNA Nasal	SARS	Preclinical	

Tab. 2.1: list of company and research line challenging the RNAi-based therapeutic products market (source: PharmaCircle™ - September 2009).

2 – Nucleic Acid Based Drugs (NABDs)

Company Name	Molecule/Pipeline	Target	Clinical Phase	Country
Kylin Therapeutics, Inc.	RNAi Cancer Program	Cancer	Research	USA
MDRna, Inc. – Nastechn (12 molecules in preclinical studies)	G00101	Multiple influenza strains, including avian flu strains (H5N1)	Preclinical	USA
	Nastechn siRNA Inflammatory Program	Rheumatoid Arthritis	Preclinical	
	MDR-04227	Targeting Apolipoprotein B (ApoB) (Lipid lowering)	Preclinical	
	MDR-09521	Bladder cancer	Preclinical	
	MDR-06155	IBD and rheumatoid arthritis	Preclinical	
Mirus Bio, Corp.	Mirus/Pfizer RNAi Program	Undisclosed	N/A	USA
Nucleonics, Inc.	NUC-B1000	Hepatitis B	Phase I	USA
	Nucleonics HCV Program	Hepatitis C	Preclinical	
	Nucleonics Influenza Program	Influenza	Preclinical	
Quark Pharmaceuticals, Inc. – PAb-W4 Quark Biotech (10 molecules in preclinical studies)	PF-4523655	Wet Age-related Macular Degeneration (wet-AMD)	Phase II	USA
		Diabetic Macular Degeneration (DME)	Phase II	
		Diabetic Retinopathy	Preclinical	
Silence Therapeutics Plc	QPI-1002	Acute Renal Failure	Phase I	USA
RXi Pharmaceuticals, Corp. – Argonaut Pharmaceuticals, Inc. (5 molecules in preclinical studies)	RXi RNAi Infectious Diseases Program	Infections (CMV)	Preclinical	USA
	RXi ALS Program	Amyotrophic Lateral Sclerosis	Preclinical	
Sirna Therapeutics – Ribozyme Pharmaceuticals, Inc. (5 molecules in preclinical studies)	AGN-745	Wet Age-related Macular Degeneration (wet-AMD)	Phase II	USA
Sirnaomics, Inc. (3 molecules in preclinical studies)	STP-601	Wet Age-related Macular Degeneration (wet-AMD)	Preclinical	USA
		Eye diseases	Preclinical	
		Diabetic Retinopathy	Preclinical	
siRNAsense AS	Tissue Factor Program	Melanoma Malignant Cancer	Preclinical	Norway

Tab. 2.1: continue from previous page

SiRNAs have also been considered for other human disease; they are able to interfere with the replication of different viruses responsible for human pathologies such as Hepatitis, HIV, Enterovirus and others [88-91], they can be used for the treatment of genetic disease such as Diabetes related disease and Cystic Fibrosis and finally, for the controlling of multifactorial disease (Macular Degeneration, Rheumatoid Arthritis, Allergy). In order to place the accent on the therapeutics potential of RNAi, in *table 2.1* are showed the company that are going to challenging the market with pharmaceutical products based on that technology

2.2.6 – Antisense oligonucleotide

Antisense oligonucleotides (ASOs) are short single-stranded segments of DNA or RNA (13-25 nucleotides long) that hybridizes with complementary RNA molecules via Watson-Crick base pairing. The DNA/RNA or the RNA/RNA duplexes induce an inhibition of gene expression by several mechanisms that can occurs at the same time [92-93].

- a) Translational Blocking of the target mRNA into protein by steric hindrance of ribosomal movement along the transcript. This effect is particularly efficient when ASOs are targeted to the 5' mRNA untranslated region but not to mRNA coding regions where ASOs probably, are easier to remove by ribosomal machinery [94].
- b) Activation of endogenous RNase H (a ubiquitous enzyme) that cleaves the DNA/RNA heteroduplex (in the case of DNA ASOs). After the mRNA cleavage, the DNA ASOs is free for another binding [95].
- c) Splicing and mRNA maturation inhibition by ASOs hybridization to the 5' or 3' pre-mRNA regions and intron/exon cutting sequences. The consequence is the prevention of 5' capping, 3' polyadenylation and introns excision with the accumulation of splicing intermediates and reduction in mRNA stability [96].

Whereas in principle any RNA sequence can be targeted by ASOs, some variables related to the thermodynamic stability of the ASO/RNA duplex, the secondary structure of the target mRNA and the proximity of the hybridization site to functional RNA motifs [97] limit the number of sequences which can be efficiently targeted.

So far, Formivirsen (Vitravene) is the only ASOs approved by USA FDA [98]. This is a phosphorothioate oligonucleotide which targets the immediate-early RNA encoded by the cytomegalovirus (CMV) thus inhibiting CMV-induced retinitis. Another attractive field were ASOs have been tested includes the prevention of in-stent restenosis with ASOs directed towards cell cycle regulator genes to inhibit VSMC proliferation. The effectiveness of a phosphorothioate ASO against the proto-oncogene *c-myc* after local administration in the rat carotid, was demonstrated

[99] and a phase II trial, currently is underway using a phosphorodiamidate morpholino called AVI-4126 against the translation initiation start site of c-myc. Other study on mice model, demonstrate the capability of a single administration of an ASO against proliferating cell nuclear antigen (PCNA) or cdc2 kinase to inhibited neointimal formation after angioplasty [100]. A similar effect was obtained after treatment of cyclin B1 and cdc2 ASOs combination [101], intracellular signal transducers such ras and raf kinases [102] or the anti-apoptotic Bcl-x [103].

The therapeutic potential of ASOs obviously covers many other human pathologies among which cancer diseases [104]. In this regard, for examples, an anti h-ras ASO and anti insulin-like growth factor receptor tyrosine kinase IGF-1R demonstrated the therapeutic potential for hepatocellular cancer (HCC) both *in vitro* and *in vivo* [105-106].

2.2.7 – Aptamers

Aptamers are short stretches of single-stranded DNA or RNA potentially able to recognize with high affinity any given molecular targets, such as proteins, carbohydrates, metal ions and small chemicals modulating biological functions in an agonistic or antagonistic fashion. They can prevent protein functions

- a) by recognizing a secondary structure of the protein thus occupying an active site and blocking its function,
- b) by inducing the conformational change of the protein following the recognition of a specific site,
- c) by interfering with the assembly of high order protein complexes *via* the binding to a site necessary for quaternary structure or for protein-protein interactions.

Moreover, aptamers can also recognize secondary structures of mRNA involved in maturation/splicing processes. Generally, the aptamers fold into a specific three-dimensional structure forming pockets that recognize the cognate target by shape complementary [107]. Notably, low order structured aptamers can efficiently bind a target too [108]. Optimal aptamers can be easily identified and selected by systematic evolution of ligand *via* exponential enrichment (SELEX). Recently, moreover, the introduction of capillary electrophoresis (CE-SELEX) greatly reduced the round for the selection of the best ligand [109].

The first aptamer approved by FDA is *Macugen* (pegaptanib sodium), a 29-mer RNA with a chemically modified backbone conjugated at 5'-terminus to 40kDa polyethylenglicole. This molecule is specific for the VEGF isoform 165 and is used for the treatment of the age-related macular degeneration of the retina. The high specificity allows to down-regulate only the isoform 165 inhibiting cell proliferation and vascular permeability without affecting the physiological

isoform VEGF₁₂₁ [110]. For its safety profile and the therapeutic benefit in regression or block of the retinal neovascularization, Macugen use has been extended to patients with diabetic macular edema and with macular edema secondary to central retinal vein occlusion [111].

Aptamers have also found potential applications in the cardiovascular field. Aptamers acting as antagonist of thrombin were the first molecules tested and demonstrated to produce a rapid anticoagulation effect [112]. Moreover, aptamers directed against the transcription factor E2F3 have been shown to down-modulate VSMC proliferation, a key event in vein graft occlusion, in coronary by-pass surgery and in-stent restenosis [113].

Another challenging in the use of aptamers is the cancer therapy. In few years, they were successfully used to target key proteins implicated in tumours as glioblastoma [114], breast cancer [115], colon cancer [116] and non small cell lung cancer [117]. In mice, tumour angiogenesis was reduced by aptamers anti platelet-derived growth factor [118]. Recently, was identified an aptamer anti eEF1A, a protein involved in the onset and progression of human cancers modulating survival and growth mechanisms through cytoskeletal reorganization, protein degradation, apoptosis and signal pathways [119]. Notably, non-tumour cells were not sensitive to the selected aptamer suggesting a possible target in tumour therapy [108, 120-122]. Actually, only one aptamer named AS1411 and developed by Aptamera Louisville (NY) was selected for phase I clinical trials. Targeting nucleolin, a protein overexpressed in many tumours, it is able to inhibit cancer growth [123-124].

Finally, aptamers could be used in diagnostic. The first experiments were performed in rat and mice *in vivo* models detecting, through aptameric labelling of specific proteins, inflamed tissue [125] and tumour extension [126].

2.3 – NABD delivery strategies

The potential therapeutic applications of NABDs were clearly demonstrated by a number of studies and research lines but, *in vivo*, their utility has been hampered by the difficulty to properly deliver on the target tissue.

The first barrier, in case of systemic applications, is represented by the blood nuclease that can rapidly degrade a naked NABD [127]. In proximity of the target tissue, in the extracellular matrix compartment, NABDs are subject to other enzymes that are able to nullify its activity. The fraction of NABD which escape degradation, have to pass through the cell membrane which is a difficult step because of the nature of NABDs and membrane lipid double layer. The hydrophilic nature of NABDs does not allow the lipophilic membrane crossing and, moreover, an electrostatic

repulsion between negatively charged phosphate group and negatively polarized cell membrane occur. Once in the cellular environment, NABD are susceptible to further degradation by intracellular nucleases and the cellular trafficking such as endosomal release and cytoplasmic transport should be considered [128-129]. Considering all that barriers, only a small fraction of NABD reach to the target resulting in a negligible biological effects.

In order to overcome these problems, several approaches have been developed but, basically, they can be divided in two major categories: endogenous and exogenous. The first is based on the use of viral vectors, commonly used in gene therapy studies. This approach implies the introduction of the nucleic acid materials coding for the NABD into the backbone of a viral vector which in turn carries the NABD into the cell. Once in the cells, the NABD is continuously expressed from the viral backbone by means of appropriate promoters. The limitation of this approach is due to the possibility to delivery only RNA based NABDs which can be transcribed from a double stranded DNA molecule, and not DNA based NABDs. Moreover, concerns about viral vector safeties are still unsolved. Opposite, the advantages of viral vector, regarding the transfection efficiency and long term effect. In contrast to the endogenous systems, the exogenous methods can be used to deliver all kinds of NABD with apparent no relevant side effects. This approach is based on the chemical modification of NABD structure and/or the complexation/binding to different synthetic vectors. The advantages consist in the flexibility, strategies coupling, lower immunogenicity and applicability to any type of NABDs, included the plasmidic expression cassettes for a much stable effects; disadvantage is constitute by the difficulty to achieve a comparable transfection efficiency and specificity of viral vector.

2.3.1 – NABD chemical modifications

Physiologic nucleotides that constitute genetic material are made by three different chemical groups:

- a) a five carbon atoms sugar, ribose in RNA and deoxyribose in DNA
- b) an organic base containing nitrogen, such as purine and pirimidine
- c) phosphate groups, that are linked with a phosphodiester bond to the carbon 5' of the sugar structure.

All of those building blocks have been proposed for chemical modifications in NABDs in order to improve the bio-availability and cell penetration *in vivo* conditions [127, 130].

2.3.1.1 – Modification involving phosphate moiety

Phosphorothioate modification (PS) involves the substitution of the non-bridge oxygen of the phosphate group with a sulphur atom and is the most known modification regarding this group (Fig.2.5B). The introduction of some PS nucleotides in to the final oligonucleotide, resulting in an increased resistance to nucleases *in vivo* and a greater plasmatic half-life, as a consequence of an high serum protein affinity [131-132], maintaining a similar or lower activity than native one [133-134]. *Formiverson* (Commercialized as *Vitravene*TM), a NABDs against CMV, is the first example of PS oligonucleotide on the market and many other are in advanced clinical experimentation with promising results [135]. The possibility to use PS nucleotides to obtain functional and active oligonucleotides depends on the chain architecture [136]. Generally, the introduction of PS nucleotides in the centre of oligonucleotides inactivate siRNA activity, while the modification in the extremities of the molecule does not [137]. Oligonucleotides containing few PS modified units and unmodified nucleotides had success in various animal experimentation [127, 138], while oligonucleotides caring many PS nucleotide have been described to be toxic without evidence of any biodistribution improvement [133, 139].

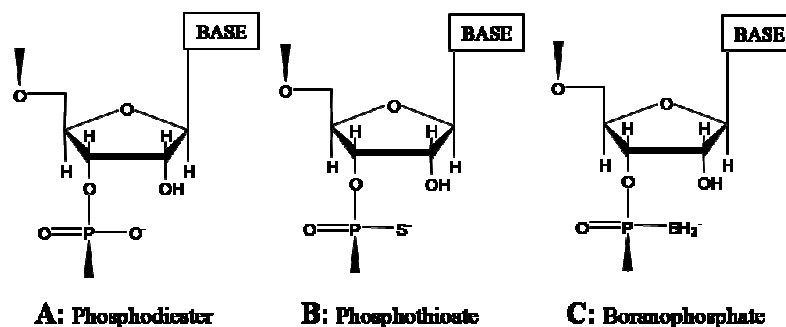


Fig. 2.5: phosphate moiety modifications. Representation of typical phosphate moiety modifications compared with the physiological nucleotides (A).

Another modification is the boranophosphate that concerns the insertion of a boran group -BH₃- in the place of the native free hydroxylic moiety (Fig. 2.5C). According to some authors, besides the increased stability against nucleases this modification is more profitable than sulphur substitution because, when present in nucleotides at the end of the chain, confers to siRNA increased activity in comparison to the respective unmodified nucleotides [134]. Unfortunately, the methods for introduction of BH₃ groups in oligonucleotides is plodding and not suitable for large scale production [140].

Other modifications have been operated on phosphoric moiety, such as complete substitution of the phosphoric group with an amide group [141] and the displacement of the phosphoric moiety from the oxygen on 3' to the oxygen on 2' [139]. However both substitutions gave oligonucleotides with low activity [139].

2.3.1.2 – Modification involving sugar moiety

Sugar modifications are the most frequently proposed modification of oligonucleotides (Fig. 2.6). The hydroxyl group on position 2' of the sugar moiety (2'-OH) has been extensively modified, being possible to change the bearing group on this position without any activity loss [142]. The simplest modification on this position is the 2'-O-Methylation (2'-O-Me) of nucleotide that causes an increase in mRNA target affinity and improves its stability towards nucleases (Fig. 2.6B). In ASOs, the methylation, on one side improves duplex stability but make it unable to activate the RNase-H otherwise, the capacity to reduce target protein level by the steric block of translation still retained [143]. In many different experimental observations was found that only the partial 2'-O-Me modification gives perfect functional siRNAs instead, full modification of the double strand, decrease siRNA activity [144] or produces complete ineffective oligonucleotides [145]. In any case, different results most likely depend on the heterogeneity of the oligonucleotide groups considered and on the targets chosen.

Another possible modification on 2' ribose position is 2'-O-Methoxyethyl (2'-O-MOE) (Fig. 2.6C). The resulting oligonucleotides have higher affinity and specificity to targets than their 2'-O-Me analogs [146-147]. ASO bearing 2'-O-Methoxyethyl modification have demonstrated a good *in vivo* bioavailability especially in combination with other modifications [148] such as on partially phosphorothioate oligonucleotides [149].

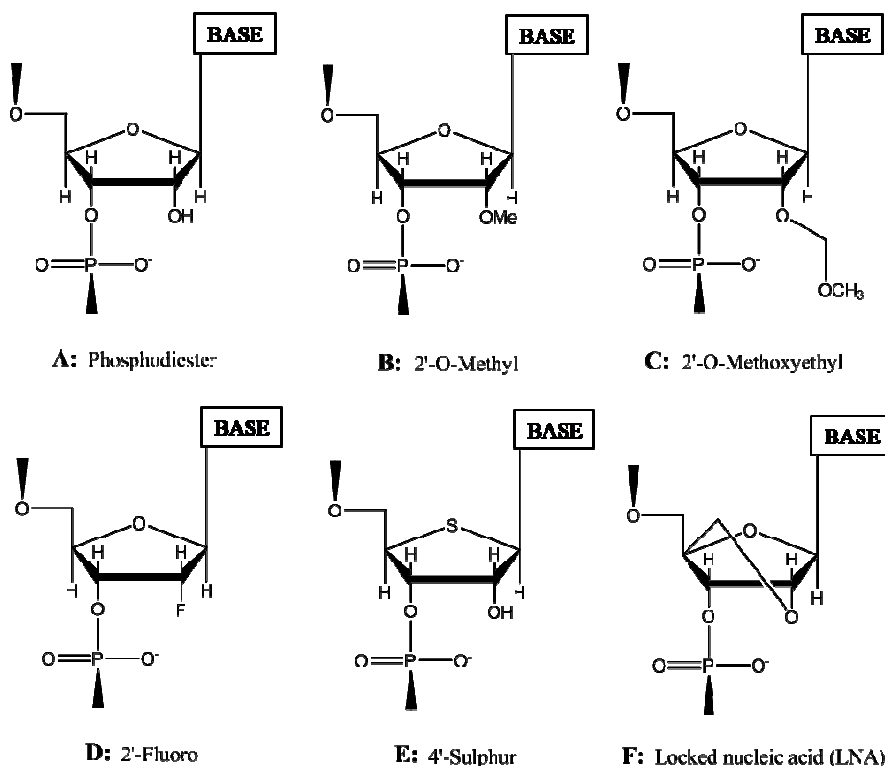


Fig. 2.6: sugar moiety modifications. Representation of typical sugar moiety modifications compared with the physiological nucleotides (A).

Commonly use modification is the 2'-OH substitution with a fluorine atom (2'-F) (*Fig. 2.6D*). Partial modification is tolerated in both siRNA strands obtaining functional derivatives [142] and it has been demonstrated that 2'-F modification, increases nuclease resistance in mouse plasma, but not the activity or half-life [150]. Some authors have also synthesized full fluorinated oligonucleotides that, in contrast with the previous described modification, have demonstrated good activity [151]. 2'-F oligonucleotides with modified stereochemistry were synthesized obtaining 2'-F epimeric derivatives, called 2'-deoxy-2'-fluoro β -D-arabinonucleic acids (2'-FANA) [152]. They are resistant to nuclease degradation and the use of FANA units in oligonucleotides is well tolerated throughout the sense strand of the duplex siRNA increasing half-life, as well activity [153]. Experimental evidence shown that the substitution of two riboses with FANA at the 3' end of the antisense strand was sufficient to increase the potency over the native siRNA, with prolonged protein knockdown [154].

In addition to changes on 2' positions, other ribose modifications have been explored and one of the most interesting is the change of the oxygen in the ring with sulphur resulting in a 4'-S-oligonucleotide (*Fig. 2.6E*). This modification has been proposed with good results especially on nucleotides inserted in terminal position in the oligonucleotides [155] with enormous advantages in nucleases resistance. However it was also evidenced that the insertion of 4'-S modified nucleotides in inner positions of oligonucleotides leads to loss of the activity [156]. In ASOs, these kind of modifications have demonstrated to increase biodistribution due to the increased affinity to the serum proteins that act as depot system able to slowly release the oligonucleotides [155]. 4'-S modification has been used successfully in combination with other modification, such as 2'-O-MOE conferring great activity and excellent resistance to serum degradation [156]. Another combined modification involves 4'-S and 2'-FANA in the same nucleotide structure. These interesting nucleotides, usually, do not generate unstable double stranded oligonucleotides, a fact which can occur increasing the amount of modified nucleotides [153].

Another modification on the sugar moiety is represented by a methylic bridge between the oxygen in 2' and the 4' carbon, that lead to the formation of the locked nucleotide (LNA) (*Fig. 2.6F*) [157]. The insertion of the bridge give an increased structural rigidity blocking the ribose in the 3'endo conformation [158-159] and resulting in a great thermodynamic stability [160]. The insertion of LNA in oligonucleotides can be performed only in few positions, commonly on the termini of the siRNA sense strand [161] or in 3' overhangs of the antisense strand [162]. Heavy siRNA modifications or modifications in the centre of the structure lead up to strong activity loss [163]. Some works report functional siRNAs with an heavy content in LNA nucleotides, but only in the sense strand [163]. In ASOs, LNA inserts generate oligonucleotides with good blood serum

resistance and interaction with RNase-H [164-165]. An ASO containing a mix of LNA and native DNA nucleotides from Santaris Pharma (SPC-2996) is in phase I/II clinical trials in patients with severe chronic lymphocytic leukaemia [166]. It should be noted that some oligonucleotides containing LNA have demonstrated hepatotoxicity [167], a fact that make further investigation necessary.

2.3.1.3 – Deep modification of the chemical structure

Some authors have proposed to introduce strong modification in the entire structure of the oligonucleotide (*Fig. 2.7*). Peptide nucleic acids (PNA) are oligonucleotide mimic molecules, with polyamide backbone replacing phosphate and ribose bearing portions. This modification confer high affinity and specificity to complementary sequences of DNA and RNA and also improve resistance to nuclease without proteinase susceptibility [168].

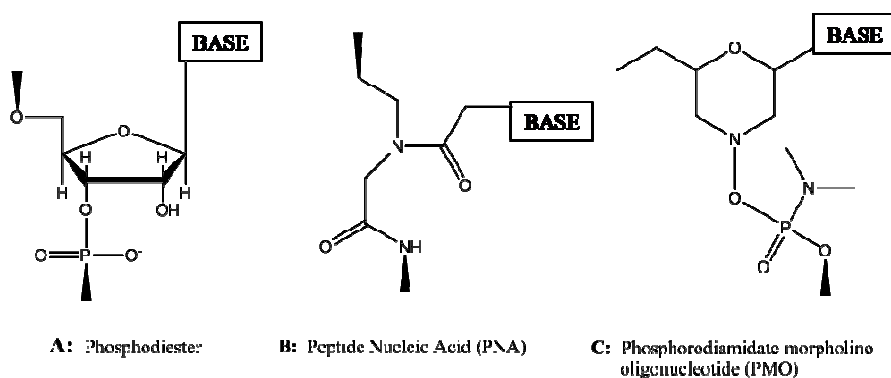


Fig. 2.7: deep phosphodiester modifications. Representation of typical deep phosphodiester modifications compared with the physiological nucleotides (A).

Another oligonucleotide mimic molecules studied is the phosphorodiamidate morpholino oligonucleotide (PMO) where ribose is replaced by morpholin [169]. Morpholino derivatives in ASOs raised great interest for their RNase-H independent activity as steric blocking agents towards the target mRNA [170]. Several animal models have demonstrated *in vivo* the antisense specificity and efficacy of morpholino derivatives against their targets with good biological stability and safety profile [171-173]. Some authors proposed the delivery of these types of oligonucleotides by peptide carrier [174].

2.3.1.4 – Oligoconjugates

This approach consists of the chemical conjugation to the NABDs of various molecules, such as cholesterol and derivatives, aminoacids, polyethylen glycol, or peptides. It has been demonstrated that, oligoconjugation is able to improve siRNA thermodynamic and nuclease stability, to increase *in vivo* half-life and cellular uptake [175-176] and to achieve cell specific

targeting [127, 177-178]. Conjugation was also successfully applied to ASOs [179] and to TFOs. In particular, TFO-cholesterol conjugate showed improved pharmacokinetic profile and liver accumulation after systemic administration [25].

An interesting optimization, is the conjugation with cell penetrating peptide (CPP) that is a class of peptides with helical structure composed by many cationic aminoacids [180] with the capacity to penetrate plasma membrane improving intracellular delivery [181]. Moreover, a disulphide bridge could be easily used as conjugation strategy by introduction of a cysteine and a thiolic group respectively in CPP and oligonucleotides structure. Once in the cell environment, the disulfide link is reduced thus releasing the active oligonucleotide in the cytoplasm [175].

2.3.2 – Synthetic vector for NABDs release

Synthetic vectors can be subdivided into three classes on the basis of their characteristic length [182]: nano, micro and macro scales vectors. In general, nanoscale vectors are represented by polycationic polymers or lipids that self-assemble with NABD to form polyelectrolyte complexes. Microscale vectors usually consist of NABD entrapped within a polymeric matrix and macroscale vectors are two/three dimensional scaffolds or matrices (mainly polymeric but not only) hosting the desired NABD. Of course, it is possible to embed nanoscale vectors inside macroscale vectors so, the first protect the NABDs and favour the cell internalization, while the second modulate the release kinetics at the site of action.

The net superficial charge of the delivery system-NABD complex plays a key role for what concerns extra-cellular barrier crossing. Anionic and cationic complexes both usually show good solubility and stability in the physiological environment.

On the other side, anionic complexes, in principle cannot transfect cells in virtue of the electrostatic repulsion with the negatively charged cell membrane. Instead, cationic complex strongly bind to the membrane leading to non-specific cellular uptake through endocytosis [183] unlucky, this strong interaction, can cause membrane disruption and consequent cell death. Moreover, the presence of negatively charged blood proteins can induce the formation of complex-protein aggregates that are no longer soluble, precipitate and are quickly cleared by phagocytic cells [184]. Whereas neutral complexes are not affected by the above mentioned problems, in the physiological environment they tend to associate each other resulting in a limited solubility.

2.3.2.1 – Liposomes

Liposomes are vesicles containing an internal aqueous compartment separated from the external environment by a bilayer membrane (approximately 4 nm thick) constituted by amphiphilic

lipids. The polar heads are oriented towards the external and internal environments while, the apolar tails form a hydrophobic environment inside the membrane. Environmental conditions (such as lipids concentration, temperature, pH and so on) and lipids chemical-physical properties strongly influence the membrane characteristics, liposome topology and size ranging between 50 nm and 1 μm . The Liposome-NABD complex (also known as lipoplexes) is able to cross cellular membrane and to release NABD in the cytoplasm or in the nucleus [185]. Liposomes for NABDs delivery are based on cytofectins that are a class of synthetic cationic amphiphiles with a positive charged head group attached by a linker to a hydrophobic moiety [185]. The most important lipids used for gene delivery are made by oligoamines linked to cholesterol or dialkyl groups called cytofectins [186]. Cytofectins show low immunogenicity responses [187] and commonly are used in combination with neutral lipids. The first commercially available liposome was *Lipofectin*TM, a 1:1 ratio of DOTMA cytofectin (N-[1-(2,3-dioleloxy)propyl]-N,N,N-trimethylammonium chloride) and the naturally occurring neutral lipid DOPE (dioleoyl-1- α -phosphatidylethanolamine) [188]. From this starting point, many other cationic liposomes were developed [185, 189]. The surface of many liposomal carriers could be covered with a stealthing agent in order to overcome the problems of interaction with polyanionic physiologic molecules, such as glycosaminoglycans and serum proteins (i.e. albumin) [190]. The most commonly used stealthing agents are PEGs and their derivatives that are able to decrease the auto aggregation of liposomes, the immunostimulation and to increase the NABD/liposome complex stabilization [191-192].

Despite the simplicity of the general mechanism, a deep understanding of liposome-mediated NABD delivery requires to consider three main aspects:

- a) the characteristics of the liposome-NABD complex,
- b) the mechanisms involved in complex entry into cells,
- c) the NABD delivery to nucleus.

It is commonly known that NABD electrostatically bound on liposome surface and/or is encapsulated into the core of liposome during the lipids self-assembling but, experimental evidences have shown that liposome/NABD complexes are very heterogeneous and dynamic, varying in size and shape depending upon the molar ratio of liposomes to DNA (most important changes in structure taking place when the positive/negative charge ratio is around 1) with the establish of an equilibrium (30-60 min after mixing) between encapsulated, surface bound and naked NABD [185]. It has been proposed that liposomes can neutralize the negative charge of NABD to induce a cooperative collapse of the NABD structure. As consequence of the conspicuous reduction of the exposed surface area, collapsed NABD could then be efficiently encapsulated by lipid [193] preventing NABD from degradation induced by nucleases and ultrasonic action [194].

X-ray analysis confirm that NABD can be encapsulated in highly ordered multilamellar structures and sandwiched between cationic bilayers [195].

Although phagocytosis and cellular membrane fusion cannot be totally excluded, it is believed that endocytosis is the leading mechanism ruling liposome-NABD complex entry into cells [196] and that this phenomenon is mediated by proteoglycan interactions [197]. After initial association to the cell surface the complex is endocytosed and storing inside endosomes. Here, retained complexes destabilise endosome membrane according to a flip-flop mechanism involving endosome membrane anionic lipids. This destabilisation allows NABD escaping from the endosome to reach the cytoplasm. In case endosome escape does not occur, liposome-NABD complexes accumulate in the perinuclear region (~24 h) due to endosome migration towards the nucleus. Then, endosome fusion allows enclosed complexes coalescence to form macromolecular lipid/NABD structures. In case the nucleus is the NABD target, the NABD fraction escaped from endosomes needs to overcome the nuclear membrane and the successfully crossing depends on the NABD size. Whereas small NABD readily accumulates into the nucleus, larger NABD cannot cross the nuclear membrane whose cut-off is of about 40 kDa [198]. In general, complex entry into the cells is a very efficient process (although not rapid: it takes more than 6 hours). However, only the NABD fraction escaping endosomes can exert its biological effect.

Excellent hepatocellular carcinoma cells siRNA and aptamer delivery efficiencies was observed using *Lipofectamine*[™], a commercially available 3:1 (w/w) liposome formulation of the polycationic lipid DOSPA (2,3-dioleoyloxy-N-[2(sperminecarboxamido)ethyl]-N,Ndimethyl-1-propanaminium trifluoroacetate) and the neutral lipid DOPE (Farra et al, unpublished results). siRNAs were delivered with good results formulated as liposome prepared with DOTAP and PEG-phosphatidylethanolamine, using arginine octamer on liposome surface as cell penetrating peptide (CPP). This lipoplexe had high stability and conferring to carried siRNA resistance towards degradation in serum even after 24 h of incubation and high transfection efficiency in lung tumour cells [199]. Other authors proposed a mixture of b-L-arginyl-2,3-L-diaminopropionic acid-N-palmityl-N-oleyl-amide trihydrochloride (AtuFECT01), 1,2-diphytanoyl-sn-glycero-3-phosphoethanolamine (DPhyPE) a neutral lipid, and 1 mol% PEGylated lipid N-(carbonyl-methoxypolyethyleneglycol-2000)-1,2-distearoyl-sn-glycero-3-phosphoethanol-amine sodium salt (DSPE-PEG), demonstrating that the resulting liposomes are able to delivery siRNA into the tested cell lines efficiently silencing the target protein. Moreover the presence of small quantity of PEG was able to reduce *in vivo* toxic side effects showing also a delay in the clearance rate [200].

Cholesterol modified cationic lipids (AH-Chol-liposomes) [201-202] were used to encapsulate anti c-myc ASO-protamine aggregates and deliver it to U937 cells (protamine is a

nucleotide condenser and stabilizer protein similar to histones). The result demonstrate an increased stability of ASO due to the protection against nucleases, a significantly reduction of toxic effects exerted by the AH-Chol-liposomes alone (most likely depend on the neutralization of AH-Chol-liposomes by ASO-protamine aggregates) and most important, a marked reduction of target gene amount in contrast to the ASO-protamine aggregates alone.

Particularly original is the release of an siRNA-coding DNA plasmid by means of an envelope-type nano device (MEND) [203]. The MEND is composed of a plasmid DNA condensed by protamine contained in a lipid envelope made by DOPE and cholesteryl hemisuccinate in a molar ratio of 9:2) and modified by an octaarginine (R8) peptide, a CPP. The transfection activity of MEND in COS7 cells was as high as that of an adenoviral vector and of the commercially available transfection reagent Lipofectamine 2000 without elicit significant cyto-toxicity. The cellular uptake of the MEND, directed by R8 peptide, was found to be mainly by macropinocytosis, a fact which was responsible for the high transfection activity by virtue of its escaping lysosomal degradation. Importantly, the expressed siRNA was able to reduce the amount of the target mRNA down to 30% of control.

A new and interesting category of liposomes is represented by the echogenic liposomes [189] that is category is constituted by usual liposomes incorporating a gas that can reside in the internal aqueous environment or in the lipidic bilayer (*Fig. 2.8*) and make liposomes sensitive to ultrasound wave having frequencies equal or greater than 20 kHz. The stability of gas encapsulation is highly dependent upon the encapsulated gas kind and the lipid shell properties such as gas diffusion across the lipid shell, thickness of the lipid shell, size of the microbubbles and the presence of human serum and albumin [189]. The ultrasound cause compression and expansion of the transmitting medium and a little oscillatory displacement of the medium upon wave passage. The effects on cells and liposomes can be divided in thermal effects (associated with the absorption of acoustic energy) and non-thermal effects, the most important of which is cavitation that implies the rapid growth and collapse of bubbles (inertial cavitation) or the sustained oscillatory motion of bubbles (stable cavitation). The collapse of cavitation bubbles leads to the formation of shock waves or high-velocity microjets with consequent cells damage and liposomes explosion allowing NABDs release. However, the presence of pre-existent cavitation nuclei such as the gas phase contained in echogenic liposomes, considerably lower ultrasound intensity thus minimizing cellular damage and therefore, is possible to use a low intensity ultrasound field to induce a cavitation effect able to allow NABD release with limited cells and tissues damage by the formation of transient pores in the cellular membrane by-pass the problem of NABD escape from endosomes [204-205].

The sensitivity of echogenic liposomes to ultrasonic stimulation is related to liposomal composition as well as to the encapsulated gas and the ultrasound application parameters [189].

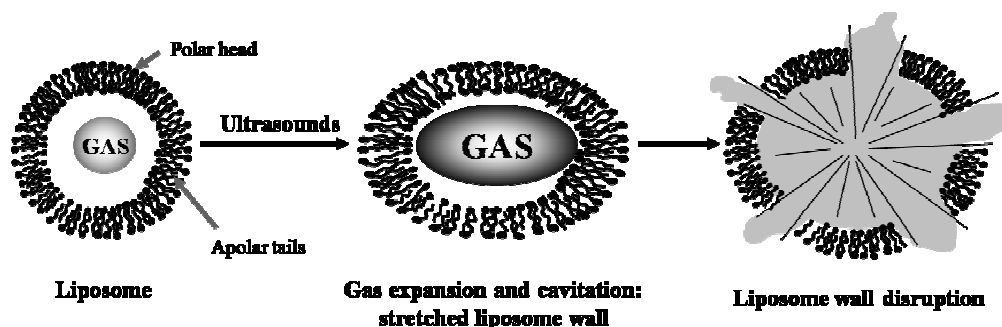


Fig. 2.8: echogenic liposomes. Liposome wall is made up by molecules showing a polar head and an a-polar tail. Echogenic liposomes contain an inner gas phase that, in presence of ultrasounds, undergoes expansion, contraction and vibration (cavitation). These phenomena comport liposome wall stretching up to rupture.

Cell culture experiments proved the applicability of this technology using a polyethyleneglycol modified liposome (PEG-L) to successfully targeting a fluorescent siRNA on COS7 and NIH3T3 cell lines with ultrasound stimuli of just 10 seconds [206]. Other experiments demonstrate that the use of echogenic liposomes comported significant improvement (up to 18-fold) in DNA transfection [207]. *In vivo* this approach seems to be attractive as it can deliver siRNA in the presence of serum, an element which can significantly impair the efficacy of common transfectants. On this regards, it has been observed that when this approach has been used to transfer the siRNA *in vivo* into the tibialis muscles of rat, the silencing effect lasted for more than 3 weeks. It should be noted that the use of the US mediated delivery has been proven to be suitable also for decoy ODN [208].

Concluding, echogenic liposomes can be use to realizing a targeted delivery by focusing ultrasound, can be easily visualized by ultrasound diagnostic and can improving NABD cellular internalization.

2.3.2.2 – Mesoporous silica nanoparticles

Mesoporous silica are solid materials, typically with a particle diameter ranges between 50 and 300 nm, composed by a honeycomb-like porous structure characterized by many empty not interconnected channels (mesopores) that are able to absorb/encapsulate relatively large amounts of bioactive molecules (up to hundred milligrams per gram of nanoparticles) (Fig. 2.9). Examples of this material are MCM-42 and SBA-15 silica. Characteristic such as biocompatibility, high surface area ($> 900 \text{ m}^2/\text{g}$), large pore volume ($>0.9 \text{ cm}^3/\text{g}$), tuneable pore size with a narrow distribution (2-10 nm), good chemical and thermal stability in addition to the availability of surface modification, make mesoporous silica very interesting for controlled release applications [209]. Surface

modifications are particularly important in the case of NABDs delivery in order to facilitate cellular uptake. Even if the silica affinity for the head-groups of many membrane phospholipids is well known, some modification can improve the internalization by specific interactions between cell membrane and mesoporous silica surface. Although no cell surface receptors for silica nanoparticles are known, their cellular internalization occurs according to the energy-dependent mechanisms of clathrin-coated endocytosis and pinocytosis [210]. Proper functional groups modification of particle surface make possible to control nanoparticle uptake efficiency as well as their ability of escaping from endosomal compartments. This surface modification can take place according to three techniques: co-condensation, grafting (post synthesis modification,) and imprinting coating method [211]. Typically, ureidoalkyl, mercaptoalkyl, cyanoalkyl, aminoalkyl, allyl, isocyanatoalkyl, epoxyalkyl, phosphonatoalkyl and metal-aminoalkyl functional groups can be introduced on nanoparticles surface.

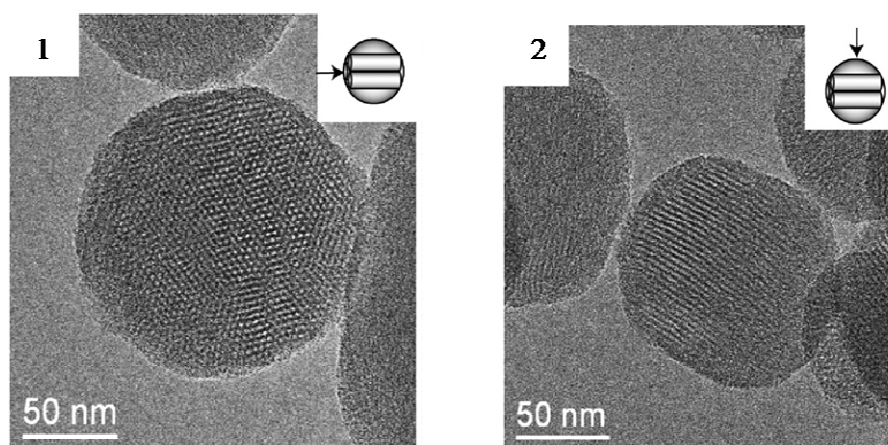


Fig. 2.9: mesoporous silica nanoparticles. TEM image of mesoporous silica nanoparticles according to the direction parallel (1) or perpendicular (2) to mesochannels long axis.

Normally, the active principles are stored into the channels of the mesoporous silica nanoparticles and the release is caused simply by the emptying of the channels. The new generation of silica nanoparticles are characterized by a stimuli responsive drug delivery made possible using the technique of “gatekeepers” [209]. The principle is based on the fact that, the drug present inside the channels can be released only upon removal of the obstruction from the terminal part of silica nanoparticles channels. The obstruction (the gatekeeper) is an organic molecule, a supramolecular assembly or another nanoparticle responsive to particular photochemical, pH and redox conditions. For example, Slowing and co-workers [209], used gold nanoparticles and PAMAM dendrimer (see below) as gatekeepers for plasmid DNA delivery from silica nanoparticles obtaining a transfection efficacy two-three times higher than common non-viral transfection agents.

2.3.2.3 – Polymeric micelles and capsules

Polymeric micelles consist of unimers (typically diblock, triblock or randomly graft copolymers) organized, in aqueous solution, with the hydrophobic tails towards the inner core while the hydrophilic heads towards the external shell (*Fig. 2.10*). Micelles with a diameter less than 1 μm , spontaneously form when the unimers exceeds a critical aggregation concentration (CAC) but micelles responsive to an external stimulus can be also produced. In that case, a stimulus such as temperature, pH, or salt concentration can render hydrophobic or hydrophilic the unimer tail inducing formation/destruction of micelles. Chemical or physical crosslink have been also considerate in order to avoid the spontaneous dissociation below CAC, in particularly regarding reversible crosslink cleaved by an external stimulus or reagent for an easy excretion [212]. The NABDs can be carried and protected by the micelles using a cationic polymer for the unimer hydrophilic head. An example of micelles produced for that purpose, is composed by poly(styrene-block-4-vinylpyridine) with the conformation blocked by a cross-linked radical oligomerization. In that case, the hydrophobic core was constituted by polystyrene while the hydrophilic shell consisted in the cationic poly(4-vinylpyridine) [213].

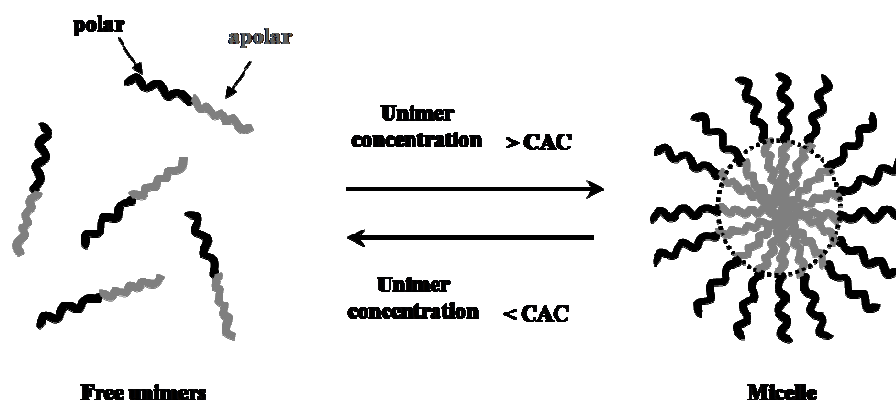


Fig. 2.10: polymeric micelles. Mechanism of micelle formation; as soon as critical aggregation concentration (CAC) is exceeded, unimers get together to form micelle; CAC depends on several environmental factors such as temperature and pH.

By several cycles of centrifugation and re-suspension in polyelectrolyte solutions, is possible to coat the micelles with an alternation of negatively charged NABDs and a positive charged polymer in order to produce a multilayer structure [214]. The core of this structures, constituted by the polymeric micelles, can be removed at the end of the process living hollow multilayer capsules able to storing active molecules (in our case a NABD). There is essentially two NABD storing possibility into a capsule: a) NABD in the capsule wall, b) NABD in the capsule void. The delivery from the capsules can be controlled by promoting the disassembly of NABD-containing films, for example using ultrasound [214]. Interestingly, the layering process can also take place on a polyplex (NABD-cationic polymer complex, see section below) without

disassembling the original core complex. This allows stabilization or further functionalization of the polyplex.

2.3.2.4 – Polyplexes

Polyplexes in general, are complexes formed by the electrostatic interactions between two oppositely charged polyelectrolytes. For NABDs delivery, the interaction involves a cationic polymers and the negatively charged phosphate backbone of polynucleotides resulting in NABD protection from enzymatic degradation and increasing of serum half-life [212, 214]. The net charge of polyplexes is the most important characteristic for the cellular uptake efficiency. Neutral polyplexes do not show particular problems in the interaction with the negatively charged cellular membrane but on over hand, they show low solubility and stability in physiological media. Negatively or positively charged polyplexes instead, are both stable and soluble in aqueous media but different behaviour when approaching the cellular membrane. While the firsts have many problems in crossing membranes because the electrostatic repulsion, the seconds have a favourable electrostatic interaction but, in case of too strong interaction, non-specific cellular uptake or membrane damaging can occur [212].

To overcome the above mentioned drawbacks and to improve transfection, many different materials have been tested [182]. The most studied polymers for gene delivery is the poly(L-Lysine) (PLL) [215]. Despite the capacity of polyplexes with NABD, it has a significant cytotoxicity and many efforts have been spent in order to overcome that problem. For example, PLL conjugation with poly(ethylene glycol) (PEG) reduced cytotoxicity and improved stability in the presence of serum proteins. In addition, to confer specificity to NABD release, PLL has been conjugated with sugar (lactose and galactose) for targeting asialoglycoprotein of hepatocytes [216]. PLL has been also conjugated with antibodies such as the monoclonal antibody against leukaemia-specific JL-1 antigen or with folate to target tumour cells bearing the folate receptor system [215].

Due to its remarkable transfection efficiency in many different kinds of cells, poly(ethylenimine) (PEI) is another widely used polymer in the gene delivery field [215]. PEI can escape from endosomes according to a “proton sponge” effect that consists of the osmotic swelling of endosome up to rupture allowing NABD release into the cytoplasm [212]. SiRNA release from PEI polyplexes has been tested in various cell lines and *in vivo* models [217-218] and it has been demonstrated to work as antitumor molecules in mice [218]. As PLL, also PEI displays a certain cyto-toxicity and several conjugation strategies have been exploited in order to solve this problem [219-220]. Typical example is represented by PEG grafted in different ratios obtaining polyplexes ranging from 200 to 400 nm [221]. Recently, nontoxic branched PEI derivatives obtained through medications of amine groups by ethyl acrylate, acetylation of primary amines, or introduction of

negatively charged propionic acid or succinic acid groups to the polymer structure have been tested [222]. For example, succinylation of branched PEI resulted in a considerable reduction in polymer toxicity in comparison to unmodified PEI, allowing the use of a higher polymer amount. This is most likely the reason for the improved NABD protein knock down compared to the unmodified PEI. In addition, PEI has been conjugated with antibodies (such as a monoclonal antibody against human epidermal growth factor receptor) or grafted with folate-PEG-folate to efficiently condense plasmid DNA forming spheroids with mean diameter of 150 nm [215].

PLL and PEI unfortunately, are not biodegradable carriers and this makes difficult the removal by physiological clearance systems with risks of accumulation inside cells or tissues and possible triggering of cyto-toxic effects. For its efficient interaction with plasmid DNA, poly(α -[4-aminobutyl]-L-glycolic acid) have been considered as an alternative biodegradable polycations. The polyplex form 326 nm diameter particles and has been proved to transfect cells more efficiently than pure PLL without showing any evident cyto-toxic effect. Others examples are represented by poly(β -amino ester)s that, in conjunction with plasmid DNA, forms particles with diameter ranging from 50 to 200 nm. Also in this case, cyto-toxicity is neatly lower than that competing to PEI.

Hydrophilic-block-cationic copolymers represent an interesting alternative to the above discussed systems. In that case, the electrostatic interactions through the cationic block stabilize the polynucleotide while the hydrophilic block provides steric stabilization of the entire complex. The presence of the hydrophilic block allows the formation of neutral complexes that may solve stability and circulation problems typical of polyelectrolyte polyplexes. Usually, the water soluble PEG or the poly(N-(2-hydroxypropyl)methacrylamide) are used as hydrophilic block, while the cationic block generally consists of tertiary or quaternary amines. Binding/release properties can be tuned by acting on the choice of cationic monomer and polymer block architecture. For example, quaternization of tertiary amines with varying alkyl groups or the random copolymerization of the cationic block with a neutral monomer results in polymers with different binding strengths [215]. Also neutral polymers such as polyvinyl alcohol and polyvinylpyrrolidone can be used for gene transfer. Indeed, polymer-NABD interaction takes place according to hydrogen bonding and/or Van der Waals interactions. These polymers are able to protect NABD from enzymatic degradation and to improve transfection [223].

Recently was tested an interesting example of NABD delivery system where siRNA was conjugated with prostaglandin E2 (PGE2), a ligand specific for target cells, and combined with the polyplexes technology [224]. In this work authors have conjugated PGE2 to siRNA against Fas, an important regulator of ischemia induced apoptosis. PGE2 was used as specific ligand for cardiomyocyte and the resulting siRNA-conjugate was complexed by a poly(amido-amine)

containing a disulphide bridge, obtained by Michael addition of cystamine bis-acrylamide on 1,6-diaminohexane (poly(DAH/CBA)). The final complex was stable in the extracellular environment and was able to release PGE-siRNA by reducing the S-S bridge in the cytoplasm environment. The PGE2-siRNA/poly(DAH/CBA) polyplex showed small sizes (100-150 nm) and the possibility to be uptaken by cardiomyocytes *via* receptor mediated transport, thus inducing significant target gene silencing.

Finally, polysaccharides should be mentioned. For example, low molecular weight chitosan (22 kDa) can form complexes with plasmid DNA providing protection from enzymatic degradation and improving transfection. Moreover, conjugation of deoxycholic acid with chitosan gave origin to a hydrophobic carrier assembling in particles characterised by an average diameter of around 160 nm and efficient cellular transfection properties [225]. Another interesting example is the use of hyaluronic acid (HA) chemical conjugated with PEI for the siRNA delivery. HA receptor mediate efficient endocytosis of anti-VEGF siRNA/HA-PEI complex into *in vitro* mice tumour model [226].

A particularly class of polyplex are the complexes formed by NABDs in association with cyclodextrins and dendrimers that are presented in the below sections.

2.3.2.5 – Dendrimers

Dendrimers consist of a central core molecule which acts as the root from which a number of highly branched, tree-like arms originate in an ordered and symmetric fashion [227]. In *Fig. 2.11* it is showed a schematic representation of a dendrimer whose core (black central circle) is represented by a four covalent root attachment points (di- or tri covalent core are also common). Root valency determines the number of linked dendrons and the overall dendrimer symmetry. Each dendrons layer (or generation) is added on the previous one by repetition of branch unit covalent coupling. In higher generation dendrimers, molecular density is high in the external part (shell) and low in the inner part where cavities, able to host other molecules, are present. Nevertheless, the density of the terminal groups cannot overcome a threshold beyond which further branching is no longer possible.

In order to using for NABDs delivery, dendrimers have to be constituted by materials conferring a net cationic surface charge to the structure such as the commercially available poly(propylenimine) (PPI) and poly(amidoamine) (PAMAM), but also PLL has been used [228]. PPI dendrimers are based on polypropylenimine units with butylenediamine as core molecule [227]. PAMAM instead, are usually based on ethylenediamine or ammonia core with three or four branching points, respectively, where methylacrylate and the amidation of its ester with ethylenediamine are added [229]. PAMAM dendrimers were tested either with plasmids or ODNs, [230-231] and, in a comparative study of different polyplexes based on linear, branched or dendritic

polymers, it was found that they were inferior to only to 22 kDA PEI (ExGen 500TM) [232]. Some authors reported that PAMAM dendrimers were not really useful with siRNA [233]. The dendritic α (-poly(L-lysine))s complex (DPL) is similar to PAMAM dendrimer but contains the amino acids, L-lysine residue, as a branch unit and is known to form stable complexes with plasmid DNAs. DLPs was used to efficiently transfer to HeLa cells ASO with an effect dependent on the complex branch structure [234].

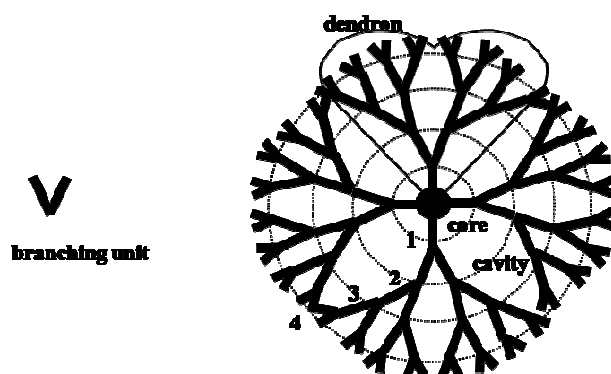


Fig. 2.11: dendrimer tree-like structure. Schematic representation of a dendrimer tree-like structure. Starting from a central poly-functional molecule (core), branch units are jointed together in a sequence of successive generations (indicated as 1, 2, 3 and 4 in the picture). Each core functionality gives origin to a dendron (grey area)

Carbosilane dendrimers (CBS) represent another dendrimer-based strategy used to deliver NABD by the formation of a “dendriplex” via electrostatic interactions between the negatively charged oligonucleotide backbone and the positively charged functional groups located on the dendrimer extremities. CBS dendrimers possess interior carbon–silicon bonds that are slowly hydrolyzed when the dendrimer is dissolved in water. This results in a gradual liberation of the exterior branches and their cargoes, a phenomenon which mostly occurs between 4 and 24 h. CBS showed very low toxicity at concentrations necessary to reach a siRNA concentration of 500 nM. At this dosage, CBS-mediated delivery of siRNAs to T cell proved to reduce the amount of the target RNA, represented by the HIV, down to 60% of control. These data are encouraging in the light of the fact that HIV-susceptible cells are very difficult to transfect. Moreover, in contrast to many transfectants, CBS dendrimers can deliver siRNA also in the presence of serum, a fundamental advantage that will allow dendrimers to be used for the *in vivo* scenario [235].

Although most dendrimer categories proved to be relatively non-toxic, cytotoxicity increases with generation (i.e. with size) and charge ratio [236-237]. An electrostatic interaction occurs between NABD and dendrimers forming a polyplex complex in a manner substantially without difference from that occurring with usual cationic polymers. Despite the considerable structural differences, NABD-dendrimer complexes substantially follow the same transfection path typical of NABD–linear polymer complexes with an initial electrostatic interaction with cell membrane

followed by endocytosis. Interestingly, experimental evidences would suggest that dendrimers have an intrinsic ability to escape from endosomes [238] and moreover, PAMAM dendrimer itself has the ability to accumulate to some extent in the nucleus [239].

2.3.2.6 – Cyclodextrins

Cyclodextrins (CDs) are natural cyclic oligosaccharides composed of 6, 7 or 8 D-glucose units linked by α -1,4-linkages and named α -, β -, or γ -CD respectively. CDs are characterized by a cup like shape with hydrophobic internal cavity able to hosting various molecules to form supramolecular inclusion complexes (*Fig. 2.12* and *Tab. 2.2*).

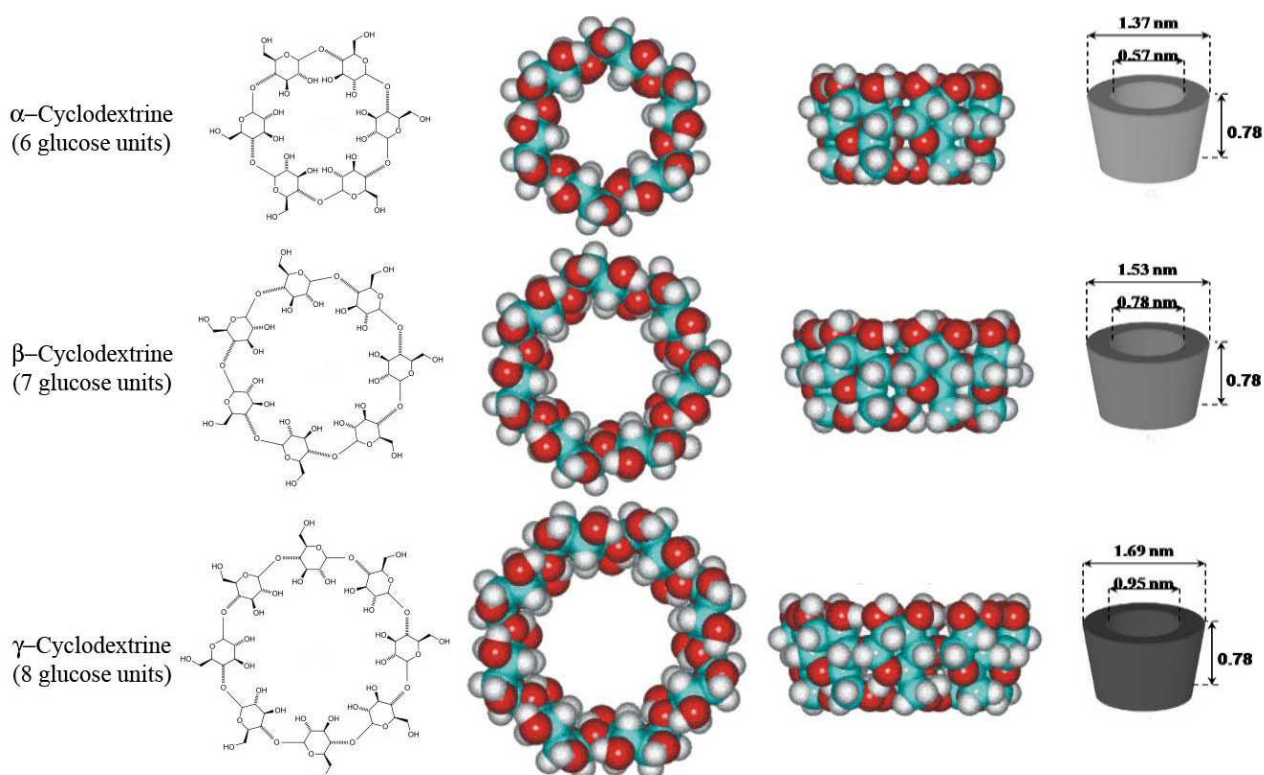


Fig. 2.12: cyclodextrins. Cyclodextrins are a series of natural cyclic oligosaccharides composed of 6, 7 or 8 D-glucose units linked by α -1,4-linkages, named, respectively, α -, β -, or γ -CD. They assume a cup like conformation characterised by an internal hydrophobic surface.

CDs can be used to directly complex NABD or inserted in a polymeric structure with a linear or branched polymer, star polymer or dendrimer in order to reduce cytotoxicity and increase cellular transfection of the final polyplex [240]. In addition, once formed, polyplex properties can be altered by the formation of inclusion complex due to the abundance of CD moieties in the polymeric structure [241]. For example, the conjugation of multiple oligoethylenimine arms (1 to 14 ethylenimine units per arms) onto α -CD, produce a star polymer with lower toxicity and higher transfection efficiency than PEI alone [242].

A new interesting application of CD in the NABD delivery field is represented by polyrotaxanes, a multiple oligoethylenimine-grafted β -CDs blocked on a Pluronic chain [243]. The cationic supramolecular complex formed by NABD and polyrotaxan demonstrate good binding ability, low cytotoxicity and high transfection efficiency, similar to that of high molecular weight PEI.

2.3.2.7 – Microbubbles

Extending the concept of echogenic liposomes to a generic micro-sphere containing a gas, we come to the definition of a class of controlled release systems named microbubbles (MB). The gas filled micro-spheres have diameters typically ranging between 1 and 8 μm and a shell thickness typically ranging between 2 and 500 nm [244]. The first MB generation contained air but, nowadays, perfluorocarbons or sulphur hexafluoride are preferred because have reduced blood solubility and low diffusion coefficient across MB shell ensuring a longer lifespan. As for echogenic liposomes, the use of MB for NABDs delivery allows the release only in a specific insonated area. The MB properties such as stiffness, resistance to ultrasound or probability of recognizing and clearance from reticuloendothelial system, mainly depend on the shell characteristic and size. Generally, larger MB are more sensible to ultrasound but, exceed about 6-8 μm , they can encounter difficulties to pass through normal pulmonary and systemic capillary beds in intravascular use. For very low acoustic field with a mechanical index $<0,05$ – $0,1$ lipidic MB oscillate in an approximately symmetrical linear way (ultrasound beam mechanical index or MI, is the amount of negative acoustic pressure within an ultrasonic field; FDA allows an MI of up to 1.9 except for ophthalmic application for which the maximal values is of 0.23). For $0.1 < \text{MI} < 0.3$ (low intensity field), the bigger resistance to compression with respect to expansion (non inertial cavitation) makes lipidic MB oscillating in a non linear manner. Finally, for high acoustic pressures ($\text{MI} > 0.3$ - 0.6), lipidic MB undergo forced expansion and compression leading to MB destruction due to gas escaping during the compression phase or due to MB shell fragmentation [245]. Polymeric MBs are less sensible to the ultrasound field comparing with liposomes in virtue of the higher shell stiffness that means higher ultrasound intensity is needed in order to determine the release.

In order to targeting selectively the drugs, MB can be designed to adhered to a particular cellular epitopes or receptor by modifying the shell with antibodies, carbohydrates or peptides that recognize the target. The interaction with NABDs is possible by MB surface modification with a positive charge; the complexation simply requires the mixing in aqueous solution and the NABDs resulting protected from enzymatic degradation [246]. Although MB overall transfection efficacy is

still below that competing to more conventional strategies (liposomes), the MB mediated delivery of plasmid DNA and oligonucleotides have been studied [247]. In particular, with regard to plasmid delivery, this approach seems promising for what concerns cardiovascular applications [248].

2.3.2.8 – Matrices for NABDs delivery

Matrices represent a macroscale delivery system which can offer interesting perspectives for a precise designing of NABD delivery and release kinetics [249], especially in combination with nanoscale delivery system presented above.

The controlled release of a solute from a matrix is realized by three methodology: matrix erosion, matrix topology (a time dependent process in the case of swelling matrices) or a combination of both [250]. In the first case the destruction of matrix network is the leading cause of the drug release with a kinetic determined by the matrix erosion; drug motion due to diffusion is negligible in comparison to the kinetics of network break-up. In the second case instead, the difference between the drug chemical potential in the matrix phase and in the release environment, is the driving force for drug release. Delivery kinetics is highly affected by drug steric and physico-chemical interactions and, in this respect, network meshes mean dimension plays a predominant role. The third case, represent a combination of aspects, network destruction and topology. Coupling different NABD-synthetic vector complexes and appropriate matrices, in possible to obtain a high level of release kinetics and precise pharmacological design. In the case of surface erosion controlled matrices, it would be possible to get the simultaneous release of different complex types each one optimised for the transfection of a particular cell type. Additionally, by a proper spatial loading (for example high complex concentration in the external matrix portion and a low concentration in the inner part) it would be possible releasing the attack dose followed by the maintenance one. In case of topology controlled matrices, instead, release kinetics can be controlled by complex mobility inside the matrix (mobility is represented by complex diffusion coefficient). The naked NABDs should have the higher mobility, followed by the NABDs polyplexes and than by NABD-(micelles or capsules or dendrimers or cyclodextrins) complexes; the lower mobility systems should be NABD-liposome and NABD-silica due to their dimension. Loading different complex kinds, it would be possible an accurate controlling of NABD release kinetics. In this sense, a numerical simulation of NABD release to coronary wall (in-stent restenosis pathology) from a polymeric matrix loaded with different ratios of low and high mobile complexes. demonstrated that, theoretically, it is possible to finely control NABD release kinetics over the desired period of time [251].

As examples of controlled release from matrices there is the study performed on poly(vinyl-alcohol) (PVA) hydrogel, cross-liked alginate hydrogel and collagen. In the first case, DNA interact

with PVA hydrogel via hydrogen bonds and the release could be modulated changing the matrix topology by modification in the DNA-PVA hydrogel preparation parameters (pressure, temperature, concentration, duration) [252]. In the second example, Kong et al. [253] by modulation of erosion kinetics in a cross-linking alginate hydrogel matrix were able to correlate the release processes of plasmid DNA (pDNA) and pDNA-PEI complex with the erosion constants by a parabolic relation. Finally, the pDNA delivery from collagen matrices could be achieved by enhanced binding via polycations complexing agents (PEI and PLL) or cationic liposomes. The *in vitro* tests were promising comparing to naked pDNA but, unfortunately, they were in contrast with *in vivo* tests and further explanation is needed [254]. Despite being applied to pDNA, it is certainly reasonable to expand the use of matrices to NABD delivery.

2.3.2.9 – Other delivery strategies

Cationic and amphipatic peptides have been tested for the delivery of NABD, in particular the cell penetrating peptides (CPPs) that have the ability to rapidly translocate into most mammalian cells. A decoy ODN targeted against the cell cycle regulator c-myc was connected, using a bridging PNA, to a CPP called TP-10 and then delivered to the neuroblastoma cell line N2A [255]. Increased uptake of CPP decoy ODN was observed together with a decreased proliferative capacity of the neuroblastoma cell line N2A compared to naked c-myc decoy. This approach may open the way for a cell specific delivery of NABD using appropriate CPPs.

For ocular application, NABD not only have to reach target cells, i.e. corneal epithelium, but they also need to reside for the appropriate time on them. To accomplish this requirement, a ribozyme was delivered, in a rabbit model, to corneal epithelium embedded in polyacrylic acid that has the unique property of being a liquid at pH 5 and a gel at pH 7 [256]. The gelation could be reversed by permeation of cations into the gelled polymer. Ribozymes were loaded into the liquid solution that was gellified by changing the pH. Once gellified, the ribozyme containing gel is applied on the corneal epithelium where cations from the tear fluid and secretion from the epithelial cells, collapse the gel to a fluid allowing ribozyme release. By this approach it was possible to show a peak of ribozyme uptake 30 minutes after application with a ribozyme persistence for 3 hours. This approach demonstrated the possibility to reach a sort of controlled release for NABD in the ocular field.

Polymeric multilayered films based on the electrostatic self-assembly of polycations and polyanions is a different approach to get a controlled release for NABD. Positively-charged cationic phosphorylcholine copolymer (PC copolymer) and negatively-charged c-myc ASO was used to create an alternate multilayered film for ASO delivery to HeLa cells [257]. The ASO release, occurring *via* swelling, was characterized by two distinguishable release regimes: a fast release

regime during the first 6 hour period and a slow release regime from 6 hours to the 8th day. High transfection levels and reduce cell growth was provided by this approach. These results demonstrate the possibility to deliver a prescribed amount of ASO with a controllable kinetic profile making this approach versatile and suitable for different applications.

NABD delivery from films/gel represents an attractive strategy not only to get a controlled release but also to allow NABD in situ permanence in unfavorable physiological conditions, in particular regarding gel systems suitable for NABD delivery to the artery wall. In addition to the common problem related to the *in vivo* release, the endo-vascular delivery is characterized by the necessity to prevent NABD/transfectant reagent wash-out by blood flow. A possible solution could be represented by the endoluminal gel paving technique where NABD/liposome complexes are subsequently embedded into a bi-layer gel adherent to the artery wall. The part in contact with blood flow is characterized by a strong layer (made by alginate) and the part facing the arterial wall is made by a softer gel (pluronic gel). The polymeric blend have thermo-reversible properties (liquid at temperature below 18 C° and solid at temperature above 30 C°) allowing the NABD/liposome loading and percutaneous transluminal application to the artery wall before the body temperature induce gelification. A subsequent quick exposure to divalent cations such as Cu⁺⁺, induces the gelification of the alginate facing blood flow. The result is the creation of a strong alginate layer to protect NABD/liposome from washing-out while a soft pluronic layer facing the arterial wall. Another advantage of this technique is the creation of a physical barrier which the complexes cannot cross thus favoring their migration through the softer gel layer and in turn to the arterial wall. Data suggest that the NABD/liposome complexes do not substantially alter gel properties and a satisfactory complexes release to VSMC, a major target for therapeutic vascular approaches, can be modulated by varying gel concentration [258-259]. Theoretical studies was also performed in order to completely comprehend the NABD release kinetics in the artery wall end to contributing to the NABD vascular release optimization [252, 260] This approach can be used to down modulate the excessive VSMC proliferation, a hallmark of hyper-proliferative vascular diseases.

Single walled carbon nanotubes (SWCNs) is an emerging system for transport and delivery of biological molecules (including NABDs) inside various type of mammalian cells [261]. SWCNs surface modifications enables attachment of small molecules and proteins and the incorporation of cleavable bond into the functionalization enable the controlled molecular release from nanotubes. Kam and colleagues [262] approach consists in a noncovalent absorption of phospholipid linked to PEG chain with a terminal amine group (PL-PEG-NH₂). Disulfide bond were than incorporated by linking a thiolated oligonucleotide via heterobifunctional cross-linker (*Fig. 2.13*). The author

demonstrates the enzymatic cleavage of the disulfide bond into the lysosomal compartment for releasing and delivering molecules to the cytosol. Moreover, this system increases siRNA efficiency in HeLa cells model compared to lipofectamine.

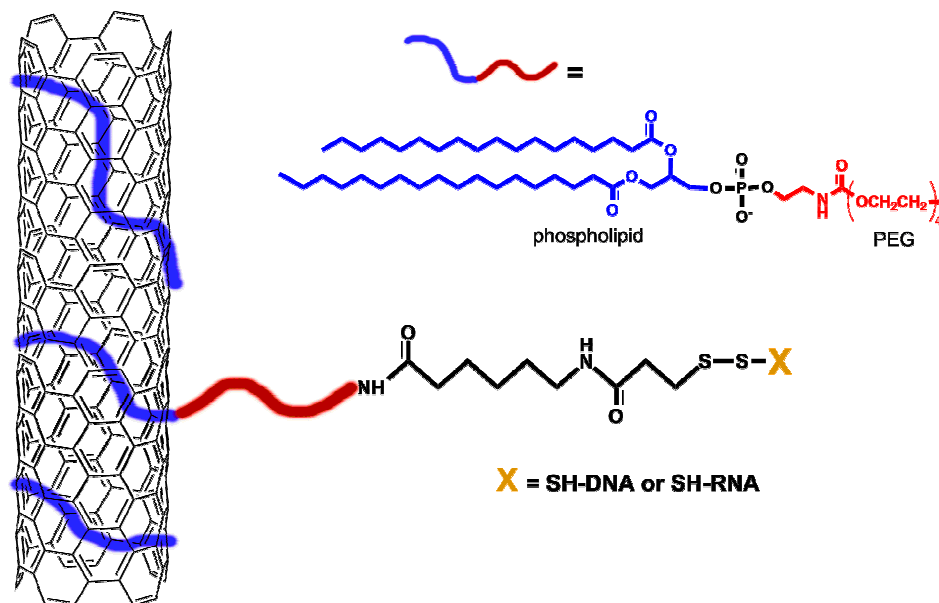


Fig. 2.13: nanotubes for NABDs delivery. A schematic representation of Kam and colleague approach in the use of nanotubes as carriers for NABDs delivery. Phospholipid PEG conjugate is absorbed onto the nanotube surface. SH-DNA or SH-RNA molecules should be covalently attached to the complex by an etero-bifunctional linker. Oligonucleotides are released after cleavage of disulfide bond by intracellular enzymes.

The last mentionable NABDs delivery system consists in polyvalent oligonucleotide functionalized gold nanoparticle (DNA-Au-NPs or RNA-Au-NPs). DNA-Au-NPs are used and sometimes are also commercially available for detection and diagnostic assay but, recently, the ability to perform antisense gene regulation was proved using either DNA or RNA gold NP conjugate. Double strand oligonucleotide may be modified by linking an oligo(ethylene glycol)-thiol (OEG-Thiol) as spacer (cleavable disulfide bond can also added between the two). The thiol groups interact with the gold NPs obtaining the NPs functionalization then additional OEG-Thiol or other polymeric coating can be added on the NPs surface in order to stabilize the complex. This system proves at least the same *in vitro* silencing efficiency compared to commercially available lipidic carriers [263-264].

2.3.3 – Viral vector NABDs delivery systems

Several viral vector system have been used for nucleic acid delivery exploit the nature of virus to deliver and express their genes into host cells. However, natural viruses are optimised for infecting and expressing their genome in the host cells, but not necessarily for surviving of the transducer host cell and maintenance of the expressed genes. Nevertheless, the strategy consists in

the modification of viral genome with the insertion of an expression cassettes coding for the NABD and the removal of some viral genes in order to obtain a replication-defective virus [265]. For these reasons, viral vector technology in gene therapy and NABDs delivery extensively overlap because, in both case, the goal is the expression of exogenous genes by the hosting cell.

The main advantages in the use of viral vector is due to the strong cellular uptake and intracellular efficiency, therefore few viral particles are sufficient for the transduction of cells [265]. Moreover, sustained and theoretically inheritable permanent NABD expression could be achieved [266-267]. Most frequently, replication-defective viral vectors are applied that can replicate only in a special producer cells but not in the host cells. However, for some applications, the viral replication can be used to multiply the therapeutic effect strongly amplifies the copy number of the therapeutic gene carried by the viral vector [265]. On the other side, several disadvantages limit the practical use of viral based delivery. First of all, it is possible to apply this technology only to RNA based NABDs because their production is submitted to the expression of a double stranded DNA (directly or indirectly derived from the viral genome) by the hosting cells. Moreover, the *in vivo* use can produce an immune response to viruses that impedes the delivery and can also cause severe complications for the patients [268].

Retrovirus (RV) and Adenovirus (ADV) vector have been commonly used in clinical trials but also other viruses were used to develop viral vector including Adeno-Associated Virus (AAV), Herpes Simplex Virus (HSV), Poxvirus, Baculovirus (BV) and more recently Lentivirus (LV) and Alphavirus (both RVs subfamily) [265, 267]. RV system including LVs are effective in most cell lines and primary cells cultures [269] and have the particular capacity to integrate in the host cell genome permitting long-term and progeny inherit of transgene expression [267]. RVs are constituted by lipid-enveloped particles containing two identical copies of a linear single-stranded RNA genome of around 7–11 kb. They usually require binding to a specific membrane-bound receptor for viral entry. Cells not expressing the appropriate receptor are resistant to infection by a specific retrovirus. In cytoplasm, viral reverse transcriptase retrotranscribes the viral genome into double-stranded DNA (dsDNA), which binds to cellular proteins to form a nucleoprotein preintegration complex (PIC), which contains karyophilic elements that facilitate its migration to the nucleus. Nuclear membrane is a physical barrier for these PICs. The size and ability of these PICs to migrate to the nucleus determine their capacity to reach the cellular genome and transduce quiescent cells. In fact, for most retroviruses, such as Moloney Murine Leukaemia Virus MoMLV, PIC cannot cross the nuclear membrane, which renders these viruses and vectors incapable of infecting cells unless they undergo a mitotic cycle which actually disrupts the nuclear membrane.

LVs, such as Human Immunodeficiency Virus (HIV), does not have this limitation, and it is capable of transducing quiescent cells, although transduction efficiency by LVs vectors is much higher in dividing cells than in nondividing cells [267]. Both types of vectors, RVs and LVs, have been reported to mediate an efficient and stable siRNA expression [270-271]. Typically, the vectors use a Pol III promoter, such as the U6, H1 or tRNA promoters. Vector systems for siRNA expression can be classified in two main groups depending on whether the expressed RNAs are hairpin-type or tandem-type. The former transcribe hairpin RNAs, which are subsequently processed into siRNA duplexes by endogenous Dicer. The tandem-type siRNA-expression vectors include both sense and antisense sequences, which are transcribed and subsequently annealed to generate the siRNA duplexes [272]. Using an MoMLV-based vector encoding a siRNA specific for the p53 gene and a truncated form of human CD4 as a reporter gene, p53 expression was dramatically reduced in cultured cells [273]. Another study was performed on HCT-116 colon cancer cells where a LV based vector encoding for a siRNA against thymidylate kinase (TMPK), a key enzyme for dTTP synthesis significantly increase doxorubicin sensitivity [274]. Several examples of siRNA delivery using LVs can be also find in the fields of neurodegenerative diseases and viral infection (see [275] for a review). Despite the potentiality of RV based vector, their application still limited because the random integration in the host genome thereby disturbing host gene function and may cause insertional mutation.

Adenovirus based vectors is another promising tool for gene therapy and siRNA delivery. ADV vector do not integrate into host genome, therefore gene expression is only short term. They can efficiently transfer genes into both dividing and nondividing cells [265]. These system have been demonstrated to mediate gen silencing in an *in vitro* lung model [276] and to induce RNAi in a range of animal tissues [277]. Unfortunately, natural immunity against ADV and acute inflammatory and immunological response limit clinical application. In fact, systemic administration of large amount of ADV (i.e. into the liver) may cause serious side effects [278]. In order to improve the vectors safety, several unneeded genes was removed from ADV genome but, despite the improvements, inflammatory, apoptotic and immunological host responses, in general exclude repeated *in vivo* administration of viral vectors [265].

As last example of siRNA viral delivery system is mentionable the use Herpes Simplex Virus (HSV) that is particularly interesting fro neuronal delivery. HSV-1 is a naturally neurotrophic double-stranded DNA virus able to establish life-long latency in neurons. Unlike other viruses that infect neurons, HSV has evolved to be efficiently transported from the nerve terminals innervating the infection site to cell bodies *in vivo*. The utility of HSV vectors for gene silencing in mice

peripheral neurons was established by *in vivo* targeting the endogenous *trpv1* gene in dorsal root ganglia injecting an HSV replication defective vector into the sciatic nerve [279].

The virus based NABDs delivery is not limited to the siRNA but, some interesting work have also applied this methodology to ribozymes. Smith and colleague [280] have used Semliki Forest Virus (SFV), an Alphavirus (RVs subfamily), in order to deliver an hammerhead ribozyme target a highly conserved sequence in the U5 region of the HIV-1 with promising results in BHK cell line. Opposite to others RVs, in the Alphavirus the entire life cycle takes place in the cytoplasm avoid problems related to the host genome integration. The same target was reached by a BVs based vector [281]. BV genome was modified bearing a ribozyme-synthesizing cassette driven by the tRNA(i)(Met) promoter and enhanced transduction efficiency was obtained by displaying vesicular stomatitis virus glycoprotein (VSV-G) on the viral envelope. The resulting vector demonstrates potent inhibition of HIV-1 replication in HeLa CD4(+) cells.

2.3.4 – Join approaches: chemo-virus, Chimerical virus and synthetic virus-like systems

The merge of viral and nonviral vector research efforts could be an encouraging strategy for the future optimization of both vector classes. Viral vectors may greatly benefit from chemical modifications to develop chemo-viruses; nonviral vectors may benefit from modifications mimicking viral intracellular delivery functions to generate synthetic viruses. In addition, hybrid strategies (including both nonviral and viral gene vector parts) may also provide interesting solutions (*Fig. 2.14*). The combination of chemical and genetic modification of recombinant viruses aim is to delete all undesired viral functions from the viral vector and to mask the original surface of the virus with retargeting ligands and shielding shell/domains using chemical or recombinant procedures [265].

Coating of adenoviral vectors with hydrophilic polymers such as PEG [282-284] or poly(N-2-hydroxypropyl-methacrylamide) (pHPMA) [285] shielded the virus from interaction with its native receptor or neutralizing antibodies and the incorporated ligands enabled retargeting (*Fig. 2.14*, chemo-virus). A very encouraging example of systemic adenovirus retargeting was recently described [286]. PEGylated adenoviruses were retargeted using anti-E-selectin antibodies. These viruses showed longer persistence in the blood circulation compared with unmodified viruses and selectively targeted inflamed skin in mice resulting in local gene expression. For combination of genetic and chemical adenoviral vector particle modifications, a novel cystein-based vector platform was developed by Kreppel and colleagues [287]. They genetically introduced cysteines at solvent-exposed positions of the adenovirus fibers. The corresponding thiol groups (36 per

adenovirus) were highly reactive in controlled chemical coupling to protein ligands such as transferrin. Such particles were efficiently targeted to the transferrin receptor pathway. This targeting concept via cysteine modifications could also be successfully combined with PEGylation of adenovirus amino groups, providing shielding (detargeting) against nontarget interactions.

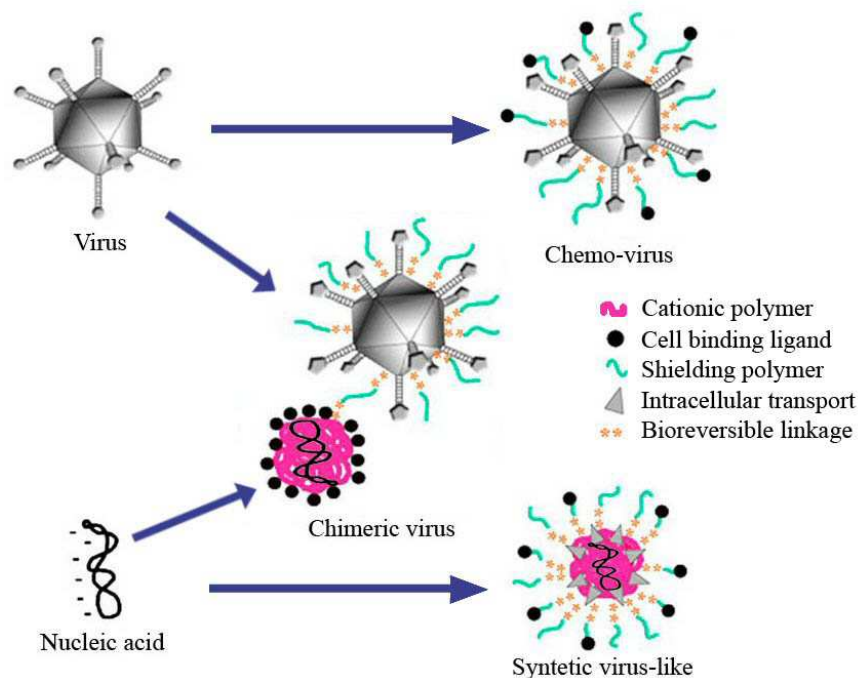


Fig. 2.14: hybrid delivery systems. Chemo-viruses (top left) are generated by chemical modification of a genetically modified virus. Addition of a shielding polymer allows the reduction of inflammatory response and a cell binding ligand, allow the retargeting of the virus to a specific cell population. The NABD is carried by the viral genome and infection allows the NABD expression directly by the target cells. In chimeric virus (center), a chemo-virus is linked to a NABD-cationic polymer complex (polyplex); retargeting cell binding ligand should be also added. The NABD should be carried by both virus and polyplex for a synergic action. Synthetic virus-like systems (bottom left), consists of a NABD polyplex core linked to a shielding polymer, cell binding ligands for specific targeting and intracellular transporter fro cell penetration (such as cell-penetrating peptides). These types of complex mimic the action of a real virus.

Another strategy is to generate hybrid vectors combining viral and nonviral elements. For example, a virus particle (i.e.. adenovirus) can be covalently linked to a separate nonviral formulation (i.e.. expression plasmid) (*Fig. 2.14*, Chimerical virus). The viral vector genome (within the virus) and the separate nonviral gene expression cassette (outside the virus) may synergize in some applications; for example, a helper plasmid attached to the surface of the virus may activate virus replication or regulate the viral gene expression cassette. In addition, the nonviral part may be modified with targeting ligands to allow retargeting of the hybrid vector, whereas the virus part may confer greatly improved intracellular efficiency [288-289].

Another type of hybrid strategy incorporates a whole viral genome into a non-viral formulation (*Fig. 2.14*, synthetic virus-like). One of the first prototypes of synthetic virus-like particles was generated by Plank et al. [290]. The particles contained a targeting ligand (synthetic tetra-antennary carbohydrate ligand for hepatic asialoglycoprotein receptor) and a membrane-active

peptide to induce endosomal release (synthetic acidic peptide analog derived from the N-terminal HA-2 subunit of influenza virus hemagglutinin). Both components were covalently attached to PLL in order to complexing oligonucleotides. The polyplex components were found to compact DNA to small particles with virus-like dimension of ~100 nm. Application of these particles to hepatocytes resulted in efficient, ligand-specific gene expression, which was highest in the presence of the endosome-destabilizing peptide. This early approach, however, displayed also clear limitations: compared with viral vector particles, the system was still very inefficient; the complex formulation was a crude heterogeneous composition that did not contain any measures to shield the particle surface, and therefore particles aggregated with time.

References

1. Lee, I.K., et al., *Advantages of the circular dumbbell decoy in gene therapy and studies of gene regulation*. *Curr Drug Targets*, 2003. **4**(8): p. 619-23.
2. Kukielka, G.L., et al., *Interleukin-8 gene induction in the myocardium after ischemia and reperfusion in vivo*. *J Clin Invest*, 1995. **95**(1): p. 89-103.
3. Ehsan, A., et al., *Long-term stabilization of vein graft wall architecture and prolonged resistance to experimental atherosclerosis after E2F decoy oligonucleotide gene therapy*. *J Thorac Cardiovasc Surg*, 2001. **121**(4): p. 714-22.
4. Tomita, N., et al., *An oligonucleotide decoy for transcription factor E2F inhibits mesangial cell proliferation in vitro*. *Am J Physiol*, 1998. **275**(2 Pt 2): p. F278-84.
5. Egashira, K., et al., *Long-term follow up of initial clinical cases with NF-kappaB decoy oligodeoxynucleotide transfection at the site of coronary stenting*. *J Gene Med*, 2008. **10**(7): p. 805-9.
6. Morishita, R., et al., *A gene therapy strategy using a transcription factor decoy of the E2F binding site inhibits smooth muscle proliferation in vivo*. *Proc Natl Acad Sci U S A*, 1995. **92**(13): p. 5855-9.
7. Edwards, M.R., et al., *Targeting the NF-kappaB pathway in asthma and chronic obstructive pulmonary disease*. *Pharmacol Ther*, 2009. **121**(1): p. 1-13.
8. Bezzerri, V., et al., *Transcription factor oligodeoxynucleotides to NF-kappaB inhibit transcription of IL-8 in bronchial cells*. *Am J Respir Cell Mol Biol*, 2008. **39**(1): p. 86-96.
9. Moriyama, I., et al., *Decoy oligodeoxynucleotide targeting activator protein-1 (AP-1) attenuates intestinal inflammation in murine experimental colitis*. *Lab Invest*, 2008. **88**(6): p. 652-63.
10. Cho, J.W., Y.C. Cha, and K.S. Lee, *AP-1 transcription factor decoy reduces the TGF-beta1-induced cell growth in scleroderma fibroblasts through inhibition of cyclin E*. *Oncol Rep*, 2008. **19**(3): p. 737-41.
11. Ahn, J.D., et al., *E2F decoy oligodeoxynucleotides effectively inhibit growth of human tumor cells*. *Biochem Biophys Res Commun*, 2003. **310**(4): p. 1048-53.
12. Gill, J.S., et al., *Effects of NFkappaB decoy oligonucleotides released from biodegradable polymer microparticles on a glioblastoma cell line*. *Biomaterials*, 2002. **23**(13): p. 2773-81.
13. Sun, X., et al., *Growth inhibition of human hepatocellular carcinoma cells by blocking STAT3 activation with decoy-ODN*. *Cancer Lett*, 2008. **262**(2): p. 201-13.
14. Gu, J., et al., *Blockage of the STAT3 signaling pathway with a decoy oligonucleotide suppresses growth of human malignant glioma cells*. *J Neurooncol*, 2008. **89**(1): p. 9-17.

15. Felsenfeld, G., *DDRaRA. Triple helix*. Journal of American Chemical Society, 1957. **79**: p. 2023-2024.
16. Goni, J.R., X. de la Cruz, and M. Orozco, *Triplex-forming oligonucleotide target sequences in the human genome*. Nucleic Acids Res, 2004. **32**(1): p. 354-60.
17. Sun, J.S., et al., *Triple helix structures: sequence dependence, flexibility and mismatch effects*. J Biomol Struct Dyn, 1991. **9**(3): p. 411-24.
18. Giovannangeli, C. and C. Helene, *Triplex-forming molecules for modulation of DNA information processing*. Curr Opin Mol Ther, 2000. **2**(3): p. 288-96.
19. Ziemba, A.J., et al., *A bis-alkylating triplex forming oligonucleotide inhibits intracellular reporter gene expression and prevents triplex unwinding due to helicase activity*. Biochemistry, 2003. **42**(17): p. 5013-24.
20. Liu, J., et al., *Triplex targeting of human PDGF-B (c-sis, proto-oncogene) promoter specifically inhibits factors binding and PDGF-B transcription*. Nucleic Acids Res, 2001. **29**(3): p. 783-91.
21. Kim, H.G. and D.M. Miller, *Inhibition of in vitro transcription by a triplex-forming oligonucleotide targeted to human c-myc P2 promoter*. Biochemistry, 1995. **34**(25): p. 8165-71.
22. Scaggiante, B., et al., *Effect of unmodified triple helix-forming oligodeoxyribonucleotide targeted to human multidrug-resistance gene mdrl in MDR cancer cells*. FEBS Lett, 1994. **352**(3): p. 380-4.
23. Duca, M., et al., *The triple helix: 50 years later, the outcome*. Nucleic Acids Res, 2008. **36**(16): p. 5123-38.
24. Chin, J.Y., E.B. Schleifman, and P.M. Glazer, *Repair and recombination induced by triple helix DNA*. Front Biosci, 2007. **12**: p. 4288-97.
25. Cheng, K., et al., *Enhanced hepatic uptake and bioactivity of type alpha1(I) collagen gene promoter-specific triplex-forming oligonucleotides after conjugation with cholesterol*. J Pharmacol Exp Ther, 2006. **317**(2): p. 797-805.
26. Dahm, S.C. and O.C. Uhlenbeck, *Role of divalent metal ions in the hammerhead RNA cleavage reaction*. Biochemistry, 1991. **30**(39): p. 9464-9.
27. Stage-Zimmermann, T.K. and O.C. Uhlenbeck, *Hammerhead ribozyme kinetics*. RNA, 1998. **4**(8): p. 875-89.
28. Uhlenbeck, O.C., *A small catalytic oligoribonucleotide*. Nature, 1987. **328**(6131): p. 596-600.
29. Birikh, K.R., P.A. Heaton, and F. Eckstein, *The structure, function and application of the hammerhead ribozyme*. Eur J Biochem, 1997. **245**(1): p. 1-16.
30. Symons, R.H., *Small catalytic RNAs*. Annu Rev Biochem, 1992. **61**: p. 641-71.
31. Haseloff, J. and W.L. Gerlach, *Simple RNA enzymes with new and highly specific endoribonuclease activities*. Nature, 1988. **334**(6183): p. 585-91.
32. Vaish, N.K., et al., *In vitro selection of a purine nucleotide-specific hammerheadlike ribozyme*. Proc Natl Acad Sci U S A, 1998. **95**(5): p. 2158-62.
33. Grassi, G., et al., *Therapeutic potential of hammerhead ribozymes in the treatment of hyperproliferative diseases*. Curr Pharm Biotechnol, 2004. **5**(4): p. 369-86.
34. Grassi, G., et al., *Selection and characterization of active hammerhead ribozymes targeted against cyclin E and E2F1 full-length mRNA*. Antisense Nucleic Acid Drug Dev, 2001. **11**(5): p. 271-87.
35. Yang, J., et al., *Systemic targeting inhibitor of kappaB kinase inhibits melanoma tumor growth*. Cancer Res, 2007. **67**(7): p. 3127-34.
36. Leopold, L.H., et al., *Multi-unit ribozyme-mediated cleavage of bcr-abl mRNA in myeloid leukemias*. Blood, 1995. **85**(8): p. 2162-70.

37. Scherr, M., et al., *Specific hammerhead ribozyme-mediated cleavage of mutant N-ras mRNA in vitro and ex vivo. Oligoribonucleotides as therapeutic agents.* J Biol Chem, 1997. **272**(22): p. 14304-13.
38. Wiechen, K., C. Zimmer, and M. Dietel, *Selection of a high activity c-erbB-2 ribozyme using a fusion gene of c-erbB-2 and the enhanced green fluorescent protein.* Cancer Gene Ther, 1998. **5**(1): p. 45-51.
39. Funato, T., et al., *Anti-K-ras ribozyme induces growth inhibition and increased chemosensitivity in human colon cancer cells.* Cancer Gene Ther, 2000. **7**(3): p. 495-500.
40. Cheng, J., et al., *Inhibition of cell proliferation in HCC-9204 hepatoma cells by a c-myc specific ribozyme.* Cancer Gene Ther, 2000. **7**(3): p. 407-12.
41. Samoto, K., et al., *Expression of vascular endothelial growth factor and its possible relation with neovascularization in human brain tumors.* Cancer Res, 1995. **55**(5): p. 1189-93.
42. Kamochi, J., et al., *Ribozyme mediated suppression of vascular endothelial growth factor gene expression enhances matrix metalloproteinase 1 expression in a human hepatocellular carcinoma cell line.* Int J Oncol, 2002. **21**(1): p. 81-4.
43. Ke, L.D., et al., *A novel approach to glioma gene therapy: down-regulation of the vascular endothelial growth factor in glioma cells using ribozymes.* Int J Oncol, 1998. **12**(6): p. 1391-6.
44. Sullenger, B.A. and E. Gilboa, *Emerging clinical applications of RNA.* Nature, 2002. **418**(6894): p. 252-8.
45. Scanlon, K.J., H. Ishida, and M. Kashani-Sabet, *Ribozyme-mediated reversal of the multidrug-resistant phenotype.* Proc Natl Acad Sci U S A, 1994. **91**(23): p. 11123-7.
46. Funato, T., et al., *Reversal of cisplatin resistance in vivo by an anti-fos ribozyme.* In Vivo, 1997. **11**(3): p. 217-20.
47. Masuda, Y., et al., *Reversal of multidrug resistance by a liposome-MDR1 ribozyme complex.* Cancer Chemother Pharmacol, 1998. **42**(1): p. 9-16.
48. Nagata, J., et al., *Reversal of drug resistance using hammerhead ribozymes against multidrug resistance-associated protein and multidrug resistance 1 gene.* Int J Oncol, 2002. **21**(5): p. 1021-6.
49. Osada, H., et al., *Reversal of drug resistance mediated by hammerhead ribozyme against multidrug resistance-associated protein 1 in a human glioma cell line.* Int J Oncol, 2003. **22**(4): p. 823-7.
50. Fei, Q., et al., *Experimental cancer gene therapy by multiple anti-survivin hammerhead ribozymes.* Acta Biochim Biophys Sin (Shanghai), 2008. **40**(6): p. 466-77.
51. Shay, J.W. and W.E. Wright, *Telomerase: a target for cancer therapeutics.* Cancer Cell, 2002. **2**(4): p. 257-65.
52. Kanazawa, Y., et al., *Hammerhead ribozyme-mediated inhibition of telomerase activity in extracts of human hepatocellular carcinoma cells.* Biochem Biophys Res Commun, 1996. **225**(2): p. 570-6.
53. Wan, M.S., P.L. Fell, and S. Akhtar, *Synthetic 2'-O-methyl-modified hammerhead ribozymes targeted to the RNA component of telomerase as sequence-specific inhibitors of telomerase activity.* Antisense Nucleic Acid Drug Dev, 1998. **8**(4): p. 309-17.
54. Yokoyama, Y., et al., *Hammerhead ribozymes to modulate telomerase activity of endometrial carcinoma cells.* Hum Cell, 2001. **14**(3): p. 223-31.
55. Folini, M., et al., *Inhibition of telomerase activity by a hammerhead ribozyme targeting the RNA component of telomerase in human melanoma cells.* J Invest Dermatol, 2000. **114**(2): p. 259-67.
56. Li, S., M. Nosrati, and M. Kashani-Sabet, *Knockdown of telomerase RNA using hammerhead ribozymes and RNA interference.* Methods Mol Biol, 2007. **405**: p. 113-31.
57. Jackson, C.L. and S.M. Schwartz, *Pharmacology of smooth muscle cell replication.* Hypertension, 1992. **20**(6): p. 713-36.

58. Grassi, G., et al., *Hammerhead ribozymes targeted against cyclin E and E2F1 cooperate to down-regulate coronary smooth muscle cell proliferation*. J Gene Med, 2005. **7**(9): p. 1223-34.
59. Dyson, N., *The regulation of E2F by pRB-family proteins*. Genes Dev, 1998. **12**(15): p. 2245-62.
60. Ohtsubo, M., et al., *Human cyclin E, a nuclear protein essential for the G1-to-S phase transition*. Mol Cell Biol, 1995. **15**(5): p. 2612-24.
61. Ellington, A.D. and J.W. Szostak, *In vitro selection of RNA molecules that bind specific ligands*. Nature, 1990. **346**(6287): p. 818-22.
62. Achenbach, J.C., et al., *DNAzymes: from creation in vitro to application in vivo*. Curr Pharm Biotechnol, 2004. **5**(4): p. 321-36.
63. Santoro, S.W. and G.F. Joyce, *A general purpose RNA-cleaving DNA enzyme*. Proc Natl Acad Sci U S A, 1997. **94**(9): p. 4262-6.
64. Santoro, S.W. and G.F. Joyce, *Mechanism and utility of an RNA-cleaving DNA enzyme*. Biochemistry, 1998. **37**(38): p. 13330-42.
65. Warashina, M., et al., *Extremely high and specific activity of DNA enzymes in cells with a Philadelphia chromosome*. Chem Biol, 1999. **6**(4): p. 237-50.
66. Wu, Y., et al., *Inhibition of bcr-abl oncogene expression by novel deoxyribozymes (DNAzymes)*. Hum Gene Ther, 1999. **10**(17): p. 2847-57.
67. Liu, C., et al., *Suppression of platelet-type 12-lipoxygenase activity in human erythroleukemia cells by an RNA-cleaving DNAzyme*. Biochem Biophys Res Commun, 2001. **284**(4): p. 1077-82.
68. Dass, C.R., L.M. Khachigian, and P.F. Choong, *c-Jun knockdown sensitizes osteosarcoma to doxorubicin*. Mol Cancer Ther, 2008. **7**(7): p. 1909-12.
69. Qu, Y., et al., *Effects of DNAzymes targeting Aurora kinase A on the growth of human prostate cancer*. Cancer Gene Ther, 2008. **15**(8): p. 517-25.
70. Dass, C.R. and P.F. Choong, *C-jun: pharmaceutical target for DNAzyme therapy of multiple pathologies*. Pharmazie, 2008. **63**(6): p. 411-4.
71. Benson, V.L., L.M. Khachigian, and H.C. Lowe, *DNAzymes and cardiovascular disease*. Br J Pharmacol, 2008. **154**(4): p. 741-8.
72. Trepanier, J.B., J.E. Tanner, and C. Alfieri, *Reduction in intracellular HCV RNA and virus protein expression in human hepatoma cells following treatment with 2'-O-methyl-modified anti-core deoxyribozyme*. Virology, 2008. **377**(2): p. 339-44.
73. Opalinska, J.B. and A.M. Gewirtz, *Nucleic-acid therapeutics: basic principles and recent applications*. Nat Rev Drug Discov, 2002. **1**(7): p. 503-14.
74. Jorgensen, R., *Altered gene expression in plants due to trans interactions between homologous genes*. Trends Biotechnol, 1990. **8**(12): p. 340-4.
75. Fire, A., *RNA-triggered gene silencing*. Trends Genet, 1999. **15**(9): p. 358-63.
76. Elbashir, S.M., et al., *Duplexes of 21-nucleotide RNAs mediate RNA interference in cultured mammalian cells*. Nature, 2001. **411**(6836): p. 494-8.
77. Novina, C.D. and P.A. Sharp, *The RNAi revolution*. Nature, 2004. **430**(6996): p. 161-4.
78. Sharp, P.A., *RNA interference--2001*. Genes Dev, 2001. **15**(5): p. 485-90.
79. Poliseno, L., et al., *The energy profiling of short interfering RNAs is highly predictive of their activity*. Oligonucleotides, 2004. **14**(3): p. 227-32.
80. Wilda, M., et al., *Killing of leukemic cells with a BCR/ABL fusion gene by RNA interference (RNAi)*. Oncogene, 2002. **21**(37): p. 5716-24.
81. Heidenreich, O., *Oncogene suppression by small interfering RNAs*. Curr Pharm Biotechnol, 2004. **5**(4): p. 349-54.
82. Cho, S.W., et al., *Delivery of small interfering RNA for inhibition of endothelial cell apoptosis by hypoxia and serum deprivation*. Biochem Biophys Res Commun, 2008. **376**(1): p. 158-63.

83. Spankuch, B. and K. Strebhardt, *Combinatorial application of nucleic acid-based agents targeting protein kinases for cancer treatment*. *Curr Pharm Des*, 2008. **14**(11): p. 1098-112.
84. Erb, P., et al., *Apoptosis and pathogenesis of melanoma and nonmelanoma skin cancer*. *Adv Exp Med Biol*, 2008. **624**: p. 283-95.
85. Guo, X., et al., *siRNA-mediated inhibition of hTERT enhances chemosensitivity of hepatocellular carcinoma*. *Cancer Biol Ther*, 2008. **7**(10): p. 1555-60.
86. Agostini, F., et al., *Potential applications of small interfering RNAs in the cardiovascular field*. *Drug of the Future*, 2006. **31**: p. 513-25.
87. Dapas, B., et al., *Role of E2F1-cyclin E1-cyclin E2 circuit in human coronary smooth muscle cell proliferation and therapeutic potential of its downregulation by siRNAs*. *Mol Med*, 2009. **15**(9-10): p. 297-306.
88. Chen, Y., G. Cheng, and R.I. Mahato, *RNAi for treating hepatitis B viral infection*. *Pharm Res*, 2008. **25**(1): p. 72-86.
89. Singh, S.K., *RNA interference and its therapeutic potential against HIV infection*. *Expert Opin Biol Ther*, 2008. **8**(4): p. 449-61.
90. Spurgers, K.B., et al., *Oligonucleotide antiviral therapeutics: antisense and RNA interference for highly pathogenic RNA viruses*. *Antiviral Res*, 2008. **78**(1): p. 26-36.
91. Lang, C., et al., *Connective tissue growth factor: a crucial cytokine-mediating cardiac fibrosis in ongoing enterovirus myocarditis*. *J Mol Med*, 2008. **86**(1): p. 49-60.
92. Pirollo, K.F., et al., *Antisense therapeutics: from theory to clinical practice*. *Pharmacol Ther*, 2003. **99**(1): p. 55-77.
93. Wu, H., et al., *Determination of the role of the human RNase H1 in the pharmacology of DNA-like antisense drugs*. *J Biol Chem*, 2004. **279**(17): p. 17181-9.
94. Dias, N. and C.A. Stein, *Antisense oligonucleotides: basic concepts and mechanisms*. *Mol Cancer Ther*, 2002. **1**(5): p. 347-55.
95. Larrouy, B., et al., *RNase H-mediated inhibition of translation by antisense oligodeoxyribonucleotides: use of backbone modification to improve specificity*. *Gene*, 1992. **121**(2): p. 189-94.
96. Kole, R. and P. Sazani, *Antisense effects in the cell nucleus: modification of splicing*. *Curr Opin Mol Ther*, 2001. **3**(3): p. 229-34.
97. Chan, J.H., S. Lim, and W.S. Wong, *Antisense oligonucleotides: from design to therapeutic application*. *Clin Exp Pharmacol Physiol*, 2006. **33**(5-6): p. 533-40.
98. Anderson, K.P., et al., *Inhibition of human cytomegalovirus immediate-early gene expression by an antisense oligonucleotide complementary to immediate-early RNA*. *Antimicrob Agents Chemother*, 1996. **40**(9): p. 2004-11.
99. Simons, M., et al., *Antisense c-myc oligonucleotides inhibit intimal arterial smooth muscle cell accumulation in vivo*. *Nature*, 1992. **359**(6390): p. 67-70.
100. Morishita, R., et al., *Single intraluminal delivery of antisense cdc2 kinase and proliferating-cell nuclear antigen oligonucleotides results in chronic inhibition of neointimal hyperplasia*. *Proc Natl Acad Sci U S A*, 1993. **90**(18): p. 8474-8.
101. Morishita, R., et al., *Intimal hyperplasia after vascular injury is inhibited by antisense cdk 2 kinase oligonucleotides*. *J Clin Invest*, 1994. **93**(4): p. 1458-64.
102. Cioffi, C.L., et al., *Selective inhibition of A-Raf and C-Raf mRNA expression by antisense oligodeoxynucleotides in rat vascular smooth muscle cells: role of A-Raf and C-Raf in serum-induced proliferation*. *Mol Pharmacol*, 1997. **51**(3): p. 383-9.
103. Pollman, M.J., et al., *Inhibition of neointimal cell bcl-x expression induces apoptosis and regression of vascular disease*. *Nat Med*, 1998. **4**(2): p. 222-7.
104. Dy, G.K. and A.A. Adjei, *Systemic cancer therapy: evolution over the last 60 years*. *Cancer*, 2008. **113**(7 Suppl): p. 1857-87.

105. Liao, Y., et al., *Modulation of apoptosis, tumorigenesis and metastatic potential with antisense H-ras oligodeoxynucleotides in a high metastatic tumor model of hepatoma: LCI-D20*. Hepatogastroenterology, 2000. **47**(32): p. 365-70.
106. Ellouk-Achard, S., et al., *Induction of apoptosis in rat hepatocarcinoma cells by expression of IGF-I antisense c-DNA*. J Hepatol, 1998. **29**(5): p. 807-18.
107. Rimmele, M., *Nucleic acid aptamers as tools and drugs: recent developments*. Chembiochem, 2003. **4**(10): p. 963-71.
108. Scaggiante, B., et al., *Interaction of G-rich GT oligonucleotides with nuclear-associated eEF1A is correlated with their antiproliferative effect in haematopoietic human cancer cell lines*. FEBS J, 2006. **273**(7): p. 1350-61.
109. Berezovski, M., et al., *Nonequilibrium capillary electrophoresis of equilibrium mixtures: a universal tool for development of aptamers*. J Am Chem Soc, 2005. **127**(9): p. 3165-71.
110. Ruckman, J., et al., *2'-Fluoropyrimidine RNA-based aptamers to the 165-amino acid form of vascular endothelial growth factor (VEGF165). Inhibition of receptor binding and VEGF-induced vascular permeability through interactions requiring the exon 7-encoded domain*. J Biol Chem, 1998. **273**(32): p. 20556-67.
111. Shukla, D., et al., *Pegaptanib sodium for ocular vascular disease*. Indian J Ophthalmol, 2007. **55**(6): p. 427-30.
112. Griffin, L.C., et al., *In vivo anticoagulant properties of a novel nucleotide-based thrombin inhibitor and demonstration of regional anticoagulation in extracorporeal circuits*. Blood, 1993. **81**(12): p. 3271-6.
113. Giangrande, P.H., et al., *Distinct roles of E2F proteins in vascular smooth muscle cell proliferation and intimal hyperplasia*. Proc Natl Acad Sci U S A, 2007. **104**(32): p. 12988-93.
114. Daniels, D.A., et al., *A tenascin-C aptamer identified by tumor cell SELEX: systematic evolution of ligands by exponential enrichment*. Proc Natl Acad Sci U S A, 2003. **100**(26): p. 15416-21.
115. Zhang, L., et al., *Targeting Ku protein for sensitizing of breast cancer cells to DNA-damage*. Int J Mol Med, 2004. **14**(2): p. 153-9.
116. Choi, K.H., et al., *Intracellular expression of the T-cell factor-1 RNA aptamer as an intramer*. Mol Cancer Ther, 2006. **5**(9): p. 2428-34.
117. Mi, J., et al., *RNA aptamer-targeted inhibition of NF-kappa B suppresses non-small cell lung cancer resistance to doxorubicin*. Mol Ther, 2008. **16**(1): p. 66-73.
118. Sennino, B., et al., *Sequential loss of tumor vessel pericytes and endothelial cells after inhibition of platelet-derived growth factor B by selective aptamer AX102*. Cancer Res, 2007. **67**(15): p. 7358-67.
119. Scaggiante, B., et al., *The role of the eEF1A family in human cancer.*, in *Oncogene proteins: new research*, A. Malloy and E. Carson, Editors. 2007: New York. p. 177-93.
120. Scaggiante, B., et al., *Human cancer cell lines growth inhibition by GTn oligodeoxyribonucleotides recognizing single-stranded DNA-binding proteins*. Eur J Biochem, 1998. **252**(2): p. 207-15.
121. Morassutti, C., et al., *Effect of oligomer length and base substitutions on the cytotoxic activity and specific nuclear protein recognition of GTn oligonucleotides in the human leukemic CCRF-CEM cell line*. Nucleosides Nucleotides, 1999. **18**(6-7): p. 1711-6.
122. Dapas, B., et al., *Identification of different isoforms of eEF1A in the nuclear fraction of human T-lymphoblastic cancer cell line specifically binding to aptameric cytotoxic GT oligomers*. Eur J Biochem, 2003. **270**(15): p. 3251-62.
123. Bates, P.J., et al., *Antiproliferative activity of G-rich oligonucleotides correlates with protein binding*. J Biol Chem, 1999. **274**(37): p. 26369-77.
124. Ireson, C.R. and L.R. Kelland, *Discovery and development of anticancer aptamers*. Mol Cancer Ther, 2006. **5**(12): p. 2957-62.

125. Charlton, J., J. Sennello, and D. Smith, *In vivo imaging of inflammation using an aptamer inhibitor of human neutrophil elastase*. Chem Biol, 1997. **4**(11): p. 809-16.
126. Hicke, B.J., et al., *Tumor targeting by an aptamer*. J Nucl Med, 2006. **47**(4): p. 668-78.
127. Soutschek, J., et al., *Therapeutic silencing of an endogenous gene by systemic administration of modified siRNAs*. Nature, 2004. **432**(7014): p. 173-8.
128. Kaneda, Y., *Gene therapy: a battle against biological barriers*. Curr Mol Med, 2001. **1**(4): p. 493-9.
129. Brown, M.D., A.G. Schatzlein, and I.F. Uchegbu, *Gene delivery with synthetic (non viral) carriers*. Int J Pharm, 2001. **229**(1-2): p. 1-21.
130. Nishina, K., et al., *Efficient in vivo delivery of siRNA to the liver by conjugation of alpha-tocopherol*. Mol Ther, 2008. **16**(4): p. 734-40.
131. Geary, R.S., R.Z. Yu, and A.A. Levin, *Pharmacokinetics of phosphorothioate antisense oligodeoxynucleotides*. Curr Opin Investig Drugs, 2001. **2**(4): p. 562-73.
132. Watanabe, T.A., R.S. Geary, and A.A. Levin, *Plasma protein binding of an antisense oligonucleotide targeting human ICAM-1 (ISIS 2302)*. Oligonucleotides, 2006. **16**(2): p. 169-80.
133. Amarguioui, M., et al., *Tolerance for mutations and chemical modifications in a siRNA*. Nucleic Acids Res, 2003. **31**(2): p. 589-95.
134. Hall, A.H., et al., *RNA interference using boranophosphate siRNAs: structure-activity relationships*. Nucleic Acids Res, 2004. **32**(20): p. 5991-6000.
135. Liu, G., *Technology evaluation: ISIS-113715, Isis*. Curr Opin Mol Ther, 2004. **6**(3): p. 331-6.
136. Kraynack, B.A. and B.F. Baker, *Small interfering RNAs containing full 2'-O-methylribonucleotide-modified sense strands display Argonaute2/eIF2C2-dependent activity*. RNA, 2006. **12**(1): p. 163-76.
137. Schwarz, D.S., Y. Tomari, and P.D. Zamore, *The RNA-induced silencing complex is a Mg²⁺-dependent endonuclease*. Curr Biol, 2004. **14**(9): p. 787-91.
138. Morrissey, D.V., et al., *Potent and persistent in vivo anti-HBV activity of chemically modified siRNAs*. Nat Biotechnol, 2005. **23**(8): p. 1002-7.
139. Prakash, T.P., et al., *RNA interference by 2',5'-linked nucleic acid duplexes in mammalian cells*. Bioorg Med Chem Lett, 2006. **16**(12): p. 3238-40.
140. Corey, D.R., *Chemical modification: the key to clinical application of RNA interference?* J Clin Invest, 2007. **117**(12): p. 3615-22.
141. Iwase, R., T. Toyama, and K. Nishimori, *Solid-phase synthesis of modified RNAs containing amide-linked oligoribonucleosides at their 3'-end and their application to siRNA*. Nucleosides Nucleotides Nucleic Acids, 2007. **26**(10-12): p. 1451-4.
142. Chiu, Y.L. and T.M. Rana, *siRNA function in RNAi: a chemical modification analysis*. RNA, 2003. **9**(9): p. 1034-48.
143. Urban, E. and C.R. Noe, *Structural modifications of antisense oligonucleotides*. Farmaco, 2003. **58**(3): p. 243-58.
144. Braasch, D.A., et al., *RNA interference in mammalian cells by chemically-modified RNA*. Biochemistry, 2003. **42**(26): p. 7967-75.
145. Choung, S., et al., *Chemical modification of siRNAs to improve serum stability without loss of efficacy*. Biochem Biophys Res Commun, 2006. **342**(3): p. 919-27.
146. Martin, P., *A new access to 2-O-alkylated ribonucleosides and properties of 2-O-alkylated oligoribonucleosides*. Helvetica Chim Acta, 1995. **78**: p. 7967-75.
147. Weiler, J., J. Hunziker, and J. Hall, *Anti-miRNA oligonucleotides (AMOs): ammunition to target miRNAs implicated in human disease?* Gene Ther, 2006. **13**(6): p. 496-502.
148. Geary, R.S., et al., *Absolute bioavailability of 2'-O-(2-methoxyethyl)-modified antisense oligonucleotides following intraduodenal instillation in rats*. J Pharmacol Exp Ther, 2001. **296**(3): p. 898-904.

149. Wang, Z., et al., *Antisense oligonucleotides: efficient synthesis of 2'-O-methoxyethyl phosphorothioate oligonucleotides using 4,5-dicyanoimidazole. Are these oligonucleotides comparable to those synthesized using 1H-tetrazole as coupling activator?* Bioorg Med Chem, 2006. **14**(14): p. 5049-60.
150. Layzer, J.M., et al., *In vivo activity of nuclease-resistant siRNAs.* RNA, 2004. **10**(5): p. 766-71.
151. Blidner, R.A., et al., *Fully 2'-deoxy-2'-fluoro substituted nucleic acids induce RNA interference in mammalian cell culture.* Chem Biol Drug Des, 2007. **70**(2): p. 113-22.
152. Wilds, C.J. and M.J. Damha, *2'-Deoxy-2'-fluoro-beta-D-arabinonucleosides and oligonucleotides (2'F-ANA): synthesis and physicochemical studies.* Nucleic Acids Res, 2000. **28**(18): p. 3625-35.
153. Watts, J.K., et al., *2'-fluoro-4'-thioarabino-modified oligonucleotides: conformational switches linked to siRNA activity.* Nucleic Acids Res, 2007. **35**(5): p. 1441-51.
154. Dowler, T., et al., *Improvements in siRNA properties mediated by 2'-deoxy-2'-fluoro-beta-D-arabinonucleic acid (FANA).* Nucleic Acids Res, 2006. **34**(6): p. 1669-75.
155. Hoshika, S., et al., *RNA interference induced by siRNAs modified with 4'-thioribonucleosides in cultured mammalian cells.* FEBS Lett, 2005. **579**(14): p. 3115-8.
156. Dande, P., et al., *Improving RNA interference in mammalian cells by 4'-thio-modified small interfering RNA (siRNA): effect on siRNA activity and nuclease stability when used in combination with 2'-O-alkyl modifications.* J Med Chem, 2006. **49**(5): p. 1624-34.
157. Petersen, M. and J. Wengel, *LNA: a versatile tool for therapeutics and genomics.* Trends Biotechnol, 2003. **21**(2): p. 74-81.
158. Bondensgaard, K., et al., *Structural studies of LNA:RNA duplexes by NMR: conformations and implications for RNase H activity.* Chemistry, 2000. **6**(15): p. 2687-95.
159. Braasch, D.A. and D.R. Corey, *Locked nucleic acid (LNA): fine-tuning the recognition of DNA and RNA.* Chem Biol, 2001. **8**(1): p. 1-7.
160. Kaur, H., et al., *Thermodynamic, counterion, and hydration effects for the incorporation of locked nucleic acid nucleotides into DNA duplexes.* Biochemistry, 2006. **45**(23): p. 7347-55.
161. Hornung, V., et al., *Sequence-specific potent induction of IFN-alpha by short interfering RNA in plasmacytoid dendritic cells through TLR7.* Nat Med, 2005. **11**(3): p. 263-70.
162. Mook, O.R., et al., *Evaluation of locked nucleic acid-modified small interfering RNA in vitro and in vivo.* Mol Cancer Ther, 2007. **6**(3): p. 833-43.
163. Elmen, J., et al., *Locked nucleic acid (LNA) mediated improvements in siRNA stability and functionality.* Nucleic Acids Res, 2005. **33**(1): p. 439-47.
164. Wahlestedt, C., et al., *Potent and nontoxic antisense oligonucleotides containing locked nucleic acids.* Proc Natl Acad Sci U S A, 2000. **97**(10): p. 5633-8.
165. Jepsen, J.S., H.M. Pfundheller, and A.E. Lykkesfeldt, *Downregulation of p21(WAF1/CIP1) and estrogen receptor alpha in MCF-7 cells by antisense oligonucleotides containing locked nucleic acid (LNA).* Oligonucleotides, 2004. **14**(2): p. 147-56.
166. Frieden, M. and H. Orum, *The application of locked nucleic acids in the treatment of cancer.* IDrugs, 2006. **9**(10): p. 706-11.
167. Swayze, E.E., et al., *Antisense oligonucleotides containing locked nucleic acid improve potency but cause significant hepatotoxicity in animals.* Nucleic Acids Res, 2007. **35**(2): p. 687-700.
168. Nielsen, P., et al., *Peptide nucleic acid (PNA): oligonucleotide analogs with a polyamide backbone*, in *Antisense research and applications*, S. Crooke and B. Lebleu, Editors. 1993, CRC Press: Boca Rato, FL. p. 363-73.
169. Summerton, J. and D. Weller, *Morpholino antisense oligomers: design, preparation, and properties.* Antisense Nucleic Acid Drug Dev, 1997. **7**(3): p. 187-95.
170. Summerton, J., *Morpholino antisense oligomers: the case for an RNase H-independent structural type.* Biochim Biophys Acta, 1999. **1489**(1): p. 141-58.

171. Arora, V., et al., *Transdermal use of phosphorodiamidate morpholino oligomer AVI-4472 inhibits cytochrome P450 3A2 activity in male rats*. *Pharm Res*, 2002. **19**(10): p. 1465-70.
172. Iversen, P.L., et al., *Efficacy of antisense morpholino oligomer targeted to c-myc in prostate cancer xenograft murine model and a Phase I safety study in humans*. *Clin Cancer Res*, 2003. **9**(7): p. 2510-9.
173. Fletcher, S., et al., *Dystrophin expression in the mdx mouse after localised and systemic administration of a morpholino antisense oligonucleotide*. *J Gene Med*, 2006. **8**(2): p. 207-16.
174. Abes, S., et al., *Vectorization of morpholino oligomers by the (R-Ahx-R)₄ peptide allows efficient splicing correction in the absence of endosomolytic agents*. *J Control Release*, 2006. **116**(3): p. 304-13.
175. Muratovska, A. and M.R. Eccles, *Conjugate for efficient delivery of short interfering RNA (siRNA) into mammalian cells*. *FEBS Lett*, 2004. **558**(1-3): p. 63-8.
176. Kim, W.J., et al., *Cholesteryl oligoarginine delivering vascular endothelial growth factor siRNA effectively inhibits tumor growth in colon adenocarcinoma*. *Mol Ther*, 2006. **14**(3): p. 343-50.
177. Juliano, R., et al., *Mechanisms and strategies for effective delivery of antisense and siRNA oligonucleotides*. *Nucleic Acids Res*, 2008. **36**(12): p. 4158-71.
178. Lorenz, C., et al., *Steroid and lipid conjugates of siRNAs to enhance cellular uptake and gene silencing in liver cells*. *Bioorg Med Chem Lett*, 2004. **14**(19): p. 4975-7.
179. Manoharan, M., *Oligonucleotide conjugates as potential antisense drugs with improved uptake, biodistribution, targeted delivery, and mechanism of action*. *Antisense Nucleic Acid Drug Dev*, 2002. **12**(2): p. 103-28.
180. Mahat, R.I., et al., *Peptide-based gene delivery*. *Curr Opin Mol Ther*, 1999. **1**(2): p. 226-43.
181. Schepers, U., *RNA interference in practice: principles, basics and methods for gene silencing in C. elegans, drosophila and mammals*. 2005, New York.
182. Putnam, D., *Polymers for gene delivery across length scales*. *Nat Mater*, 2006. **5**(6): p. 439-51.
183. Leonetti, J.P., G. Degols, and B. Lebleu, *Biological activity of oligonucleotide-poly(L-lysine) conjugates: mechanism of cell uptake*. *Bioconjug Chem*, 1990. **1**(2): p. 149-53.
184. Pack, D.W., et al., *Design and development of polymers for gene delivery*. *Nat Rev Drug Discov*, 2005. **4**(7): p. 581-93.
185. Miller, A.D., *Cationic liposome systems in gene therapy*. *IDrugs*, 1998. **1**(5): p. 574-83.
186. Mahato, R.I., et al., *Biodistribution and gene expression of lipid/plasmid complexes after systemic administration*. *Hum Gene Ther*, 1998. **9**(14): p. 2083-99.
187. Karmali, P.P. and A. Chaudhuri, *Cationic liposomes as non-viral carriers of gene medicines: resolved issues, open questions, and future promises*. *Med Res Rev*, 2007. **27**(5): p. 696-722.
188. Felgner, P.L., et al., *Lipofection: a highly efficient, lipid-mediated DNA-transfection procedure*. *Proc Natl Acad Sci U S A*, 1987. **84**(21): p. 7413-7.
189. Huang, S.L., *Liposomes in ultrasonic drug and gene delivery*. *Adv Drug Deliv Rev*, 2008. **60**(10): p. 1167-76.
190. Mahato, R.I., Y. Takakura, and M. Hashida, *Development of targeted delivery systems for nucleic acid drugs*. *J Drug Target*, 1997. **4**(6): p. 337-57.
191. Chono, S., et al., *An efficient and low immunostimulatory nanoparticle formulation for systemic siRNA delivery to the tumor*. *J Control Release*, 2008. **131**(1): p. 64-9.
192. Auguste, D.T., et al., *Triggered release of siRNA from poly(ethylene glycol)-protected, pH-dependent liposomes*. *J Control Release*, 2008. **130**(3): p. 266-74.
193. Gershon, H., et al., *Mode of formation and structural features of DNA-cationic liposome complexes used for transfection*. *Biochemistry*, 1993. **32**(28): p. 7143-51.

194. Wasan, E.K., D.L. Reimer, and M.B. Bally, *Plasmid DNA is protected against ultrasonic cavitation-induced damage when complexed to cationic liposomes*. J Pharm Sci, 1996. **85**(4): p. 427-33.
195. Radler, J.O., et al., *Structure of DNA-cationic liposome complexes: DNA intercalation in multilamellar membranes in distinct interhelical packing regimes*. Science, 1997. **275**(5301): p. 810-4.
196. Friend, D.S., D. Papahadjopoulos, and R.J. Debs, *Endocytosis and intracellular processing accompanying transfection mediated by cationic liposomes*. Biochim Biophys Acta, 1996. **1278**(1): p. 41-50.
197. Mislick, K.A. and J.D. Baldeschwieler, *Evidence for the role of proteoglycans in cation-mediated gene transfer*. Proc Natl Acad Sci U S A, 1996. **93**(22): p. 12349-54.
198. Lang, I., M. Scholz, and R. Peters, *Molecular mobility and nucleocytoplasmic flux in hepatoma cells*. J Cell Biol, 1986. **102**(4): p. 1183-90.
199. Zhang, C., et al., *siRNA-containing liposomes modified with polyarginine effectively silence the targeted gene*. J Control Release, 2006. **112**(2): p. 229-39.
200. Santel, A., et al., *A novel siRNA-lipoplex technology for RNA interference in the mouse vascular endothelium*. Gene Ther, 2006. **13**(16): p. 1222-34.
201. Junghans, M., et al., *Cationic lipid-protamine-DNA (LPD) complexes for delivery of antisense c-myc oligonucleotides*. Eur J Pharm Biopharm, 2005. **60**(2): p. 287-94.
202. Zimmer, A., et al., *Synthesis of cholesterol modified cationic lipids for liposomal drug delivery of antisense oligonucleotides*. Eur J Pharm Biopharm, 1999. **47**(2): p. 175-8.
203. Moriguchi, R., et al., *A multifunctional envelope-type nano device for novel gene delivery of siRNA plasmids*. Int J Pharm, 2005. **301**(1-2): p. 277-85.
204. Hussein, G.A. and W.G. Pitt, *Micelles and nanoparticles for ultrasonic drug and gene delivery*. Adv Drug Deliv Rev, 2008. **60**(10): p. 1137-52.
205. Nyborg, W.L., *Ultrasound, contrast agents and biological cells; a simplified model for their interaction during in vitro experiments*. Ultrasound Med Biol, 2006. **32**(10): p. 1557-68.
206. Negishi, Y., et al., *Delivery of siRNA into the cytoplasm by liposomal bubbles and ultrasound*. J Control Release, 2008. **132**(2): p. 124-30.
207. Anwer, K., et al., *Ultrasound enhancement of cationic lipid-mediated gene transfer to primary tumors following systemic administration*. Gene Ther, 2000. **7**(21): p. 1833-9.
208. Hashiya, N., et al., *Local delivery of E2F decoy oligodeoxynucleotides using ultrasound with microbubble agent (Optison) inhibits intimal hyperplasia after balloon injury in rat carotid artery model*. Biochem Biophys Res Commun, 2004. **317**(2): p. 508-14.
209. Slowing, II, et al., *Mesoporous silica nanoparticles as controlled release drug delivery and gene transfection carriers*. Adv Drug Deliv Rev, 2008. **60**(11): p. 1278-88.
210. Huh, S., et al., *Tuning of particle morphology and pore properties in mesoporous silicas with multiple organic functional groups*. Chem Commun (Camb), 2003(18): p. 2364-5.
211. Burleigh, M.C., et al., *Stepwise assembly of surface imprint sites on MCM-41 for selective metal ion separations*, in ACS Symposium Series. 2001. p. 146-58.
212. York, A.W., S.E. Kirkland, and C.L. McCormick, *Advances in the synthesis of amphiphilic block copolymers via RAFT polymerization: stimuli-responsive drug and gene delivery*. Adv Drug Deliv Rev, 2008. **60**(9): p. 1018-36.
213. Thurmond, K.B., 2nd, et al., *Packaging of DNA by shell crosslinked nanoparticles*. Nucleic Acids Res, 1999. **27**(14): p. 2966-71.
214. Jewell, C.M. and D.M. Lynn, *Multilayered polyelectrolyte assemblies as platforms for the delivery of DNA and other nucleic acid-based therapeutics*. Adv Drug Deliv Rev, 2008. **60**(9): p. 979-99.
215. Park, T.G., J.H. Jeong, and S.W. Kim, *Current status of polymeric gene delivery systems*. Adv Drug Deliv Rev, 2006. **58**(4): p. 467-86.

216. Midoux, P., et al., *Specific gene transfer mediated by lactosylated poly-L-lysine into hepatoma cells*. Nucleic Acids Res, 1993. **21**(4): p. 871-8.
217. Grzelinski, M., et al., *RNA interference-mediated gene silencing of pleiotrophin through polyethylenimine-complexed small interfering RNAs in vivo exerts antitumoral effects in glioblastoma xenografts*. Hum Gene Ther, 2006. **17**(7): p. 751-66.
218. Urban-Klein, B., et al., *RNAi-mediated gene-targeting through systemic application of polyethylenimine (PEI)-complexed siRNA in vivo*. Gene Ther, 2005. **12**(5): p. 461-6.
219. Wang, D.A., et al., *Novel branched poly(ethylenimine)-cholesterol water-soluble lipopolymers for gene delivery*. Biomacromolecules, 2002. **3**(6): p. 1197-207.
220. Patil, S.D., D.G. Rhodes, and D.J. Burgess, *DNA-based therapeutics and DNA delivery systems: a comprehensive review*. AAPS J, 2005. **7**(1): p. E61-77.
221. Lee, H., J.H. Jeong, and T.G. Park, *A new gene delivery formulation of polyethylenimine/DNA complexes coated with PEG conjugated fusogenic peptide*. J Control Release, 2001. **76**(1-2): p. 183-92.
222. Zintchenko, A., A. Philipp, and E. Wagner, *Simple modification of branched PEI lead to highly efficient siRNA carriers with low toxicity*. Bioconjug Chem, 2008. **19**: p. 1448-55.
223. Rolland, A.P. and R.J. Mumper, *Plasmid delivery to muscle: Recent advances in polymer delivery systems*. Adv Drug Deliv Rev, 1998. **30**(1-3): p. 151-172.
224. Kim, S.H., et al., *Cardiomyocyte-targeted siRNA delivery by prostaglandin E(2)-Fas siRNA polyplexes formulated with reducible poly(amido amine) for preventing cardiomyocyte apoptosis*. Biomaterials, 2008. **29**(33): p. 4439-46.
225. Lee, K.Y., et al., *Preparation of chitosan self-aggregates as a gene delivery system*. J Control Release, 1998. **51**(2-3): p. 213-20.
226. Jiang, G., et al., *Target specific intracellular delivery of siRNA/PEI-HA complex by receptor mediated endocytosis*. Molecular Pharmaceutics, 2008. **6**(3): p. 727-37.
227. Dufes, C., I.F. Uchegbu, and A.G. Schatzlein, *Dendrimers in gene delivery*. Adv Drug Deliv Rev, 2005. **57**(15): p. 2177-202.
228. Inoue, Y., et al., *Efficient delivery of siRNA using dendritic poly(L-lysine) for loss-of-function analysis*. J Control Release, 2008. **126**(1): p. 59-66.
229. Patil, M.L., et al., *Surface-modified and internally cationic polyamidoamine dendrimers for efficient siRNA delivery*. Bioconjug Chem, 2008. **19**(7): p. 1396-403.
230. Santhakumaran, L.M., T. Thomas, and T.J. Thomas, *Enhanced cellular uptake of a triplex-forming oligonucleotide by nanoparticle formation in the presence of polypropylenimine dendrimers*. Nucleic Acids Res, 2004. **32**(7): p. 2102-12.
231. Choi, Y., et al., *Synthesis and functional evaluation of DNA-assembled polyamidoamine dendrimer clusters for cancer cell-specific targeting*. Chem Biol, 2005. **12**(1): p. 35-43.
232. Gebhart, C.L. and A.V. Kabanov, *Evaluation of polyplexes as gene transfer agents*. J Control Release, 2001. **73**(2-3): p. 401-16.
233. Kang, H., et al., *Tat-conjugated PAMAM dendrimers as delivery agents for antisense and siRNA oligonucleotides*. Pharm Res, 2005. **22**(12): p. 2099-106.
234. Eom, K.D., et al., *Dendritic alpha,epsilon-poly(L-lysine)s as delivery agents for antisense oligonucleotides*. Pharm Res, 2007. **24**(8): p. 1581-9.
235. Weber, N., et al., *Characterization of carbosilane dendrimers as effective carriers of siRNA to HIV-infected lymphocytes*. J Control Release, 2008. **132**(1): p. 55-64.
236. Zinselmayer, J.C., M.K. Bhalgat, and R.T. Zera, *The lower-generation polypropylenimine dendrimers are effective gene-transfer agents*. Pharm Res, 2002. **19**(960-7).
237. Roberts, J.C., M.K. Bhalgat, and R.T. Zera, *Preliminary biological evaluation of polyamidoamine (PAMAM) Starburst dendrimers*. J Biomed Mater Res, 1996. **30**(1): p. 53-65.
238. Haensler, J. and F.C. Szoka, Jr., *Polyamidoamine cascade polymers mediate efficient transfection of cells in culture*. Bioconjug Chem, 1993. **4**(5): p. 372-9.

239. Godbey, W.T., K.K. Wu, and A.G. Mikos, *Tracking the intracellular path of poly(ethylenimine)/DNA complexes for gene delivery*. Proc Natl Acad Sci U S A, 1999. **96**(9): p. 5177-81.
240. Li, J. and X.J. Loh, *Cyclodextrin-based supramolecular architectures: syntheses, structures, and applications for drug and gene delivery*. Adv Drug Deliv Rev, 2008. **60**(9): p. 1000-17.
241. Davis, M.E. and M.E. Brewster, *Cyclodextrin-based pharmaceuticals: past, present and future*. Nat Rev Drug Discov, 2004. **3**(12): p. 1023-35.
242. Yang, C., et al., *Cationic star polymers consisting of alpha-cyclodextrin core and oligoethylenimine arms as nonviral gene delivery vectors*. Biomaterials, 2007. **28**(21): p. 3245-54.
243. Li, J., et al., *cationic supramolecules composed of multiple oligoethylenimide-grafted beta-cyclodextrins threted on a polymer chain for efficient gene delivery*. Advanced Materials, 2006. **18**: p. 2969-74.
244. Hernot, S. and A.L. Klibanov, *Microbubbles in ultrasound-triggered drug and gene delivery*. Adv Drug Deliv Rev, 2008. **60**(10): p. 1153-66.
245. Chomas, J.E., et al., *Mechanisms of contrast agent destruction*. IEEE Trans Ultrason Ferroelectr Freq Control, 2001. **48**(1): p. 232-48.
246. Christiansen, J.P., et al., *Targeted tissue transfection with ultrasound destruction of plasmid-bearing cationic microbubbles*. Ultrasound Med Biol, 2003. **29**(12): p. 1759-67.
247. Teupe, C., et al., *Vascular gene transfer of phosphomimetic endothelial nitric oxide synthase (S1177D) using ultrasound-enhanced destruction of plasmid-loaded microbubbles improves vasoreactivity*. Circulation, 2002. **105**(9): p. 1104-9.
248. Mayer, C.R. and R. Bekeredian, *Ultrasonic gene and drug delivery to the cardiovascular system*. Adv Drug Deliv Rev, 2008. **60**(10): p. 1177-92.
249. De Laporte, L. and L.D. Shea, *Matrices and scaffolds for DNA delivery in tissue engineering*. Adv Drug Deliv Rev, 2007. **59**: p. 292-307.
250. Grassi, M., et al., *Understanding drug release and absorption mechanisms*. 2007, CRC Press: Boca Raton.
251. Davia, L., et al., *Mathematical modelling of NABD release from endoluminal gel paved stent*. Comput Biol Chem, 2009. **33**(1): p. 33-40.
252. Kimura, T., et al., *Preparation of poly(vinyl alcohol)/DNA hydrogels via hydrogen bonds formed on ultra-high pressurization and controlled release of DNA from the hydrogels for gene delivery*. J Artif Organs, 2007. **10**(2): p. 104-8.
253. Kong, H.J., et al., *Design of biodegradable hydrogel for the local and sustained delivery of angiogenic plasmid DNA*. Pharm Res, 2008. **25**(5): p. 1230-8.
254. Cohen-Sacks, H., et al., *Delivery and expression of pDNA embedded in collagen matrices*. J Control Release, 2004. **95**(2): p. 309-20.
255. El Andaloussi, S., et al., *TP10 a delivery vector for decoy oligonucleotides targeting the Myc protein*. J Control Release, 2005. **110**: p. 189-201.
256. Ayers, D., et al., *polyacrylic acid mediated acular delivery of ribozyme*. Journal of Controlled Release, 1996. **38**: p. 167-75.
257. Zhang, Z., et al., *Controlled delivery of anti-sense oligodeoxynucleotide from multilayered biocompatible phosphorylcholine polymer films*. J Control Release, 2008. **130**(1): p. 69-76.
258. Grassi, G., et al., *Characterization of nucleic acid molecule/liposome complex and rheological effects on pluronic/alginate matrices*. Journal of Drug Delivery Science and Technology, 2007. **17**.
259. Grassi, G., et al., *Rheological properties of aqueous Pluronic-alginate systems containing liposomes*. J Colloid Interface Sci, 2006. **301**(1): p. 282-90.
260. Grassi, M., et al., *Novel design of drug elivery in stented arteries: a numerical comparative study*. Mathematical Biol Engeneering, 2008. **in pres**.

261. Kam, N.W.S. and H. Dai, *Carbon Nanotubes as Intracellular Protein Transporters: Generality and Biological Functionality*. J Am Chem Soc, 2004. **127**(16): p. 6021–6.
262. Kam, N.W.S. and H. Dai, *Functionalization of Carbon Nanotubes via Cleavable Disulfide Bonds for Efficient Intracellular Delivery of siRNA and Potent Gene Silencing*. J Am Chem Soc, 2005. **127**(36): p. 12492–3.
263. Giljohann, D.A., et al., *Gene Regulation with Polyvalent siRNA–Nanoparticle Conjugates*. Journal of the American Chemical Society, 2009. **131**(6): p. 2072-2073.
264. Lee, J.-S., et al., *Gold, Poly(β -amino ester) Nanoparticles for Small Interfering RNA Delivery*. Nano Letters, 2009. **9**(6): p. 2402-2406.
265. Boeckle, S. and E. Wagner, *Optimizing targeted gene delivery: chemical modification of viral vectors and synthesis of artificial virus vector systems*. AAPS J, 2006. **8**(4): p. E731-42.
266. Behlke, M.A., *Progress towards in vivo use of siRNAs*. Mol Ther, 2006. **13**(4): p. 644-70.
267. Barquintero, J., H. Eixarch, and M. Perez-Melgosa, *Retroviral vectors: new applications for an old tool*. Gene Ther, 2004. **11 Suppl 1**: p. S3-9.
268. Teichler Zallen, D., *US gene therapy in crisis*. Trends Genet, 2006. **16**(6): p. 272-5.
269. Zentilin, L. and M. Giacca, *In vivo transfer and expression of genes coding for short interfering RNAs*. Curr Pharm Biotechnol, 2004. **5**(4): p. 341-7.
270. Yu, J.Y., S.L. DeRuijter, and D.L. Turner, *RNA interference by expression of short-interfering RNAs and hairpin RNAs in mammalian cells*. Proc Natl Acad Sci U S A, 2002. **99**(9): p. 6047-52.
271. McManus, M.T. and P.A. Sharp, *Gene silencing in mammals by small interfering RNAs*. Nat Rev Genet, 2002. **3**(10): p. 737-47.
272. Singer, O. and I.M. Verma, *Applications of lentiviral vectors for shRNA delivery and transgenesis*. Curr Gene Ther, 2008. **8**(6): p. 483-8.
273. Barton, G.M. and R. Medzhitov, *Retroviral delivery of small interfering RNA into primary cells*. Proc Natl Acad Sci U S A, 2002. **99**(23): p. 14943-5.
274. Hu, C.M. and Z.F. Chang, *Synthetic lethality by lentiviral short hairpin RNA silencing of thymidylate kinase and doxorubicin in colon cancer cells regardless of the p53 status*. Cancer Res, 2008. **68**(8): p. 2831-40.
275. Manjunath, N., et al., *Lentiviral delivery of short hairpin RNAs*. Adv Drug Deliv Rev, 2009. **61**(9): p. 732-45.
276. Shen, C., et al., *Gene silencing by adenovirus-delivered siRNA*. FEBS Lett, 2003. **539**(1-3): p. 111-4.
277. Narvaiza, I., et al., *Effect of adenovirus-mediated RNA interference on endogenous microRNAs in a mouse model of multidrug resistance protein 2 gene silencing*. J Virol, 2006. **80**(24): p. 12236-47.
278. Marshall, E., *Gene therapy death prompts review of adenovirus vector*. Science, 1999. **286**(5448): p. 2244-5.
279. Anesti, A.M., et al., *Efficient delivery of RNA Interference to peripheral neurons in vivo using herpes simplex virus*. Nucleic Acids Res, 2008. **36**(14): p. e86.
280. Smith, S.M., F. Maldarelli, and K.T. Jeang, *Efficient expression by an alphavirus replicon of a functional ribozyme targeted to human immunodeficiency virus type 1*. J Virol, 1997. **71**(12): p. 9713-21.
281. Kaneko, H., et al., *Inhibition of HIV-1 replication by vesicular stomatitis virus envelope glycoprotein pseudotyped baculovirus vector-transduced ribozyme in mammalian cells*. Biochem Biophys Res Commun, 2006. **349**(4): p. 1220-7.
282. Croyle, M.A., et al., *"Stealth" adenoviruses blunt cell-mediated and humoral immune responses against the virus and allow for significant gene expression upon readministration in the lung*. J Virol, 2001. **75**(10): p. 4792-801.

283. Lanciotti, J., et al., *Targeting adenoviral vectors using heterofunctional polyethylene glycol FGF2 conjugates*. Mol Ther, 2003. **8**(1): p. 99-107.
284. O'Riordan, C.R., et al., *PEGylation of adenovirus with retention of infectivity and protection from neutralizing antibody in vitro and in vivo*. Hum Gene Ther, 1999. **10**(8): p. 1349-58.
285. Fisher, K.D., et al., *Polymer-coated adenovirus permits efficient retargeting and evades neutralising antibodies*. Gene Ther, 2001. **8**(5): p. 341-8.
286. Ogawara, K., et al., *A novel strategy to modify adenovirus tropism and enhance transgene delivery to activated vascular endothelial cells in vitro and in vivo*. Hum Gene Ther, 2004. **15**(5): p. 433-43.
287. Kreppel, F., et al., *Combined genetic and chemical capsid modifications enable flexible and efficient de- and retargeting of adenovirus vectors*. Mol Ther, 2005. **12**(1): p. 107-17.
288. Curiel, D.T., et al., *High-efficiency gene transfer mediated by adenovirus coupled to DNA-polylysine complexes*. Hum Gene Ther, 1992. **3**(2): p. 147-54.
289. Wagner, E., et al., *Coupling of adenovirus to transferrin-polylysine/DNA complexes greatly enhances receptor-mediated gene delivery and expression of transfected genes*. Proc Natl Acad Sci U S A, 1992. **89**(13): p. 6099-103.
290. Plank, C., et al., *Gene transfer into hepatocytes using asialoglycoprotein receptor mediated endocytosis of DNA complexed with an artificial tetra-antennary galactose ligand*. Bioconjug Chem, 1992. **3**(6): p. 533-9.

3 – Polymeric Drug Delivery Systems

3.1 – Polymer in drug delivery systems (DDS)

A drug delivery system (DDS) has been defined by Flynn as “whatever means possible, be it chemical, physicochemical, or mechanical, to regulate a drug access rate to the body’s central compartment, or in some case, directly to the involved tissue” [1]. In a DDS, the most important characteristics are the biocompatibility, the biodegradability, the mechanical, thermal and chemical resistance. While the first two requirements must achieve a certain minimum level, the mechanical, thermal and chemical resistance, depend on the chosen system configurations and from the physiological environment where the material is going to work. The usefulness of polymers in DDS is well established. Continued improvement and accelerating research and development in polymeric materials has played a vital role in the progress of most controlled release technologies. In the past 25 years there was a considerable increase in interest in this technology, as shown by the increasing numbers of publications and patents in the area of controlled drug release systems using synthetic as well as naturally occurring polymeric materials [2-7].

The polymeric DDS can be distinguished on the base of the release mechanism: physical (diffusion or osmosis) and chemical (included enzyme catalyzed reaction). The physical mechanisms of the diffusion are able to control the release of an active molecule through the aqueous phase filling the pore of the polymeric structure (porous system) or through the swollen polymeric mesh (non-porous system). In the release systems controlled by the osmosis, the active principle is embedded into an osmotic nucleus coated by a water permeable membrane with release pores. Finally, in the chemical controlled release systems, chemical/enzymatic reactions dissolve the polymeric matrices or cut the link between polymers chain and active molecules.

On the base of the system configuration, it is possible to distinguish the polymers for drug release in matrices, reservoir system with membrane, bioerodible systems and pendant chain systems [4].

3.1.1 – Matrices

Matrices are continuous system where the crosslinking can be physical or chemical. The active molecule is dispersed into the polymeric matrix and the release occurs by the diffusion of the substance through the polymeric network according to the Fick's laws of diffusion [8]. The solvent plays an important role on the release regulation because it can swell the matrix and it is responsible for the solid drug dissolution when the drug is dispersed in the polymeric network. The drug can be dispersed at molecular level into the polymeric mesh (amorphous) or it can be partially present crystalline form. Release kinetics depends also on the initial concentration of the active molecule into the polymeric mesh and on the system geometry therefore, it is possible to distinguish:

1. matrices with the active molecule concentration lower than the polymeric solubility threshold.
2. Matrices with the active molecule concentration higher than the polymeric solubility threshold. These systems are called disperse because the drug is present as solid particles into the polymeric mesh
3. *Reservoir matrices* are similar to disperse systems but with an external shield less permeable to the drug than the polymeric mesh that regulate the release.
4. Porous matrices containing the dispersed drug.

These systems can be prepared by different methodologies: in the first and second type generally, the active molecule is mixed as a fine powder with the pre-polymer then, the mixture is polymerised into a mould. Another method can be applied in the first type. Matrices can be polymerised in advance and then, immersed into a saturated solution of active molecule for the adsorption [9].

In the reservoir matrices, another step is required in order to shielding the matrices with an external layer. Normally, a central nucleus is prepared as described and then, an outer layer is added by solvent evaporation of a shielding agent solution. Another technique consists in the active molecule extraction by a solvent from the matrices outer layer. At the same time, the matrix outer layer adsorbs from the solvent a crosslinking agent that can be polymerised by UV irradiation, creating a membrane that covers a central nucleus loaded with the active molecule.

Porous matrices can be realised, by simply mixing the active molecule and the polymer as a fine powder. Then, the mixture is pressed in order to obtain the final product. The main advantage of this methodology consists in maintaining active compound biological activity [8].

A particularly interesting class of active compound that can take advantages from the use of polymeric matrices are the nucleic acid based drugs (NABDs).

3.1.2 – Reservoir systems

In many reservoir systems, the active molecule, in form of highly concentrated solution or at the solid state, is confined within two semipermeable membranes [8]. That can be constituted by:

- amorphous or semicrystalline polymers such as the polyethylene or ethylene and vinyl acetate copolymers above the glass transition temperature
- Hydrogels at the glass state that swell upon contact with water

Active molecule transport depends on the concentration gradient in the porous membranes. The presence of a limiting layer in between the membrane and the release environment reduces the release kinetics [8].

Osmotic systems belong to the class of reservoir systems. They are called *miniosmotic pump* and *elementary osmotic pump*. In miniosmotic pump, the storing cavity, containing a concentrated solution of the active molecule, is separated from the osmotic agent by a mobile septum. A semipermeable membrane and a rigid impermeable membrane with an orifice close the osmotic and storing compartment respectively. In the elementary osmotic pump there is no distinction within the storing and osmotic compartment and the system is reduced to a semipermeable membrane with an orifice delimiting the osmotic agent and the concentrated active molecule together. In both cases, when the system is placed in contact with water, a certain quantity is adsorbed and a correspondent volume of concentrated active molecule solution is released from the orifice [8].

One problem related to reservoir systems is that the release system must be removed from the body after complete drug depletion. Another potential problem is that if the reservoir membrane is accidentally broken, a large amount of drug may be suddenly released (drug dumping) [8].

3.1.3 – Bioerodible systems

The release from matrices and reservoir systems is limited by diffusion rate that depends on polymer permeability and/or drug characteristics. Moreover, it was recognised that surgical removal of the drug-depleted delivery systems is difficult, leaving non-degradable foreign materials in the body [10-11]. In order to overcome such problems, a class of bioerodible and biodegradable polymeric system was developed. At the base of the release from a bioerodible/biodegradable systems there are the *in vivo* erosion/degradation of the polymeric structure [8]. Two different type of erosion can be distinguished: physical and chemical/enzymatic. Physical erosion consists in a progressive breaking of the physical linkages between polymer chains caused by the hydrodynamic conditions imposed in the release environment. This type of erosion starts from the outer layer of the matrix with a progressive reduction of the volume up to complete system dissolution.

The chemical/enzymatic erosion, instead, is realized by three different mechanisms:

- breaking of the linkages between polymeric chains. This is the case, for example, of hydrosoluble polymers that are crosslinked in order to obtain an insoluble matrix. After the breakup of crosslinks, the polymer returns soluble.
- Breaking of polymer backbone. While high molecular weight polymers are, usually, insoluble, low molecular weight polymer can be soluble.
- Protonation, hydrolysis or ionization of a side group. This transforms the polymer from insoluble to soluble.

The erosion can be also a combination of the three factor described and thereby, the mathematical description of the phenomena became quite complicated [12]. The chemical/enzymatic erosion can be homogeneous when involves all the polymeric mass. On the contrary it is heterogeneous when it involves only the delivery system surface [13-14]. There are two methods to realize a bioerodible system: encapsulating the active molecule into an erodible membrane similarly to the reservoir systems, or dispersing the active molecule into bioerodible matrix. In both cases, the release speed depends on the ratio between drug diffusion in the polymeric phase and polymer erosion speed.

3.1.4 – *Pendant chain systems*

In *pendant chain* systems, the active molecule is attached to the backbone of the polymer. Breakup of the linkage by hydrolysis or by enzymatic cleavage allows drug release. Release rate depends on both cleavage rate and diffusion in the polymeric network [8, 13]. There are two methods to realize this type of configuration: the active molecule is converted in to a derivatives that can be polymerised in order to obtain the final product or the active molecule (or a derivate) is chemically linked to a side group of the main polymer chain eventually with the addition of a spacer [13]. Ester, amide, orthoester, urethan, anhydride and carbonate are typical hydrolysable or biodegradable bonds employed in pendant chain systems [15]. It is important to underline that, despite their versatility, these systems are rarely marketed as they are considered a new chemical entities and the path needed to get an FDA approval is arduous and expensive [16].

3.2 – *Gels*

Gels can be defined as coherent systems with mechanical properties in-between the solids and the liquids. They are constituted by a continuous liquid medium where very small particles or high molecular weight molecules are dispersed and organised, in spatial manner, to form a three-

dimensional continuous network pervading the entire system. Particles can be ultramicroscopic crystal or polymeric chains. The three-dimensional network is formed by polymeric chain linked each other's by point junctions (chemical bond) or extended in the space (physical bond) [17].

Both, natural and synthetic polymers are able to form a gel (gelation). Chemical bonds are frequent in synthetic polymer gels while, in natural polymer gels, generally, the interaction occurring is of physical type and regards portion of the polymeric chains. In this type of linkage, it is possible to distinguish, on the same chain, binding regions and free regions. Some examples of sufficiently strong physical interactions are the hydrogen bonding and the electrostatic interaction. Nevertheless both these interactions are substantially weaker than chemical bonds. Physical gels results stable because many interactions cooperate in sequence. Typical gel forming substances are polysaccharides and proteins.

The dynamic-mechanical properties of gels are tightly related to the three-dimensional structures of their network. In static conditions or under small amplitude deformations, gels demonstrate behaviour similar to the elastic solids. By means of Rheology, it is possible to distinguish gels in two categories: strong or weak gels. Oscillatory tests serve to characterize gels structure. Storage modulus G' and the loss modulus G'' represent the elastic energy viscous aspect of gel network. A gel is considered strong if G' is at least, one order of magnitude higher than the loss modulus and G' , G'' are independent from the applied oscillation frequency [16].

Two important properties of gels are swelling and the syneresis. Swelling consists in solvent migration into the gel network with a consequent volume increase. Syneresis is the opposite phenomenon consisting in the spontaneous gel contraction with solvent expulsion from the gel mesh [16].

3.3 – Hydrogels

3.3.1 – Overview on hydrogel systems

In the pharmaceutical field, the most used class of gels is the hydrogels where the continuous media is water. These types of polymeric materials are able to absorb a large amount of water maintaining a well defined tridimensional structure. According to their nature, the hydrogels can be divided in two type: *aerogels* and *xerogels*. An aerogel is a dry porous material that is able to absorb water into the pores without, substantially, any swelling phenomenon while, a xerogel, is a non-porous material that absorbs water and swells [18].

Hydrogels include materials with a wide range of properties by a small variation on the polymer formulations and because of this diversity they are interesting for the pharmaceutical

applications The swelling behavior can be ruled by change in the external environment (solvent concentration, pH, temperature, ionic strength), depending on the polymer type [19]. Any hydrophilic polymers that can be reticulated in an elastic tridimensional structure can be used to form an hydrogel. The hydrophilicity is normally related to the presence of side groups on the main chain such as hydroxylic, ammidic, methacrylic, carboxylic and sulfonic. Crosslinking can be due to chemical reaction between side groups of the linear polymers chains, ionizing radiation bombing and formation of physical interactions [18].

Hydrogels can be constituted by natural polymers, synthetic polymers or by a combination of both. In the class of synthetic polymers, a wide range of monomers are commonly mixed for the hydrogels productions by a copolymerization. They can be distinguished in: *neutral hydrophilic monomers*, *neutral hydrophobic monomers* and *ionic monomers*. The first type forms polymers that are able to swell in water while the second gives water insoluble polymers. Same examples of hydrophilic monomers are the hydroxyalkyl-methacrylates, the methacryl-amides, the N-vinyl-2-pyrrolidon; examples of hydrophobic monomers are the methacrylate, the vinyl-acetate, the acrylonitrile, the styrene; finally, ionic monomers are the methacrylic acid, propionic acid, the sodium styrene sulfonate, the vinyl-pyridine, the amino-ethyl-methacrylates [18]. Hydrogels properties can be modulated by different combinations of hydrophobic, hydrophilic and ionic monomers or by acting on the type and concentration of the crosslinks or on the reaction conditions. Synthetic hydrogels can be also chemically converted from one to another as it happened, for example, for poly(acrylonitrile) that can be converted in poly(acrylamide) and then in poly(acrylic acid) [18].

Linear polymer such as the poly(ethylene glycol) (PEG, also called poly(ethylene oxide) or PEO) and the poly(vinyl-alcohol) (PVA) can be crosslinked by different strategies in order to form a three-dimensional hydrogel network. The typical way to induce crosslinking is to make use of ionizing radiation (high energy electron, UV, gamma ray), and crosslinking agents. Ionizing radiations cause the formations of free radicals on the polymeric chain that can react with the formation of the crosslinks between chains or can break the polymeric chain degrading the polymer. The final crosslink density depends on the balance between degradation and crosslinking [20].

Crosslinking by covalent bond between polymer chains can be performed by the condensation of bifunctional compounds with the side groups of the polymers. The bifunctional compound forms a bridge between polymers chains. These types of reactions are, normally, performed in water solution with hydrophilic polymers. An estimation of the crosslinking degree ρ_x is given by the ratio between the moles of crosslinking agent and the moles of polymer repeating. [20].

Physical reticulation, even if less used than the chemicals, is also important in the pharmaceutical field. The physical includes the entanglements, specific interactions (hydrophobic), unspecific interactions (hydrogen bond), semicrystalline polymers. In the case of semicrystalline polymers, there are narrow crystalline regions that work as crosslinking junction. In water solution, the amorphous regions are able to absorb the water while the crystalline regions, insoluble, prevent from system dissolution [18].

Although synthetic hydrogels are reproducible and versatile, hydrogels based on natural polymers have a great importance because their biocompatibility, biodegradability, availability and reduced cost. Some natural polymers spontaneously form strong physical hydrogels under certain conditions (as the ion dependent gelation of alginate an and the thermo dependent agarose gellation) [18]. The natural or semisynthetic polymer hydrogels constitutes an important class of compounds for the development of drug release systems. These systems are able to increase the drugs thermal stability, prevent the premature metabolic digestion, control the release speed of active agent and realize a target specific releasing [21]. Moreover, given their characteristics, is not negligible their utility in tissue engineering applications [22].

In the following sections the natural and synthetic polymers used in this work will be presented.

3.4.2 – Alginates

Alginates family includes a broad variety of anionic polysaccharides of natural origin with an increasing numbers of applications in the biotechnological field. Since many years, these compounds were successfully used in the food industry as thickening agents, gelling agents and colloidal stabilizer for food and beverage. Their particular characteristics are ideal for the development of hydrogels matrices intended for controlled release or immobilization of biological agents such as live cells, proteins or active molecules in general. Indeed, alginate hydrogels have a relatively inert aqueous environment inside the matrix and the encapsulation processes can occur at room temperature without the use of organic solvent allowing the prevention of activity loosing of biological agents. Moreover, the hydrogels porosity can be easily modulated and the systems is biodegradable in the physiologic conditions [23].

Alginates commercially available mainly derive from three species of brown seaweeds: *Laminaria hyperborea*, *Ascophyllum nodosum* and *Macrocystis pyrifera*. Other minor sources include the species *Laminaria japonica*, *Eclonia maxima*, *Lessonia nigrescens* and the species of the genus *Sargassum* (Fig. 3.1). In all these species, the alginate is the principle polysaccharides in the seaweed matrix (up to 40% by weight of dry seaweed) [23-24].



Fig. 3.1: seaweed used for alginates extraction. From left to right: *Laminaria hyperborea*, *Ascophyllum nodosum*, *Macrocystis pyrifera* and the genus *Sargassum*.

In figures 3.2, it is showed the alginate biosynthetic pathways. The production from seaweed consists in milling the harvest materials, then the alginate is extracted by mineral acid that removes the other homopolymers and, at the same time, it exchanges the alkali cation with H^+ . The final steps consists in the conversion of the insoluble protonate form in the soluble sodium salt, purification and conversion back to acid form, in other salt form or ester form [23].

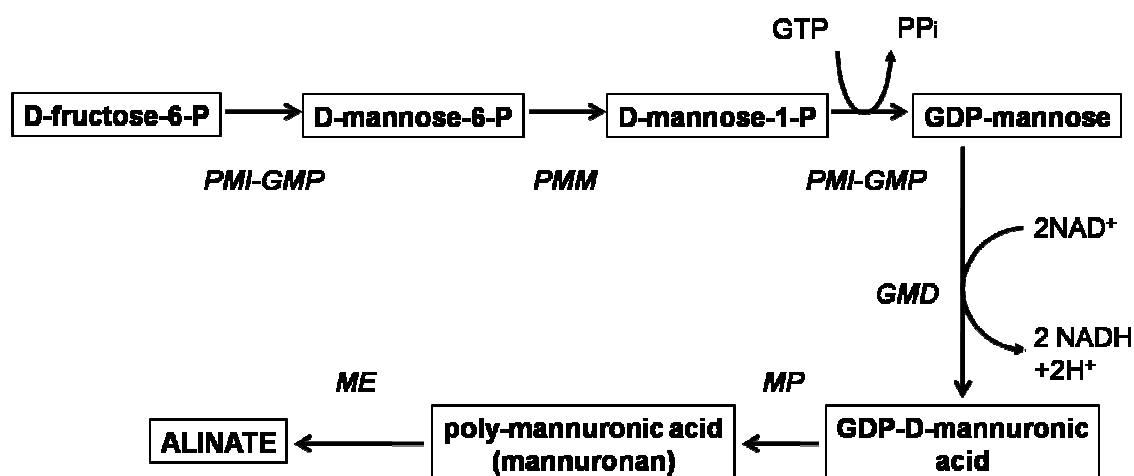


Fig. 3.2: alginate biosynthetic pathway. The enzymes involved in the biosynthesis are also showed. *PMI*, phosphomannose isomerase; *GMP*, guanosine diphosphomannose pyrophosphorylase; *PMM*, phosphomannomutase; *GMD*, GDP-mannose dehydrogenase; *MP*, mannuronate polymerase; *ME*, mannuronate C-5 epimerase.

The alginate chains are unbranched linear copolymers consisting of (1-4) linked β -D-mannuronic acid (M) and α -D-guluronic acid (G) that are organized in different sequences or blocks. The monomers can appear in homopolymeric blocks of consecutive G-residues (G-blocks), consecutive M-residues (M-blocks), heteropolymeric blocks of regularly alternated M- and G-residues (MG-block), or randomly organized blocks (Fig. 3.3). The polymer characteristics are strongly influenced by the blocks sequences belonging to the polymeric chain. The alginates family

have an high sequence variability that depends on the source organism, tissue, season and growth conditions [23-24]. High content of G are generally found in alginate prepared from old *L. hyperborea* plants whereas, alginate prepared from *A. nodosum* and *M. pyrifera*, are characterized by low G content and low gel strength. Recently, particular preparation of alginate with very high content of G or M (up to 100%) can be obtained from culturing of bacteria (*Azotobacter vinelandii* and the genus *Pseudomonas* are some natural producer), from particular algae tissue (outer cortex), or by enzymatic modification using mannuronan C-5 epimerase that converts M-units in G-units [24]. The units links difference in G-blocks and M-blocks, reflect a different conformations belong the polymeric chain: while the M-blocks are substantially linear and flat, the G-blocks assuming a buckled conformations (Fig. 3.3). This difference influences chain flexibility. Indeed, M-blocks regions are more flexible than G-blocks regions because the carboxylic steric effect. In other words, the higher the mannuronic content the higher the M-blocks regions and more flexible is the alginate chain in solution [25].

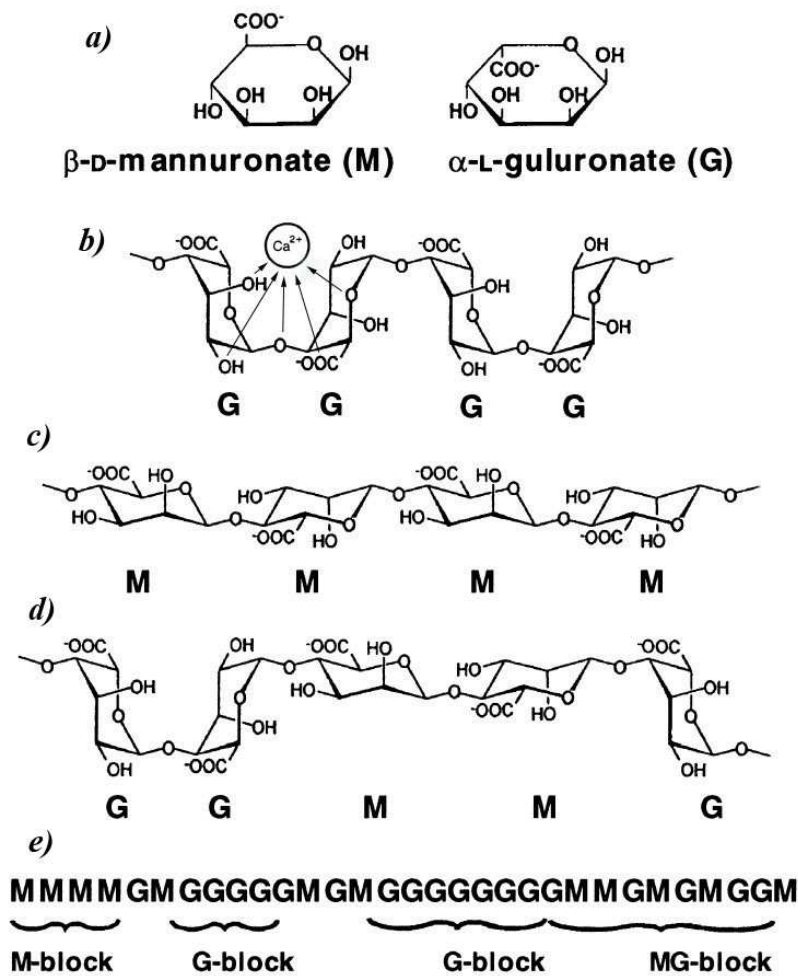


Fig. 3.3: alginate structure and monomers. *a*) structure of β -D-mannuronic acid (M) and α -D-guluronic acid (G). *b*) G-blocks region, the coordination with a Ca^{2+} ion is also showed *c*) M-blocks region *d*) MG-blocks region. *e*) examples of blocks distributions inside polymer chain.

The most important consequence of the monomers arrangement consists in the capability of the alginates (especially of the sodium alginate) to form hydrogels in water solutions in presence of bivalent cations. The gelation is consequence of the ions exchange between the Na^+ of the G monomers, with the bivalent cations. Contrarily to the monovalent cations, bivalent cations promoting the physical interaction between G-blocks regions belonging to different chains in a characteristic structure called *egg-box*. Each chain is able to interact with many other originating the gel networking (Fig. 3.4). The most used cation is the Ca^{2+} but also Ba^{2+} and Sr^{2+} are used because of their ability to produce stronger gelation than calcium. Pb^{2+} , Cu^{2+} , Cd^{2+} , Co^{2+} , Ni^{2+} , Zn^{2+} and Mn^{2+} also results in a gelation but their use is limited because of potential toxicity problems. Mg^{2+} does not produce gelation. Alginates with a G contents equal or higher than 70% in weight and G-blocks longer than 15 units allow the production of hydrogels characterized by a low shrinkage, high mechanical resistance and high stability. These systems can be also distinguished for their rigidity and fragility while, in hydrogels with higher content of M, the elastic characters are prevalent [23].

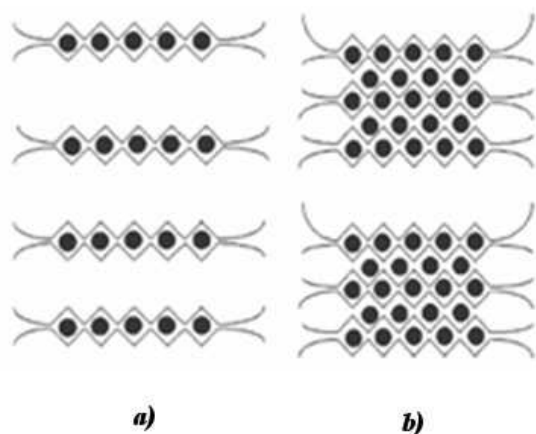


Fig. 3.4: schematic representation of the egg-box structure in alginates in presence of low (a) or high (b) concentration of divalent cations. The black dots represent the cations linking guluronic sequences.

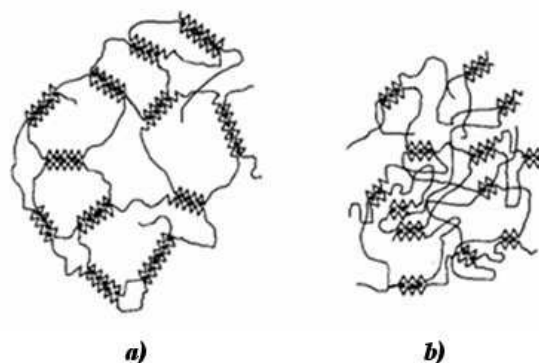


Fig. 3.5: structural network model in presence of high guluronic acid (a) or low guluronic acid (b) content.

The alginate used in this work is the commercial available Protanal™ LF 10/60 from FMC BioPolymers which has an average molecular weight of 200 kDa and a G/M ratio (in weight) between 65/35 and 75/25. Gel preparation can be realized by two methodologies: the *diffusional setting* and the *internal setting*. In the first case, alginate solution is placed in contact with solution of bivalent cations that diffuse across the polymeric matrix and trigger gelation. Examples of this methodology are the dropping of polymeric solutions in bivalent cations solution to obtain *large drop* (>1 mm); the atomization of alginate solution on salt solution to produce *microbeads* (<0,2 mm); covering a films of alginate solutions with the salt solution. In order to obtain a good homogeneity in the gel, it is better to use high concentrated cations solutions while, low

concentrated solutions, results in dishomogeneity. The presence of other non-gelling ions also increase gel homogeneity. Because of ions diffusion problems, the diffusional setting technique give better results, in terms of product homogeneity, only in case of small size objects [23].

On the contrary, in the internal setting technique, the bivalent cations are released into the polymeric solution exploiting a combination of alginate, bivalent ions source (normally a salt) and a chelating agent. The chelating agent sequesters the bivalent cations preventing the gelation during components mixing and formation. Cations release from the chelator agent is triggered by environment change such as temperature, pH or solubility and results in a uniform gelation of all the alginate solution. It is clear how the internal setting is particularly useful in the production of bulk gel, fibers or large objects. However, due to the limited amount of divalent cations that can be carried by the chelator agent, hydrogels prepared by internal settings results to be softer than those prepared by diffusional setting. For pharmaceutical applications, the biological agent can be incorporated in the preparation by simple mixing with the polymeric solution before gelation.

The different structures resulting from gelation and the flexibility of the M-blocks and MG-blocks not interested by the physical interactions represent an important parameter for the diffusion control of the incorporated molecules. Molecules diffusion into the hydrogels matrix can be caused by two mechanisms: diffusion through the network meshes or the structure breakup. The electronic microscope analysis of the calcium alginate gels shows mesh variability in the range of 5 and 200 nm. A wide number of different compounds can be included in the alginate matrix: ionic or neutral, big or small (proteins, glucose, ethanol etc.). Possible molecules interactions with the polymeric network must be evaluated. High rigidity alginates (high content of G) produce an open and static structures and therefore are more permeable while, the presence of long, flexible M-blocks causes structure collapsing in an entanglements configuration (*Fig. 3.5*) [26]. Moreover, in general the diffusion inside the gels decreases with increasing of the alginate concentrations. The mesh of these systems can be significantly reduced by dehydrating the swollen materials. Depending on the starting hydrogel composition, different results can be achieved: an high G alginate, after dehydration, can be only partially re-swollen resulting in a more concentrated system at lower mesh [23].

Regarding the structural stability, because of the reversibility of the physical chain links, alginate hydrogels are affected by degradation processes. Alginates hydrogel dissolutions is promoted by the bivalent ions subtraction from a chelating agent that destabilize the chains interactions causing the entrapped materials release and the polysaccharides dissolution. The same phenomena occurs when the system is exposed to high concentration of monovalent cations or Mg^{2+} that compete with the bivalent cations for the polymers interaction. In order to prevent the hydrogel

dissolutions, it is possible to store the system in a bivalent cations containing environment (i.e. a Ca^{2+} solution) or complexing the alginate with polycations (i.e. chitosan), polypeptides (i.e. poly(L-lysine)) or synthetic polymers (i.e. poly(ethylenimine)). The complex stabilize the hydrogels, reduce the mesh size and it does not dissolve in presence of a chelator [23].

Alginate hydrogels are interesting in the field of DDS for several factors. More than the diversifications in terms of molecular structure, biocompatibility and bioadhesive properties are significant. The first aspect considers the immunological response that is maintained to minimum levels, especially in case of high G content hydrogels. The second aspect regards the elevated capability of the polyanionic molecules, like alginates, to stick on the tissues. Several studies show an adhesive efficiency higher than polycationic and non-ionic polymers (poly(styrene), chitosan, carboxymethyl cellulose, poly(lactic acid)) [23].

3.4.3 – Pluronic™

Pluronic™ is the BASF commercial name of a class of block copolymers constituted by poly(ethylene oxide) (PEO) and poly(propylene oxide) (PPO) also known as Poloxamer. The Pluronic™ is commercialized in more than fifty different types but the detailed description of all the family members is outside the purpose of this work. Here, it will be treated only the general aspects of the Pluronic™ systems with a particular regard to the Pluronic™ F127, used in this study.

3.4.3.1 – General aspect of the Pluronic™ polymers

Normally, the different type of blocks in a copolymer, are mutually incompatible and the polymer has an amphiphile behavior: in water solutions associative mechanisms cause the polymeric chain aggregation in structures. The Pluronics™ are non-ionic copolymers characterized by a three blocks structures of poly(ethylene oxide)-poly(propylene oxide)- poly(ethylene oxide), usually represented also by the abbreviations PEO-PPO-PEO or $(\text{EO})_n(\text{PO})_m(\text{EO})_n$, where the hydrophobic block PPO is embedded between two hydrophilic blocks of PEO (*Fig. 3.6b*). The possibility to change the copolymer composition (in terms of PPO/PEO ratio) and the molecular weight (in terms of blocks length) make this class of polymers versatile for several technological applications. In the biomedical fields, in particular, these products can find many applications in virtue of being chemically inert with respect to tissues and organic fluids, good solvents and water solubility. All these characteristics correspond to the Pluronic™ polymers and therefore, it is justified the large usage, expacially in the pharmaceutical field [27].

Pluronics™ synthesis is a two steps process. Firstly the hydrophobic central block is created by the polymerization of propylene oxide (PO) on the two sides of propylene glycol. In the second step, the ethylene oxide (EO) is introduced on the two sides of the PPO block polymerizing in the external PEO blocks. The reaction takes place in presence of an alkaline catalyst, generally sodium or potassium hydroxide (*Fig 3.6a*). Reaction tuning allows the production of polymer with the desiderate characteristics therefore, Pluronics™ are commercialized in a wide range of variety in terms of copolymers composition and molecular weight. Their classifications is based on a precise nomenclature where, each polymer is identified by a sign composed of one letter followed by two or three numbers. The letter specifies the physical form: “L” for liquid, “P” for paste and “F” for solid. The first number (or first two numbers in case of three numbers), multiplied by 300 gives the approximated molecular weight of the hydrophobic block (PPO). The last number, multiplied by 10, indicate the weight percent of PEO. For example, Pluronic™ F127 used in this work is commercialized as solid (F), the PPO block molecular weight is approximate 3600 Da (12x300) while the PEO weight fraction is about the 70% of the total mass. The wide range of Pluronics™ formulations is justified by their use not only as hydrogels but also in the preparation of emulsions, dispersions, detergents, foams and lubricant (indeed they are surfactants) [27].

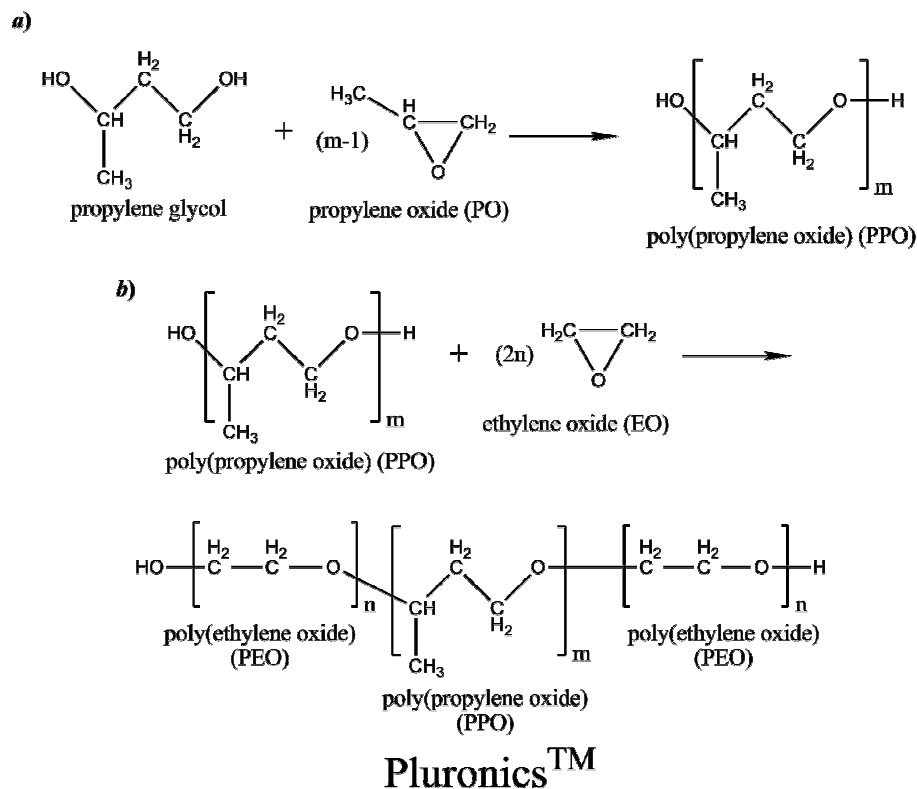


Fig. 3.6: Pluronics™ synthesis. *a)* formation of the central hydrophobic PPO block followed by the addition of the hydrophilic PEO side blocks (*b*).

3.4.3.2 – Pluronics™ micellation in water solution

At low temperatures and/or low concentrations, Pluronic™ copolymers, are present in water solution as single molecules also called *unimers*. As consequence of a temperature and/or concentration increase, in solution the formations of thermodynamically stable micelles occur. Therefore, Pluronics™ can be considered both thermotropic and liotropic (respectively temperature and concentration dependent) structures forming species [28].

The micellation process occurs when a threshold is exceeded: respectively *critical micellation temperature* (CMT) and *critical micellation concentration* (CMC). The transition it is not instantaneous (stair-step kinetics) but takes place in an interval of concentration (up to one order of magnitude) or temperature (up to 10°C). The transition interval is mainly caused by the polydispersity of the polymeric chains and the presence of impurities. Moreover, literatures data are not always in agreement with respect to the values of CMT and CMC. The commonly used techniques available for the micellation study are: the *small-angle neutron scattering* (SANS), the *light scattering*, the *differential scanning calorimetry* (DSC), the surface tension and fluorescence measurements, spectroscopy methodology and Rheology. The different sensibility of these methods can be one of the reasons for literatures data mismatching [28].

Polymer aggregations in water solution is mainly caused by the interaction between hydrophobic PPO blocks from different unimers. The associative process results in the micelles formations with a central hydrophobic core surrounded by the external hydrophilic PEO. The aggregation process is temperature dependent indeed, at low temperatures, the hydrophobic behavior of the PPO is not enough to prevent the hydration by the water molecules and the central block is maintained in solution with the two hydrophilic PEO side blocks. At higher temperatures, this structure is destabilized and the PPO blocks, free from water hydration, can aggregates while PEO remains in solution this resulting in the micellation process (*Fig 3.7a*). For a fixed Pluronic™ chemical structure, once set the temperature, micellation occurs at the correspondent CMC while, once set polymer concentration, the micellation occurs at the correspondent CMT. The dependence of CMT and CMC can be summarized as follows: the higher the polymeric solution concentration, the lower the CMT is. On the contrary the higher the temperature, the lower the CMC is. [29].

The associative processes are also influenced by polymer structure. Indeed, experimental data showed that, less hydrophobic polymers (high EO content or low PO content) have the tendency to aggregate at higher temperatures compared with more hydrophobic polymers. From the thermodynamic point of view, the micellation a process is driven by the entropic contribute and the micellation free energy is strongly dependent on the PPO blocks characteristics. Comparison of polymer constituted by the same molecular weight PEO blocks but different PPO blocks, showed a

decrease of the CMC with the increase of the PPO length. This means that systems with wide hydrophobic domain are able to form micelles at low concentration. In analogue manner, CMT was reduced when PPO length is increased (micellation occurs at lower temperature). The inverse response was obtained changing the hydrophilic component composition (PEO), being constant the PPO block. CMC and CMT increase with the increasing of the PEO length and the micellation exacts the polymer hydrophilic properties. However, the effects produced by PEO blocks variation are less important than the PPO block variations. Finally, being constant the PPO/PEO ratio, CMT and CMC decrease with an increase of the total polymer molecular weight [30].

To explain the micellation phenomena from the thermodynamics point of view, it is better to remember the free energy variation (ΔG^0), in standard conditions, for one amphiphilic chain mole transfer from solution to the micelles phase:

$$\Delta G^0 = \Delta H^0 - T\Delta S^0 \quad (3.1)$$

where ΔH^0 and ΔS^0 are, respectively, the micellation enthalpy and entropy in standard conditions and T is the absolute system temperature. The thermodynamic approach and the DSC measurements, have demonstrated the positivity of the ΔH^0 term, indicating that micellation is an endothermic process. In order to have a spontaneous micellation due to a temperature or concentration increase, ΔG^0 must be negative and, therefore, the micellation driving force is entropy. The hydrophobic effect is believed to be the mechanism mainly involved in the micelles formations. According to this theory, the presence, in water solution, of hydrophobic hydrocarbon groups such as the PPO block, causes a significant reduction of the water entropy, this promoting the structuring increase of water molecules. During the PPO blocks association, the hydrogen bonds between the water molecules are restored. The consequent entropic gain neutralizes and exceeds the entropy decreasing caused by the hydrophobic blocks localizations inside the micelles [27]. In literatures it is possible to find data about the relation between the thermodynamic parameters and the polymers characteristics. The micellation free energy of high molecular weight Pluronics™ tends to more negative values while, the ΔG^0 values, normalized with respect the PPO and PEO copolymer blocks sum, are grouped in a curve independent from the PPO/PEO ratio [27]. ΔH^0 , normalized according to the same criteria, tends to a null value when the PPO/PEO ratio tends to zero (underlining the importance of the hydrophobic region) while it is substantially constant in case of copolymer molecular weight variation (same PPO/PEO) [27]. For the Pluronic™ F127, in particular, data obtained by DSC, do not show a clear ΔH^0 dependence on the PEO blocks length (hydrophilic portions) but demonstrate the proportionality with the PPO block length (hydrophobic portion). This evidence supports the theory of the hydrophobic block dehydration as a key step in the micellation transition [27].

The commonly accepted model for the representation of the resulting system, consists in a micelle solution where the spherical aggregates coexist in equilibrium with residual unimers in solution. Although the wide systems variety, the micelles properties can be summarized by three parameters: the aggregation number N , representing the number of unimers associated in micelle (generally between 10 and 100), the micelles hydrodynamic radius R_m (normally around 10 nm) and the micelles hydrophobic core radius R_{HI} . In the particular case of the Pluronic™ F127, literature [28] shows the following data:

- $N=10,2$ nm (constant CMC in the temperature interval 35-45°C)
- $R_m=3$ (35°C); $R_m=9$ (40°C); $R_m=12$ (45°C)
- $R_{HI}=6-7$ nm (low temperature); $R_{HI}=7-8$ nm (high temperature)

Another micelles microenvironment characterization derives from the fluorescent emission spectroscopy analysis of the pyrene, a fluorescent molecule that is entrapped in the hydrophobic micelles core. The data is in accordance with the indication of a progressive micelles hydrophobic core reduction with temperature decrease [27].

3.4.3.3 – Pluronics™ gelation

Starting from the micelles solution, where micelles and unimers coexist, some copolymers of the Pluronics™ class (such as the Pluronic™ F127), are able to generate higher ordered structures that result in the formation of thermoreversible gel systems. Several studies had investigated the Pluronic™ copolymer gelation but, up till now, many aspects remain unclear. The accepted mechanism consists in a response to the temperature increase that brings to the increase of the micelles volume fraction. When this parameter, in solution, exceeds the critical values of 0,53, the micelles solution assumes a crystalline structure that results in a physical networking and system gelation. In this structure, the micelles become hard spheres packed together and organized in cells that constitute the crystalline units [27-28]. In the case of Pluronic™ F127, by means of SANS measurements, some authors had determined the crystalline structural units geometry as a simple cubic cell excluding the formation of other geometries as hexagonal cell, body centered cubic cell or face centered cubic cell [29-30].

As for the micellation process, it is possible to define a *critical gelation temperature* (CGT). Some authors have used rheological studies in order to measure the viscoelastic properties of Pluronics™ solutions in relation to the temperature increase. The results showed, during micelles aggregation in a network, a sudden increase of shear modulus (G) covering several order of magnitude [28, 30]. Pluronics™ solutions 20% by weight, at room temperature shows a sudden

evolution of the rheological behavior changing from low viscosity liquids, to gel system with strong elastic properties [30].

In the case of Pluronic™ F108, Lau and colleagues [28], proposed two possible mechanism for the gelation (*Fig. 3.7b* and *c*). In the first mechanism, in the initial stage, the copolymer is dissolved in water as hydrated unimers (*Fig. 3.7aI*). The warming trigger the endothermic phase of chain dehydration with consequent micelles formation. After this step, even if dehydrated, some unimers remain free in solution, excluded from the micelles because unable to find an arrangement (*Fig. 3.7aII*). Further warming allow the free unimers to acquire enough mobility to interact each other forming new micelles. The results is an intermicelles distance decreasing and the possibility for the micelles to form entanglements between closer external hydrophilic layers. If micelles association is strong enough, the physical junctions generate the networking results in a gel structure with the mentioned elastic properties (*Fig. 3.7aIII*). The increased micelles packaging contributes to increase the single structural units and finally to increase the viscous component. This first mechanism forecasting that no micelles dimension variations occurs but only micelles number increases. On the contrary, the second mechanism, considers a micelles diameter increase with the temperature. In this case, the remaining free unimers after the micellation step (*Fig. 3.7bII*), aggregate to the existing micelles increasing the size (*Fig. 3.7aIII*). Similarly, the intermicelles distance decreases with the same consequences described before. The authors do not exclude the coexistence of both processes [28].

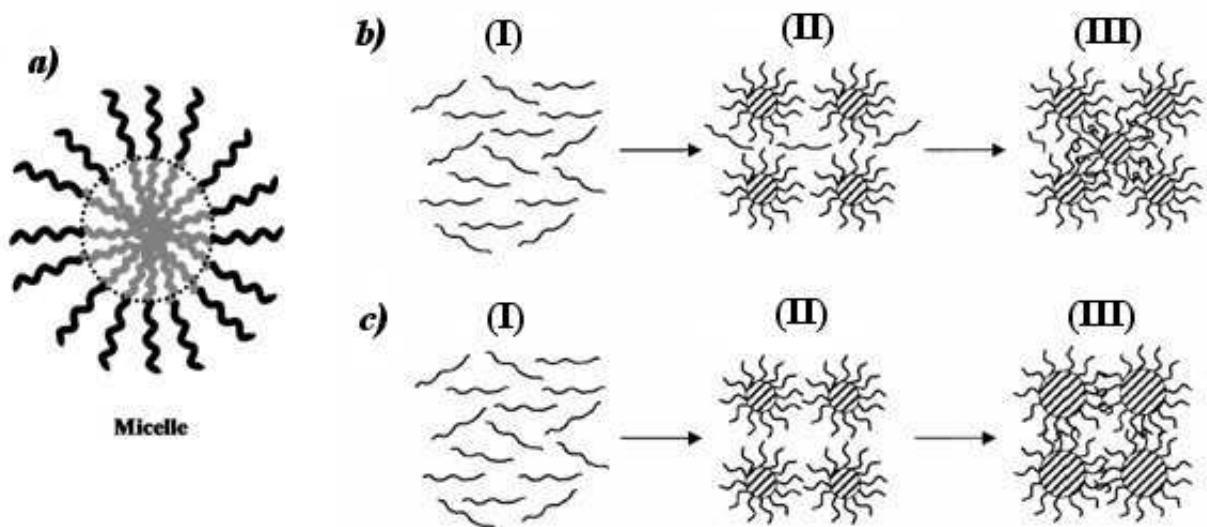


Fig. 3.7: *a*) a Pluronic™ micelles representation with the inner hydrophobic core and the hydrophilic chains exposed outside. *b*) and *c*), possible gelation mechanisms: increasing of the micelles number (*a*) and increasing in the micelles size (*b*).

3.4.4 – Dextran based interpenetrating networks (IPNs)

The medical and pharmaceutical applications have a continuous needing for new materials. The in-situ and injectable hydrogels formation is an interesting approach in several pharmaceutical and biomedical applications [31-33]. In this sense, several polysaccharides have the necessary characteristics for the described purpose. Most of them intrinsically shows hydrogels properties or can be easily treated to acquire [34]. The hydrogels obtained from the mixture of two different polymeric systems result in a new material that can have different properties from both the single starting polymers.

The *interpenetrating polymer network* (IPN) is a methodology that can be used to produce hydrogels with these type of synergic properties. From the literatures definition, IPN is a polymer comprising two or more networks which are at least partially interlaced on a molecular scale but not covalently bonded to each other and cannot be separated unless chemical bonds are broken (*Fig. 3.8a*). The *semi-IPNs* are a particular class of IPNs and are different because include one or more polymers that do not form a network (*Fig. 3.8b*). A simple mixture of two or more polymers or preformed polymer networks is not an IPN [35]. IPN can swell in solvents without dissolving [36].

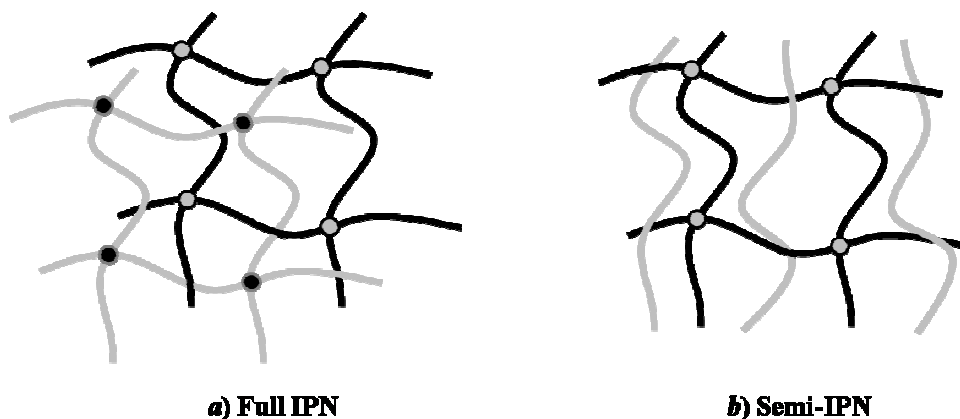


Fig. 3.8: schematic representation of an IPN (*a*) and a semi-IPN (*b*).

IPNs production can be performed by two methodologies: sequential or simultaneous. In the sequential methodology, the monomers for the production of the first polymer are polymerized and then, by the addition of a crosslinking agent, the first network is created. This network is swollen in presence of the second polymer monomers then, the polymerization and crosslinking of the second network is realized obtaining an IPN formed by two polymers networks entangled each other (*Fig. 3.9a*). In the simultaneous production, polymerization and crosslinking of all the polymers part of the final IPN take place in one single step (*Fig. 3.9b*). The key for the success of this process is that all the components must polymerize and crosslink by reactions that will not interfere with one another [36].

Several studies were performed in IPN constituted by synthetic polymers but only in few examples polysaccharides were used for the IPN productions. For this reason, the matrices realized by calcium-alginate and dextran-methacrylate (Dex-Ma) result to be systems with wide applicability potential. Dextrans are branched glucose polysaccharides (glucans) with variable molecular weight (from 10 to 150 kDa). The glucose monomers on the main chain are linked by $\alpha(1-6)$ glycosidic bond while the branches begins from $\alpha(1-4)$ glycosidic bond (but in some cases also $\alpha(1-2)$ and $\alpha(1-3)$ are present as well). Dextrans were used for more than 50 years in the treatment of hypovolemia as succedaneums of plasma. These molecules are reach of hydroxyl groups able to easily bind other compounds and, for this reason, were purposed as carriers for drugs, proteins, enzymes and contrast agents. Dextrans were also used for vaccines preparation (for example for the Calmette-Guerrin Bacillus, BCG).

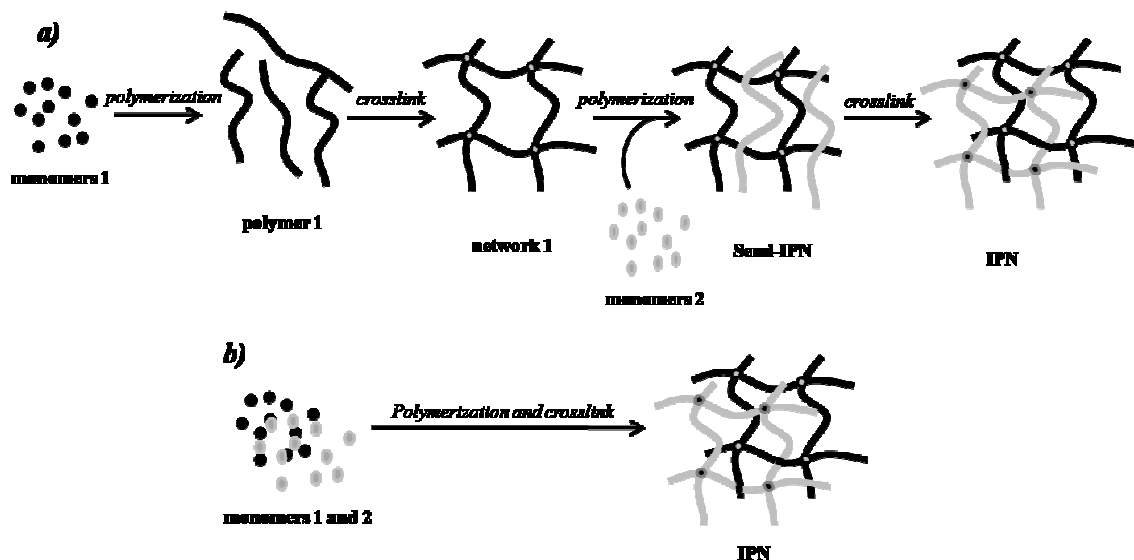


Fig. 3.9: IPN production methodologies: a) sequential b) simultaneous.

From a pharmacokinetics point of view, dextran shows a low oral absorption therefore, they are mainly used in parental preparations. Dextrans, depending on the molecular weight, are able to influence the pharmacokinetics and pharmacodynamics of the linked substances. This characteristic can be used for the improvement of the efficiency and tolerability profiles of therapeutics or diagnostics agents [37].

In particular, the polymeric system obtained from the dispersion of Dex-Ma within a calcium alginate network, realize an hydrogel with new rheological properties compared with both the starting polymers alone. The Dex-Ma chains interacts with the egg-box structure of the alginate modifying the alginate gel properties. The irradiation with UV light of this hydrogels causes the methacrylate groups crosslinking realizing a semi-IPN system with the characteristics of a strong

gel. Release studies on model molecules (proteins and others), prove the usefulness of this IPN as DDS for bioactive molecules [36, 38].

3.4.5 – Polyethylene glycol (PEG) and benzofulvene derivatives

The polymerization or copolymerization of macromolecules is an interesting growing field for the synthesis of cylindrical brushed polymers. Several studies were performed about the synthesis of macromolecules constituted by chains derived from the ethylene oxide oligomers conjugated with biocompatible benzofulvene derivatives. This compound were evaluated for the polymerization properties and biomedical applications [39]. In this section, some examples and properties of PEG, benzofulvene and their derivatives will be cited.

2.3.5.1 – Polyethylene glycol (PEG) derivatives

Poly(ethylene glycol) or PEG, is a polyester derived from the polymerization of the ethylene oxide. For its properties, PEG is one of the most used and studied polymers in the pharmaceutical field. PEG is commercialized in a wide range of molecular weight, from 300 Da to 10.000 kDa (under 20kDa are considered oligomers). It is soluble in water, methanol, benzene, dichloromethane but not in diethyl ether or hexane. It is biocompatible, FDA approved [40] and, it is cheap. PEG is used as matrices in liposomes and nanoparticles release systems [41-42] and in general as protective agents of many bioactive compounds [43-44].

Recently, an interesting approach in the use of PEG consists in the covalent binding of PEG oligomers to other polymeric matrices. In particular, PEG oligomers hydroxyl terminals are modified in methacrylic groups resulting in oligo(ethylene glycol methacrylate) (OEGMA) that is able to perform a radical reaction with other polymers. The obtained systems are characterized by particular polydispersity and water solubility properties [45-51]. Another approach is described below and consists in the covalent binding of methyl PEG oligomers (MOEG) where one PEG end is capped with a CH₃, with benzofulvene derivatives.

2.3.5.2 – Benzofulvene derivatives

Benzofulvene derivatives are a class of hydrophobic monomers that are able to polymerize in order to produce polymers with different properties. In this sense, Cappelli and colleagues [52-58] realized different interesting polymeric systems obtained from the benzofulvene derivatives included the one that was characterized in this work.

Two methodologies are used for poly(BF1) production: the spontaneous polymerization (poly(BF1-SP)) and the anionic polymerization (poly(BF1-AP)). The anionic polymerization results

in a mixture of polymers and oligomers characterized by low molecular weight, compared to poly(BF1-SP) [52, 57].

Another particular class of benzofulvenes is the BF3 family that are trans- dienes able to spontaneously polymerize/depolymerize. The studies on the polyBF3 have shows that most of the properties demonstrated (such as molecular weight, structure, polymerization/depolymerization, thermal reversibility and nanostructures aggregation) depends on the stereoelectronic characteristics of the substituent on the side chain (*Fig. 3.10b*) [53].

As a demonstration of the usefulness of the benzofulvene derivates in DDS, good results were obtained in the release studies performed on the angiotensin II receptor antagonists (AT1) entrapped in poly(BF1) (*Fig. 3.10c*) [53]. The similarity of BF1 with methacrylate and cyano-methacrylate, had stimulated the synthesis of macromolecules constituted by methyl-oligo-ethylene-glycol (MOEG) conjugated with BF1 (MOEG-BF1 macromers or simple *1b*). The polymers resulting from macromers polymerization, called *poly-1a* and *poly-1b*, present a methyl terminal on the MOEG side chain and are different for the length of the MOEG chain (*Fig. 3.10d*). In the new benzofulvene derivates, the MOEG chain, plays a fundamental role in the determination of the amphiphilic properties that, with the brush polymeric structure, result in a physical, biocompatible hydrogel [54]. This work attempts to evaluate the tendency to the spontaneous polymerization and the properties of the *poly-1b*.

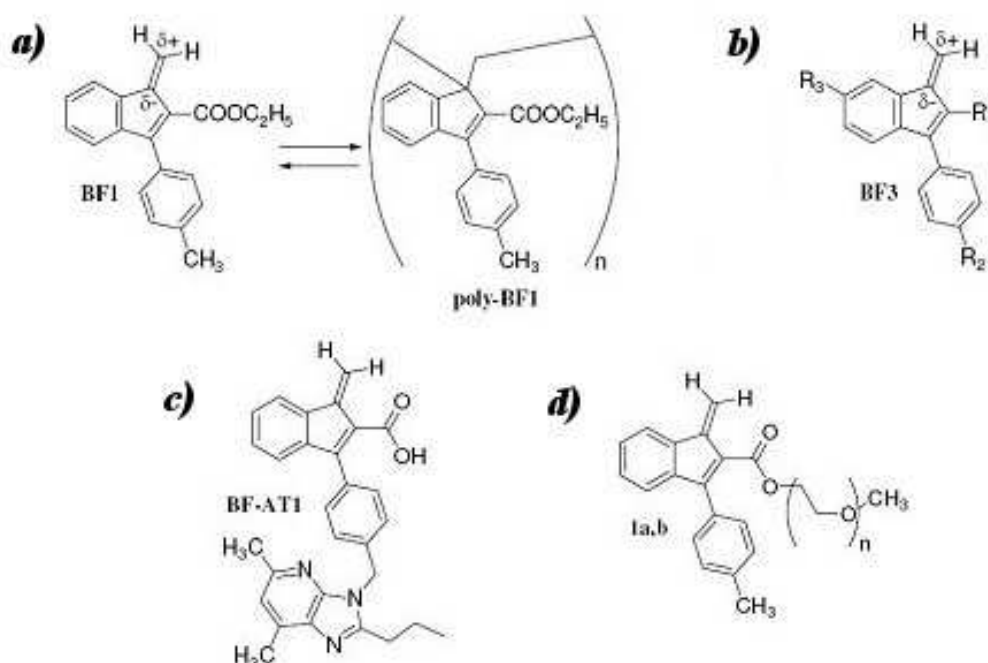


Fig. 3.10: benzofulvene derivatives. *a)* polymerization equilibrium of poly(BF1); *b)* the structure of the BF3 family monomers; *c)* the angiotensin II receptor antagonists (AT1) entrapped on poly(BF1); *d)* the structure of *1a* ($n=3$) and *1b* ($n=9$), monomers of *poly-1a* and *poly-1b* respectively.

2.3.5.3 – *Poly-1a* and *poly-1b* properties

Fresh made *poly-1a* is soluble in chloroform but, the solubility decrease if it is in a vitreous form. *Poly-1a* interacts with many organic solvents and with water with the formation of transparent gel aggregates. Gel swelling is quite fast in chloroform and slower in DMF, DMA, DMSO, ethanol and methanol. The complete gel dissolution spans from few weeks to several months it depends on temperature. Water addition to *poly-1b* solution in THF, DMA or ethanol does not results in polymer precipitation, suggesting that *poly-1b* is able to form gels stabilized by non covalent weak linkages rather than OEGMA entanglements.

The molecular weight distribution (Fig. 3.11) demonstrates the high molecular weight of the two polymers: 108 kDa and 175 kDa for *poly-1a* and *poly-1b*, respectively. The polydispersity index M_w/M_n (M_n is the mean molecular weight), for both polymers (2,4 and 3,0 respectively for *poly-1a* and *poly-1b*), is higher than the poly(BF1) (1,6-2,0) [54].

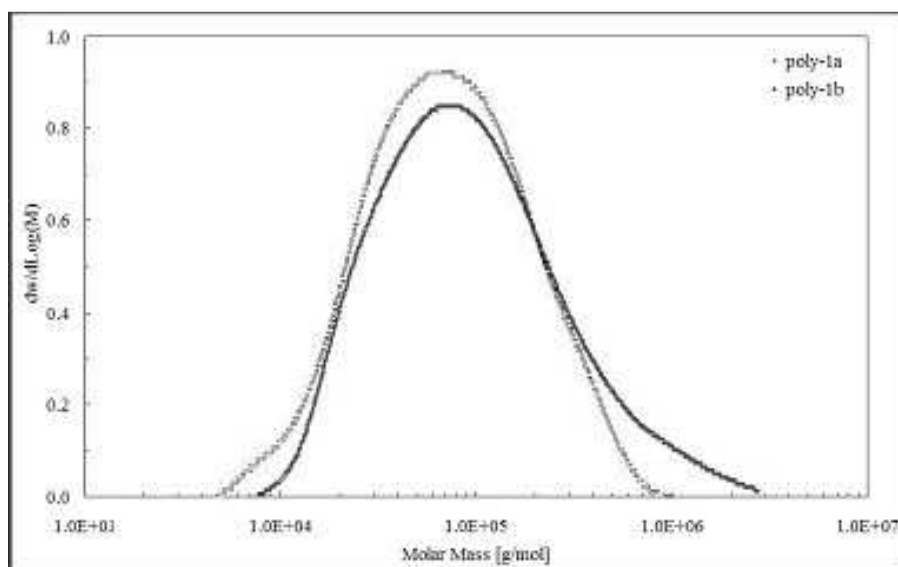


Fig. 3.11: molecular weight distribution of *poly-1a* (gray) and *poly-1b* (black).

References

1. Birch, J.R., *Cell sell*. Chemtech, 1987. **17**(6): p. 378-81.
2. Wise, D.L., *Biopolymeric controlled release systems*. Vol. 1. 1984, Boca Raton FL: CRC Press.
3. Guiot, P. and P. Couvreur, *polymeric nanoparticles and microspheres*. 1986, Boca Raton FL: CRC press
4. Langer, R.S. and D.L. Wise, *Medical applications of controlled release*. Vol. 1. 1984, Boca Raton FL: CRC Press.
5. Tirrel, D.A., L.G. Donaruma, and A.B. Turek, *Macromolecules as drugs and as carriers for biologically active materials*. Annals of The New York Accademy of Science. Vol. 446. 1986, New York.

6. Illum, L. and S.S. Davis, *Polymer in controlled drug delivery*. 1987, Bristol, England: Wright.
7. Kost, J. and R. Langer, *Responsive polymeric delivery systems*. *Adv Drug Deliv Rev*, 2001. **46**(1-3): p. 125-48.
8. Ranade, V.V. and M.A. Holliger, *Drug delivery systems*. 2nd ed. 2004, Boca Raton FL: CRC Press.
9. Hsieh, D., *Controlled release systems: fabrication technology*. 1988, Boca Raton FL: CRC Press.
10. Baker, R.W. and H.K. Lonsdale, *controlled release of biologically active agents*, in *Controlled release: mechanism and rates*, A.C. Tarquasy and R.E. Lacey, Editors. 1974, Plenum Press: New York. p. 15.
11. Rogers, C.E., *Solubility and diffusivity*, in *Physics and chemistry of the organica compounds*, D. Fox, M.M. Labes, and A. Weisseberger, Editors. 1965, Wiley Interscience: New York.
12. Sun, Y. and D.C. Watts, *Biodegradable polymers and their degradation mechanisms*. *Am Pharm Rev*, 2001. **4**: p. 8-18.
13. Kydonieus, A., *Treatise on controlled drug delivery*. 1992, New York: Marcel Dekker.
14. Siepman, J. and A. Gopferich, *Mathematical modeling of bioerodible, polymeric drug delivery systems*. *Adv Drug Deliv Rev*, 2001. **48**: p. 229.
15. Elvira, C., et al., *Covalent Polymer-Drug Conjugates*. *Molecules*, 2005. **10**(1): p. 114-25.
16. Grassi, M., et al., *Understanding drug release and absorption mechanisms*. 2007, CRC Press: Boca Raton.
17. Lapasin, R. and S. Pricl, *Rheology of industrial polysaccharides: theory and applications*, ed. B.A. Professional. 1992, London: Chapman And Hall.
18. Gehrke, S.H. and P.I. Lee, *Hydrogels for drug delivery systems*, in *Specialized drug delivery systems: manufacturing and production technology*, P. Tyle, Editor. 1990, Dekker, M: New York.
19. Peppas, N.A. and J.J. Sahlin, *Hydrogel in pharmaceutical formulation*. *Eur J Pharm Biopharm*, 2000. **50**.
20. Peppas, N.A. and A.G. Mikos, *Hydrogels in medicine and pharmacy*. Vol. 2nd. 1987, Boca Raton: CRC Press.
21. Sefton, M.V., *Heparinized Hydrogels in Hydrogels in medicine and pharmacy: properties and applications*, N.A. Peppas, Editor, CRC Press: Boca Raton FL.
22. Drury, J.L. and D.J. Mooney, *Hydrogels for tissue engineering: scaffold design variables and applications* *Biomaterials*, 2003. **24**(24): p. 4337-51
23. Gombotz, W.R. and S.F. Wee, *Protein release from alginate matrices*. *Adv Drug Deliv Rev*, 1998. **31**(3): p. 267-85.
24. Draget, K.I., O. Smidsrød, and G. Skjåk-Bræk, *Alginates from algae*, in *Polysaccharides and polyamides in the food industries. Properties, production and patents*, A. Steinbüchel and S.K. Rhee, Editors. 2005, Willey-VCH: Weinheim.
25. Amsden, B. and N. Turner, *Diffusion characteristics of calcium alginate gels*. *Biotechnology and Bioengineering*, 1999. **65**(5): p. 605-610.
26. Draget, K.I., G. Skjåk-Bræk, and O. Smidsrød, *Alginate based new materials*. *j Biol Macromol*, 1997. **21**: p. 47-55.
27. Alexandridis, P. and T.A. Hatton, *Poly(ethylene oxide)-poly(propylene oxide)-poly(ethylene oxide) block copolymer surfactants in aqueous solutions and at interfaces: thermodynamics, structure, dynamics, and modeling*. *Colloids Surf A*, 1995. **96**: p. 1-46.
28. Lau, B.K., et al., *Micellization to gelation of a triblock copolymer in water: Thermoreversibility and scaling*. *J. Polym. Sci. Part B*, 2004. **42**: p. 2014-25.

29. Wanka, G., H. Hoffmann, and W. Ulbricht, *The aggregation behavior of poly-(oxyethylene)-poly-(oxypropylene)-poly-(oxyethylene)-block-copolymers in aqueous solution*. Colloid Polym Sci, 1990. **268**: p. 101-117.
30. Yu, G.E., et al., *Micellisation and gelation of triblock copoly(oxyethylene/oxypropylene/oxyethylene), F127*. J Chem Soc, Faraday Trans, 1992. **88**: p. 2537 - 2544.
31. Lee, K.Y. and D.J. Mooney, *Hydrogels for Tissue Engineering*. Chem Rev, 2001. **101**(7): p. 1869-80.
32. Gutowska, A., B. Jeong, and M. asionowski, *Injectable gels for tissue engineering*. Anat Rec, 2001. **263**(4): p. 242-49.
33. Hatefi, A. and B.J. Amsden, *Biodegradable injectable in situ forming drug delivery systems* J Control Release, 2002. **80**(1-3): p. 9-28.
34. Hennink, W.E. and C.F. van Nostrum, *Novel crosslinking methods to design hydrogels* Adv Drug Deliv Rev, 2002. **54**(1): p. 13-36.
35. McNaught, A.D. and W. Wilkinson, *IUPAC. Compendium of Chemical Terminology*. 2nd ed. 1997, Oxford: Blackwell Scientific Publications.
36. Sperling, L.K., *An Overview of Interpenetrating Networks in Polymeric Materials Encyclopedia*, S.J. C., Editor. 1996, CRC Press: Boca Raton.
37. Mehvar, R., *Dextrans for targeted and sustained delivery of therapeutic and imaging agents* J Control Release, 2000. **69**(1): p. 1-25.
38. Bae, Y.H. and S.W. Kim, *Hydrogel delivery systems based on polymer blends, block copolymers or interpenetrating networks*. Advanced Drug Delivery Reviews, 1993. **11**(1-2): p. 109-135.
39. Zhang, M. and A.H.E. Müller, *Cylindrical polymer brushes*. Journal of Polymer Science Part A: Polymer Chemistry, 2005. **43**(16): p. 3461-3481.
40. *U.S. Food and Drug Administration*. 2009; Available from: www.fda.gov.
41. Langer, R., *Drug delivery and targeting*. Nature, 1998. **392**(6679 Suppl): p. 5-10.
42. Peracchia, M.T., et al., *Development of sterically stabilized poly(isobutyl 2-cyanoacrylate) nanoparticles by chemical coupling of poly(ethylene glycol)*. Journal of Biomedical Materials Research, 1997. **34**(3): p. 317-326.
43. Duncan, R., *The dawning era of polymer therapeutics*. Nat Rev Drug Discov, 2003. **2**: p. 347-60.
44. Langer, R., *New methods of drug delivery*. Science, 1990. **249**(4976): p. 1527-33.
45. Lutz, J.F., et al., *Biocompatible, Thermoresponsive, and Biodegradable: Simple Preparation of "All-in-One" Biorelevant Polymers*. Macromolecules, 2007. **40**(24): p. 8540–8543.
46. Lutz, J.F. and A. Hoth, *Preparation of Ideal PEG Analogues with a Tunable Thermosensitivity by Controlled Radical Copolymerization of 2-(2-Methoxyethoxy)ethyl Methacrylate and Oligo(ethylene glycol) Methacrylate*. Macromolecules, 2006. **39**(2): p. 893–896.
47. Oh, J.K., K. Min, and K. Matyjaszewski, *Preparation of Poly(oligo(ethylene glycol) monomethyl ether methacrylate) by Homogeneous Aqueous AGET ATRP*. Macromolecules, 2006. **39**(9): p. 3161–3167.
48. Tao, L., et al., *α -Aldehyde Terminally Functional Methacrylic Polymers from Living Radical Polymerization: Application in Protein Conjugation "Pegylation"*. J Am Chem Soc, 2004. **126**(41): p. 13220–13221.
49. Han, S., M. Hagiwara, and T. Ishizone, *Synthesis of Thermally Sensitive Water-Soluble Polymethacrylates by Living Anionic Polymerizations of Oligo(ethylene glycol) Methyl Ether Methacrylates*. macromolecules, 2003. **36**(22): p. 8312–8319.

50. Wang, X.S. and S.P. Armes, *Facile Atom Transfer Radical Polymerization of Methoxy-Capped Oligo(ethylene glycol) Methacrylate in Aqueous Media at Ambient Temperature*. *Macromolecules*, 2000. **33**(18): p. 6640–6647.
51. Wang, X.S., et al., *Facile synthesis of well-defined water-soluble polymers via atom transfer radical polymerization in aqueous media at ambient temperature*. *Macromolecules*, 1999: p. 1817-1818.
52. Cappelli, A., et al., *New π -stacked benzofulvene polymer showing thermoreversible polymerization: Studies in macromolecular and aggregate structures and polymerization mechanism*. *J Polym Sci Part A*, 2005. **43**(15): p. 3289-3304.
53. Cappelli, A., et al., *Anionic Polymerization of a Benzofulvene Monomer Leading to a Thermoreversible π -Stacked Polymer. Studies in Macromolecular and Aggregate Structure*. *Macromolecules*, 2008. **41**(7): p. 2324–2334.
54. Cappelli, A., et al., *Structural Manipulation of Benzofulvene Derivatives Showing Spontaneous Thermoreversible Polymerization. Role of the Substituents in the Modulation of Polymer Properties*. *Macromolecules*, 2007. **40**(9): p. 3005–3014.
55. Cappelli, A., et al., *Synthesis and Spontaneous Polymerization of Oligo(ethylene glycol)-Conjugated Benzofulvene Macromonomers. A Polymer Brush Forming a Physical Hydrogel*. *Macromolecules*, 2009. **42**(7): p. 2368–78.
56. Cappelli, A., et al., *A nanocomposite material formed by benzofulvene polymer nanoparticles loaded with a potent 5-HT₃ receptor antagonist (CR3124)*. *J Nanopart Res*, 2009.
57. Cappelli, A., et al., *Synthesis and Characterization of a New Benzofulvene Polymer Showing a Thermoreversible Polymerization Behavior*. *J Org Chem*, 2003. **68**(24): p. 9473–9476.
58. Cappelli, A., et al., *Further Studies on Imidazo[4,5-*b*]pyridine AT₁ Angiotensin II Receptor Antagonists. Effects of the Transformation of the 4-Phenylquinoline Backbone into 4-Phenylisoquinolinone or 1-Phenylindene Scaffolds*. *J Med Chem*, 2006. **26**(22): p. 6451–64.

4 – Techniques for Hydrogels and Zeolite Structural Characterization

In this chapter, three main techniques for gel structure characterization were presented. The first one is the *Nuclear Magnetic Resonance* (NMR), in particular the low field NMR analysis, that allows the investigation of microscopic hydrogels characteristics. The second one is the *Rheology* that, instead, allows to study the effect of the hydrogels structure on the macroscopic and mechanical behaviour. The last technique is called *Cryoporometry*, an indirect method for the determination of pore size and shape in matrices. In the following sections it is explained how it is possible to adapt this technique also for the estimation of the hydrogels mesh size. The last section describes other methods for the pore characterization in solid materials.

4.1 – Nuclear magnetic resonance (NMR) spectroscopy

The physic principles of the Nuclear Magnetic Resonance (NMR) spectroscopy, are based on the magnetic properties of the atomic nuclei [1]. According to the quantum mechanics rules, the interaction of the magnetic moment of an atomic nucleus with an external magnetic field (B_0) separates the nuclear energetic levels. The energetic levels separation happens because, the nuclear magnetic energy is restricted to discrete values E_p called *autovalues*. The autovalues are associated to the *autostates*, also called *steady states* that are the only possible existing states of an elementary particle. Irradiating the nucleolus with an electromagnetic radiation of appropriate frequency, it is possible to induce a transition within steady states and the energetic abortion could be detected by the instrument and registered as a signal on a spectrum.

With this method it is possible to obtain the spectrum of a compound that contains atoms with nuclear magnetic moment different from zero. The most analyzed nuclei are the protons (^1H), fluorine (^{19}F), the isotopes ^{14}N and ^{15}N of the nitrogen and the isotope ^{13}C of carbon [1].

4.1.1 – NMR principles

4.1.1.1 – Quantum mechanics model for an isolated nucleus

Many atomic nuclei have an *angular momentum* (P) that is responsible for the exhibition of a *magnetic moment* (μ) [2]. The relation within P and μ is expressed by the equation:

$$\mu = \gamma P \quad (4. 2)$$

Where γ is the *gyromagnetic ratio*, a characteristic of the specific nucleus. For the Quantum theory, the angular momentum and the magnetic moment are quantized, a fact that is not explained by the classic physics. The allowed autovalues of the angular momentum maximum component in the z direction in an arbitrary cartesian system, are defined by the relation:

$$P_z = \frac{h}{2\pi} m_l \quad (4. 3)$$

where m_l is the *magnetic quantum number* of the correspondent nucleus steady states and h is the *Plank constant*. According to the quantistic condition, the magnetic quantum numbers m_l are related to *nuclear spin quantum number* (I) and can assumes a integer number within $+I$ and $-I$. Therefore, the number of steady states or possible energy levels is:

$$\text{Number of possible energy levels} = 2I + 1 \quad (4. 4)$$

For the proton (^1H nucleus), the nuclear spin quantum number is $I = \frac{1}{2}$ and the angular moment z component becomes:

$$P_z = \pm \frac{h}{2\pi} I \quad (4. 5)$$

In consequence of I , the proton can exist in only two spin state with a magnetic quantum number respectively of $m_l = +\frac{1}{2}$ and $m_l = -\frac{1}{2}$. The magnetic moment in the z direction is:

$$\mu_z = \gamma \frac{h}{2\pi} m_l = \pm \gamma \frac{h}{4\pi} \quad (4. 6)$$

The proton therefore, can be represented as a magnetic dipole where μ_z is parallel or anti-parallel to the positive direction of z axes in the cartesian coordinates and the direction of μ vector is quantified (*Fig. 4.1a*).

In normal situation, without an orienting system, the two states have the same energy and are so called degenerated. In presence of an external magnetic field B_0 , the interaction with μ cause an energetic differentiation of the two states. If B_0 is parallel to z axes, the energy of a magnetic dipole is $+\mu_z B_0$ when the dipole is oriented in the same direction of B_0 , while it is $-\mu_z B_0$, when it

is oriented in opposite direction (Fig. 4.1b). Therefore, the energy difference within the two spin states is proportional to the intensity applied magnetic field B_0 (Fig. 4.2) with the relation:

$$\Delta E = 2\mu_z B_0 \quad (4.7)$$

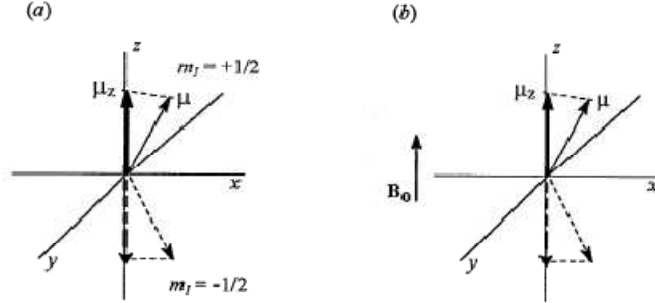


Fig. 4.1: the quantified magnetic moment μ vector direction in absence (a) or in presence (b) of an external magnetic field B_0 .

The lower energy state $m_l = +\frac{1}{2}$ is more stable and to induce the transition to the higher energy level a quantum of energy corresponding to ΔE is required.

$$\Delta E = h\nu_o = 2\mu_z B_0 = \gamma \frac{h}{2\pi} B_0 \quad (4.8)$$

In other terms, the nucleus must to be irradiated with a frequency equal to:

$$\nu_o = \frac{\gamma B_0}{2\pi} \quad (4.9)$$

or, considering $\omega_o = 2\pi\nu_o$, equation (4.8) can be written as:

$$\omega_o = \gamma B_0 \quad (4.10)$$

This equation, expresses the resonance condition, when the radiations frequency is equal to ΔE within the two states. In the equation (4.8), ν_o (in Hertz; Hz=cycle sec^{-1}) or ω_o (rad sec^{-1}) is the *Larmor frequency* and depends linearly on the applied B_0 intensity. For example, the proton has a giromagnetic ratio $\gamma_H = 2,675 \times 10^8 \text{ T}^{-1} \text{sec}^{-1}$. In a magnetic field of 1,41 T, the Larmor frequency is 60MHz ($\lambda=5$ meters, in the region of radio wave). Figure 4.3 shows different ν_o values as function of imposed magnetic field [3].

For systems with $I=1$, the quantum mechanics treatment gives a results not expected by the classical physics. The magnetic quantum number m_l can be -1, 0, +1 so that, only closer levels transitions are allowed. For example, for $I=1$ three energy levels are possible with m_l equal to -1, 0 and +1 respectively and the possible level transitions are $m_l=+1 \leftrightarrow m_l=0$ and $m_l=0 \leftrightarrow m_l=-1$; energy levels transitions within $m_l=+1 \leftrightarrow m_l=-1$ are not allowed (Fig. 4.4).

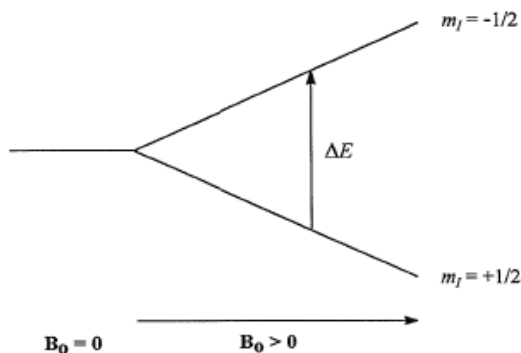


Fig. 4.2: energetic separation ΔE within two state proportional to the applied magnetic field B_0 .

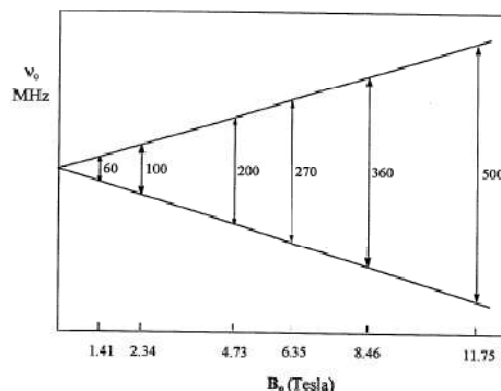


Fig. 4.3: nuclear energetic separation levels (expressed as resonance frequency ν_0), in function of the magnetic field B_0 (in Tesla).

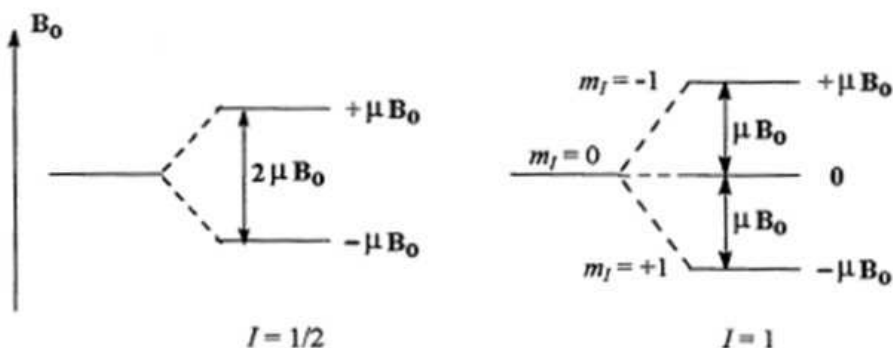


Fig. 4.4: on the left, separation in two energetic levels of a nucleus with spin quantum number $I=1/2$ in a magnetic field B_0 ; on the right, separation in three energetic levels of a nucleus with $I=1$.

From above considerations, the nuclear magnetic moment can be expressed as a function of the giromagnetic ratio:

$$\gamma = \frac{2\pi\mu}{Ih} \quad (4.11)$$

Moreover, it is possible to demonstrate, for a rotating spherical particle of mass M and charge e uniformly distributed on the surface, the generation of a magnetic moment defined as:

$$\mu = \frac{eh}{4\pi Mc} \quad (4.12)$$

where c is the light speed. For the proton equation (4.11) became:

$$\mu_N = \frac{eh}{4\pi Mc} = 5,0505 \times 10^{-27} \text{ (J T}^{-1}\text{)} \quad (4.13)$$

In reality, the value of the proton magnetic moment is about 2,79 times higher than the calculated by using this simplified model. Although a simplified model to explain or predict the

nuclear magnetic moment does not exist, the calculated values represent a usefully starting point (μ_N is called *magneton*). For these reasons, the general equation for the nuclear magnetic moment reads:

$$\mu = g_N \frac{ehI}{4\pi Mc} \quad (4.14)$$

Equation (4.13) can be simplified by expressing μ in terms of units of magneton becoming

$$\mu = g_N I \quad (4.15)$$

Where g_N is the g nuclear factor, an empiric parameter. In *table 4.1*, some nuclear magnetic moments expressed in magnetons are reported.

Nucleus	I	μ (μ_N units)	γ (10^{-8} rad/T s)	ν_0 (MHz) (field 1 T)	Relative sensitivity to constant field	Isotopes naturally abundance (%)
^1H	1/2	2,79277	2,676	42,577	1,000	99,98
^2H	1	0,85735	0,411	6,536	0,009	0,0156
^{10}B	3	1,8007	0,288	4,575	0,02	18,83
^{11}B	3/2	2,6880	0,858	13,660	0,165	81,17
^{13}C	1/2	0,70216	0,673	10,705	0,016	1,108
^{14}N	1	0,40369	0,193	3,076	0,001	99,635
^{15}N	1/2	-0,28298	-0,271	4,315	0,001	0,365
^{17}O	5/2	-1,8930	-0,363	5,772	0,029	0,037
^{19}F	1/2	2,6273	2,517	40,055	0,834	100,0
^{29}Si	1/2	-0,55492	-0,531	8,460	0,079	4,70
^{31}P	1/2	1,1316	1,083	17,235	0,066	100,0

Table 4.1: properties of some nuclei interesting for the NMR spectroscopy [3].

4.1.1.2 – Energy absorption mechanism: the resonance

The nuclei with $I=1/2$, as the protons ^1H , are usually represented as magnetic bar but, because of their spin movement, their behavior is different from that of macroscopic magnetic bar. In a magnetic field, the rotating nucleus does not allaying its magnetic moment to the direction of the field. On the contrary, as a spinning top in the gravitational field, their spin axes assume a precession movement around the magnetic field direction (*Fig. 4.5*). The *precession frequency* corresponds to the Larmor frequency as seen in equation (4.8) and (4.9), and it could be expressed as ω_0 in (radiats sec^{-1}) or ν_0 (Hz) [1-3].

An increase in the intensity of magnetic field, results in a faster precession but, it is possible to modify the orientation of magnetic moment μ by application of a rotating magnetic field (B_1) perpendicular to B_0 . When B_1 rotation frequency (ν_{RF}) has the same value of precession frequency ν_0 , resonance condition is established and the system absorbs energy with a variation of the angle θ within vector μ and the static magnetic field B_0 (Fig. 4.6). The process occurs without variation of the precession frequency.

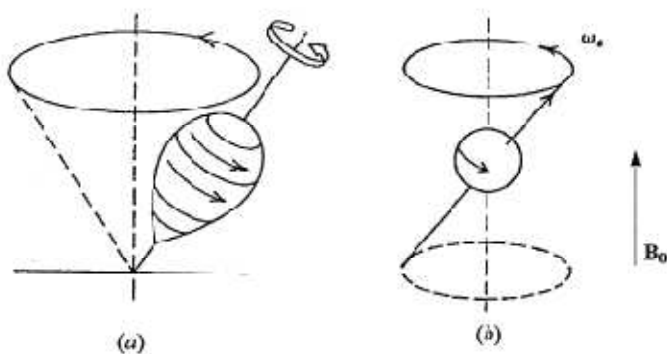


Fig. 4.5: as a spinner precess in the hearth gravitational field (a), the nuclear magnetic moment precess in a magnetic field. (b)

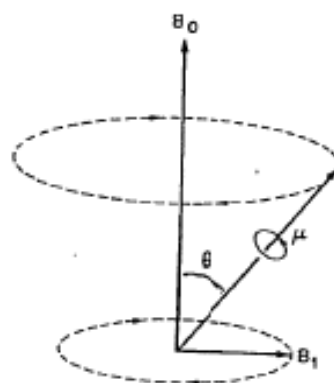


Fig. 4.6: the application of a rotating magnetic field B_1 perpendicular to B_0 , turn the nuclear magnetic moment μ by an angle θ .

4.1.1.3 – Macroscopic magnetization

During an NMR experiment, there is not only one nucleus under examination but a huge amount. Therefore, in order to describe the properties of *nuclear magnetization* (defined as magnetic moment per unit volume), it is possible to apply a simple treatment. The magnetization M is a vector that can be divided into three component in the x , y and z directions. M_z , is conventionally aligned to the direction of B_0 whereas M_x and M_y , are perpendicular. For a nucleus with $I=1/2$, all the magnetic moment precess at the same frequency and, because the direction x and y are equivalent, no phase coherence occurs on xy plane and $M_{xy}=0$. On the contrary, in the z direction, there is a small excess of nuclei parallel to the B_0 direction because the Boltzmann distribution favors the lower energy state. The nuclei populations difference within parallel and antiparallel magnetization, generate a macroscopic net magnetization M_z (Fig. 4.7a and b).

$$M_z = \gamma \hbar (N_1 - N_2) \quad (4.16)$$

The application of a radiofrequency (RF) field B_1 rotating at the resonance frequency ($\omega_0 = \gamma B_0$; equation 4.9), allows the spin resonance with a modification of the casual orientation in the xy plane and the appearing of a magnetization component $M_{xy} \neq 0$. Spin systems originating net component of the magnetization in the xy plane (M_{xy}) are in phase coherence (Fig. 4.7c).

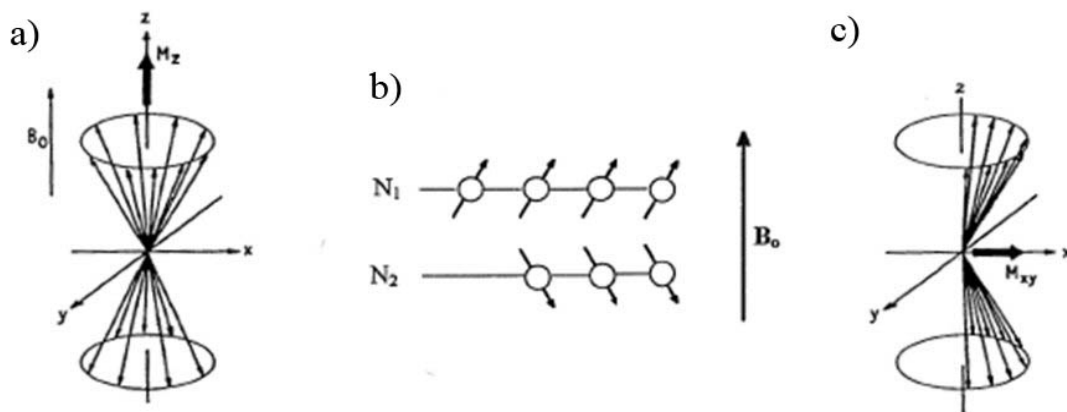


Fig. 4.7: (a) an identical magnetic moment of $I=1/2$ nuclei precess around the z axis (for convention, all the vector are considerate with a common origin). The population difference within $+z$ and $-z$ direction cause a net magnetization M_z . There is no phase coherence and therefore no magnetization M_{xy} . (b) Excess of nuclei with magnetic moment aligned with B_0 . (c) Spin system in phase coherence, $M_{xy} \neq 0$.

4.1.2 – The NMR experiment

During an NMR experiment, the sample is subjected to a highly homogeneous static magnetic field B_0 . To produce a phase coherence within spins, a rotating magnetic field (B_1) is applied perpendicular to B_0 by a tuned spire allowing the generation M_{xy} magnetization component with a ω_0 precession frequency (resonance frequency) (Fig. 4.8). When B_1 is removed, a *relaxation* process causes the loss of phase coherence to the initial equilibrium situation with $M_{xy}=0$. The relaxation process consists in a exponential decay of M_{xy} with a time constant T_2 (*transversal relaxation time* or *spin-spin*). The results of the relaxation is a transient signal, captured by a sensor on x axes, with ω_0 frequency and decay speed of $1/T_2$ called Free Induction Decay (FID) (Fig. 4.9a) [4].

The NMR spectral signals are produced by the small displacement of resonance frequency ω_0 in the nuclei population under analysis caused by the physic-chemical environment. When different ω_0 and, as consequence different $1/T_2$ are present, the resulting FID is a superimposition of all signals. The complex FID originated by multiple signals can be resolved using a mathematical processing known as Fourier Transformation (FT) that changes the transient signal in a normal spectrum (Fig. 4.9b). Whereas NMR spectrum is a diagram where intensity is a function of frequency, in FID, the intensity is a function of time. The time domain and frequency domain is linked by the Fourier Transformation [4].

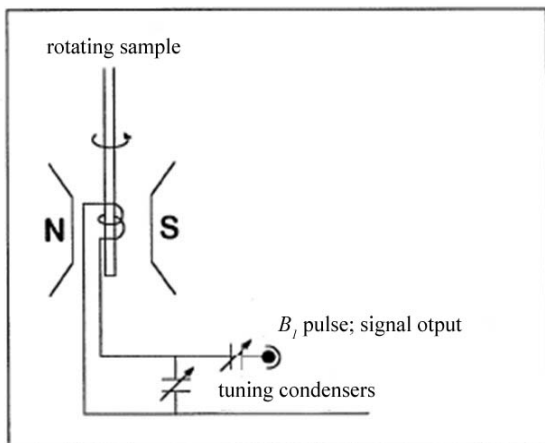


Fig. 4.8: schematic representation of the NMR spectroscope. The sample is positioned within the magnetic field B_0 generated by a magnet (N-S) and surrounded by a spire, tuned on the resonance frequency, that produce the B_1 pulse.

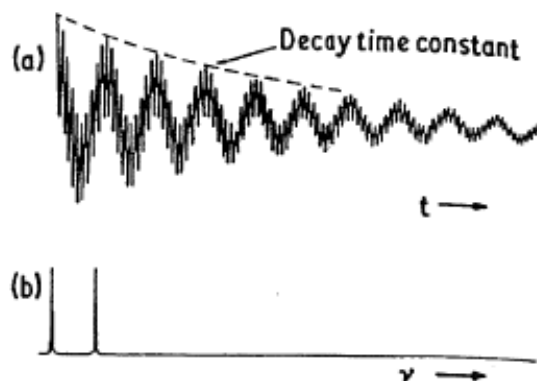


Fig.4.9: (a) FID of two NMR signal. (b) the spectrum obtained applying the Fourier transform to the FID.

At this stage, it is important the definition of the applied magnetic field pulse B_1 in terms of angle. Similar to the precession in the B_0 field, the precession concept can be extended to B_1 using the expedient of a rotating reference system so B_1 became static. When B_1 is applied, it occurs the situation in *figure 4.10a* where B_1 is aligned to the rotating axes x' and the equilibrium magnetization M_0 , aligned to z , precess around B_1 . The precession frequency of M_0 is:

$$\omega_1 = \gamma B_1 \quad (4.17)$$

ω_1 is an angular frequency (radius sec^{-1}). The M_0 rotation angle is:

$$\theta = \gamma B_1 t_p \quad (4.18)$$

Where t_p is the B_1 pulse application time and γB_1 is the pulse amplitude or power. After a pulse at 90° (or $\pi/2$ in radius), $M_{xy}=M_0$ (*Fig. 4.10b*), while after 180° pulse (or π in radius) $M_z=-M_0$ and $M_{xy}=0$ (*Fig. 4.10c*).

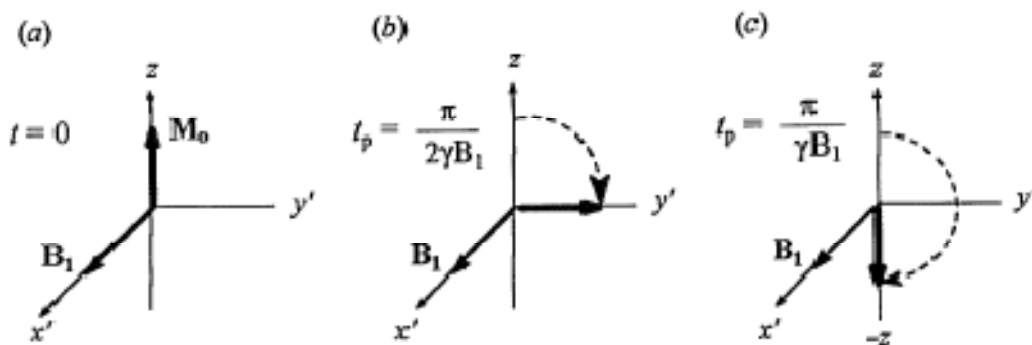


Fig. 4.10: effect of the rotating magnetic field B_1 application on the magnetization M_0 (x' and y' belong to a reference system rotating with the same frequency of B_1). (a) Time zero; (b) after a 90° pulse; (c) after 180° pulse.

To evaluate the effect of a radiofrequency pulse on the nuclear levels populations, let's consider a system of two state levels α and β containing N nuclei that could be in one state or in the other. For degenerate levels, there should be $N/2$ nuclei in each state but, because the α magnetic moment is oriented parallel to the B_0 field, α has a lower energy compared to β (antiparallel magnetic moment). This energy difference causes a small excess of nuclei in the α state and, defining δ as the excess of nuclei, the number of nuclei in each population can be written as $(N+\delta)/2$ or $(N-\delta)/2$ respectively for α and for β (Fig. 4.11).

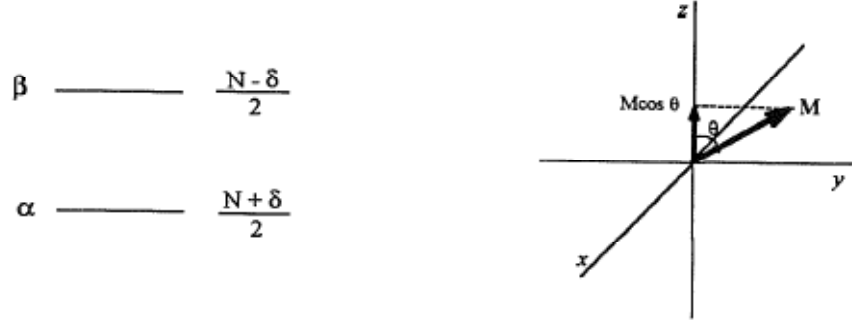


Fig. 4.11: on the left, initial number of nuclei in α and β energetic levels population. On the right, the effect on a pulse that rotate the magnetization of an angle θ .

In order to understand what happens to the nuclei populations when the macroscopic magnetization is deflected by an angle θ due to a radiofrequency pulse it is better focusing the attention to the M_z component. On the contrary considering the whole α and β nuclei population, it is better considering the deviation from $N/2$ defined as $P_\alpha = +\delta/2$ and $P_\beta = -\delta/2$.

In every moment, M_z is proportional to the difference within levels:

$$M_z \propto P_\alpha - P_\beta \quad (4.19)$$

or, it is possible to say that $M_o \propto \delta$. Moreover, it is known that:

$$P_\alpha + P_\beta = 0 \quad (4.20)$$

After the radiofrequency pulse, the M_z magnetization component becomes

$$M_z = M_o \cos \theta \quad (4.21)$$

and, consequently:

$$P_\alpha - P_\beta = \delta \cos \theta \quad (4.22)$$

that, combined with equation (4.19), allows to calculate the new population:

$$P_\alpha = \frac{\delta \cos \theta}{2} \quad (4.23)$$

$$P_{\beta} = \frac{-\delta \cos \theta}{2} \quad (4.24)$$

These equations allow to correlate the change occurring to the magnetization for a $\pi/2$ and π pulse. For $\theta=\pi/2$, $\cos\theta=0$ and no nuclei excess is present in any state and the radiofrequency pulse equals the populations. For $\theta=\pi$, $\cos\theta=-1$ and the populations are inverted [4].

Practically, a short, strong and repeated radiofrequency pulse is applied to the nuclei system allowing the simultaneous excitation of nuclei with a Larmor precession ν_0 in a interval $\Delta\nu$ (Fig. 4.12).

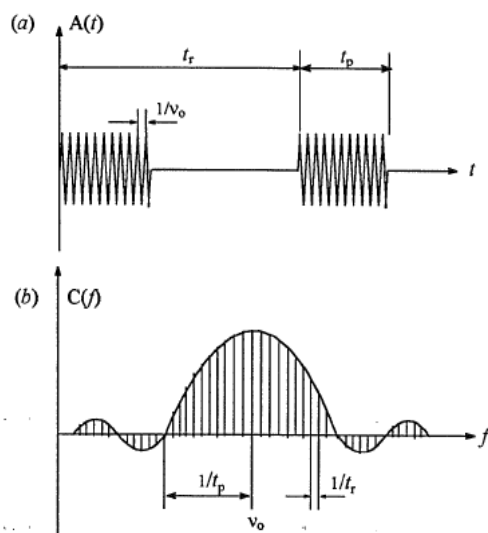


Fig. 4.12: (a) RF pulse sequence of ν_0 , duration length t_p , and repetition time t_r . (b) the correspondent frequency component.

Equation (4.17) relates the deflection angle θ caused by the pulse with the pulse amplitude (or intensity) γB_1 and the pulse time t_p . Both can be modified in order to obtain the desired deflection angle. One of the most important is $\theta=90^\circ$ (or $\pi/2$) where all the magnetization is on the xy plane and the signal has the maximum intensity (Fig. 4.10b). Another is $\theta=180^\circ$ (or π). In this case the magnetization is inverted and becomes antiparallel to the z axis (Fig. 4.10c).

Summarizing, the RF pulse deflects the vector M_z (same direction of B_0) with a certain angle θ generating the M_{xy} magnetization component. M_{xy} exponentially decay with the time constant T_2 emitting a signal that was detected as a alternate voltage on a receiving spire on the x axis. The signal collected is called free induction decay (FID). Figure 4.13 illustrates in details the change of the magnetization during a pulsed NMR experiment in a rotating coordinate system. At the beginning the net magnetization M_o is aligned to the magnetic field B_0 (Fig. 4.13a). After application of an RF pulse that rotates the magnetization of $\pi/2$ (90°), magnetization vector moves (Fig. 4.13b) and, for a pulse of sufficient duration, reaches the final position on the $x'y'$ plane, generating the M_{xy} magnetization component (Fig. 4.13c). At the end of RF pulse ($B_1=0$), the

relaxation process starts and the phase coherency is lost, causing decay of M_{xy} component (Fig. 4.13d and e). This relaxation process is called *transversal relaxation* or *spin-spin* and it proceeds with a constant time T_2 by the energy transfer within height energy nuclei without loss of energy [1-2].

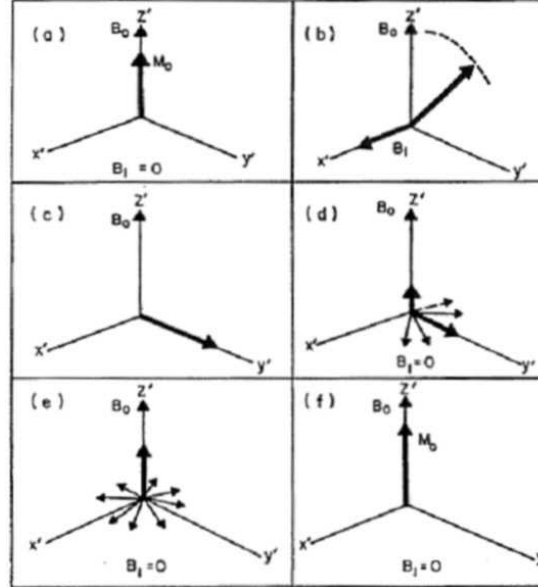


Fig. 4.13: diagrams in the rotating coordinate system $x'y'z'$ showing the magnetization during an NMR experiment. (a) The net magnetization M_0 is aligned to B_0 . (b) and (c) an RF B_1 pulse is applied perpendiculat to B_0 ; the pulse length is sufficient to rotate the magnetization by 90° . (d) and (e) after B_1 ceasing, the spins start to relax by a spin-spin mechanism on the $x'y'$ plane (time constant T_2) and by a spin-lattice mechanism on the z' direction (time constant T_1). (f) After sufficient time, the starting equilibrium magnetization M_0 is re-established.

During the transversal relaxation process, the M_{xy} component decay to 0 by the low

$$\frac{dM_{xy}}{dt} = -\frac{M_{xy}}{T_2} \quad (4.25)$$

or

$$M_{xy} = M_0 \cdot e^{-(t/T_2)} \quad (4.26)$$

The relaxation time T_2 is related to the width of the spectral peak at middle height ($\Delta\nu_{0.5}$) by the equation

$$\Delta\nu_{0.5} = \frac{1}{\pi T_2} \quad (4.27)$$

At the same time, it is possible to observe also the longitudinal component of magnetization M_z that, during relaxation, comes back to the initial equilibrium magnetization M_0 (Fig. 4.13d, e and f). This type of relaxation process is known as *longitudinal relaxation* or *spin-lattice* and proceed with a time constant T_1 .

$$\frac{dM_z}{dt} = \frac{M_o - M_z}{T_1} \quad (4.28)$$

$$M_z = M_o \cdot (1 - e^{-t/T_1}) \quad (4.29)$$

4.1.3 – Low field NMR

4.1.3.1 – Introduction to the low field NMR

As T_2 and T_1 depend also on the chemical and physical environment embedding the particular nucleus, low field NMR can provide information on the structure of the matter. The technique can be easily applied to solid samples, liquid samples, suspension, gel systems or emulsion as it is not destructive and independent from the color or the surface on the sample. The field of application is between 10 and 65 MHz (corresponding to a magnetic field within 0,23 and 1,53 T) and a temperature varying within -10 and +70 °C [5].

The shape and amplitude of the resonance signal are related to the physical environment of the nucleus under examination. In particular, the amplitude is function of the nucleolus degrees of freedom movement in the specific physical environment, an information usefully in polymer chemistry and solid state physics. From the qualitative side, the transversal relaxation time T_2 depends on the nucleus mobility. In the solids there is a reduced mobility so that T_2 is low (1-100 ms). In case of intermediate mobility, such as gel systems, the T_2 is medium (200-800 ms) and finally, into liquids, nuclei mobility is higher and the T_2 is slower (800-2500 ms).

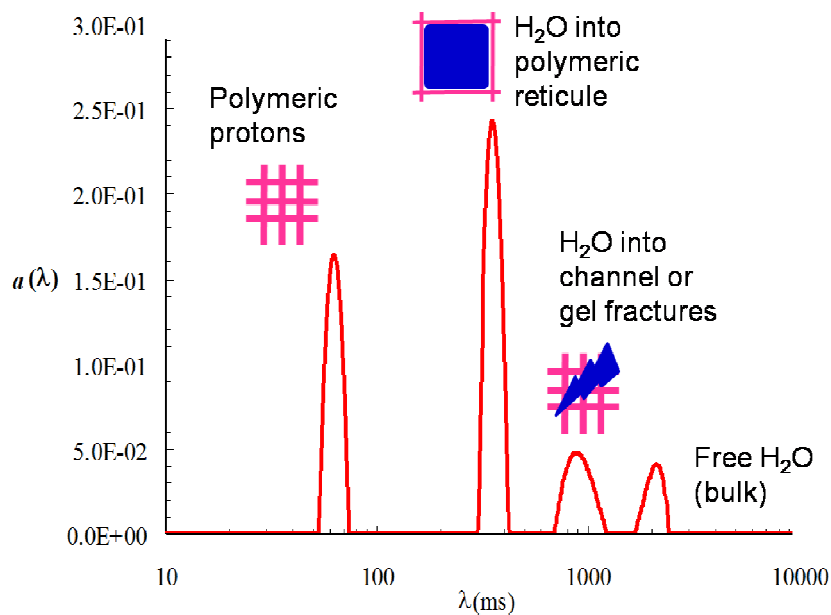


Fig. 4.14: typical example of ^1H relaxation spectrum of a non homogeneous hydrogel.

The low field NMR finds applications in many different areas: food science and technology, industrial analysis, pharmaceuticals and cosmetics for a fast and non destructive analysis of protonic content in oil and fat, moisture and water content determination in different type of materials. One of the most recent applications is the quantitative analysis of a particular isotope by the integration of peak area under the absorbance signal. For hydrogels analysis, the time domain NMR spectrum (a mathematical elaboration of the NMR data also called relaxation spectrum) of the ^1H proton allows to distinguish different sample phases such as the polymers protons, the water entrapped into the polymeric network and the water in small channel or fracture and the free water (*Fig. 4.14*) [5].

4.1.3.2 – T_2 measurements and analysis in low field NMR

A typical instruments for low field NMR is a Bruker minispec mq20TM, that operating to a frequency of 20 MHz (corresponding to $\sim 0,47\text{ T}$; in NMR, the B_0 field applied by the instruments is commonly expressed as the correspondent ^1H proton Larmor frequency) in controlled temperature conditions (*Fig. 4.15*). The typical sequence adopted is the Carr-Purcell-Meiboom-Gill sequence (CPMG):

$$90^\circ - \tau - \{ [180^\circ - 2\tau -]_M 180^\circ - \tau - \text{measurement} - \tau \}_N$$

The sequence consists in the application of a first 90° pulse followed by a time interval τ . Then, a series of M 180° pulse applied at 2τ intervals are forwarded by the last 180° pulse after a τ interval. The sequence is repeated 8 times every 5 seconds.



Fig. 4.15: the low field NMR spectrometer Bruker minispec mq20TM.

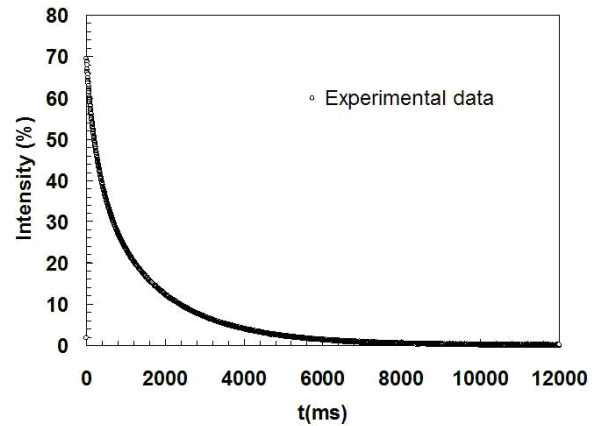


Fig. 4.16: Exponential curve of the transversal relaxation time T_2 .

The exponential T_2 relaxations curve obtained during the measures (*Fig. 4.16*) is fitted by a studied multi-exponential function [6]:

$$\sum_{k=1}^N A_k e^{(-t/T_2^k)} \quad (4.30)$$

where t is the time, A_k is the pre-exponential factor of the k component and T_2^k is the relaxation time of the k component. The number N of considered exponential that minimizing the product ($N \chi^2$), where χ^2 is the sum of square difference within the fitting function (4.29) and the experimental data.

Once N , A_1 , ..., A_N , T_2^1 , ..., T_2^N have been determined by the best fitting, the T_2 continuous distribution can be determined assuming for each instant \bar{t} , the intensity $I(\bar{t})$ is the sum of an infinite number of terms $a(T_2)e^{(-t/T_2)}dT_2$:

$$I(\bar{t}) = \int_{T_2^{\min}}^{T_2^{\max}} a(T_2)e^{(-t/T_2)}dT_2 \quad (4.31)$$

T_2^{\min} - T_2^{\max} represents the extension of the continuous T_2 distribution. The integral of equation (4.30), can be approximated by the trapezium method as:

$$I(\bar{t}) = \int_{T_2^{\min}}^{T_2^{\max}} a(T_2)e^{(-t/T_2)}dT_2 \approx \sum_{i=1}^{i=N-1} 0.5[a_i(T_2^i)e^{-\bar{t}/T_2^i} + a_{i+1}(T_2^{i+1})e^{-\bar{t}/T_2^{i+1}}](T_2^{i+1} - T_2^i) \quad (4.32)$$

where $T_2^1 = T_2^{\min}$ and $T_2^N = T_2^{\max}$. This simplification involves the approximation of the T_2 distribution with a discrete one constituted by N elements each corresponding to a relaxation time T_2^i and characterized by a_i weight. For the determination of a_i , we have to solve a linear system of equations ($N \times N$) similar to equation (4.31) and evaluated at different \bar{t} .

After some mathematical manipulations, equation (4.31) becomes:

$$a_1[e^{-\bar{t}_j/T_2^1}(T_2^2 - T_2^1)] + \sum_{i=2}^{i=N-1} a_i[e^{-\bar{t}_j/T_2^i}(T_2^{i+1} - T_2^{i-1})] + a_N[e^{-\bar{t}_j/T_2^N}(T_2^N - T_2^{N-1})] = 2I_j(\bar{t}_j) \quad (4.33)$$

where

$$I_j(\bar{t}_j) = \sum_{k=1}^{k=N} A_k e^{(-\bar{t}_j/T_2^k)} \quad (4.34)$$

Unfortunately, this system is ill conditioned and a direct resolution, generally, fails. Therefore, it is necessary the application of an iterative procedure that require to choose a first attempt solution vector $\mathbf{a}(a_1, \dots, a_i, \dots, a_N)$. Choosing $\bar{t}_j = T_2^i$ (with $j=i$), the system is, approximately, an upper triangular system as the a_i coefficient values under the diagonal are close to zero. For this reason, a reasonable first attempt choice for the vector $\mathbf{a}^0(a_1^0, \dots, a_i^0, \dots, a_N^0)$ is:

$$a_N^0 = \frac{2I_N}{T_2^N - T_2^{N-1}}$$

$$a_i^0 = \frac{2I_i - \sum_{m=N}^{m=i+1} a_m^0 (T_2^{m+1} - T_2^{m-1}) e^{-\tilde{t}_i/T_2^m}}{T_2^{i+1} - T_2^{i-1}} \quad (4.35)$$

$$a_1^0 = \frac{2I_1 - \sum_{m=N}^{m=2} a_m^0 (T_2^{m+1} - T_2^{m-1}) e^{-\tilde{t}_1/T_2^m}}{T_2^2 - T_2^1}$$

The new solution vector ($\mathbf{a}^n(a_1^n, \dots, a_i^n, \dots, a_N^n)$) is evaluated as follows:

$$a_N^n = \frac{2I_N - \sum_{m=1}^{m=N-1} a_m^{n-1} (T_2^{m+1} - T_2^{m-1}) e^{-\tilde{t}_N/T_2^m}}{T_2^N - T_2^{N-1}}$$

$$a_i^n = \frac{2I_i - \sum_{\substack{m(\neq i)=N \\ m(\neq i)=1}} a_m^{n-1} e^{-\tilde{t}_i/T_2^m}}{T_2^{i+1} - T_2^{i-1}} \quad (4.36)$$

$$a_1^n = \frac{2I_1 - \sum_{m=2}^{m=N} a_m^{n-1} e^{-\tilde{t}_1/T_2^m}}{T_{22} - T_{21}}$$

The iterative process stops when the absolute value of the difference $|a_i^n - a_i^{n-1}|$ is less than a prefixed tolerance [6]. The solution represents the continuous T_2 spectrum.

4.2 – Rheological characterization

Rheology is the science field dealing with the relation between *stress* (τ) and *deformation* (γ). In other words, its aim is to study, theoretically and experimentally, the effect (deformation state) of a stress imposed on a material (and vice versa). In this work the rheological characterizations is performed by a *rotational rheometer* HAAKE Rheostress RS-150™ (*controlled stress*) equipped with a set of different geometry sensors able to stress the samples with a shear strain. The rheometer applies on the sample, a *torque* T (generated by a magnetic field) registering the displacement of the mobile portion of the measuring probe. The probes used are basically constituted by two parallel plates and the sample is placed in between filling all the volume that separate the two plates.



Fig. 4.17: the rotational rheometer HAAKE RheoStress RS-150™.

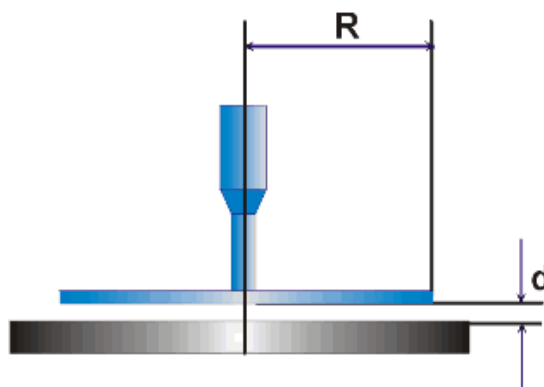


Fig. 4.18: schematic representation of the parallel plates sensor: R is the plates radius and d , the gap between plates

4.2.1 – The parallel plates measuring system geometry

The parallel plates measuring geometry (*Fig. 4.18*) is widely used for measuring the *non-Newtonian fluids* properties and for the characterization of *viscoelastic* materials. The reasons reside in some advantages: the easier sample loading, the possibility to modify the shear rate independently from the *rotational speed* Ω by simply changing the gap d between the plates. On the other side, the torque measuring systems, need a particular attention in order to avoid (or limit) systematic errors during the operative phase. The most common sources of errors are listed below.

- *Inertial effects:* especially at high shear rate, toroidal secondary fluxes generated in the sample leads to an overestimation of the viscous properties and, as consequence, the torque moment results higher of that related only to the rheological properties.
- *Geometrical effects:* if the fluid is loaded in excess, the free surface is not spherical and *edge effects* are generated; others error can be generated by wrong assets that results in acentricity, non alignment and vertical oscillations.
- *Instability effects:* the materials does not preserve its shape in all the conditions so, at high speed, the sample separates in two parts and finally it is pulled out by the centrifugal forces (*splitting*).
- *Shear heating:* due to energy dissipation, a not uniform temperature field can take place inside the gap.

In particular, during this studies, was used the parallel plate sensor PP35 Ti96010 witch have diameter of 35 mm and milled surface in order to minimize the slippage phenomena (*Fig. 4.19*). In order to ensure more consistent environmental conditions and to limit the evaporation, a glass bell (*solvent trap*) was used to cover the measuring device in all the experiments (*Fig. 4.20*).



Fig. 4.19: the parallel plates sensor PP25 Ti96010.



Fig. 4.20: the PP25 Ti96010 sensor isolated by a solvent trap in order to limit the water evaporation from the systems.

4.2.2 – Stress sweep tests

The stress sweep test (SS), serve for the identification of the *linear viscoelastic region*. Within the linear viscoelastic limits, the storage modulus G' (also called elastic modulus) and the loss modulus G'' (also called viscous modulus), are independent from the applied deformation and remain constant up the limit deformation γ_0 (called *critical deformation*). For higher deformation, G' and G'' rapidly decrease. G' give information related to the elastic energy accumulated by the materials during a deformation while, G'' is related to the energy dissipated. The SS test is based on the sample sollicitation by a sinusoidal stress of constant *frequency* f (1 Hz) and increasing amplitude.

For a stress (or deformation) lower than the linear viscoelastic limit, the value of G' and G'' are independent from the applied stress and the system conditions, can be considered as equilibrium state because the material structure does not undergo significant alterations or disruption. Above the critical deformation γ_0 , the material structure collapses and both modulus values change, normally with a decreasing. Deformation γ , deformation speed $\dot{\gamma}$ and stress τ , are related by the following equations:

$$\gamma = \gamma_0 \sin(\omega t) \quad (4.37)$$

$$\dot{\gamma} = \gamma_0 \omega \cos(\omega t) = \dot{\gamma}_0 \cos(\omega t) \quad (4.38)$$

$$\tau = \tau_0 \sin(\omega t + \delta) = \tau_0 \cos \delta \cdot \sin(\omega t) + \tau_0 \sin \delta \cdot \cos(\omega t) \quad (4.39)$$

where, $\dot{\gamma}_0$ is the *critical deformation speed*, ω the *angular frequency* or pulsation ($\omega=2\pi f$) and δ the *loss angle* between stress and deformation.

The first term of the equation (4.38), $\tau_0 \cos \delta \cdot \sin(\omega t)$, is related to the elastic component while, the second, $\tau_0 \sin \delta \cdot \cos(\omega t)$, is related to the viscous component. In the two limiting cases of $\delta=0$ or $\delta=\pi/2$, the material behavior is totally elastic or totally viscous, respectively. Equation (4.38) can be also written as:

$$\tau = G' \gamma_0 \cdot \sin(\omega t) + G'' \gamma_0 \cdot \cos(\omega t) \quad (4.40)$$

Where, the storage modulus G' is related to the component in phase with the applied deformation while, the dissipative loss modulus G'' , is in square phase with it.

The complex modulus G^* is represented by the ratio within maximum stress and maximum applied deformation:

$$|G^*| = \sqrt{(G')^2 + (G'')^2} = \sqrt{\left(\frac{\tau_0 \cos \delta}{\gamma_0}\right)^2 + \left(\frac{\tau_0 \sin \delta}{\gamma_0}\right)^2} = \frac{\tau_0}{\gamma_0} \quad (3.41)$$

The loss angle δ is defined as:

$$\text{tg} \delta = \frac{G''}{G'} \quad (4.42)$$

4.2.3 – Gap determination: short stress sweep tests

The determination of the best sensor gap is a crucial point in the experimental procedure because the errors caused by inaccurate settings can be relevant due to possible wall slippage. The method used to determine the optimal gap and samples compression, consists in the applications of a series of short stress sweep test gradually reducing the plates gap. In order to avoid irreversible effects on the systems, the short SS were performed inside the linear viscoelastic field (shear stress τ around 1 Pa). Fixed the initial gap, the short SS was performed registering the G' at 1 Hz. The test continues with others short SS reducing each time the plates gap till the detection of a plateau in the G' trend (or a maximum value). The distance so determinate was identified as the optimal gap in order to minimize wall slippage effects and was applied in all the following rheological tests (*Fig. 4.21 and 4.22*) [7].

The advantages of this methodology consist in the capability to reproduce the same G' characteristics without preparing the gel in situ within the rheometer plates and the possibility to perform the experiments without knowing the exact thickness of the gel system.

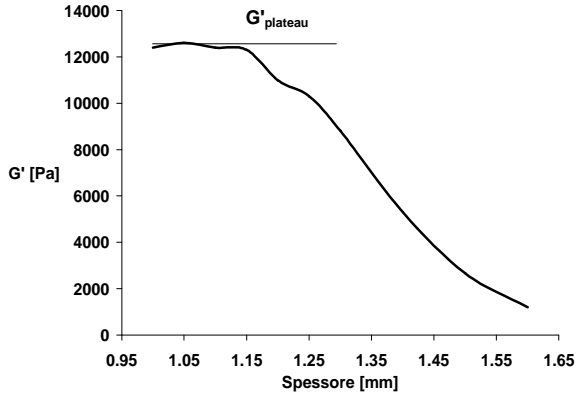


Fig. 4.21: example of G' trend as function of the plates gap during a short SS test; the gap applied when G' reaches the plateau (1,15 mm) was considered the optimal plates distance for the sample.

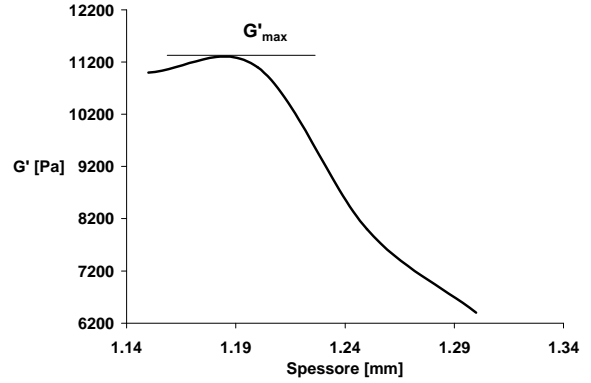


Fig. 4.22: another example of G' trend as function of the pleats gap during a short SS test; the gap applied when G' reaches a maximum (1,2 mm) was considered the optimal plates distance for the sample.

4.2.4 – Frequency sweep tests

The frequency sweep test (FS) is performed in order to obtain the mechanical spectrum of a material; this allows the characterization of structural properties under equilibrium. The test consists in the application of asinusoidal stress of constant amplitude but varying frequency f ($\omega=2\pi f$), usually in the range 0,01-100 Hz. Stress amplitude must belong to the linear viscoelastic field. An important parameter for the materials behavior classification, is the *number of Deborah* (De). This parameter, is the ratio within the characteristic *relaxation time* (λ) (referred to the mechanical properties, not related to the relaxation time T_2 in NMR spectroscopy) and the characteristic deformation process time Λ applied to the material:

$$De = \lambda/\Lambda \quad (4.43)$$

as

$$\Lambda \propto 1/\omega \quad (4.44)$$

we have:

$$De \propto \lambda\omega \quad (4.45)$$

Elastic behavior implies $De=\infty$, while liquid behavior implies $De=0$. A viscoelastic behavior happens for $0 < De < \infty$ (typical $De \approx 1$ or 10).

4.2.5 – Correlation models

Among the different models that can be used for the interpretation of FS test, Maxwell model is one of the most popular. According to this model, the mechanical properties are

represented by a dashpot and a spring in series (Fig. 4.23a). The equation describing the mechanical behavior of the Maxwell model is:

$$\tau + \frac{\eta}{g} \frac{\partial \tau}{\partial t} = -\eta \dot{\gamma} \quad (4.46)$$

where τ is stress, γ is deformation, t is time, η is the dashpot viscosity, g is the spring constant and $\lambda = \eta/g$ is the relaxation time. The relaxation time λ represents the time necessary to the structure to relax the strain after the application of a constant deformation. In the frequency sweep tests, low values of De , correspond to a deformation applied in longer time than the material relaxation time therefore, the time frame for the material is enough to relax from the strain and respond as a viscous-like system. Opposite, for high values of De , the deformation is applied in a short time and the system does not relax completely; the behavior assumes the typical elastic response.

The solution of equation (4.45), in the case of a sinusoidal deformation $\gamma = \gamma_0 \sin(\omega t)$, leads to

$$\tau = \gamma_0 G' \sin(\omega t) + \gamma_0 G'' \cos(\omega t) \quad (4.47)$$

where:

$$G'(\omega) = \frac{g(\lambda\omega)^2}{1 + (\lambda\omega)^2} \quad (4.48)$$

$$G''(\omega) = \frac{g\omega\lambda}{1 + (\lambda\omega)^2} \quad (4.49)$$

These equations of $G'(\omega)$ and $G''(\omega)$ can be plotted into a bi-logarithmic chart. The interception point represent $\omega = 1/\lambda$ corresponding to a G'' maximum and $De = 1$.

In general Maxwell model is not enough for a good description of properties. At this purpose it is possible to combine in parallel n Maxwell elements (Fig. 4.23b). In this case equation (4.45) solution leads to:

$$G'(\omega) = \sum_{k=1}^n \frac{g_k (\lambda_k \omega)^2}{1 + (\lambda_k \omega)^2} \quad (4.50)$$

$$G''(\omega) = \sum_{k=1}^n \frac{g_k \omega \lambda_k}{1 + (\lambda_k \omega)^2} \quad (4.51)$$

This is the *generalized Maxwell model* and the fitting parameters are $2n$: the relaxation times λ_k and the viscosities η_k (or, alternatively, the storage moduli $g_k = \eta_k / \lambda_k$). It is also possible to add a residual terms G'_e that represents the asymptotic limit of the elastic component at low

frequency, correspondent to a Maxwell element in the limit condition of pure elasticity with infinite relaxation time. Relation $g_k(\lambda_k)$ is called relaxation spectrum.

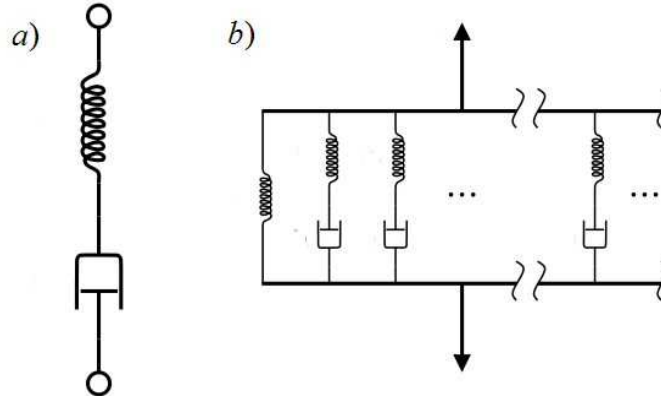


Fig. 4.23: *a)* schematic representation of a viscoelastic element in the Maxwell model constituted by a spring in series with a dashpot that represents the elastic and viscous component respectively. *b)* The generalized Maxwell model constituted by several viscoelastic elements in parallel (the spring on the left represent the pure elastic element).

4.3 – Crosslink density

An important parameter characterizing a polymeric network is the *crosslink density* ρ_x defined as the moles of polymeric inter-chains junctions per gel unit volume.

It is interesting to see the relation between ρ_x and the gel elastic (E) and shear (G) moduli. Let's suppose to form a gel by crosslinking a polymeric solution with a volumetric fraction v_{2r} ; the gel obtained has an initial volume V_0 and x_0, y_0, z_0 initial dimension in a Cartesian coordinate system. Then lets the gel to swell from the initial volume to a final volume V and final polymeric volume fraction v_2 . If the swelled gel is subjected to a deformation (compression or elongation) in the x direction maintaining the volume V constant, the length variation caused by the combination of swelling and deformation effects in the x, y, z directions are:

$$\alpha_x = \frac{x}{x_0} \quad \alpha_y = \frac{y}{y_0} \quad \alpha_z = \frac{z}{z_0}$$

Therefore it is possible to write:

$$\alpha_x \alpha_y \alpha_z = \frac{xyz}{x_0 y_0 z_0} = \left(\frac{xyz}{x_s y_s z_s} \right) \left(\frac{x_s y_s z_s}{x_0 y_0 z_0} \right) = \frac{I}{v_2} v_{2r} \quad (3.52)$$

where $(x_s, y_s, z_s) = V_s$ is the volume of the polymer alone, without any solvent component.

Since the swelling is an isotropic process and x_{0s}, y_{0s}, z_{0s} , are the dimension of the swelled gel before mechanical deformation,

$$\frac{x_{0s}}{x_0} = \frac{y_{0s}}{y_0} = \frac{z_{0s}}{z_0} \quad (4.53)$$

Therefore, the gel volume variation caused by the isotropic swelling is:

$$\frac{V}{V_0} = \frac{x_{0s} y_{0s} z_{0s}}{x_0 y_0 z_0} = \left(\frac{x_{0s}}{x_0} \right)^3 = \frac{v_{2r}}{v_2} \quad (4.54)$$

Combining the effect of the swelling deformation and mechanical deformation, the length variation along x axis became:

$$\alpha_x = \underbrace{\left(\frac{x_{0s}}{x_0} \right)}_{\text{isotropic swelling}} \cdot \underbrace{\left(\frac{x}{x_{0s}} \right)}_{\text{mechanical longation}} \quad (4.55)$$

Inserting equation (4.53) in equation (4.54) leads to:

$$\alpha_x = \alpha \left(\frac{V}{V_0} \right)^{1/3} \quad (4.56)$$

and

$$\alpha_x = \alpha \left(\frac{v_{2r}}{v_2} \right)^{1/3} \quad (4.57)$$

Because of symmetric reasons $\alpha_y = \alpha_z$, thus equation (4.51) became:

$$(\alpha_z)^2 \alpha_x = \frac{v_{2r}}{v_2} \quad (4.58)$$

and equation (4.77) can be transformed in:

$$(\alpha_z)^2 = \frac{v_{2r}}{v_2 \alpha_x} = \frac{v_{2r}}{v_2} \frac{1}{\alpha} \left(\frac{v_2}{v_{2r}} \right)^{1/3} = \frac{1}{\alpha} \left(\frac{v_{2r}}{v_2} \right)^{2/3} \quad (4.59)$$

then:

$$\alpha_z = \alpha_y = \sqrt{\frac{1}{\alpha} \left(\frac{v_{2r}}{v_2} \right)^{2/3}} = \left(\frac{v_{2r}}{v_2} \right)^{1/3} \sqrt{\frac{1}{\alpha}} \quad (4.60)$$

Remembering that, the configurational entropy variation caused by the combinatorial effect of swelling and deformation is expressed by the equation [8]:

$$\Delta S = -\frac{\kappa V_e}{2} \left[\alpha^2 \left(\frac{v_{2r}}{v_2} \right)^{2/3} + \frac{2}{\alpha} \left(\frac{v_{2r}}{v_2} \right)^{2/3} - \ln \left(\frac{v_{2r}}{v_2} \right) \right] \quad (4.61)$$

where κ is the *Boltzman* constant and v_e the number of crosslink's. Remembering that, for an ideal rubber, the recall elastic force f_r is [8]:

$$f_r = -\frac{T}{x_{0s}} \left(\frac{\partial S}{\partial \alpha} \right)_{T,V} \quad (4.62)$$

We have:

$$f_r = -\frac{T}{x_{0s}} \left\{ -\frac{\kappa V_e}{2} \left[2\alpha \left(\frac{v_{2r}}{v_2} \right)^{2/3} - \frac{2}{\alpha^2} \left(\frac{v_{2r}}{v_2} \right)^{2/3} \right] \right\} = \frac{T\kappa V_e}{x_{0s}} \left(\alpha - \frac{1}{\alpha^2} \right) \left(\frac{v_{20}}{v_2} \right)^{2/3} \quad (4.63)$$

Dividing f_r by $y_s \cdot z_s$ (swollen not deformed surface), is possible to obtain the stress for swollen not deformed surface unit:

$$\tau = \frac{f_r}{y_{0s} z_{0s}} = \frac{T\kappa V_e}{x_{0s} y_{0s} z_{0s}} \left(\alpha - \frac{1}{\alpha^2} \right) \left(\frac{v_{2r}}{v_2} \right)^{2/3} \quad (4.64)$$

Then, remembering that:

$$x_{0s} y_{0s} z_{0s} = \frac{v_{2r}}{v_2} V_0 \quad (4.65)$$

$$\nu = \frac{V_e}{N_A} \quad (4.66)$$

where ν is the number of crosslink's moles ($N_A =$ Avogadro's number). The (4.63) became:

$$\tau = \frac{\nu}{V_0} N_A \kappa T \frac{v_2}{v_{2r}} \left(\alpha - \frac{1}{\alpha^2} \right) \left(\frac{v_{2r}}{v_2} \right)^{2/3} = RT \underbrace{\left(\frac{\nu}{V_0} \right)}_{\rho_X} \left(\alpha - \frac{1}{\alpha^2} \right) \left(\frac{v_2}{v_{2r}} \right)^{1/3} \quad (4.67)$$

For small deformation γ , $\alpha - (1/\alpha^2) \approx 3\varepsilon$ (where ε is the deformation to normal stress) then equation (4.66) can be transformed in:

$$\tau = RT\rho_X 3\varepsilon \left(\frac{v_2}{v_{2r}} \right)^{1/3} \quad (4.68)$$

Because the tangential stress τ is linked to the deformation γ by the *Young modulus* E with the relation $\tau = E\gamma$, using equation (4.67), the Young modulus can be expressed as:

$$E = 3RT\rho_x \left(\frac{v_2}{v_{2r}} \right)^{1/3} \quad (4.69)$$

Since in the linear viscoelastic limits and for not compressible materials, the Young modulus E and the *shear modulus* G are proportional as ($E=3G$) [9], G can be expressed as:

$$G = RT\rho_x \left(\frac{v_2}{v_{2r}} \right)^{1/3} \quad (4.70)$$

Finally, if no swelling occurs in the matrix ($v_2=v_{2r}$), before the mechanical solicitation both modulus became [8-10]:

$$G = RT\rho_x \quad \text{Shear modulus} \quad (4.71)$$

$$E = 3RT\rho_x \quad \text{Young modulus} \quad (4.72)$$

In the case polymer crosslink occurs in the dry state ($v_{2r}=1$), we have

$$\tau = \frac{f}{y_{0s}z_{0s}} = \frac{TKv_e}{x_{0s}y_{0s}z_{0s}} v_2^{-2/3} 3\mathcal{E} = RT \underbrace{\left(\frac{v}{x_{0s}y_{0s}z_{0s}} \right)}_{\rho_x \text{ (referred to the swolled volume)}} v_2^{-2/3} 3\mathcal{E} \quad (3.73)$$

$$\tau = RT\rho_x 3\mathcal{E}(v_2)^{-2/3}$$

$$G = RT\rho_x (v_2)^{-2/3} = E / 3 \quad \text{Shear modulus} \quad (4.74)$$

$$E = 3RT\rho_x (v_2)^{-2/3} \quad \text{Young modulus} \quad (4.75)$$

4.4 – Pores diameter distribution

From rheological studies, it is possible to register the effects of the material structure on the macroscopic and mechanical behavior whereas, the studies of the ^1H proton relaxation time from low field NMR spectroscopy, investigates the microscopic characteristics. The whole information from these two characterization methodologies, allows the determination of polymeric network mesh size distribution.

Assuming the complex modulus G of the gel as the sum of all the Maxwell elastic elements constant g_k , it is possible to determine the gel crosslink density ρ_x by the Flory theory [8]. According to (4.69) we have:

$$G = \sum_{k=1}^N g_k \quad (4.76)$$

$$\rho_x = \frac{G}{RT} \left(\frac{v_{2r}}{v_2} \right)^{1/3} \quad (4.77)$$

From the knowledge of ρ_x , it is possible to estimate the *mean mesh size* φ of the polymeric network as predicted by the *Equivalent Network theory* [11]. Multiplying the crosslink density by the Avogadro's number ($\rho_x N_A$), it is possible to obtain the number of crosslinks unit volume and so that $\frac{1}{\rho_x N_A}$ is equal to the mean volume associated to each crosslink. Considering spherical pores, it is possible to write:

$$\frac{1}{\rho_x N_A} = \frac{4}{3} \pi \left(\frac{\varphi}{2} \right)^3 \quad (4.78)$$

or

$$\varphi = \sqrt[3]{\frac{6}{\pi \rho_x N_A}} \quad (4.79)$$

Once φ is known, it is possible using low field NMR analysis to estimate the mesh size distribution. Indeed, the relaxation time T_2 of the water into the gel nanopores (the polymeric network mesh) is the product of the mean mesh diameter by a constant k that depends from the pores geometry (spherical, cylindrical, etc.) and from the chemical properties of the internal pores surface [12]. The k determination derives directly from the mean relaxation time (\bar{T}_2) definition:

$$\bar{T}_2 = \frac{\int_{T_{2min}}^{T_{2max}} a(T_2) T_2 dT_2}{\int_{T_{2min}}^{T_{2max}} a(T_2) dT_2} \stackrel{T_2=k\varphi}{=} \frac{k^2 \int_{k\varphi_{min}}^{k\varphi_{max}} a(\varphi) \varphi d\varphi}{k \int_{k\varphi_{min}}^{k\varphi_{max}} a(\varphi) d\varphi} \stackrel{\text{eq.(4.93)}}{=} k \varphi = k \sqrt[3]{\frac{6}{\pi N_A \rho_x}} \quad (4.80)$$

where $a(T_2)$ is the local intensity of low field NMR relaxation curve, while $(T_{2max} - T_{2min})$ is the relaxation time extension of and $(\varphi_{max} - \varphi_{min})$ is the mesh diameter range. The measuring unit of k is (ms/nm).

Thus:

$$k = \bar{T}_2 \sqrt[3]{\frac{6}{\pi \rho_x N_A}} \quad (3.81)$$

Once k is known, it is possible converting the T_2 distribution into mesh size distribution.

4.5 – Cryoporometry

4.5.1 – Introduction

Porous materials have many, different, important role in several industrial field such as chemicals and petrochemicals, papers, textile, constructions, leathers, etc. The extensive need for different characteristics stimulated intensive researches on porous materials.

The porimetric techniques can be classified in direct methods and indirect methods.

- *Direct methods* are based on the direct observation by the electronic microscopes, X ray diffraction crystallography techniques and others. Unfortunately, these methods, though allowing the direct observations, are not suitable for the mesoporous materials study where the porus radius is between 2 and 50 nm.
- *Indirect methods* are based on the analysis of the capillarity phenomena. The most used are the mercury porimetry (for big pores) and the Gas porosimetry (for small pores). Substantially, the phase transitions of a substance filling a porous material, allows the internal structure characterization.

Cryoporometry is a new calorimetric methods that recently emerged among indirect methods for pores size determination [13]. Cryoporometry is based on the solid-liquid transition of a substance inside porous structure. Many authors observed that the melting temperature of a pure disperse substance depends on the curvature radius of the solid-liquid interface. Inside a pore, the radius strictly depends on the pore dimension. Therefore, the solidification/melting temperature vary for each pores of the material as function of the pore diameters [14]. In particular the smaller the curvature radius, the lower the melting temperature is. This means that a DSC analysis of a liquid filled porous material can provide its pore size distribution.

For its biological, water is usually the election liquid in cryoporometric studies [15]. In addition, due to its high *specific melting heat* ($\Delta h=334 \text{ J/gr}$, one order of magnitude higher than most of others organic solvents) DSC is increased. Main disadvantage of this method consists in the possibility of network corruption due to the liquid solidification. Cryoporometry is not a common methods, not diffused as nitrogen porimetry or mercury porimetry but, can be adopted for the pore size determinations when we know [16]:

- liquid probe surface tension and heat of fusion
- contact angle within sample material and liquid probe
- liquid probe density
- heat capacity dependence on temperature

The experiments were performed on a Perkin Elmer Pyris 1 DSC (Fig. 4.24) following the procedure below:

1. cooling from 25°C to -50°C at 10°C/min
2. hold at -50°C for 1 min.
3. warming from -50°C to 25°C.

The temperature increased speed in step 3 depends on the sample under investigation: 3°C/min and 10°C/min were set respectively for zeolites Si100 and Si40 while, for the hydrogel systems, was reduced at 2°C/min.



Fig. 4.24: the DSC instrument Perkin Elmer Pyris 1 DSC.

4.5.2 – Determinations of the pores size distribution

4.5.2.1 – Nanopores volume (V_p) distribution as function of the pore radius R_p

Gibbs-Duhem equation describes the thermal, mechanical and chemical potential relations into a plane system at the equilibrium where the solid, liquid and gas phases coexist.

$$S_s dT_s - V_s dP_s + n_s d\mu_s = 0 \quad (4. 82)$$

$$S_l dT_l - V_l dP_l + n_l d\mu_l = 0 \quad (4. 83)$$

$$S_v dT_v - V_v dP_v + n_v d\mu_v = 0 \quad (4. 84)$$

S_s , S_l , S_v are the entropies of the solid, liquid and gas phase respectively; V_s , V_l , V_v are the volumes of the solid, liquid and gas phase respectively; P_s , P_l , P_v are the pressures of the solid, liquid and gas phase respectively; μ_s , μ_l , μ_v are the chemical potentials of the solid, liquid and gas phase respectively; n_s , n_l , n_v are the moles of the solid, liquid and gas phase respectively [17-18].

Thus Laplace equation holds:

$$P_v - P_l = \gamma_{lv} \left(\frac{dA_{lv}}{dV_l} \right) \quad (4. 85)$$

$$P_v - P_s = \gamma_{vs} \left(\frac{dA_{vs}}{dV_v} \right) \quad (4.86)$$

$$P_s - P_l = \gamma_{sl} \left(\frac{dA_{sl}}{dV_s} \right) \quad (4.87)$$

where γ_{lv} , γ_{lv} , γ_{lv} , are the liquid-vapor, ice-vapor and ice-vapor surface tensions respectively at the temperature T . When a closed system constituted by a pure component in its coexisting three physic form (solid, liquid and gas) with plane interfaces, the *Gibbs phase rule* asserts that the system is invariant, i.e. there is no degrees of freedom and the triple point can exist at one and only one temperature and pressure pair. For curve contact surface, the *Defay phase rule* asserts that two other independents degrees of freedom exist. This assertion means that, fixing two independent curvature radii, it is possible to define temperature and pressure of the system triple point. This is the case of the highly dispersed systems where the interfaces are curved [17-18]. Equations (4.84) and (4.86) differentiation, leads to:

$$dP_v - dP_l = d \left[\gamma_{vl} \left(\frac{dA_{vl}}{dV_v} \right) \right] \quad (4.88)$$

$$dP_s - dP_l = d \left[\gamma_{sl} \left(\frac{dA_{sl}}{dV_s} \right) \right] \quad (4.89)$$

Considering the difference between equations (4.81)-(4.82) and (4.82)-(4.83), we have:

$$\left(\frac{s_l - s_v}{v_l - v_v} \right) dT = - \frac{v_v}{v_l - v_v} dP_v + \frac{v_l}{v_l - v_v} dP_l \quad \text{liquid-vapor} \quad (4.90)$$

$$\left(\frac{s_s - s_l}{v_s - v_l} \right) dT = - \frac{v_l}{v_s - v_l} dP_l + \frac{v_s}{v_s - v_l} dP_s \quad \text{solid-liquid} \quad (4.91)$$

($v_i=V_i/n_i$, molar volume; $s_i=S_i/n_i$, molar entropy; with $i=s, l, v$ for solid, liquid and vapor respectively). Applying another subtraction within (4.103)-(4.104) and substituting dP_v and dP_s ((4.101) and (4.102) respectively), it is possible to obtain the differential equation of the triple point.

$$\boxed{\left(\frac{s_s - s_l}{v_s - v_l} - \frac{s_l - s_v}{v_l - v_v} \right) dT = \frac{v_v}{v_l - v_v} d \left[\gamma_{lv} \left(\frac{dA_v}{dV_v} \right) \right] + \frac{v_s}{v_s - v_l} d \left[\gamma_{sl} \left(\frac{dA_s}{dV_s} \right) \right]} \quad (4.92)$$

This equation demonstrates as the melting temperature T depends on the curvature radius within the two interfaces. Choosing different interacting interfaces (lv - sv or sl - sv) two other equations can be defined similar to (4.105), depending on the considered physic system [13, 16].

Equation (4.91) is the starting point for the analysis of cryoporometric data obtained by means of DSC.

From experimental evidences [17-18], it is known that, in nanopores filled with water, it exists a water layer of thickness β , that cannot solidify because of the interaction among water molecules and nanopore wall. In order to distinguish within the two aggregation states of the water into nanopores, *freezable* water and *non-freezable* water is defined (Fig. 4.25). From the previous considerations, the melting temperature of the water nanocrystal (freezable water) depends on the crystal radius r .

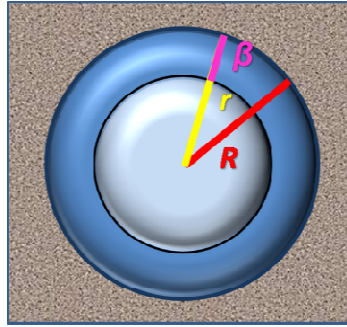


Fig. 4.25: Different water type within a pore. R_p =pore radius, β =non-freezable water layer thickness, r =water nanocrystal radius (freezable water).

Experimentally it was seen that β is constant and independent from the total radius R_p of the pore [15, 17-19]. Nanopores diameters determination, requires the definition of the following physical quantities:

$$v_p = v_f + v_{nf} \quad (4.93)$$

where v_p , v_f and v_{nf} are respectively the nanopore volume, the freezable water volume (or crystal volume) and the non-freezable water volume. Extending this concept to all the sample volume:

$$V_p = V_f + V_{nf} \quad (4.94)$$

with V_p , V_f and V_{nf} are respectively the total nanopores volume, the total freezable water volume and the total non-freezable water volume.

Supposing the existence of a continues pores radius distribution within R_{pmin} and R_{pmax} , and indicating with N the total number of nanopores, it is possible to write the following differential equations [13, 17-18]:

- *cylindrical pores:*

$$dV_p = dV_f + dV_{nf} \quad (4.95)$$

$$dV_p = \pi R_p^2 L dN \quad (4.96)$$

$$dV_f = \pi r^2 L dN \quad (4.97)$$

As consequence, dV_p and dN are respectively, the volume and the number of the pores with radius R_p and dV_f is the volume of the crystal with a radius r . Therefore:

$$dV_p = dV_f \frac{R_p^2}{r^2} = dV_f \frac{R_p^2}{(R_p - \beta)^2} \quad (4.98)$$

- *spherical pores:*

$$dV_p = \frac{4}{3} \pi R_p^3 dN \quad (4.99)$$

$$dV_f = \frac{4}{3} \pi r^3 dN \quad (4.100)$$

And, then:

$$dV_p = dV_f \frac{R_p^3}{r^3} = dV_f \frac{R_p^3}{(R_p - \beta)^3} \quad (4.101)$$

- *cubic pores:*

$$dV_f = r^3 dN \quad (4.102)$$

$$dV_p = R_p^3 dN \quad (4.103)$$

And, then:

$$dV_p = dV_f \frac{R_p^3}{(R_p - \beta)^3} \quad (4.104)$$

Equations (4.97), (4.100) and (4.103) can be generalized for a generic geometry as:

$$dV_p = dV_f \frac{R_p^z}{(R_p - \beta)^z} \quad (4.105)$$

With the exponential z equal at 2 or 3 depending on the geometry. equation (4.104) can be elaborated to obtain the pores volume distributions as function of its radius R_p :

$$\boxed{\frac{dV_p}{dR_p} = \frac{dV_f}{dR_p} \frac{R_p^z}{(R_p - \beta)^z}} \quad (4.106)$$

4.5.2.2 – Nanocrystal volume (V_f) distribution as function of pore radius R_p

In order to evaluate $\frac{dV_f}{dR_p}$, we can remember that

$$V_f = \frac{\Delta H}{\Delta h \rho} \quad (4. 107)$$

where:

- ΔH is the melting enthalpy of V_f (in Joule)
- Δh is the melting enthalpy per mass unit (*standard fusion enthalpy*) of V_f (in J/Kg)
- ρ is the density of V_f (in Kg/m³).

For the *nanocrystal fusion theory*, ΔH and Δh are function of the melting temperature T that, in turn, is function of the crystal radius r [14]. Also the density is function of the temperature and therefore, it can be expressed as function of r . For this consideration, the volume of the crystal of radius r melting at temperature T , can be expressed as:

$$dV_f = \frac{dV_f}{dr} dr \quad (4. 108)$$

As, $r=R_p-\beta$, we have $dr=dR_p$ and, therefore:

$$dV_f = \frac{dV_f}{dR_p} dR_p \quad (4. 109)$$

$$\begin{aligned} \frac{dV_f}{dR_p} &= \frac{d}{dR_p} \left(\frac{\Delta H(T(r))}{\Delta h[T(r)]\rho[T(r)]} \right) \quad (4. 110) \\ &= \frac{\frac{\Delta H}{dR_p} \Delta h \rho - (T(r)) - \Delta H \left(\rho \frac{d\Delta h}{dR_p} + \Delta h \frac{d\rho}{dR_p} \right)}{\Delta h^2 [T(r)] \rho^2 [T(r)]} = \\ &= \frac{d\Delta H}{dR_p} \frac{1}{\Delta h \rho} - \frac{\Delta H \rho}{\Delta h^2 \rho^2} \frac{d\Delta h}{dR_p} - \frac{\Delta H \Delta h}{\Delta h^2 \rho^2} \frac{d\rho}{dR_p} = \\ &= \frac{d\Delta H}{dT} \frac{dT}{dR_p} \frac{1}{\Delta h \rho} - \frac{\Delta H}{\Delta h^2 \rho} \frac{d\Delta h}{dT} \frac{dT}{dR_p} - \frac{\Delta H \Delta h}{\Delta h^2 \rho^2} \frac{d\rho}{dT} \frac{dT}{dR_p} = \\ &= \frac{dT}{dR_p} \left[\frac{d\Delta H}{dT} \frac{1}{\Delta h \rho} - \frac{\Delta H}{\Delta h^2 \rho} \frac{d\Delta h}{dT} - \frac{\Delta H}{\Delta h \rho^2} \frac{d\rho}{dT} \right] = \\ &= \frac{dT}{dR_p} \left[\frac{d\Delta H}{dt} \frac{dt}{dT} \frac{1}{\Delta h \rho} - \frac{\Delta H}{\Delta h^2 \rho} \frac{d\Delta h}{dt} \frac{dt}{dT} - \frac{\Delta H}{\Delta h \rho^2} \frac{d\rho}{dt} \frac{dt}{dT} \right] = \end{aligned}$$

$$\begin{aligned}
 &= \frac{dT}{dR_p} \left[\frac{d\Delta H}{dt} \frac{1}{\Delta h\rho} - \frac{\Delta H}{\Delta h^2\rho} \frac{d\Delta h}{dt} - \frac{\Delta H}{\Delta h\rho^2} \frac{d\rho}{dt} \right] = \\
 &= \frac{dT}{dR_p} \frac{dt}{dT} \left[\frac{d\Delta H}{dt} \frac{1}{\Delta h\rho} - \frac{\Delta H}{\Delta h^2\rho} \frac{d\Delta h}{dt} - \frac{\Delta H}{\Delta h\rho^2} \frac{d\rho}{dt} \right] = \\
 &= \frac{dT}{dR_p} \frac{\dot{Q}}{v\Delta h\rho} \left[1 - \underbrace{\frac{d \ln(\Delta h\rho)}{\ln(\Delta h\rho)}}_{\text{infinitesimal}} \right] \cong \frac{dT}{dR_p} \frac{\dot{Q}}{v\Delta h\rho}
 \end{aligned}$$

Finally, $\frac{dV_f}{dR_p}$ becomes:

$$\boxed{\frac{dV_f}{dr} = \frac{dV_f}{dR_p} = \frac{dT}{dR_p} \frac{\dot{Q}}{v\Delta h\rho}} \quad (4.111)$$

where:

$$\dot{Q} = \frac{d\Delta H}{dt} \quad (4.112)$$

is the power of the DSC trace (normally expressed as J/min) and

$$v = \frac{dT}{dt} \quad (4.113)$$

is the heating speed (normally in $^{\circ}\text{C}/\text{min}$) [17-18].

Another way to obtain the equation (4.110) is represented by the following approach. The volume of the nanocrystal with radius r , (see eq. (4.106)) is:

$$dV_f = \frac{d\Delta H}{\Delta h\rho} \quad (4.114)$$

And then:

$$\begin{aligned}
 \frac{dV_f}{dr} &= \frac{dV_f}{dR_p} = \frac{d\Delta H}{dR_p} \frac{1}{\Delta h\rho} = \\
 &= \frac{d\Delta H}{dT} \frac{dT}{dR_p} \frac{1}{\Delta h\rho} = \underbrace{\frac{d\Delta H}{dT}}_{\dot{Q}} \underbrace{\frac{dT}{dR_p}}_{\frac{1}{v}} \frac{1}{\Delta h\rho} = \\
 &= \frac{\dot{Q}}{v\Delta h\rho} \frac{dT}{dR_p} = \frac{dV_f}{dR_p} = \frac{dV_f}{dr}
 \end{aligned}$$

That is again equation (4.110).

4.5.2.3 – Pore size distribution as function of the nanocrystal melting temperature T

Combining then equations (4.105) and (4.110), it is possible to obtain [14]:

$$\frac{dV_f}{dR_p} = \frac{\dot{Q}}{v\Delta h\rho} \frac{dT}{dR_p} \frac{R_p^z}{(R_p - \beta)^z} \quad (3.115)$$

where:

- \dot{Q} is known from the DSC trace
- v is the heating speed in the DSC experiment, also known
- Δh and $\frac{dT}{dR_p}$ must be evaluated on the base of the equations (4.91)
- ρ is the ice density and must to be evaluated
- β is the thickness of the non-freezable water, evaluable by an iterative procedure later on described

Before proceeding with the evaluation of dT/dR_p , it is necessary to discuss further aspects.

Δh , is the amount of thermal energy which must be absorbed by a unit mass to change the state from solid to liquid. It is normally expressed in J/Kg and, for our purposes, it can be expressed according to Zhang [14]:

$$\Delta h = \Delta h(T_0) - \frac{3}{r} \left(\frac{\gamma_{sv}}{\rho_s} - \frac{\gamma_{sl}}{\rho_l} \right) + \int_T^{T_0} \underbrace{(cp_s - cp_l)}_{-\Delta cp} dT \quad (4.116)$$

- Δh is the ice standard fusion enthalpy
- $\Delta h(T_0)$ is the standard fusion enthalpy of the ice melting at $T_0=0^\circ C$
- T_0 is the melting temperature of the crystal with ∞ radius
- ρ_s is the solid (ice) density at the melting temperature T
- ρ_l is the liquid (water) density at the melting temperature T
- γ_{sv} is the surface tension solid-vapor at the melting temperature T
- γ_{lv} is the surface tension liquid-vapor at the melting temperature T
- cp_s is the solid *specific heat capacity* (ice)
- cp_l is the liquid *specific heat capacity* (water)

At $0^\circ C$ the standard fusion enthalpy of water is $333797 J/Kg$.

The surface tension (γ) is commonly expressed in J/m^2 . In literature [13, 17-18, 20], it is possible to find several expressions for the dependence of the surface tensions γ_{sl} (solid-liquid) and γ_{lv} (liquid-vapor) as on temperature:

$$\gamma_{lv} = [72.88 - 0.138 (T - 20)] \cdot 10^{-3} \quad (4.117) [20]$$

$$\gamma_{sl} = [40.9 + 0.39 (0 - T)] \cdot 10^{-3} \quad (4.118) [20]$$

Or:

$$\gamma_{sl} = (23.8 - 0.102 T) \cdot 10^{-3} \quad (4.119) [13]$$

$$\gamma_{sl} = (30.5 - 0.283 T) \cdot 10^{-3} \quad (4.120) [13]$$

$$\gamma_{sl} = [20.36 - 0.323 (T - 0)] \cdot 10^{-3} \quad \text{for cylindrical pores} \quad (4.121) [17-18]$$

$$\gamma_{sl} = [20.43 - 0.188 (T - 0)] \cdot 10^{-3} \quad \text{for spherical pores} \quad (4.122) [17-18]$$

(the temperature is expressed in °C).

γ_{sv} (solid-vapor) can be determined remembering that for a pure substance the Young equation reads:

$$\gamma_{sv} = \gamma_{lv} + \gamma_{sl} \quad (3.123)$$

Therefore, knowing γ_{sl} and γ_{lv} it is possible to determine γ_{sv} [13, 17-18].

Defining ρ_l as the water density and ρ_s as the ice density, the equations for the dependency on temperature can be [16]:

$$\rho_s = 0.917 (1.032 - 1.17 \cdot 10^{-4} T) \quad (4.124)$$

$$\rho_l = -7.1114 + 0.0882 T - 3.1959 \cdot 10^{-4} T^2 + 3.8649 \cdot 10^{-7} T^3 \quad (4.125)$$

In this equations the density is expressed in gr/cm^3 and the temperature in Kelvin (K).

The specific heat capacity is the measure of the energy required to increase of 1°C a unitary mass (one *gr* or one *Kg*). Defining cp_l as the water specific heat capacity and cp_s as the ice specific heat capacity, the equations for the dependency their dependency from temperature can be [13, 19]:

$$cp_s = 2.114 (1 + 373.7 \cdot T \cdot 10^{-5}) \quad (4.126)$$

$$cp_l = 4.222 (1 - 54 \cdot T \cdot 10^{-5}) \quad (4.127)$$

expressed in $J/(gr \text{ } ^\circ\text{C})$; or

$$cp_l = 4.222 (1 - 54 \cdot T \cdot 10^{-5}) \quad (4.128)$$

expressed in $J/(gr\ K)$.

4.5.4 – Evaluation of the non-freezable water layer thickness (β)

In order to solve equation (4.114) the iterative estimation of the non-freezable water layer thickness β is needed [13]. At this purpose it is convenient to define the following physical quantities:

$$W_f = \int_T^{T_0=0^\circ C} \frac{\dot{Q}}{v} \cdot \frac{1}{\Delta h} dT \quad (3.129)$$

$$V_f = \int_T^{T_0=0^\circ C} \frac{\dot{Q}}{v} \cdot \frac{dT}{\rho_{ICE} \Delta h} \quad (4.130)$$

$$W_{H_2O} = \int_{T_0}^{T > T_0} \frac{\dot{Q}}{v} \cdot \frac{1}{\Delta h(T_0)} dT \quad (4.131)$$

$$W_{nf} = W_t - W_f - W_{H_2O} \quad (4.132)$$

$$V_p = \frac{V_{nf}}{\rho_{ICE} (0^\circ C)} + V_f \quad (4.133)$$

where:

- Δh is the ice melting enthalpy as defined in the equation (4.115) (expressed in J/Kg , dependent from the nanocrystal melting temperature)
- V_p is the total nanopores volume
- V_f is the volume of *freezable* water inside the nanopores
- V_{nf} is the volume of *non-freezable* water inside the nanopores
-
- $\Delta h(T_0)$ is the melting enthalpy of the ice melting at $T_0=0^\circ C$ (expressed in J/Kg)
- v_f is volume of the freezable water (expressed in m^3 , can be obtained from the DSC trace)
- v is the heating speed set during DSC experiment
- ρ_{ice} is the ice density at temperature T
- W_{nf} is the mass of non-freezable water inside the pores expressed in Kg
- W_t is the total water mass inside and outside the system expressed in Kg

- W_f is the mass of freezable water inside the pores (expressed in kg, can be obtained from the DSC trace)
- W_{H_2O} is the mass of water melting at 0°C (expressed in Kg, can be obtained from the DSC trace)
- $\rho_{ice}(0^\circ\text{C})$ is the ice density at temperature $T_0=0^\circ\text{C}$

The iterative procedure starts assuming starting value for β ($=0$) and the pores geometry parameter z . Then, pore volume ($V_{p,calc}$) can be calculated by the integral within R_{pmax} (where ice melting at 0°C) and R_{pmin} of equation (4.128):

$$V_{p,calc} = \int_{R_{pmin}}^{R_{pmax}(T=0^\circ\text{C})} \frac{\dot{Q}}{v\Delta h\rho_{ICE}} \frac{dT}{dR_p} \left(\frac{R_p}{R_p - \beta} \right)^z dR_p \quad (4.134)$$

This value is then compared to that coming from equation (4.132) and the relative difference is evaluated:

$$\frac{\Delta V}{V_p} = \frac{|V_{p,calc} - V_p|}{V_p} < \varepsilon \quad (4.135)$$

where ε is tolerance. If the (4.134) is not respected, the β values will be assumed as $\beta=\beta+\Delta\beta$ and the $V_{p,calc}$ will be recalculated through the (4.149) with the new value. The procedure stops when $\Delta V/V_p < \varepsilon$ and the final β value is accepted [6].

Once β is determinate, it is possible to determine the pore size probability distribution:

$$\frac{d\phi}{dR_p} = \frac{\frac{dV_p}{dR_p}}{\int_{R_{pmin}}^{R_{pmax}} \frac{dV_p}{dR_p} dR_p} \quad (4.136)$$

Placing $f(R_p) = \frac{d\phi}{dR_p}$, it is possible to obtain:

$$\int_{R_{pmin}}^{R_{pmax}} f(R_p) dR_p = \int_{R_{pmin}}^{R_{pmax}} \left(\frac{d\phi}{dR_p} \right) dR_p = \frac{\int_{R_{pmin}}^{R_{pmax}} \frac{dV_p}{dR_p} dR_p}{\int_{R_{pmin}}^{R_{pmax}} \frac{dV_p}{dR_p} dR_p} = 1 \quad (4.137)$$

where ϕ is the probability to have a pore of radius R_p in the system under examination.

4.5.5 – Evaluation of the melting temperature distribution as function of the pore radius (dT/dR_p)

4.5.5.1 – Pore geometry and physical conditions

Starting point is the equation (4.91) for the triple point of highly dispersed systems:

$$\left(\frac{s_s - s_l}{v_s - v_l} - \frac{s_l - s_v}{v_l - v_v} \right) dT = \frac{v_v}{v_l - v_v} d \left[\gamma_{lv} \left(\frac{dA_v}{dV_v} \right) \right] + \frac{v_s}{v_s - v_l} d \left[\gamma_{sl} \left(\frac{dA_s}{dV_s} \right) \right] \quad (4.91)$$

As mentioned before, s_s , s_l , s_v and v_s , v_l , v_v are respectively, the molar entropy and molar volume of solid, liquid and vapor phase; V_v and V_s , are the volume of vapor and solid phase; γ_{lv} and γ_{sl} are the surface tension liquid-vapor and solid-vapor. In the hypothesis that, $v_s \ll v_v$ and $v_l \ll v_v$, also

$$\frac{s_s - s_l}{v_s - v_l} \gg \frac{s_l - s_v}{v_l - v_v}$$

and therefore:

$$\left(\frac{s_s - s_l}{v_s - v_l} \right) dT = -d \left[\gamma_{lv} \left(\frac{dA_v}{dV_v} \right) \right] + \frac{v_s}{v_s - v_l} d \left[\gamma_{sl} \left(\frac{dA_s}{dV_s} \right) \right] \quad (4.138)$$

Giving $\Delta S_f = s_l - s_s = \frac{\Delta H_f}{T}$, it is possible to obtain:

$$dT = \frac{v_s - v_l}{\Delta S_f} d \left[\gamma_{lv} \left(\frac{dA_v}{dV_v} \right) \right] - \frac{v_s}{\Delta S_f} d \left[\gamma_{sl} \left(\frac{dA_s}{dV_s} \right) \right] \quad (4.139)$$

where ΔS_f is the molar melting entropy at the temperature T and ΔH_f is the molar melting enthalpy at the temperature T . Assuming that, the melting occurs at the equilibrium, the process Gibbs free energy is:

$$\Delta G_f = \Delta H_f - T \Delta S_f = 0 \quad (4.140)$$

Equation (4.138) must to be evaluated on the base of the physical and geometrical melting conditions within the porous systems under examination [13]. Three cases can be distinguished:

- a) cylindrical pores geometry with an excess of water (compared to the total pores volume) into the system
- b) cylindrical pores geometry without excess of water
- c) spherical pores (excess of water it is not considered with this pores geometry).

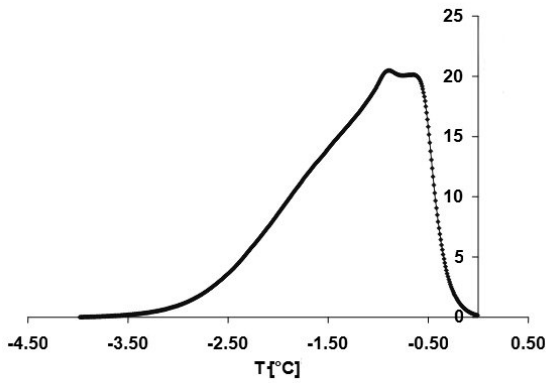


Fig. 4.26: example of an Cu^{2+} alginate hydrogel DSC trace 2% in weight. The melting spectrum evidence the presence of water structured into nanopores that melting at $T < 0^\circ\text{C}$. There is no excess of water outside the pores that melting at $T = 0^\circ\text{C}$.

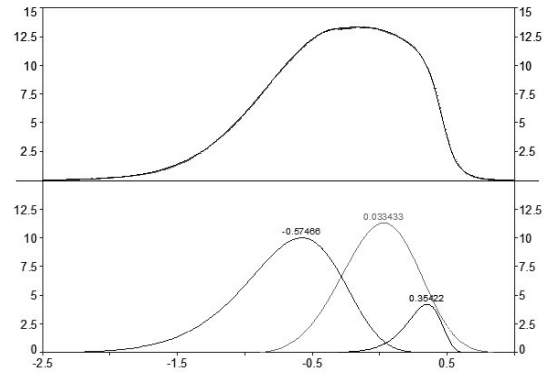


Fig. 4.27: example of an *aged* Cu^{2+} alginate hydrogel DSC trace 2% in weight. Decomposing the upper melting spectrum into three separate curves, it is possible to distinguish the water structured into smaller pores (left curve) while the rest is an excess of water outside the gel structure that melting at $T = 0^\circ\text{C}$.

The presence of an excess of water into the sample can be distinguished on the DSC trace. When a peak of water melting is present at $T = 0^\circ\text{C}$, the system contains an excess. On the contrary all the water is only inside the pores. In figures 4.26 and 4.27, both the cases are showed. In the following sections, the theoretical implications of the three cases will be examined separately.

4.5.5.2 – Cylindrical pores geometry with an excess of water

When temperature is raised, the ice starts melting inside the pores in virtue of the small curvature radius. The situation that take place is that represented in figure 4.28 [13].

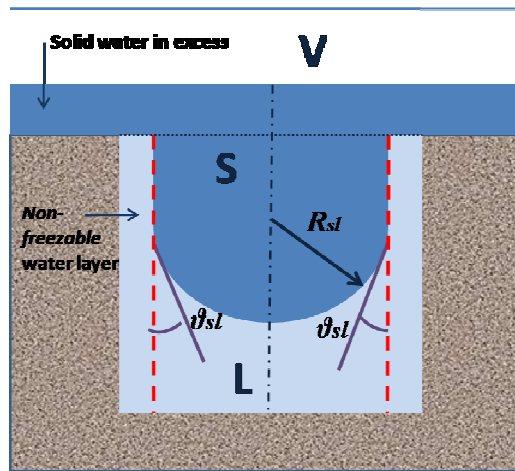


Fig. 4.28: condition of cylindrical pores with excess of water. The excess of water outside the pores is solid (S) and form a flat interface with the vapor phase (V) while, the rest into the pores form a spherical interface with the liquid phase (L) on the pores bottom. R_{sl} =curve radius of sl interface; θ_{sl} =sl contact angle.

The solid-vapor interface is flat (the interface curve radius $R_{sv} \rightarrow \infty$) and then, both the first and second curvatures of the sv interface, corresponding to the inverse of the interface curve radius

($1/R_{sv}$), are equal to 0. This means that if some solid ice becomes vapor, causing an increment of the vapor volume V_v , the interface area A_v , remain constant:

$$\frac{dA_v}{dV_v} = 0 \quad (4.141)$$

dA_s/dV_s , instead, is equal to $2/R_{sl}$ corresponding to the sum of the first and second curvatures that are equal as the sl interface is assumed spherical.

$$\frac{dA_s}{dV_s} = \frac{2}{R_{sl}} \quad (4.142)$$

R_{sl} is the interface curvature radius within ice and liquid water corresponding to the radius of the nanocrystal ($R_{sl}=r$) and determines the melting temperature of the nanocrystal. The contact angle within the liquid and solid phase is equal to 0 ($\vartheta_{sl}=0$) because of the presence of the non-freezable water layer adherent to the pore wall.

On this basis, equation (4.138) becomes:

$$dT = \underbrace{\frac{v_s - v_l}{\Delta S_f} d \left[\gamma_{lv} \left(\frac{dA_v}{dV_v} \right) \right]}_0 - \frac{v_s}{\Delta S_f} d \left[\gamma_{sl} \left(\frac{dA_s}{dV_s} \right) \right] = - \frac{v_s}{\Delta S_f} 2 d \left(\frac{\gamma_{sl}}{R_{sl}} \right) \quad (4.143)$$

Integrating within the 0°C (temperature T_0) and the nanocrystal melting temperature T , equation (4.142) becomes:

$$\int_{T_0}^T dT = T - T_0 = - \frac{2v_s}{\Delta S_f} \gamma_{sl} \int_0^{\frac{1}{R_{sl}}} d \left(\frac{1}{R_{sl}} \right) \quad (4.144)$$

The terms v_s , γ_{sl} and ΔS_f are assumed to be constant and, even if this assumption is not completely true, for the numerical methodology that will be adopted later, the approximations results reasonable. Therefore, the solution of (4.154) is:

$$T - T_0 = - \frac{2v_s \gamma_{sl}}{\Delta S_f} \frac{1}{R_{sl}} \quad (4.145)$$

$$T - T_0 = - \frac{2v_s \gamma_{sl}}{\Delta H_f} \frac{1}{R_{sl}} T \quad (4.146)$$

If, on the integral (4.159), ΔS_f is assumed as $\Delta S_f = T \cdot \Delta H_f$, the solution in *molar terms* became:

$$\boxed{\ln(T/T_0) \Delta H_f = - \frac{2v_s \gamma_{sl}}{R_{sl}}} \quad (4.147)$$

Using integration step $<0,5^{\circ}\text{C}$, the solutions (4.161) and (4.162) are equivalent.

In terms of mass unit, the solution can be written as:

$$T - T_0 = -\frac{2\gamma_{sl}}{\Delta H_f R_{sl}} \frac{1}{\rho_s} T \quad (4.148)$$

$$T_0 = T \left(1 + \frac{2\gamma_{sl}}{\Delta H_f R_{sl}} \frac{1}{\rho_s} \right) \quad (4.149)$$

$$\boxed{\ln(T/T_0)\Delta H_f = -\frac{2\gamma_{sl}}{R_{sl}\rho_s}} \quad (4.150)$$

4.5.5.3 – Cylindrical pores geometry without excess of water

In the cylindrical geometry without excess of water, melting process begins in smaller pores [13]. The physical situation taking place is depicted in *figure 4.29*. Ice melting starts at the solid-vapor interface so that a convex liquid-vapor interface arises. At the same time, a concave interface generates between the liquid and solid phases (it is assumed that pore bottom is flat so that the curvature radius is ∞).

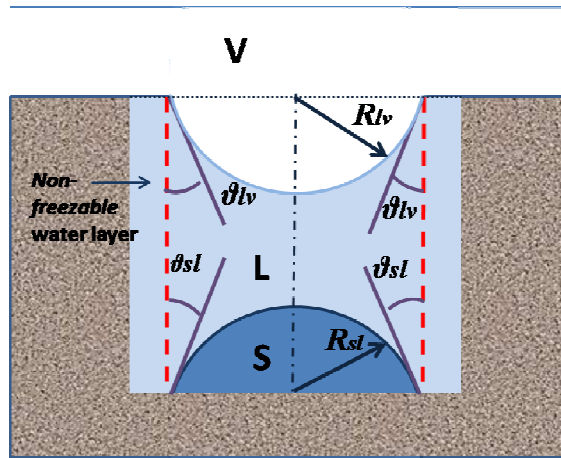


Fig. 4.29: condition of cylindrical pores without excess of water. The vapor phase outside the pores (V) form a semispherical interface with the liquid phase (L). The solid phase (S) is into the pores forming a semispherical interface with the liquid phase (L). R_{lv} =curve radius of lv interface; R_{sl} =curve radius of sl interface; θ_{sl} = sl contact angle; θ_{lv} = lv contact angle.

The solid-liquid contact angle (θ_{sl}) and liquid-vapor contact angle (θ_{lv}) are assumed equal to 0 because of the presence the *non-freezable* water layer at the pore wall. At the lv interface, the first and second curve are equal to $1/R_{lv}$ and then dA_v/dV_v is equal to $2/R_{lv}$; the same happens at the sl interface ($1/R_{sl}$):

$$\frac{dA_v}{dV_v} = \frac{2}{R_{lv}} \quad (4.151)$$

$$\frac{dA_s}{dV_s} = \frac{2}{R_{sl}} \quad (4.152)$$

The lv and sl interface curvatures are equal to the ice nanocrystal radius ($R_{lv}=R_{sl}=r$). Accordingly equation (4.138) became:

$$\begin{aligned} dT &= \frac{v_s - v_l}{\Delta S_f} d \left[\gamma_{lv} \left(\frac{dA_v}{dV_v} \right) \right] - \frac{v_s}{\Delta S_f} d \left[\gamma_{sl} \left(\frac{dA_s}{dV_s} \right) \right] = \\ &= \frac{v_s - v_l}{\Delta S_f} d \left[\gamma_{lv} \left(\frac{2}{R_{lv}} \right) \right] - \frac{v_s}{\Delta S_f} d \left[\gamma_{sl} \left(\frac{2}{R_{sl}} \right) \right] \end{aligned} \quad (4.153)$$

Integrating within T_0 and T , remembering that $R_{lv}=R_{sl}=r$ and assuming constant the terms v_s , v_l , γ_{sl} , γ_{lv} and ΔS_f , it is possible to obtain:

$$\int_{T_0}^T dT = T - T_0 = 2 \frac{v_s - v_l}{\Delta S_f} \gamma_{lv} \int_0^{\frac{1}{R_{lv}}} d \left(\frac{1}{R_{lv}} \right) - \frac{2v_s}{\Delta S_f} \gamma_{sl} \int_0^{\frac{1}{R_{sl}}} d \left(\frac{1}{R_{sl}} \right) \quad (4.154)$$

$$T - T_0 = 2 \frac{v_s - v_l}{\Delta S_f R_{lv}} \gamma_{lv} - \frac{2v_s}{\Delta S_f R_{sl}} \gamma_{sl} \quad (4.155)$$

$$T - T_0 = 2T \frac{v_s - v_l}{\Delta H_f R_{lv}} \gamma_{lv} - T \frac{2v_s}{\Delta H_f R_{sl}} \gamma_{sl} \quad (4.156)$$

$$T - T_0 = 2T \frac{v_s - v_l}{\Delta H_f R_{lv}} \gamma_{lv} - T \frac{2v_s}{\Delta H_f R_{sl}} \gamma_{sl} \quad (4.157)$$

$$T - T_0 = \frac{2T}{\Delta H_f r} [\gamma_{lv} (v_s - v_l) - \gamma_{sl} v_s] \quad (4.158)$$

$$T_0 = T \left\{ 1 + \frac{2}{\Delta H_f r} [\gamma_{sl} v_s - \gamma_{lv} (v_s - v_l)] \right\} \quad (4.159)$$

If in the integral (4.153), is assumed $\Delta S_f = T \cdot \Delta H_f$, the solution (*in molar terms*) becomes:

$$\boxed{\ln(T/T_0) \Delta H_f = -\frac{2}{r} [\gamma_{sl} v_s - \gamma_{lv} (v_s - v_l)]} \quad (4.160)$$

Again equation (4.158) and (4.159) are equivalent for temperature intervals $<0,5^\circ\text{C}$. Equation (4.158) can be expressed in *terms of mass*:

$$T_0 = T \left\{ 1 + \frac{2}{\Delta H_f r} \left[\frac{\gamma_{sl}}{\rho_s} - \gamma_{lv} \left(\frac{1}{\rho_s} - \frac{1}{\rho_l} \right) \right] \right\} \quad (4.161)$$

where $\left(\frac{1}{\rho_s} - \frac{1}{\rho_l}\right) \cong 0$

(4.159) instead, becomes:

$$\boxed{\ln(T/T_0)\Delta H_f = -\frac{2}{r}[\gamma_{sl}/\rho_s - \gamma_{lv}(1/\rho_s - 1/\rho_l)]} \quad (4.162)$$

4.5.5.4 – Spherical pores geometry

In the case of spherical pores, the only adaptable model is the simple system with two phases showed in *figure 4.30*. This model does not take in account the excess of water and therefore, at the equilibrium, only solid and liquid phase are present. For such as highly dispersed biphasic system, the coupling of the equilibrium equation with the Laplace equations is needed.

Therefore:

$$-P_l dV_l - P_s dV_s + \gamma_{sl} dA_{sl} = 0 \quad (4.163)$$

Because $dV_l = -dV_s$:

$$P_l dV_s - P_s dV_s = -\gamma_{sl} dA_{sl} \quad (4.164)$$

$$dV_s (P_l - P_s) = -\gamma_{sl} dA_{sl} \quad (4.165)$$

$$(P_s - P_l) = \gamma_{sl} \frac{dA_{sl}}{dV_s} = \frac{2\gamma_{sl}}{R_{sl}} \quad (4.166)$$

$$dP_s = dP_l + d\frac{2\gamma_{sl}}{R_{sl}} \quad (4.167)$$

In a biphasic system, the Gibbs-Duhem equations became:

$$s_s dT + du - V_s dP_s = 0 \quad (4.168)$$

$$s_l dT + du - V_l dP_l = 0 \quad (4.169)$$

Subtracting equation (4.168) from equation (4.167):

$$(s_s - s_l) dT - V_s dP_s + V_l dP_l = 0 \quad (4.170)$$

Then, substituting dP_s given by equation (4.166), we have:

$$(s_s - s_l) dT - V_s \left(dP_l + d\frac{2\gamma_{sl}}{R_{sl}} \right) + V_l dP_l = 0 \quad (4.171)$$

$$(s_s - s_l) dT + dP_l (V_l - V_s) - 2d\frac{V_s \gamma_{sl}}{R_{sl}} = 0 \quad (4.172)$$

$$(s_s - s_l)dT + (V_l - V_s)dP_l - 2V_s\gamma_{sl}d\left(\frac{1}{R_{sl}}\right) = 0 \quad (4.173)$$

Integrating equation (4.188) within T_0 and T , we have:

$$-\Delta H_f \int_{T_0}^T \frac{dT}{T} + (V_l - V_s) \int_{P_0}^P dP_l - 2V_s\gamma_{sl} \int_0^{R_{sl}} d\frac{1}{R_{sl}} = 0 \quad (4.174)$$

$$-\Delta H_f \ln(T/T_0) + (V_l - V_s)(P - P_0) - \frac{2V_s\gamma_{sl}}{R_{sl}} = 0 \quad (4.175)$$

As the liquid phase pressure does not vary with the nanocrystal radius, $(P-P_0)=0$ and therefore, in *molar terms*, equation (4.174) becomes:

$$\boxed{\ln(T/T_0)\Delta H_f = -\frac{2V_s\gamma_{sl}}{R_{sl}}} \quad (4.176)$$

Expressing the (4.175) in term of mass, the solution becomes:

$$\boxed{\ln(T/T_0)\Delta H_f = -\frac{2\gamma_{sl}}{\rho_s R_{sl}}} \quad (3.177)$$

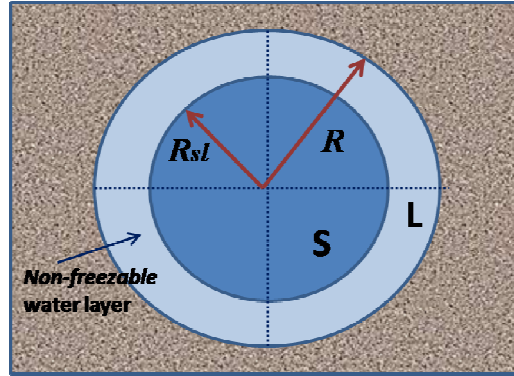


Fig. 4.30: condition of spherical pores. The system consists of only two components: solid phase (S) or the water nanocrystal of radius R_{ls} surrounded by the liquid phase (L) constituted by the *non-freezable* water layer. R_p is the pores radius.

Notably, the solutions (4.175) and (4.176) purposed for the system of spherical pores, are equivalent to the solutions proposed for the system of cylindrical pores with an excess of water (4.146) and (4.149) [13].

4.5.5.5 – Numerical determination of β and dT/dR_p

Previous discussion led to:

$$\int_{T_0}^T \Delta S dT = -\frac{A}{R_p} \quad (4.178)$$

where:

$$A = 2\gamma_{sl} / \rho_s \quad (4.179)$$

Cylindrical pores with excess of waterSpherical pores

$$A = 2 \left[\frac{\gamma_{sl}}{\rho_s} - \gamma_{lv} \left(\frac{1}{\rho_s} - \frac{1}{\rho_l} \right) \right] \quad (4.180) \quad \text{Cylindrical pores without excess of water}$$

Equation (4.177) integration between T_0 and T_1 ($=T_0+\Delta T$) assuming ΔS constant in this temperature range, yields:

$$R_1 = - \frac{A}{\Delta S_1 (T_1 - T_0)} \quad (4.181)$$

where $T_0=273,15\text{K}$ is the melting temperature of the ice outside the pores. In the same interval, Zhang [14] equation (4.115) must hold:

$$\Delta H_1 = \Delta H_0 - 3 \left(\frac{\gamma_{sv}}{\rho_s} - \frac{\gamma_{lv}}{\rho_l} \right) - \Delta cp \cdot (T_0 - T_1) \quad (4.182)$$

$$T_1 \Delta S_1 = T_0 \Delta S_0 - \frac{3}{R_{pl}} \left(\frac{\gamma_{sv}}{\rho_s} - \frac{\gamma_{lv}}{\rho_l} \right) - \Delta cp \cdot (T_0 - T_1) \quad (4.183)$$

A rearrangement of equation (4.182) leads to:

$$\frac{1}{R_{pl}} = \frac{T_0 \Delta S_0 - T_1 \Delta S_1 - \Delta cp \cdot (T_0 - T_1)}{3 \left(\frac{\gamma_{sv}}{\rho_s} - \frac{\gamma_{lv}}{\rho_l} \right)} \quad (4.184)$$

or

$$R_{pl} = \frac{-3 \left(\frac{\gamma_{sv}}{\rho_s} - \frac{\gamma_{lv}}{\rho_l} \right)}{T_1 \Delta S_1 - T_0 \Delta S_0 + \Delta cp \cdot (T_0 - T_1)} \quad (4.185)$$

Equating equations (4.180) and (4.184) yields to:

$$\frac{A}{\Delta S_1 (T_1 - T_0)} = \frac{3 \left(\frac{\gamma_{sv}}{\rho_s} - \frac{\gamma_{lv}}{\rho_l} \right)}{T_1 \Delta S_1 - T_0 \Delta S_0 + \Delta cp \cdot (T_0 - T_1)} \quad (4.186)$$

Consequently, we have:

$$\Delta S_1 = \frac{A}{3\beta} \frac{\Delta cp \cdot (T_0 - T_1) - T_0 \Delta S_0}{(T_1 - T_0) - \frac{AT_1}{3\beta}} \quad (3.187)$$

$$\text{where } \beta = \left(\frac{\gamma_{sv}}{\rho_s} - \frac{\gamma_{lv}}{\rho_l} \right)$$

$$\Delta H_i = T_i \Delta S_i \quad (4.188)$$

Following the same strategy it is possible integrating equation (4.177) between T_0 and T_i ($=T_0+i\Delta T$):

$$\int_{T_0}^{T_i} \Delta S dT = \sum_{j=1}^{i-1} \Delta S_j (T_j - T_{j-1}) + \Delta S_i (T_i - T_{i-1}) = - \frac{A}{R_{pi}} \quad (3.189)$$

$$R_{pi} = \frac{-A}{\sum_{j=1}^{i-1} \Delta S_j (T_j - T_{j-1}) + \Delta S_i (T_i - T_{i-1})} = \frac{-3\beta}{T_i \Delta S_i - T_0 \Delta S_0 + \Delta cp \cdot (T_0 - T_i)} \quad (4.190)$$

$$\sum_{j=1}^{i-1} \Delta S_j (T_j - T_{j-1}) + \Delta S_i (T_i - T_{i-1}) = \frac{A}{3\beta} [T_i \Delta S_i - T_0 \Delta S_0 + \Delta cp \cdot (T_0 - T_i)] \quad (4.191)$$

$$\Delta S_i \left[(T_i - T_{i-1}) - \frac{AT_i}{3\beta} \right] = \frac{A}{3\beta} [T_i \Delta S_i - T_0 \Delta S_0 + \Delta cp \cdot (T_0 - T_i)] - \sum_{j=1}^{i-1} \Delta S_j (T_j - T_{j-1}) \quad (4.192)$$

Finally we have:

$$\Delta S_i = \frac{\frac{A}{3\beta} [T_i \Delta S_i - T_0 \Delta S_0 + \Delta cp \cdot (T_0 - T_i)] - \sum_{j=1}^{i-1} \Delta S_j (T_j - T_{j-1})}{\left[(T_i - T_{i-1}) - \frac{AT_i}{3\beta} \right]} \quad (4.193)$$

$$\Delta H_i = T_i \Delta S_i \quad (4.194)$$

$$R_{pi} = \frac{-3\beta}{T_i \Delta S_i - T_0 \Delta S_0 + \Delta cp \cdot (T_0 - T_i)} \quad (4.195)$$

In these relations, T must be expressed in Kelvin (K).

A different methodology to calculate the integral expressed in (4.177) consist in the assumption of constant ΔH_f instead constant ΔS_f . Therefore, proceeding in the same way, it is possible to obtain similar results.

$$\int_{T_0}^{T_i} \frac{\Delta H}{T} dT = \Delta H_i \ln(T_i/T_0) = - \frac{A}{R_{pl}} \quad (4.196)$$

where:

$$A = 2\gamma_{sl} / \rho_s \quad (4.199)$$

Cylindrical pores with excess of water

Spherical pores

$$A = 2 \left[\frac{\gamma_{sl}}{\rho_s} - \gamma_{lv} \left(\frac{1}{\rho_s} - \frac{1}{\rho_s} \right) \right] \quad (4.200) \quad \underline{\text{Cylindrical pores without excess of water}}$$

Therefore:

$$R_{pl} = - \frac{A}{\Delta H_l \ln(T_l/T_0)} \quad (4.197)$$

But, according to equation (4.115), we have:

$$\Delta H_l = \Delta H_0 - \frac{3}{R_{pl}} \underbrace{\left(\frac{\gamma_{sv}}{\rho_s} - \frac{\gamma_{lv}}{\rho_l} \right)}_{\beta} - \int_{T_l}^{T_0} \underbrace{(cp_l - cp_s)}_{\Delta cp} dT \quad (4.198)$$

$$\frac{3\beta}{R_{pl}} = \Delta H_0 - \Delta H_l - \int_{T_l}^{T_0} \Delta cp \cdot dT \quad (4.199)$$

$$\boxed{R_{pl} = \frac{-3\beta}{\Delta H_l - \Delta H_0 + \int_{T_l}^{T_0} \Delta cp \cdot dT}} \quad (4.200)$$

Equating equations (4.196) to equation (4.199) leads to:

$$\frac{3\beta}{\Delta H_l - \Delta H_0 + \int_{T_l}^{T_0} \Delta cp \cdot dT} = \frac{A}{\Delta H_l \ln(T_l/T_0)} \quad (4.201)$$

$$\frac{A}{3\beta} \left(\Delta H_l - \Delta H_0 + \int_{T_l}^{T_0} \Delta cp \cdot dT \right) = \Delta H_l \ln(T_l/T_0) \quad (3.202)$$

$$\frac{A}{3\beta} \left(\int_{T_l}^{T_0} \Delta cp \cdot dT - \Delta H_0 \right) = \Delta H_l \left(\ln(T_l/T_0) - \frac{A}{3\beta} \right) \quad (4.203)$$

$$\boxed{\Delta H_l = \frac{A \int_{T_l}^{T_0} \Delta cp \cdot dT - \Delta H_0}{3\beta \ln(T_l/T_0) - \frac{A}{3\beta}}} \quad (4.204)$$

Again, the integration between T_0 and $T_i (=T_0+i\Delta T)$ leads to:

$$\int_{T_0}^{T_i} \frac{\Delta H}{T} dT = \sum_{j=1}^{i-1} \Delta H_j \ln(T_j/T_{j-1}) + \Delta H_i \ln(T_i/T_{i-1}) = - \frac{A}{R_{pi}} \quad (4.205)$$

$$R_{pi} = \frac{-A}{\int_{T_0}^{T_i} \frac{\Delta H}{T} dT = \sum_{j=1}^{i-1} \Delta H_j \ln(T_j/T_{j-1}) + \Delta H_i \ln(T_i/T_{i-1})} \quad (4.206)$$

But, again equation (4.115) can be remembered:

$$\Delta H_i = \Delta H_0 - \frac{3\beta}{R_i} - \int_{T_i}^{T_0} \Delta cp \cdot dT \quad (4.207)$$

$$\frac{3\beta}{R_i} = \Delta H_0 - \Delta H_i - \int_{T_i}^{T_0} \Delta cp \cdot dT \quad (4.208)$$

$$R_{pi} = \frac{-3\beta}{\Delta H_i - \Delta H_0 + \int_{T_i}^{T_0} \Delta cp \cdot dT} \quad (4.209)$$

Equatin equations (4.205) and (4.208) leads to:

$$\frac{A}{\sum_{j=1}^{i-1} \Delta H_j \ln(T_j/T_{j-1}) + \Delta H_i \ln(T_i/T_{i-1})} = \frac{3\beta}{\Delta H_i - \Delta H_0 + \int_{T_i}^{T_0} \Delta cp \cdot dT} \quad (4.210)$$

$$\frac{\sum_{j=1}^{i-1} \Delta H_j \ln(T_j/T_{j-1}) + \Delta H_i \ln(T_i/T_{i-1})}{A} = \frac{\Delta H_i - \Delta H_0 + \int_{T_i}^{T_0} \Delta cp \cdot dT}{3\beta} \quad (4.211)$$

$$\Delta H_i \left(\ln(T_i/T_{i-1}) - \frac{A}{3\beta} \right) = \frac{A}{3\beta} \left(\int_{T_i}^{T_0} \Delta cp \cdot dT - \Delta H_0 \right) - \sum_{j=1}^{i-1} \Delta H_j \ln(T_j/T_{j-1}) \quad (4.212)$$

And finally:

$$\Delta H_i = \frac{\frac{A}{3\beta} \left(\int_{T_i}^{T_0} \Delta cp \cdot dT - \Delta H_0 \right) - \sum_{j=1}^{i-1} \Delta H_j \ln(T_j/T_{j-1})}{\ln(T_i/T_{i-1}) - \frac{A}{3\beta}} \quad (4.213)$$

where:

$$\int_{T_i}^{T_0} \Delta cp \cdot dT_i = \int_{T_i}^{T_0} [(E - A) + (F - B)T] dT \quad (4.214)$$

$$\int_{T_i}^{T_0} \Delta cp \cdot dT_i = (E - A)(T_0 - T_i) + (F - B)(T_0^2 - T_i^2) \quad (4.215)$$

$$\int_{T_i}^{T_o} \Delta cp \cdot dT = [(E - A) + (T_o + T_i)(F - B)](T_o - T_i) \quad (4.216)$$

$$\int_{T_i}^{T_o} \Delta cp \cdot dT = \Delta cp^* \cdot (T_o - T_i) \quad (4.217)$$

$$\Delta cp^* = (E - A) + (T_o + T_i)(F - B) \quad (4.218)$$

Being A , B , E and F known parameters (see equations (4.126)-(4.127)).

4.6 – Gas porosimetry

4.6.1 – Theoretical considerations

Gas porosimetry methods is based on the capillary condensation principle and on the interaction within the vapor and liquid phase within the pores at the equilibrium [16]. *Figure 4.31* shows an example of the liquid-gas equilibrium inside a cylindrical pore. The liquid wets pore wall with a contact angle ϑ_{lw} . For perfect wetting fluid, the contact angle $\vartheta_{lw}=0$ and the curvature radius of the interface liquid-gas r_p is the same of the pore radius R_p .

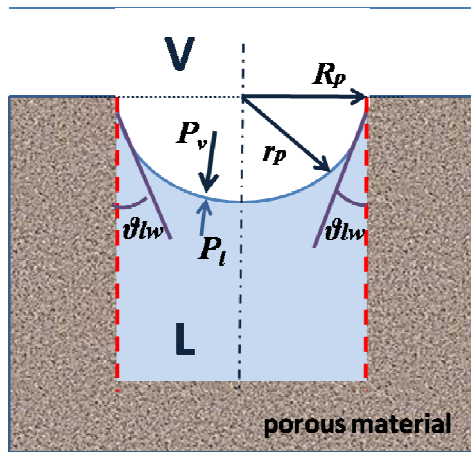


Fig. 4.31: liquid phase (L) at the equilibrium with its vapor phase (V) in a cylindrical pore. R_p =pore radius, ϑ_{lw} =contact angle within liquid and pore wall, r_p =radius of the vapor-liquid interface.



Fig. 4.32: the gas porosimeter Sorptomatic 1990.

The approach for the pore radius determination is based on the Gibbs-Duhem equations the Laplace equation. Gibbs-Duhem equations read:

$$S_l dT_l - V_l dP_l + n_l d\mu_l = 0 \quad (4.96)$$

$$S_v dT_v - V_v dP_v + n_v d\mu_v = 0 \quad (4.97)$$

where S_l, S_v are the entropies of the solid, liquid and gas phase respectively; V_l, V_v are the volumes of the solid, liquid and gas phase respectively; P_l, P_v are the pressures of the solid, liquid and gas phase respectively; μ_l, μ_v are the chemical potentials of the solid, liquid and gas phase respectively; n_l, n_v are the moles of the solid, liquid and gas phase respectively [17-18].

When thermal and chemical equilibrium are attained ($dT_l = dT_v = d\mu_l = d\mu_v = 0$), equation (4.96) and (4.97) become:

$$v_v dP_v = v_l dP_l \quad (4.219)$$

Laplace equation (4.98) tell us that:

$$P_v - P_l = \gamma_{lv} \left(\frac{dA_{lv}}{dV_l} \right) \quad (4.98)$$

thus:

$$dP_v - dP_l = d \left(\frac{2\gamma_{lv}}{r_p} \right) \quad (4.220)$$

Combining equations (4.218) and (4.219), assuming $v_l \ll v_v$ and ideal gas behavior of the gas phase ($v_v = RTP_v$), it is possible to obtain:

$$d \left(\frac{2\gamma_{lv}}{r} \right) = \left(\frac{v_l - v_v}{v_l} \right) dP_v = - \frac{RT}{v_l} \frac{dP_v}{P_v} \quad (4.221)$$

$$d \left(\frac{2\gamma_{lv}}{r} \right) = - \frac{RT}{v_l} \frac{dP_v}{P_v} \quad (4.222)$$

Then, integrating (4.221) within P_v^0 (corresponding to a $r_p = \infty$) and P_v (corresponding to a $r_p = r_p$) we have:

$$\ln \frac{P_v}{P_v^0} = - \frac{2\gamma_{lv} v_l}{r_p RT} \quad (4.223)$$

Equation (4.222) it is known as Kelvin equation and links the vapor pressure P_v , corresponding to a liquid with a molar volume v_l and a interface curve radius r_p , with the vapor pressure P_v^0 of the same liquid on a flat surface. Increasing the gas pressure, capillary condensation occurs starting from the bigger pores.

Most of the probe fluids, including nitrogen, have a contact angle ϑ_{lv} with the pore walls that can be linked to the pore radius R_p by the relation:

$$R_p = r_p \cos \vartheta_{lv} \quad (4.224)$$

Therefore, equation (4.222) becomes:

$$\ln \frac{P_v}{P_v^0} = - \frac{2\gamma_{lv}v_l}{R_p RT} \cos \vartheta_{lv} \quad (4.225)$$

Concluding, once obtained from the Gas porosimetry measurements the distribution of P_v/P_v^0 and knowing the γ_{lv} and v_l of the probe fluid, it is possible to obtain, through the (4.224), pore radius distribution [16].

4.6.2 – Experimental considerations: the BET method

The principle technique for the determination of the specific surface in a microporous material is the gas adsorption method, also called BET method from the family name of the developer: Stephen Brunauer, Paul H. Emmet and Edward Teller [21]. The BET theory is basically an extension of the Langmuir equation on the gas adsorption in layer on a solid surface. The measurements, performed at low temperature (-200°C) and pressure on Sorptomatic 1990 instrument (*Fig. 4.32*), consist in the evaluation of the probe gas volume adsorbed from the solid under evaluation at different pressure lower than the saturation pressure. The theoretical volume of one adsorbed monolayer is calculated by the BET isothermal equation that describe the surface absorption from a vapor phase.

$$\frac{1}{v_a [(P_{sat}/P_{eq}) - 1]} = \frac{c - 1}{v_m c} \left(\frac{P_v}{P_v^0} \right) + \frac{1}{v_m c} \quad (4.226)$$

In the BET isothermal equation, P_v and P_v^0 , equal to the equilibrium pressure into the porous system and the saturation pressure of the vapor at the measurement temperature, v_a is the absorbed vapor quantity (in volume units), v_m is the quantity of vapor adsorbed as a monolayer and c is the BET constant equal to:

$$c = \exp \left(\frac{E_1 - E_L}{RT} \right) \quad (4.227)$$

where E_1 is the adsorption enthalpy of the first layer, interacting with the solid, while E_L is the adsorption enthalpy of the other layers equal to the melting enthalpy.

Considering a diagram where $\frac{1}{v_a [(P_{sat}/P_{eq}) - 1]}$ is reported on the ordinate axis and (P_{eq}/P_{sat}) is reported on the abscissa axis, the BET equation correspond to a linear function from which it is possible, through the x axis intercept (i) and slope (s), obtains the quantity of vapor adsorbed as a monolayer v_m and the BET constant c .

$$v_m = \frac{I}{s + i} \quad (4.228)$$

$$c = I + \frac{S}{i} \quad (4. 229)$$

Using probe molecules with known characteristics it is possible to obtain the surface area of the porous solid [22]. The typical probe molecule is nitrogen (N_2) and its characteristics are listed below:

Molecular weight: 28,01 g/mol

Molecular area: 16,2 Å²

Monolayer thickness: 3,54 Å

References

1. Gunter, H., *NMR Spectroscopy: Basic Principles, Concepts, and Applications in Chemistry*. 2nd ed. 1995: Wiley.
2. Rahman, A.u., *Nuclear Magnetic Resonance: Basic Principles* 1986, Berlin: Springer.
3. Gambaro, A., *Risonanza Magnetica Nucleare: Appunti di Lezione*. 2008, Stan's Library.
4. Rahman, A.u. and M.I. Choudhary, *Solving Problems with NMR Spectroscopy* 1996: Academic Press.
5. Vanhamme, L., et al., *MR spectroscopy quantitation: a review of time-domain methods*. *NMR in Biomedicine*, 2001. **14**(4): p. 233-46.
6. Press, W.H., et al., *Numerical recipes in FORTRAN*. 2nd ed. 1992, Cambridge USA: University Press.
7. Meyvis, T.K.L., S.C. De Smedt, and J. Demeester, *Rheological monitoring of long-term degrading polymer hydrogels*. *J Rheol*, 1999. **43**(4): p. 933-40.
8. Flory, P.J., *Principles of Polymer Chemistry*. 1953, Ithaca, New York: Cornell University Press.
9. Lapasin, R. and S. Pricl, *Rheology of industrial polysaccharides: theory and applications*, ed. B.A. Professional. 1992, London: Chapman And Hall.
10. Flory, P.J., N. Rabjohn, and M.C. Shaffer, *Dependence of elastic properties of vulcanized rubber on the degree of cross linking*. *Journal of Polymer Science*, 1949. **4**(3): p. 225-245.
11. Schurz, J., *Rheology of polymer solutions of the network type*. *J Prog Polym Sci*, 1991. **16**(1): p. 1-53.
12. Brownstein, K.R. and C.E. Tarr, *Importance of classical diffusion in NMR studies of water in biological cells*. *Physical Review A*, 1979. **19**: p. 2446-2452.
13. Brun, M., et al., *A new method for the simultaneous determination of the size and shape of pores: the thermoporometry*. *Thermochim Acta*, 1977. **21**(1): p. 59-88.
14. Zhang, M., et al., *Size-dependent melting point depression of nanostructures: Nanocalorimetric measurements*. *Physical Review B*, 2000. **62**: p. 10548–10557.
15. Yamamoto, T., et al., *Evaluation of porous structure of resorcinol-formaldehyde hydrogels by thermoporometry* *Thermochim Acta*, 2005. **439**(1-2): p. 74-9.
16. Landry, M.R., *Thermoporometry by differential scanning calorimetry: experimental considerations and applications* *Thermochim Acta*, 2005. **433**(1-2): p. 27-50.
17. Ishikiriyama, K. and M. Todoki, *Pore Size Distribution Measurements of Silica Gels by Means of Differential Scanning Calorimetry: II. Thermoporosimetry* *J Colloid Interface Sci*, 1995. **171**(1): p. 103-11.

18. Ishikiriyama, K. and M. Todoki, *Pore Size Distribution (PSD) Measurements of Silica Gels by Means of Differential Scanning Calorimetry: I. Optimization for Determination of PSD* J Colloid Interface Sci, 1995. **171**(1): p. 92-102.
19. Ishikiriyama, K. and m. tadoki, *Evaluation of water in silica pores using differential scanning calorimetry* Thermochem Acta, 1995. **256**(2): p. 213-26.
20. Gerosa, N.P., *Determinazione della distribuzione volumetrica dei cristalli da calorimetria differenziale a scansione*, in *Chemical Engineering*. 2004/2005, Politecnico di Milano: Milan.
21. Brunauer, S., P.H. Emmett, and E. Teller, *Adsorption of gases in multimolecular layers*. J Am Chem Soc, 1938. **60**: p. 309-19.
22. Ishikiriyama, K., et al., *Pore size distribution measurements of polymer hydrogel membranes for artificial kidneys using differential scanning calorimetry*. Thermochem Acta, 1995. **267**: p. 169-80.

5 – Materials and Methods

5.1 – Sample preparation

5.1.1 – Alginate hydrogels

The alginate used in this work is a commercial available sodium salt Protanal™ LF10/60 (purchased from FMCBioPolymer, Drammen, Norway) which have an average molecular weight of 200 kDa and a G/M ratio (in weight) between 65/35 and 75/25. Alginate hydrogels were prepared by dissolving under vigorous stirring in deionised water the dry polymer powder at the concentration of 1%, 2% or 3% respectively (w/v). The polymer solutions were degassed and poured in a Petri discs (the quantity was calculated in order to obtain a thickness of about 1,5 mm). Then, the crosslinking solution was vaporised on it in order to obtain an hydrogel lens (diffusional method). The crosslinking solution consists in 0,05 M CaCl₂ or 0,025 M CuSO₄ to obtain respectively Ca-alginate or Cu-alginate. The reticulating solutions contain also 0,4 M NaCl in order to increase the gel homogeneity. All the membranes were left under crosslinking solution for 20 minutes; a longer reticulation causes the gel edge contraction [1].

Alginate membrane was washed for two minutes in deionised water in order to remove the salts on the surface without removing the cations from the gel system. Finally, the gel lens were cut by a mould cylinders of 35 mm diameter for the rheological measurements. Small cylinder parts were put into the NMR measuring tube. The gels were gently pressed into the tube in order to minimize the empty space but avoiding to cause water exit due to excessive gel squeezing.

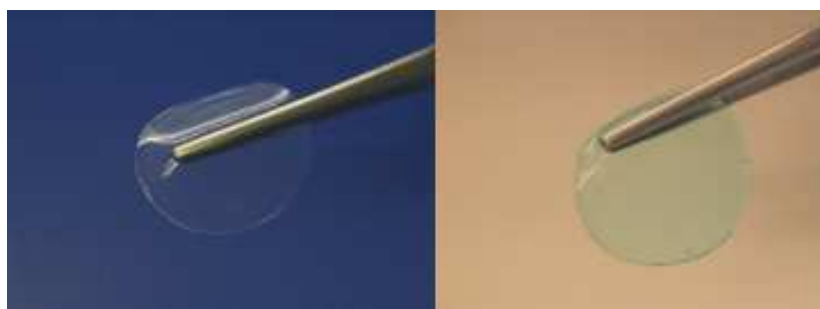


Fig. 5.1: Ca-alginate (left) and Cu-alginate (right) hydrogels cut in 35 mm discs.



Fig. 5.2: dry powder of sodium-alginate Protanal™ LF10/60

5.1.2 – Pluronic™ hydrogel

Pluronic™ F127 (Aldrich Chemistry GmbH, Germany) is a PEO-PPO-PEO blocks copolymer with an average molecular weight of 12,6 kDa, where the PEO blocks are the 70% of the total mass. As previously discussed, the 18% water solution gelation occurs about room temperatures [2]. Therefore, the *cold method* was used as described in literatures for an easy preparation on the Pluronic™ hydrogel [3-4]. A proper quantity of deionised water was put into a beaker at 8°C then, Pluronic™ flakes were added to final concentration of 18% (w/v) under gentle stirring. The surfactant properties of Pluronic™ cause the foam formation therefore, the solution was let to rest at 4°C for 15-18 hours. To obtain the final Pluronic™ hydrogel is sufficient to leave the temperature system to rise above the critical value. For the NMR measurements, the liquid solution was poured into the tube where the gelation occurs obtaining an optimal filling.

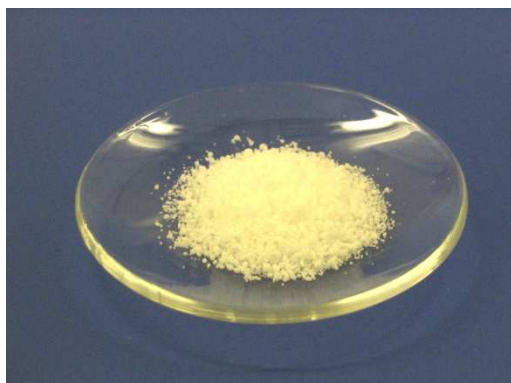


Fig. 5.3: sample of dry Pluronic™ F127 flakes

5.1.3 – Dextran methacrylate hydrogels

5.1.3.1 – Synthesis of dextran methacrylate polymers

The dextran methacrylate polymers were obtained by reaction of D40 or D500 dextrans (derived from *Leuconostoc* genus Gram-positive bacteria and purchased from Sigma-Aldrich GmbH, Germany respectively at 40kDa and 500kDa average chains length) with glycidyl-methacrylate (GMA). 10% (w/v) dextran (D40 or D500) was dissolved in di-methyl-sulfoxide (DMSO) solution then, 2% (w/v) of 4-di-methyl-amino-pyridine (DMAP) was added and finally, GMA was added at 5% or 30% (w/v) depending on the desired degree of methacrylation. The degree of methacrylation was defined as the number of methacrylate dextran monomers on the total number of monomers. The solution was left under stirring at 20°C for at least 48 hours before terminating the reaction by HCl addition followed by dialysis in Visking tube (4°C, 1,5 μ S, cut off 12-14 kDa). Finally, the sample was dried by covering with a desiccant.

5.1.3.2 – Hydrogels preparation

The two hydrogels systems, D40MA5% and D500MA30%, were obtained by crosslinking a solution of D40 5% methacrylate or D500 30% methacrylate respectively. The dextran methacrylate was dissolved in deionised water (5% w/v concentration) and then subjected to the UV irradiation by UV lamp (Helios Italquartz 125 W) for 40 minutes in order to produce crosslinking within the methacrylic groups. No weight loss caused by water evaporation was detected during gelation.

5.1.4 – Hydrogel derived from benzofulvene: the *poly-1b*

The monomer *1b* (BF1-MOEG), constituted by the benzofulvene derivate BF1 and methyl-oligo-ethylene-glycol (MOEG), is the basic units from which the *poly-1b* hydrogel system can be polymerized. This synthesis includes a series of reaction that start from the production of MOEG, continues with the condensation with benzofulvene derivate to produce the *2b* monomer followed by the conversion in *3b* and final in *1b* monomer that is going to polymerize in *poly-1b* [5-7].

5.1.4.1 – Step 1: synthesis of MOEG

A solution containing esaethylene glycol and NaOH was left under vigorous stirring for 2 hours at room temperature. Then, the reagent 5 (*Fig. 5.4*) was added to the solution and left under stirring for another hour before filtration and concentration under vacuum. The residues were purified by flesh chromatography with dimethoxyhexane/n-hexane (7:3) in order to obtain the methyl-oligo-ethylene-glycol (MOEG) as shown in *figure 5.4* (n=9).

5.1.4.2 – Step 2: synthesis of *2b*

The benzofulvene derivate (*Fig. 5.4*) was dissolved in dichloromethane at 10% (w/v) concentration then, the MOEG, the 1-ethyl-3-(3-dimethylaminopropyl) carbodiimide (EDC) and DMAP were added. The system was stirred up to complete dissolution, then the mixture was concentrated under vacuum and the residues purified by flesh chromatography with dimethoxyhexane/petroleum (6:4) in order to obtain the products *2b* as yellow oil about 68% pure.

5.1.4.3 – Step 3: synthesis of *3b*

The compound *2b* was dissolved in a dichloromethane solution then, another solution of 2M $\text{Al}(\text{CH}_3)_3$ in tetrahydrofuran (THF) was added and the mixture was vigorously stirred under nitrogen atmosphere for 30 minutes. The excess of $\text{Al}(\text{CH}_3)_3$ was decomposed by addition of a 30% NaOH solution maintaining the system under nitrogen atmosphere. The mixture was then filtered, dried with sodium sulphate and evaporated under vacuum. The residues were purified by flesh

chromatography with dimethoxyhexane/petroleum (6:4) in order to obtain the products *3b* as uncolored oil 72% pure (Fig. 5.4).

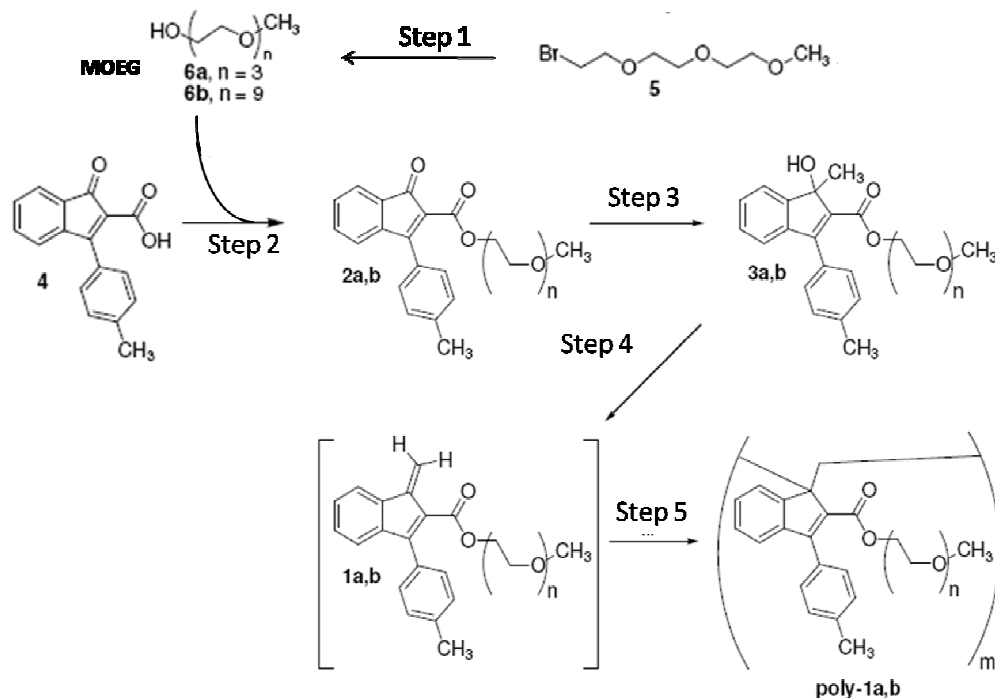


Fig. 5.4: synthetic steps of the benzofulvene derivate *poly-1b*.

5.1.4.4 – Step 4: synthesis of *1b*

The compound *3b* was dissolved in chloroform with a catalytic quantity of *p*-toluensulphonic monohydrate (PTSA) and heated for 2-4 hours. Then, the solution was cooled at room temperature and washed with a saturated solution of NaHCO₃. After drying with sodium sulphate, a solution about 0,1 M of *1b* was obtained. This system was stored under argon atmosphere (Fig. 5.4).

5.1.4.5 – Step 5: *1b* self polymerization

The *1b* benzofulvene solution in chloroform was concentrated under pressure in order to obtain viscous oil and then it was diluted in chloroform and evaporated again. The procedure was repeated 4 times. The residues of *1b* were washed by diethylether and the system was dried under pressure obtaining a solid gum of *poly-1b* with a yield of 92% (Fig. 5.4).

5.1.5 – Pluronic™-alginate hydrogels

The Pluronic™-alginate (18%-2%) polymeric blend was prepared merging the two methodology previously described for the alginate and Pluronic™ systems alone. Firstly the alginate (Protanal™ LF10/60) was dissolved at room temperature in deionised water under vigorous

stirring into a beaker to a final concentration of 2% (w/v). Then, the alginate solution was cooled at 8°C. The Pluronic™ F127 was gradually added under gentle agitation up to final concentration of 18% (w/v). The system was left to set for 12 hours before heating at 35°C in order to obtain the gelation. Then, a solution 0,1 M CuSO₄ and 0,4 M NaCl was vaporized to cover completely the hydrogel. After 20 minutes contact, the hydrogel was cooled to 8°C in order to easily remove the Pluronic™-alginate membrane on the top. The Pluronic™-alginate hydrogel membrane was washed for two minutes in deionised water in order to remove the salts on the surface without removing the cations from the gel system [1]. Finally, the gel lenses were cut by a mould cylinder (35 mm diameter) for the rheological measurements or into small fragments for NMR analysis.

A different type of hydrogel was obtained by omitting the final alginate crosslinking. This polymeric blend was also subjected to the NMR studies and was used to incorporate the liposome-nucleic acids for the biological experiments. Liposomes or liposome-siRNA/DNA complexes, prepared in H₂O, were simply mixed with the polymeric blend aqueous solution (8°C) before the gelation to get a final concentration of 70 µg liposome per ml structured system. This complex concentration has been suggested by literature *ex vivo* studies [8-11].

5.1.6 – Alginate-dextran methacrylate hydrogels

The preparation of this polymeric blend systems consists in three steps: firstly the two polymers were dissolved together in aqueous solution, secondly the alginate was crosslinked by release of Ca bivalent cations (internal settings gelation), and thirdly dextran methacrylate was crosslinked by UV radiation [3-4]. In the first step, alginate (Protanal™ LF10/60) was dissolved in water to a final concentration of 3% (w/v) then, 5% of D40 (5% methacrylate) or D500 (30% methacrylate) was added and stirred to complete dissolution. Finally, a solution of 0,5 M Ca-EGTA was added; the ratio Ca/alginate was 1/1. The EGTA (ethylene-glycol-tetraacetic-acid, Fig. 5.5) is the sequestering agent that complexes and blocks the Ca cations under neutral pH conditions preventing the alginate gelation.

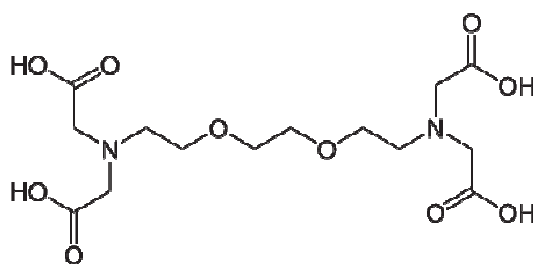


Fig. 5.5: EGTA (ethylene-glycol-tetraacetic) formula.

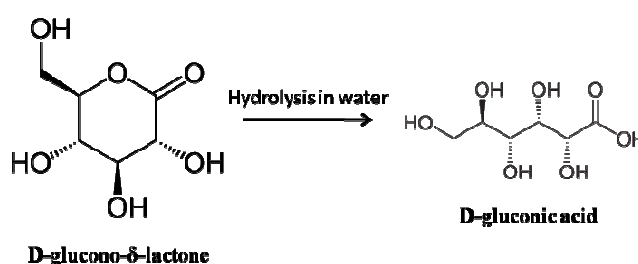


Fig. 5.6: the D-glucono-δ-lactone (GDL) hydrolysis in water produces the D-gluconic acid that decreases the pH.

In the second step, the pH is gradually decreased to 4 by the addition of D-glucono- δ -lactone (GDL, *Fig. 5.6*) that, in aqueous solutions, was slowly hydrolyzed increasing the systems acidity and favoring the homogeneous and gradually release of Ca^{2+} from the EGTA this resulted in the alginate component gelation. After this step the systems were left to set for 24 hours. In the third and last step, the dextran methacrylate (D40MA5% or D500MA30%) was crosslinked by UV irradiation as described above obtaining the final systems that were analysed [12].

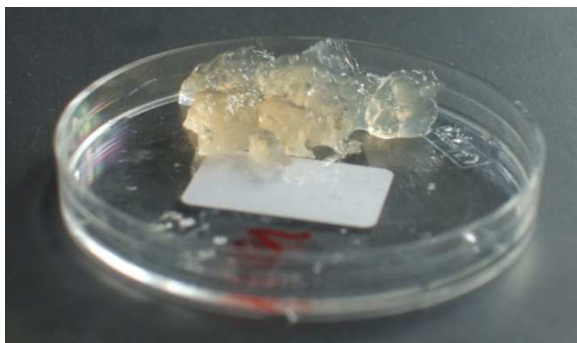


Fig. 5.7: polymeric blend hydrogel of 3% Ca-alginate and 5% D40 5% methacrylate (A3D40MA5%).



Fig. 5.8: polymeric blend hydrogel of 3% Ca-alginate and 5% D500 30% methacrylate (A3D500MA30%).

5.1.7 – Zeolites samples preparation

The zeolites sample, respectively Si60 and Si100 (Merck KGaA, Darmstadt, Germany), was prepared for the DSC analysis by submerging the materials in deionized water and applying vacuum for two hours in order to remove all the air entrapped into the zeolites pore. The resulting systems have all the pores full filled by water and some water outside the pores (see DSC traces).

For the BET Gas porosimetry, the materials were analyzed as it is. About 20 mg of material was used for experimental tests. *Table 5.1* shown the Si60 and Si100 zeolites characteristics declared by the producer.

Zeolite	Mean pores diameter φ (nm)	Density ρ (g/cm³)	Particle size (μm)
Si60	3,3	2,091	60
Si100	7,7	2,126	100

Tab. 5.1: Si60 and Si100 characteristics declared by the producer.

5.2 – Nucleic acid molecules

The nucleic acid used in these studies consists in siRNA (NAM-R) known to have antiproliferative effects [8], and the correspondent DNA duplex (NAM-D), used as siRNA substitute in many experiments. Both the nucleic acids were 21 nucleotides long targeting against

the *cyclin E1* mRNA, position 827-845. 5' fluorescent (FITC) labelled NAM-R and GL2 (a control siRNA targeting *luciferase*) were also used.

The oligonucleotides and the FITC-labelled oligonucleotides were chemically synthesised by Eurogentec, Herstal, Belgium.

NAM	sense strand:	5'- GAA AUC UAU CCU CCA AdTdT
	antisense strand:	5'-U UGG AGG AUA GAU UUC CUC dTdT
GL2	sense strand:	5'- CGU ACG CGG AAU ACU UCG AdTdT
	antisense strand:	5'-U CGA AGU AUU CCG CGU ACG dTdT

5.3 – Liposomes physical characterization

5.3.1 – Liposome-nucleic acid complexes preparation

Cellfectin™ (1 mg/ml, Invitrogen, Milano, Italy) is a 1:1,5 (M/M) liposome formulation of the cationic lipid *N*, *N*^I, *N*^{II}, *N*^{III}-Tetramethyl-*N*, *N*^I, *N*^{II}, *N*^I tetrapalmitylspermine and dioleoyl phosphatidylethanolamine.

Lipofectin™ (1 mg/ml, Invitrogen, Milano, Italy) is 1:1 (w/w) liposome formulation of the cationic lipid *N*-[1-(2,3-dioleoyloxy)propyl]-*n*,*n*,*n*-trimethylammonium chloride and dioleoyl phosphatidylethanolamine.

34 µl of each liposome (Cellfectin™ and Lipofectin™) were mixed in 70 µl of H₂O, PBS or serum free medium for 10 minutes at room temperature. In the case of liposomes containing NAM-R or NAM-D, 15 µg of the nucleic acid molecules were dissolved in 95 µl of H₂O, PBS or serum free medium for 10 minutes at room temperature and subsequently mixed with the liposome solution prepared as above. The ratio (w/w) of liposomes and NAM-R or NAM-D molecules was decided on the basis of the uptake studies and on the anti proliferative effects observed *in vitro* on VSMC [8-9].

5.3.2 – Liposomes particle size

Liposomes and the complexes NAM-R/liposome and NAM-D/liposome were analyzed for their size (diameter) 20 minutes thereafter. Dynamic laser light scattering (Coulter N4 Plus; three independent measurements for each sample were performed, dilution of sample 1:15, temperature: 25°C, detection angle: 90°, medium viscosity: 1 mPa·s) has been used to evaluate liposome diameter in H₂O, in PBS or serum free medium at room temperature.

5.3.3 – Zeta potential evaluation

The zeta potentials of liposomes and NAM-D-liposome complexes were evaluated after preparation, by means of a Zetamaster 408 VA-model ZEM (Malvern Instruments) in H₂O, KCl, PBS and serum free medium. NAM-D osmio staining has been performed, after preparing the complexes either in H₂O or PBS, by exposing the NAM-D/liposomes particles to osmio vapor, for 20 minutes at room temperature. Stained molecules were then visualized by a transmission electronic microscopy (Philips EM 208) equipped with an acquisition system Gatan TVC 673. The liposome lipid bi-layer was evidenced after drying the liposome-NAM-D particles for 30 minutes at room temperature.

5.4 – In vivo studies

5.4.1 – Cell culture

Human vascular smooth muscle cells (VSMC) were purchased from CellSystems Biotechnologies GmbH. The cells were grown in a medium (defined as complete medium) containing one third of Smooth Muscle Cell Basal Medium (Promocell, Heidelberg, Germany), one third Waymouth Medium MB 752/1 and one third of Nutrient Mixture F12 (Invitrogen, Milano, Italy) and supplemented with 1% penicillin/streptomycin (Invitrogen, Milano, Italy) and 15% foetal calf serum (FCS, Euroclone-Celbio, Pero, Italy).

Human umbilical vein cell (HUVEC), a kind gift from Prof Tedesco's lab, University of Trieste, Italy, were cultured in Medium 199, supplemented with Glutamine (200 mM final, Euroclone-Celbio, Pero, Italy), 20% FCS, 1% penicillin/streptomycin, endothelial growth factor (50 µM final concentration) and heparin (100 µM final concentration, Sigma-Aldrich, Milano, Italy). Cells were kept in a humid atmosphere with 5% CO₂ at 37°C.

5.4.2 – Uptake studies

VSMCs and HUVEC were seeded at a density of $3,5 \times 10^3$ and $1,6 \times 10^4$ cells/cm², respectively, in the presence of complete medium. Uptake studies were conducted the day after seeding in the presence of a FITC-NAM-R. The labelled nucleic acid was complexed with either the cationic liposome Cellfectin™ or Lipofectin™ in 200 µl of serum free medium using a w/w ratio of 1:2,3 (FITC-NAM-R/liposome). In VSMCs, uptake studies were also performed preparing the labeled NAM-R/liposomes in the presence of H₂O or Phosphate-Buffered Saline (PBS: NaCl 0,1369 M, KCl 0,0026 M, Na₂HPO₄ 0,0103 M, KH₂PO₄ 0,0017 M, pH 7,4). Subsequently, the

complexes were allowed to form for 20 minutes at room temperature. Afterwards, 1,3 ml of serum free medium was added to the 200 μ l, mixed and applied to the cells previously washed with 3 ml of PBS. Final FITC-NAM-R concentration was of 220 nM. Uptake studies were carried out for two hours at 37°C. Then, transfection medium was removed, cells washed with PBS, trypsinized and re-suspended in 500 μ l of PBS. The number of FITC positive cells (green fluorescence cells expressed as % of total cell population) were then evaluated by flow cytometry (FACSCanto, Becton Dickinson) using the DIVA software.

The same serum free conditions were used to obtain the PHEA (α,β -poly(N-2-hydroxyethyl) D,L-aspartamide) derivates polyplexes with GL2 siRNA. The siRNA/polymer w/w ratio was 1:2,5 and 1:2 for PHEA-spermine (Phea-Sp) or 1:6 for PHEA-spermine-butyric acid (Phea-Sp-C4), PHEA-diethylenetriamine (Phea-Deta) and PHEA-2-aminoethylcarbamate (Phea-Eda)

5.4.3 – Release studies of FITC-NAM-R/Cellfectin™ complexes

To study the release of the complexes FITC-NAM-R/Cellfectin™ from the Pluronic™-alginate blend, the complexes, prepared as above described, were mixed with increasing concentration of the polymeric blend (from 0% to 20% of Pluronic™ and 2% alginate). The polymeric blend containing the complexes (1,5 ml) was then over-layered on PBS washed VSMCs, seeded at a density of 3.5×10^3 cells/cm² the day before in 5 cm diameter plates. After four hours at 37°C, the polymeric blend was removed, VSMCs washed by PBS and then fixed by 4% para-formaldehyde in PBS for 1 hour. After a PBS washing step, VSMCs were mounted with mounting medium for fluorescence with DAPI (Vector Laboratories). VSMCs were viewed by an inverted microscope (Nikon Instruments) and phase contrast/fluorescence images acquired. For each treatment, green fluorescent cells were counted in 25 different microscopic fields.

5.4.4 – Statistical analysis

P values were calculated using the Anova one-factorial variance analysis program, led by MS Excel. P values < 0,05 were considered statistically significant.

References

1. Draget, K.I., et al., *Ionic and acid gel formation of epimerased alginates; the effect of AlgE4*. Int J Biol Macromol, 2000. **27**: p. 117-22.
2. Lau, B.K., et al., *Micellization to gelation of a triblock copolymer in water: Thermoreversibility and scaling*. J. Polym. Sci. Part B, 2004. **42**: p. 2014-25.

3. Draget, K.I., G. Skjåk-Bræk, and O. Smidsrød, *Alginate based new materials*. *J Biol Macromol*, 1997. **21**: p. 47-55.
4. Schmolka, I.R., *A review of block polymer surfactants*. *J Am Oil Chem Soc*, 1977. **54**: p. 110-6.
5. Cappelli, A., et al., *Synthesis and Spontaneous Polymerization of Oligo(ethylene glycol)-Conjugated Benzofulvene Macromonomers. A Polymer Brush Forming a Physical Hydrogel*. *Macromolecules*, 2009. **42**(7): p. 2368–78.
6. Cappelli, A., et al., *A nanocomposite material formed by benzofulvene polymer nanoparticles loaded with a potent 5-HT₃ receptor antagonist (CR3124)*. *J Nanopart Res*, 2009.
7. Cappelli, A., et al., *Further Studies on Imidazo[4,5-*b*]pyridine AT₁ Angiotensin II Receptor Antagonists. Effects of the Transformation of the 4-Phenylquinoline Backbone into 4-Phenylisoquinolinone or 1-Phenylindene Scaffolds*. *J Med Chem*, 2006. **26**(22): p. 6451–64.
8. Grassi, G., et al. *siRNAs targetted against cyclin E1 and E2F1 down regulate coronary smooth muscle cells proliferation thus showing their potential use in the prevention of in-stent restenosis*. in *13th annual congress of the European Society of Gene Therapy*. 2005. Prague.
9. Grassi, G., et al., *Temperature-sensitive hydrogels: potential therapeutic applications*. *American J Drug Del*, 2005. **3**: p. 239-51.
10. Grassi, G., et al., *Selection and characterization of active hammerhead ribozymes targeted against cyclin E and E2F1 full-length mRNA*. *Antisense Nucleic Acid Drug Dev*, 2001. **11**(5): p. 271-87.
11. Grassi, G., et al., *Hammerhead ribozymes targeted against cyclin E and E2F1 cooperate to down-regulate coronary smooth muscle cell proliferation*. *J Gene Med*, 2005. **7**(9): p. 1223-34.
12. Stokke, B.T., et al., *Small-Angle X-ray Scattering and Rheological Characterization of Alginate Gels. 1. Ca-Alginate Gels*. *Macromolecules*, 2000. **33**: p. 1853-63.

6 – Results and Discussions

6.1 – Introduction

In this section, the experimental results obtained from the analysis performed on different material are displayed and discussed. The final target is the characterization of the structural properties of polymeric hydrogels and the evaluation of the possible application in systems for controlled release of drugs or other biomedical applications. In the first step of the studies, it was evaluated the reliability of the cryoporometric method compared to gas porosimetric method and the possible applications in the hydrogel systems pores characterization. Then, continuing in the research path of an ideal system for the final applications, whatever they are, the second step concerned the study of the effects of compositional parameters by using information from Rheology, low field NMR and Cryoporometry. This phase allowed to improve the knowledge about the structural properties of the single component that could be applied in the final system. The third step was related to the construction and properties analysis of blend polymeric systems on the base of the previous results.

The final experimental phase was represented by testing of the choice system on a cellular model representing a possible application of NABDs release. In particular, the NABDs delivery system was tested for the siRNA uptake and release on vascular smooth muscle cells (VSMC) and human umbilical vein cell (HUVEC) as model.

6.2 – Zeolites Gas porosimetry and Cryoporometry studies

In order to evaluate the availability of the cryoporometric methodology for the shape and pores size analysis in systems, as the gels, where the traditional techniques can not be applied, the internal structure characterization of zeolite materials was studied comparing the results of Gas porosimetry (BET method with N₂) and Cryoporometry. The data obtained from both methods were compared using, as reference, the results available on literature. The samples used during these studies were two commercial available zeolites Si60 and Si100. The characteristics declared by the producer are listed in *table 6.1*.

Zeolite	Mean pores diameter φ (nm)	Density ρ (g/cm ³)	Particle size (μ m)
Si60	3,3	2,091	60
Si100	7,7	2,126	100

Tab. 6.1: Si60 and Si100 characteristics declared by the producer.

As results from the DSC trace (*Fig. 6.1*), the two zeolites present water inside and outside the pores system. Indeed, in both case, it was detected a peak of water melting at 0°C related to the free water and another one, below 0°C, referring to water inside nanopores. The *table 6.2*, instead, reports the resulting data obtained by BET Gas porosimetry

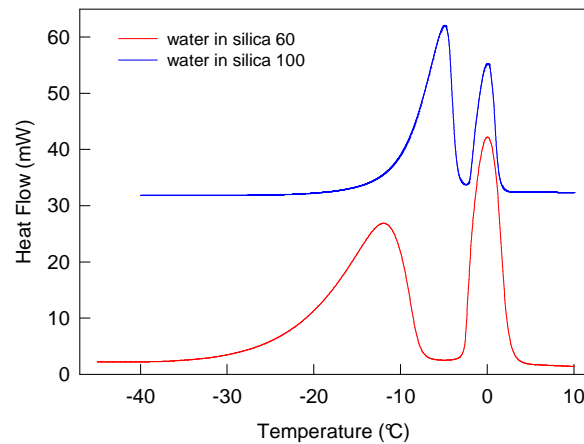


Fig. 6.1: DSC traces for zeolites Si60 and Si100. In both DSC traces is shown the presence of two type of water: structured inside the pores ($T < 0^\circ\text{C}$) and free water ($T = 0^\circ\text{C}$).

The pores radius distributions as function of the probability obtained by Gas porosimetry and Cryoporometry assuming a spherical ($z=3$) or cylindrical ($z=2$) pores geometry are reported in *figures 6.2* and *6.3* respectively for Si60 and Si100. From the figure is clear the matching between the two methodology.

Zeolite	Si60	Si100
Wet sample weight (mg)	20,093	23,981
Dry sample weight (mg)	10,477	10,264
Water in sample (mg)	9,616	13,717
Initial and final P_v/P_v^0	0,0486 – 0,326	0,0954 – 0,311
Monolayer specific volume v_m (cm ³ /g)	88,83	68,43
Specific surface area (m ² /g)	386,68	297,88
BET constant c	122,95	323,51
Pore specific volume v_p (cm ³ /g)	0,78	1,16

Tab. 6.2: BET gas porosimerty results.

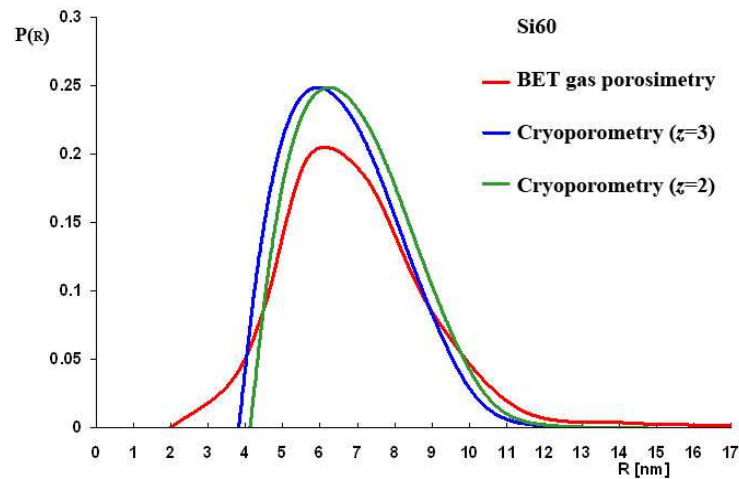


Fig. 6.2: Pores radius distributions for Si60 obtained by BET Gas porosimetry (red) and Cryoporometry assuming spherical pores geometry ($z=3$, blue) or cylindrical pores geometry ($z=2$, green).

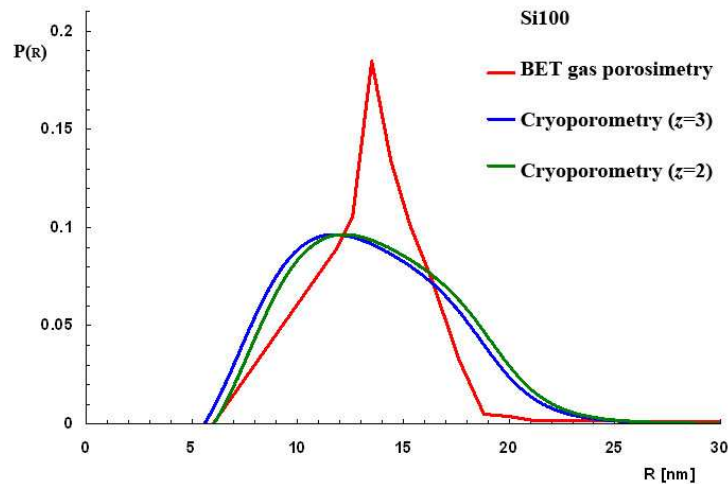


Fig. 6.3: Pores radius distributions for Si100 obtained by BET Gas porosimetry (red) and Cryoporometry assuming spherical pores geometry ($z=3$, blue) or cylindrical pores geometry ($z=2$, green).

It can be seen that, Si100 is characterized by bigger pores radii than those of Si60. In addition, only small differences occur within the results obtained considering spherical or cylindrical pores geometry. That is expected because the sample contains an excess of water compared to the total water inside the pores and, in such that condition, the spherical model and cylindrical model are equivalent. The difference instead, regarding the calculated value of the non-freezable water layer thickness β .

Using these data, the radius deviation (σ) of the spherical and cylindrical pore geometry at the same probability was evaluated by the following function:

$$\sigma = \frac{\sqrt{\sum_i (Rp_{i,N2} - Rp_{i,Crio})^2}}{N_i} \quad (6.1)$$

where $R_{p_i,N2}$ is the pore radius calculate by BET Gas porosimetry, $R_{p_i,Crio}$ is the pore radius calculated by Cryoporometry, N_i is the number of data. In order to appreciate the deviation within the two methodology, in *figure 6.4* and *6.5* are reported the values of the radius calculated by Cryoporometry in a spherical and cylindrical geometry as function of the radius obtained by BET Gas porosimetry. The calculated deviation from the BET Gas porosimetry in the Si60 correspond to 0,4995 and 0,5027 for the spherical and cylindrical geometry respectively while, in the Si100, the deviation is 1,025 and 1,139 for the spherical and cylindrical geometry respectively. Therefore, in both the zeolites, the spherical geometry better represent the porous structure.

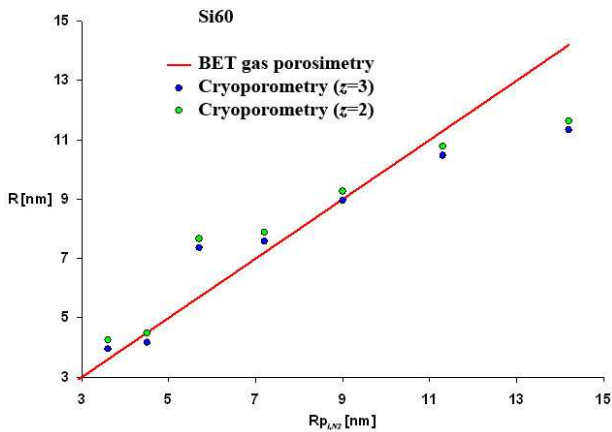


Fig. 6.4: Si60 Cryoporometry radius deviation from BET Gas porosimetry (red line) considering spherical (blue dots) or cylindrical (green dots) pores geometry.

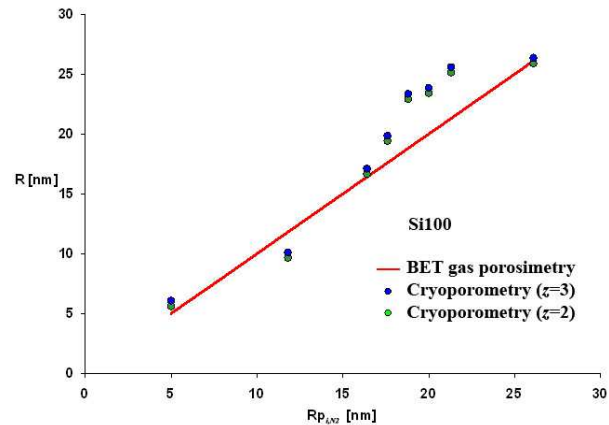


Fig. 6.5: Si100 Cryoporometry radius deviation from BET Gas porosimetry (red line) considering spherical (blue dots) or cylindrical (green dots) pores geometry.

The non-freezable layer thickness β inside the pores was determined for both systems by an iterative procedure and the results were compared with the data published in literature (*Tab. 6.3*) [1]. In both considered zeolites, the obtained values match with the published values.

Sample	β_m (nm)			β_r (nm)		
	$z = 2.0$	$z = 2.5$	$z = 3.0$	$z = 2.0$	$z = 2.5$	$z = 3.0$
SA18	0.55	0.48	0.42	0.63	0.54	0.47
SA27	0.54	0.45	0.39	0.83	0.68	0.58
SA75	0.62	0.50	0.42	1.00	0.81	0.69
SW27	0.48	0.41	0.35	0.56	0.47	0.40
SW60	0.51	0.42	0.35	1.07	0.87	0.73
SZ29	0.67	0.56	0.48	0.89	0.73	0.62
SC31	0.73	0.61	0.52	1.01	0.82	0.70
SC68	0.68	0.55	0.47	0.98	0.79	0.67
SC203	0.93	0.75	0.62	1.28	1.03	0.87
SG150	1.02	0.82	0.68	1.59	1.29	1.08
SG208	2.20	1.76	1.47	2.66	2.15	1.80
SG291	1.80	1.45	1.20	2.78	2.24	1.88

Tab. 6.3: comparison between literature data (left) [1] and experimental data (right).

Calculated β layer thickness (nm)		
Si60	spherical ($z=3$)	0,56
	cylindrical ($z=2$)	0,86
Si100	spherical ($z=3$)	0,85
	cylindrical ($z=2$)	1,31

Concluding, the radius distribution obtained by Cryoporometry and studies on the water melting DSC trace, results to be in agreement with the results obtained with the BET nitrogen Gas

porosimetry. Therefore, Cryoporometry can be reliable a reasonable method for the determination of pores size distribution.

6.3 – Alginate based hydrogels

Experimental evidence allows identifying in the alginates hydrogels a material suitable for the stent coating applications. In particular, the alginate can be used for the external shielding in order to protect an inner layer of polymeric matrix, loading the active principle, from the blood flow erosion. Moreover, the alginate coating prevents the active molecules release into the vascular lumen with consequent loosing. The advantages of this type of material derives from the network capability to resist at high shear stress [2].

The following sections show the characterization of alginate hydrogels at different concentration and temperatures. The influence of the crosslinker (bivalent cations) was also taken into account for the determination of the final hydrogels characteristics comparing the effects of Ca^{2+} and Cu^{2+} . In physiological environments, the copper systems are preferred because the calcium can interfere with biological process regulations [3-4].

6.3.1 – 1% alginate hydrogels

This section shows the characterization obtained from rheological and LF-NMR analysis of two alginate based hydrogels (Protanal™ LF10/60) crosslinked in 1% by weight polymer solutions using CaCl_2 or CuSO_4 as crosslinkeng agents (0,05M and 0,025M; 1%Ca-Alg and 1%Cu-Alg samples). The NaCl concentration is maintained constant at 0,4M for both the samples.

6.3.1.1 – Macroscopic properties characterizations by Rheology

The experimental G' and G'' curves obtained in the stress sweep test (SS, *Fig. 6.6*) performed at 25°C, have the same characteristics aspect. G' and G'' remain practically constant under applied stress variations (τ) up to a top limit value (critical stress). At this stage, the systems undergo collapse with a rapidly storage modulus falling while, the loss modulus, shows a climbing phase to a maximum values followed by a decrease. Above this stress value irreversible and the testing conditions are outside the linear viscoelastic region. For both the samples (1%Ca-Alg and 1%Cu-Alg) the viscoelastic region can be located at shear stress (τ) values lower than 10Pa, corresponding to a critical deformation γ_0 around 0,7%.

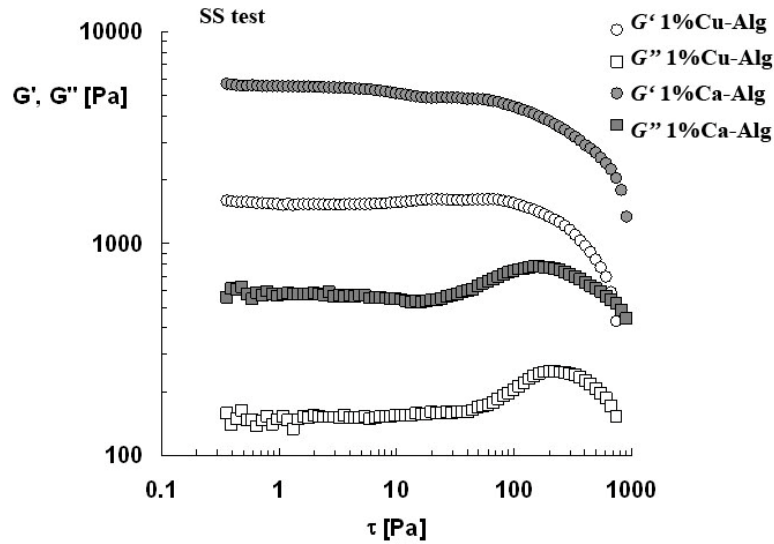


Fig. 6.6: Stress sweep tests for 1%Ca-ALg and 1%Cu-ALg performed at 25°C.

Based on the SS tests, the frequency sweep tests (FS) were performed using a constant stress τ of 3Pa at the temperature of 25°C. The mechanical spectra of both the samples show a strong gel trend with a clear prevalence of the elastic behavior (*Fig. 6.7*). More deeply, the G' and G'' values in the alginate crosslinked by copper cations (1%Cu-ALg), are three times lower than the alginate crosslinked by calcium cations (1%Ca-ALg). The data numerical analysis was performed with the generalized Maxwell model at 5 and 4 elements respectively for copper-alginate and calcium-alginate. As shown in *figure 6.7* (continues line) the model fits properly with the experimental data (squares and dots).

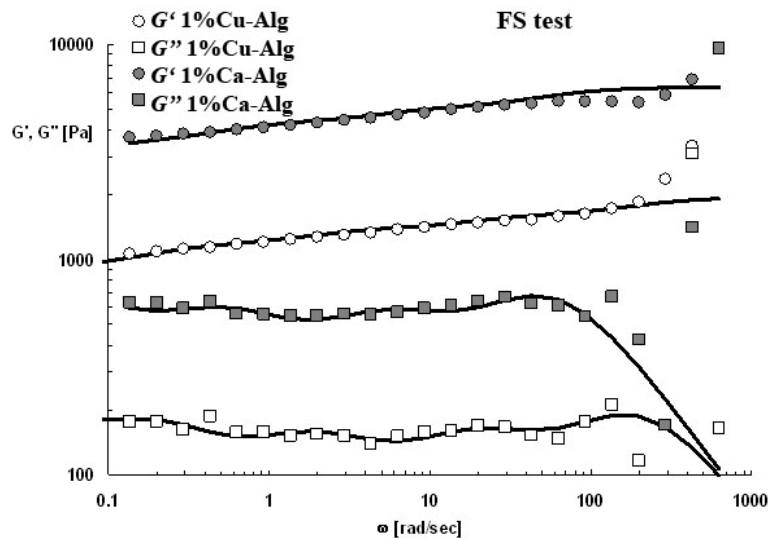


Fig. 6.7: mechanical spectra (FS test) of 1%Ca-ALg and 1%Cu-ALg performed at 25°C. The continues lines represent the generalized Maxwell model best fitting.

On the base of the generalized Maxwell model fitting to experimental data it was possible getting the mechanical relaxation spectra shown in *figure 6.8*. Here the relaxation time of each element (λ_k) is reported versus the respective elastic constant (g_k). In this figure it is clear the higher

values of g_k for the Ca-alginate system compared to the Cu-alginate one, indication of the higher material structuring degree.

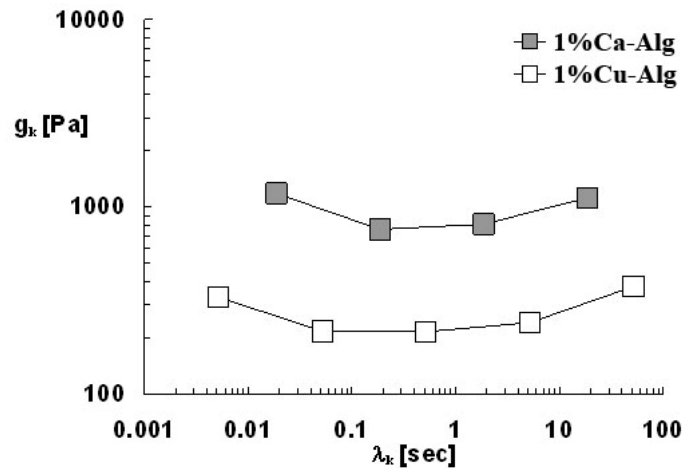


Fig. 6.8: mechanical relaxation spectra of 1%Ca-Alg and 1%Cu-Alg performed at 25°C, obtained by generalized Maxwell model fittings.

The hydrogel shear modulus G was assumed as the sum of all g_k . On the basis of Flory theory for gels [5] and the equivalent network theory [1] (see sections 4.3 and 4.4), from G it was possible estimating the crosslink density ρ_x and then, the mean mesh size ϕ (or mean pores diameter) of the polymeric network.

	crosslink density ρ_x (mol/cm ³)	mean mesh size ϕ (nm)
1%Ca-Alg	$2,5 \times 10^{-6}$	10,8
1%Cu-Alg	$7,9 \times 10^{-7}$	15,9

Tab. 6.4.

6.3.1.2 – Microscopic characterizations by low field NMR

In order to obtain more information regarding the alginates hydrogels structure, the samples was analysed by low field NMR. The microscopic characterization obtained from the ¹H protons relaxation, shows the aggregations state of the components containing hydrogen: water and polymer. Merging the rheological and NMR information, it was possible estimating the mesh diameters distribution as function of the occurrences probability [6-7].

A T_2 transversal relaxation times analysis were performed at 25°C resulting in the T_2 relaxation spectra displayed in *figures 6.9* and *6.10* respectively for 1%Ca-Alg and 1%Cu-Alg. In the first case, the T_2 distribution peaks identified three aggregation states related to the protons in the calcium-alginate gel while, in the copper-alginate gel four aggregation states were identified (four peaks). The difference is probably caused by the weaker structure of the Cu-Alg gel compared

to the Ca-Alg gel. The trend of ^1H proton T_2 spectres suggests that the first two peaks in both systems belong to the water effectively structured into the nanopores.

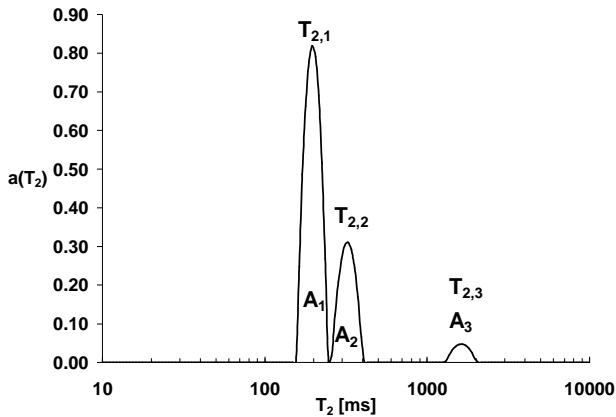


Fig. 6.9: 1%Ca-Alg ^1H proton T_2 distribution spectra obtained by LF-NMR at 25°C.

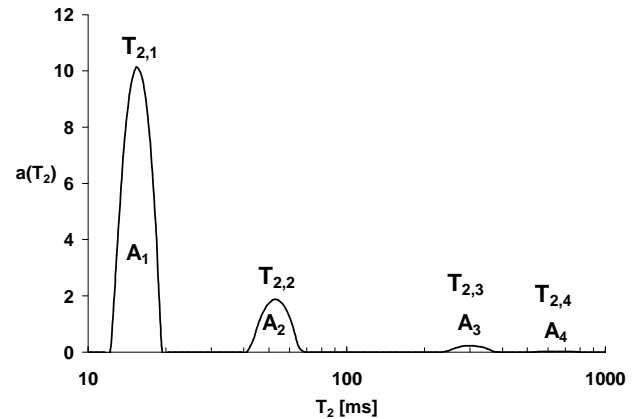


Fig. 6.10: 1%Cu-Alg ^1H proton T_2 distribution spectra obtained by LF-NMR at 25°C.

In order to verify this hypothesis, the relaxation behaviour of both samples were collected at different temperatures (10°C, 25°C and 40°C) then, each peak area (%) was plotted as function of its mean relaxation time $T_{2,i}$ obtaining a trend related to the temperature increase. The results are shown in *figures 6.11* and *6.12* respectively for 1%Ca-Alg and 1%Cu-Alg. In the first two peaks, the relaxation time does not vary significantly with the temperature for both systems while, in last one (or last two for 1%Cu-Alg), $T_{2,i}$ increase is significantly bigger than the standard deviation associated to $T_{2,i}$ at 25°C. This result supports the hypothesis that the peaks 1 and 2 represent the water inside the gel mesh because the thermal energy is not sufficient to interfering significantly with the molecular linkage between water and polymeric chains. On the opposite, peak 3 of 1%Ca-Alg, and peaks 3 and 4 in 1%Cu-Alg, represents the water not interacting or weakly interacting with the polymer indeed, the thermal energy effect is predominant on the molecular bond resistance between polymer and water.

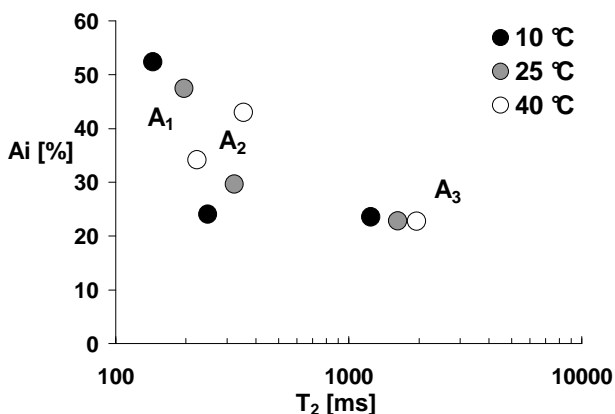


Fig. 6.11: 1%Ca-Alg mean relaxation time $T_{2,i}$ trend and respective relative area A_i at different temperature.

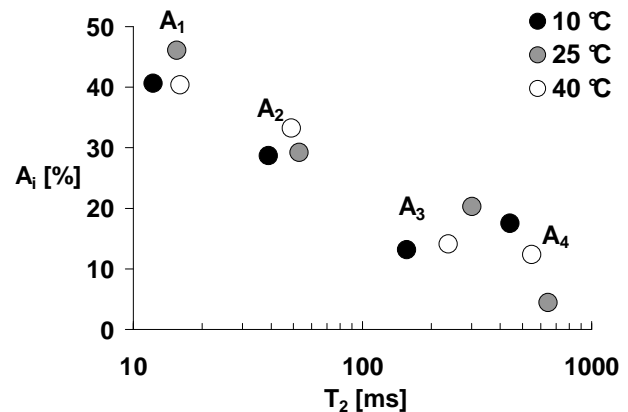


Fig. 6.12: 1%Cu-Alg mean relaxation time $T_{2,i}$ trend and respective relative area A_i at different temperature.

Another evidence supporting the initial hypothesis derives from the comparison among the theoretical peaks area and the experimental one. Indeed, remembering that the peak area A_i is proportional to the number of hydrogen relaxing at the peak mean relaxation time $T_{2,i}$, it is possible to compare the theoretical area values with the experimental ones. The theoretical areas were calculated as:

$$\text{Theoretical relative H}_2\text{O area: } 100 \cdot \frac{\frac{We_{H_2O} \cdot N_{H_2O}}{M_{H_2O}}}{\frac{We_{H_2O} \cdot N_{H_2O}}{M_{H_2O}} + \frac{We_{Alg} \cdot N_{Alg}}{M_{Alg}}} = 99,63\%$$

$$\text{Theoretical relative alginate area: } 100 \cdot \frac{\frac{We_{Alg} \cdot N_{Alg}}{M_{Alg}}}{\frac{We_{H_2O} \cdot N_{H_2O}}{M_{H_2O}} + \frac{We_{Alg} \cdot N_{Alg}}{M_{Alg}}} = 0,37\%$$

where, M_{H_2O} and M_{Alg} are the molecular weight of water and alginate monomer respectively, We_{H_2O} and We_{Alg} are the weight of water and alginate in the gel, N_{H_2O} and N_{Alg} are the number of protons in the water molecule and polymer monomer. The experimental peaks areas A_i values and the correspondent mean relaxation time $T_{2,i}$, are displayed in *Table 6.5* (1%Ca-Alg) and *Table 6.6* (1%Cu-Alg). The data were obtained from the NMR experiments performed at 25°C. As in both samples, peaks 1 and 2 together representing more than 75% of the total area therefore, it is reasonable that they represent the water inside the hydrogels meshes [8]. The rest can be considered water leaked from the gel system during the loading in the measuring system. Due to the small amount of the polymer hydrogens (0,47%), they cannot be discriminated by the NMR analysis. Accordingly, their effect is embedded in the peak corresponding to the smallest relaxation time. As this peak area (47,5% or 46,0%) is nearly higher than that competing to the alginate ^1H , we conclude that the first peak represents water that is trapped in the polymeric network.

Peak	$T_{2,i}$ (ms)	Relative A_i (%)
1	196,4	47,5
2	322,4	29,7
3	1622,3	22,8

Tab. 6.5: 1%Ca-Alg hydrogel.

Peak	$T_{2,i}$ (ms)	Relative A_i (%)
1	15,5	46,0
2	52,9	29,2
3	300,7	20,3
4	646,0	4,4

Tab. 6.6: 1%Cu-Alg hydrogel.

Knowing, for both samples, the correspondence of peaks 1 and 2 with the water entrapped into the polymeric mesh, it was possible to investigate deeply the inner polymeric network structure. Indeed, peaks distribution is strictly related to the mesh distribution [6]. The mesh size distribution was estimated considering equation (4.79) (chapter 4.4). That enables the estimation of the mean mesh size φ (or mean mesh diameter) from the crosslink density ρ_x . The calculation of the constant k linking the mean relaxation time \bar{T}_2 with φ (Tab. 6.7). Finally made possible the conversion of the relaxation time distribution into mesh size distribution.

	k (ms/nm)	\bar{T}_2 (ms)
1%Ca-Alg	23,1	248,1
1%Cu-Alg	1,9	30,4

Tab. 6.7.

In particular diameters assigned an occurrence probability $P(\varphi)$. The probability is the ratio between the local area of the specific pores and the total peaks area. The 1%Ca-Alg and 1%Cu-Alg pores size distribution are compared *figure 6.13*. The figure evidence a bimodal distribution for both the samples. In particular, a perfect overlapping is present for the first peaks of Ca-alginate and Cu-alginate where the diameters are centred around 8 nm and extending from 6 to 10 nm. The second peak represents a difference within Ca-alginate and Cu-alginate. The Ca-alginate peak spans from 10 to 18 nm and is centred on 14 nm while, the Cu-alginate peak present a broad range (22-36 nm) and is centred on 29 nm.

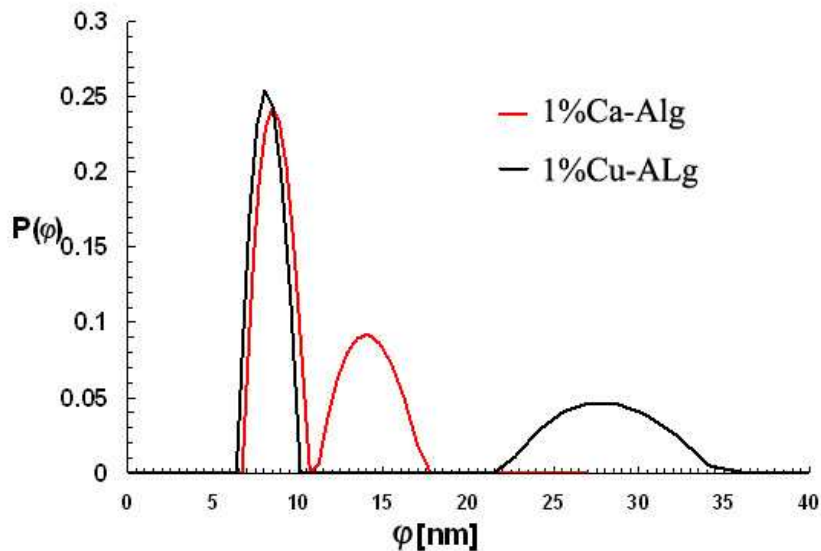


Fig. 6.13: 1%Ca-Alg and 1%Cu-Alg mesh size distribution (mesh diameters) expressed as probability $P(\varphi)$.

6.3.2 – 2% alginate hydrogels

In this section displays the rheological and LF-NMR data obtained from alginate hydrogels (Protanal™ LF10/60) crosslinked in a 2% solution. Similarly to the previous 1% alginate hydrogels, the influence of calcium or copper cations as reticulating agents were considered but more attention was placed regarding the systems behaviour at different temperatures. Cryoporometry measurements were also performed in order to compare the results with the NMR-rheology data.

6.3.2.1 – Macroscopic properties characterizations by rheological studies

The hydrogels samples, 2%Ca-Alg and 2%Cu-Alg, were prepared as described in the previous sections and placed on the measuring systems. First of all was necessary to establishing the viscoelastic limits of the systems by stress sweep tests.

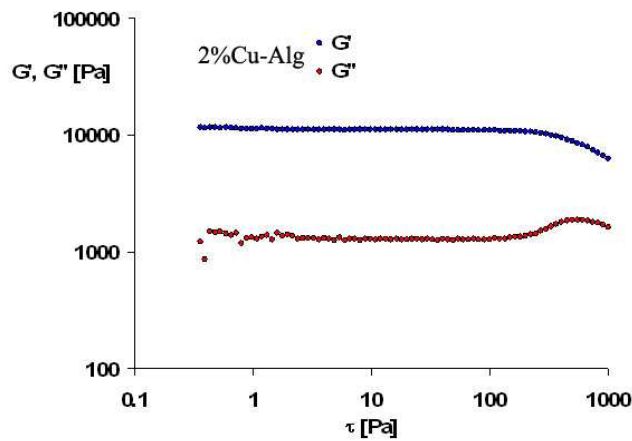


Fig. 6.14: 2%Cu-Alg SS curves at 25°C

The SS tests allow the evaluations of the critical strains and deformations of the viscoelastic region of both the systems under analysis. The tests were performed at different temperatures (10°C, 25°C and 40°C) in order to evaluate the influence of temperature (data not shown). The G' and G'' profiles as function of the applied stress (τ) for the 2%Cu-Alg at 25°C, and reported in *figure 6.14* as an example. SS tests show a viscoelastic conditions for stress lower than 10 Pa, correspondent to a critical deformation of 0,1%.

On this basis, the frequency sweep tests were conducted using a stress of 3 Pa, within the viscoelastic conditions. *Figure 6.15* compare the storage and loss modules G' and G'' of 2%Ca-Alg and 2%Cu-Alg as function of the pulsation ω at 25°C. In both samples G' and G'' are parallel and no significant differences is evidenced within the two samples even if the 2%Ca-Alg loss modulus is lower than 2%Cu-Alg. Moreover, because G' is one order of magnitude higher than G'' , the elastic behaviour is prevalent on the viscous one, (this is typical for strong gels).

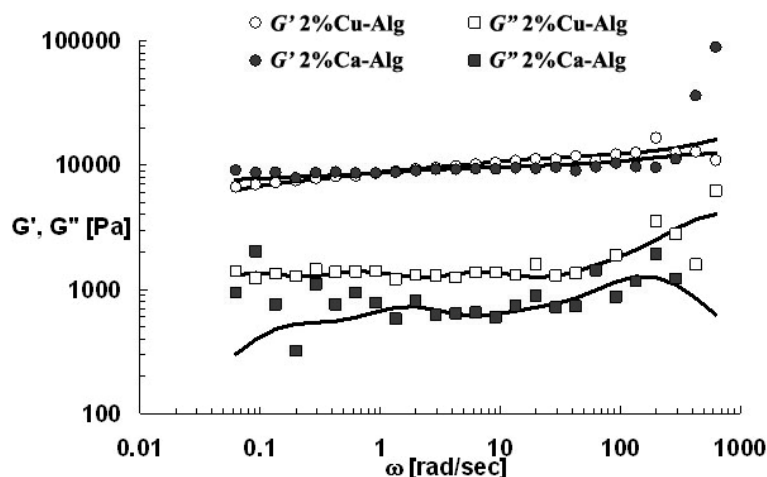


Fig. 6.15: 2%Ca-Alg and 2%Cu-Alg mechanical spectra (FS curves) at 25°C. Continue lines represent generalized Maxwell model best fitting.

The thermal effects were evaluated at 10°C, 25°C and 40°C in order to obtain information related to the structure resistance and consistency under different physical conditions. The comparison of the mechanical spectra obtained at different temperatures and the best fitting with the generalized Maxwell model are displayed in *figures 6.16* and *6.17*, respectively, for 2%Ca-Alg and 2%Cu-Alg. This figure suggests, for the 2% alginate hydrogels, a strong resistance of the system crosslinked by Cu cations to the thermal effects. Indeed the storage and loss modules are practically invariant in the tested temperatures range. On the contrary, the alginate system crosslinked by Ca cations, shows a reduction of the mechanical moduli with the temperature increase.

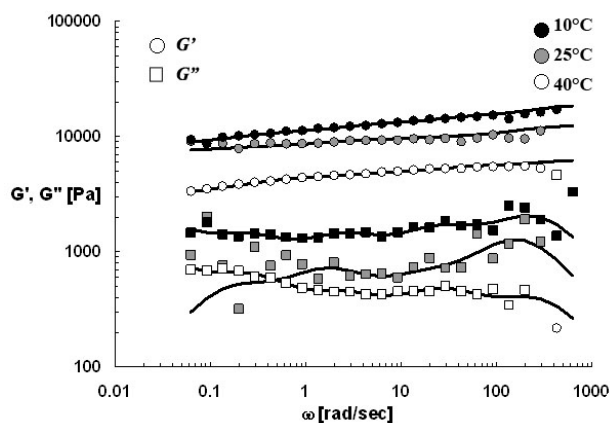


Fig. 6.16: 2%Ca-Alg mechanical spectra at different temperatures. The continue lines represent the generalized Maxwell model best fitting.

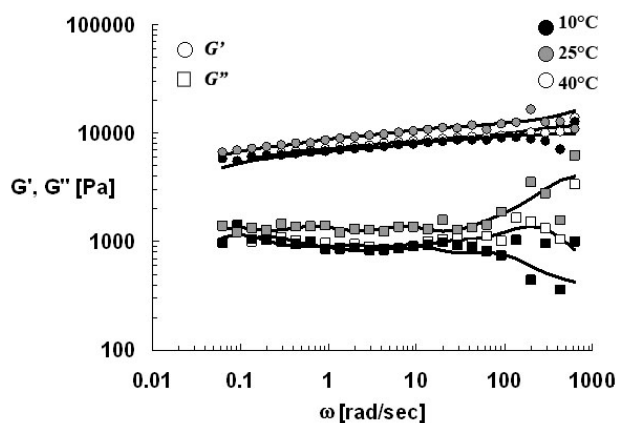


Fig. 6.16: 2%Cu-Alg mechanical spectra at different temperatures. The continue lines represent the generalized Maxwell model best fitting.

The experimental data were satisfactory fitted with the generalized Maxwell model with 4 or 5 parallel elements (*Fig.6.16* and *6.17*) and the mechanical relaxation spectra were plotted (*Fig. 6.18* and *6.19*) evidencing the temperature effects on the two systems.

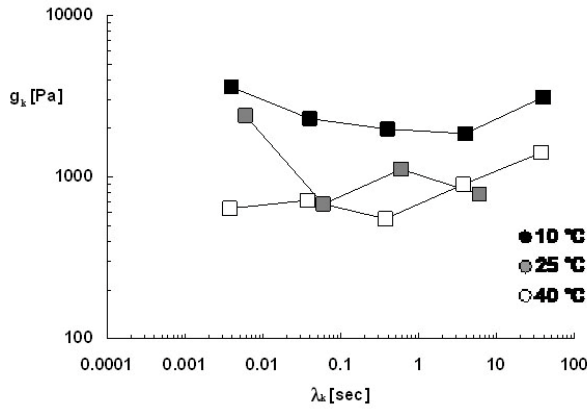


Fig. 6.18: 2%Ca-Alg mechanical relaxation spectra at different temperatures.

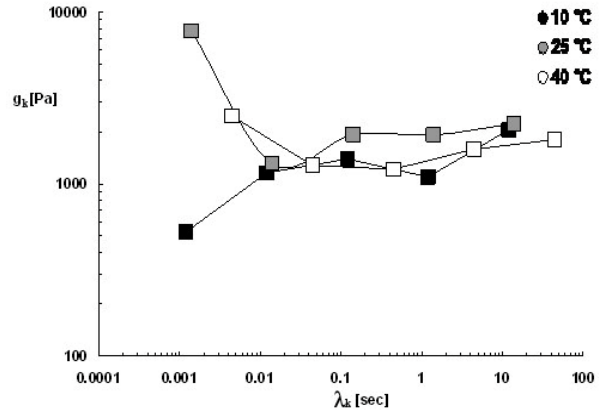


Fig. 6.19: 2%Cu-Alg mechanical relaxation spectra at different temperatures.

As for the previous systems, on the base of the Flory and equivalent network theories [1, 5], the crosslink density ρ_x and the polymeric network mean mesh size φ (or mean mesh diameter) were calculated at all the experimental temperatures (*Tab. 6.8*).

Temperature (°C)	2%Ca-Alg		2%Cu-Alg	
	crosslink density ρ_x (mol/cm ³)	mean mesh size φ (nm)	crosslink density ρ_x (mol/cm ³)	mean mesh size φ (nm)
10	$8,0 \times 10^{-6}$	7,3	$4,4 \times 10^{-6}$	9,0
25	$5,0 \times 10^{-6}$	8,5	$8,8 \times 10^{-6}$	7,3
40	$2,4 \times 10^{-6}$	11,0	$4,6 \times 10^{-6}$	8,8

Tab. 6.8: crosslink density ρ_x and polymeric network mean mesh size φ of 2%Ca-Alg and 2%Cu-Alg systems calculated at different temperature.

The data demonstrate, for the 2% Ca-alginate a decreasing in ρ_x with the temperature increase and a consequent mean pores diameters increasing while, the phenomena does not occur in the 2% Cu-alginate. Nevertheless, the mean diameter appears to be similar in both systems.

6.3.2.2 – Microscopic characterizations by low field NMR

More informations on the hydrogels structure were obtained from the low field NMR characterizations. In particular, the T_2 relaxation times distribution at 25°C show, for both the considered systems, the presence of three hydrogen aggregation states (*Fig. 6.20 - 6.21* for 2%Ca-Alg and 2%Cu-Alg respectively).

Considering the not perfect homogeneity of the systems, the three peaks can be explained as follows. Peak 3 represents the hydrogens of the water leaked from the gel during the samples loading into the NMR tubes. Peaks 1 and 2 correspond to the hydrogen of the water within the polymeric network according to a bimodal distribution.

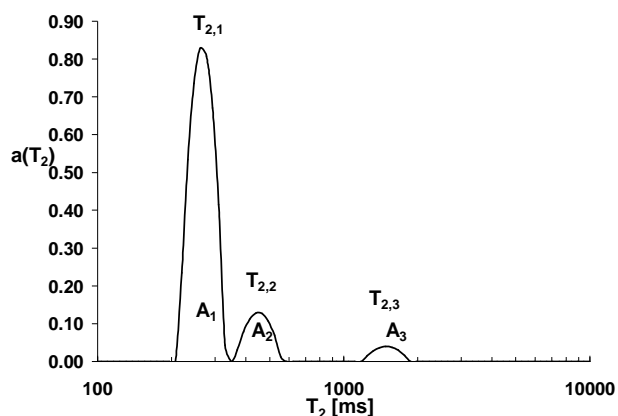


Fig. 6.20: 2%Ca-Alg ^1H proton T_2 distribution spectrum obtained by LF-NMR at 25°C.

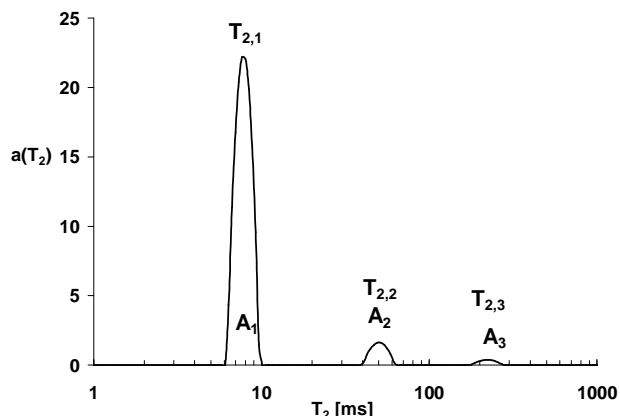


Fig. 6.21: 2%Cu-Alg ^1H proton T_2 distribution spectrum obtained by LF-NMR at 25°C.

The temperature effects on the relaxation times distribution supporting this hypothesis as shown in *figures 6.22 and 6.23*, that display the relative area of each peak A_i as function of mean relaxation time ($T_{2,i}$) at 10°C, 25°C and 40°C. In both systems, the peaks areas does not change with the temperature but, the variation of mean relaxation time of peak 3 ($T_{2,3}$) is significantly bigger than the standard deviation associated to $T_{2,3}$ at 25°C while, peaks 1 and 2 remain practically constant. As for the previous systems, this is an indication of the low interaction of this water states with the polymer because the thermal effects are predominant on the molecular interaction. On the contrary the temperature increase does not affect the water states related to the peaks 1 and 2 therefore, it is reasonable supposing that, these peaks correspond to hydrogens of the water with entrapped into the polymeric network.

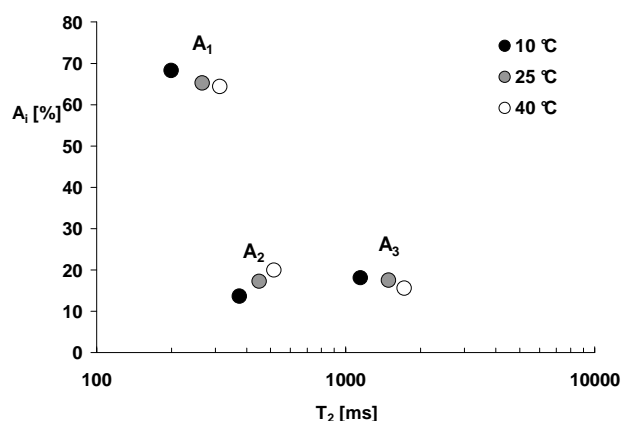


Fig. 6.22: 2%Ca-Alg mean relaxation time $T_{2,i}$ trend and respective relative area A_i at different temperature.

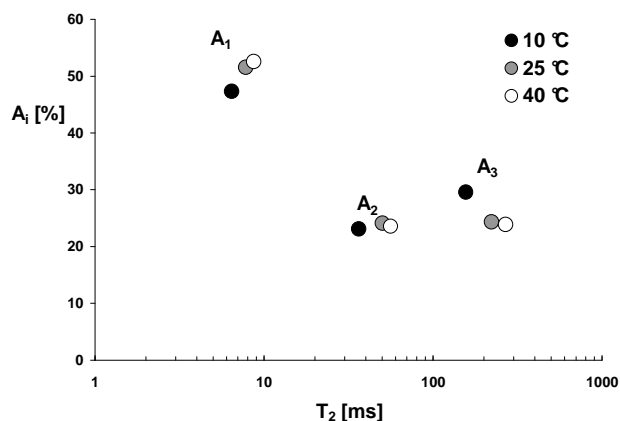


Fig. 6.23: 2%Cu-Alg mean relaxation time $T_{2,i}$ trend and respective relative area A_i at different temperature.

Another evidence supporting the peaks water interpretation regards the water and polymer hydrogen quantifications and the comparison of the theoretical and experimental peaks areas.

Theoretical relative H_2O area = 99,25%

Theoretical relative alginate area = 0,75%

The experimental relative areas values A_i and the correspondent mean relaxation time $T_{2,i}$ for the 2%Ca-Alg and 2%Cu-Alg systems at 25°C, are displayed respectively in *tables 6.9* and *6.10*.

Peak	$T_{2,i}$ (ms)	Relative A_i (%)
1	8,2	66,7
2	53,1	21,0
3	276,7	12,3

Tab. 6.9: 2%Ca-Alg hydrogel.

Peak	$T_{2,i}$ (ms)	Relative A_i (%)
1	265,6	65,2
2	449,8	17,2
3	1488,1	17,6

Tab. 6.10: 2%Cu-Alg hydrogel.

From the above tables, for both the considered systems, it is not possible to observe any area value matching to the theoretical 0,75% of the polymer hydrogen, therefore the polymer probable interact with the structured water entrapped into the hydrogel mesh and cannot be distinguished or, the signal is simply too low for its detection. Peak 3, in both systems, represent about the 15% of the total hydrogen and, considering the high $T_{2,3}$ values, can be reasonably attributed to the water outside the polymeric network. Indeed, in order to load the gel into the NMR tube, it was broken in parts and slightly pressed to minimizing the empty space. This mechanical action probably, causing a partial water release from the network. An area value around 15% for peak 3, makes reasonable this hypothesis because most of the water remains within the polymeric reticule. In both systems, peaks 1 and 2 are characterized by low $T_{2,i}$ values and together represent about the 85% of the total peaks area therefore, there are strong reasons for their relation with the water entrapped into the polymeric network [8].

Once established the correspondence of the peaks 1 and 2 with the water into the hydrogels mesh, the k parameters and the systems mean relaxation time \bar{T}_2 were calculate (*Tab. 6.11*) for both the hydrogels under investigation as described above.

	k (ms/nm)	\bar{T}_2 (ms)
2%Ca-Alg	36,0	14,4
2%Cu-Alg	2,0	308,0

Tab. 6.11.

The mean relaxation times difference between 2%Ca-Alg and 2%Cu-Alg, is in accordance with the results obtained from the mechanical properties analysis where a decrease of the mechanical modules can be distinguished when the temperature increase. Indeed, the results suggest a higher mobility (lower interaction) of the water within the Ca-alginate gel compared to the Cu-alginate gel and therefore, a temperature variation has a higher influence on the Ca-alginate system then the Cu-alginate.

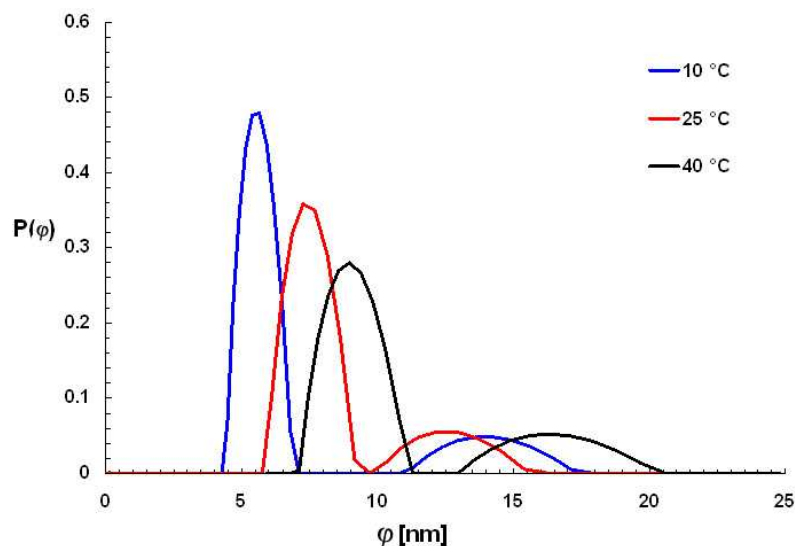


Fig. 6.24: 2%Ca-Alg bimodal mesh size distribution at different temperature obtained by NMR-rheology analysis.

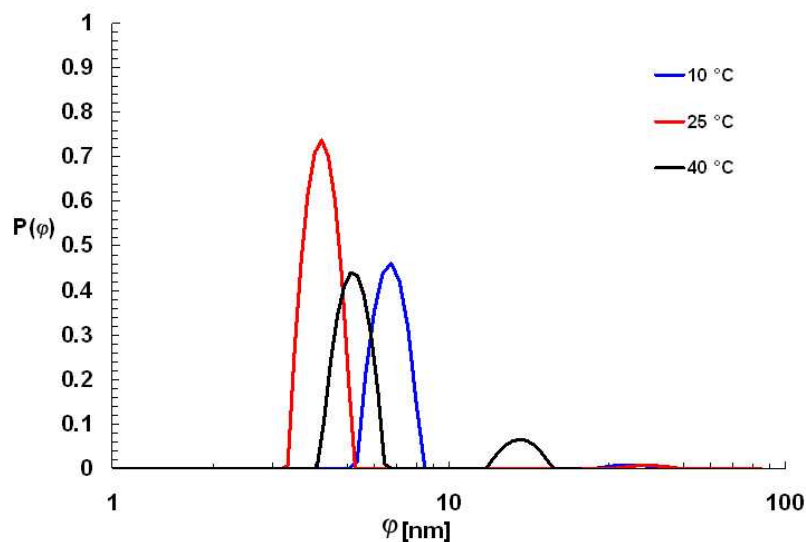


Fig. 6.25: 2%Cu-Alg bimodal mesh size distribution at different temperature obtained by NMR-rheology analysis.

Using the k parameters and the systems mean relaxation time \bar{T}_2 , the T_2 distributions were converted into mesh size distribution with the assignment of an occurrence probability $P(\varphi)$ [6-7]. *Figures 6.24* and *6.25* show the results obtained for 2%Ca-Alg and 2%Cu-Alg systems respectively, at different temperatures (10°C, 25°C and 40°C). All the analyzed systems present a bimodal probability distribution. Focusing on the Ca-alginate system (*Fig. 6.24*), the data suggest a progressive increasing of the mean mesh size with the temperature. Interestingly, the ratio between peak 1 (smaller pores) and peak 2 (bigger pores) decrease with the temperature indicating a reduction in the number of smaller pores in favour of the bigger pores. On the contrary, the random distribution of the probability function of the Cu-alginate system suggests that the polymeric network internal structure is not significantly influenced by the temperature in the considered range

(Fig. 6.25). Therefore, the temperature has a stronger influence on the mechanical properties of the alginates gel crosslinked by calcium cations than alginate crosslinked by copper cations.

The mesh size distribution indicates lower pores dimension for the Cu-alginate gel even if, as this system is highly inhomogeneous, the overall structure can be considered similar to the Ca-alginate. The advantage of the use of Cu cations consists in the crosslinking solution concentration that is half of the Ca solution. In *figure 6.26* the comparison of the 25°C mesh size distributions of 2%Ca-Alg and 2%Cu-Alg are shown.

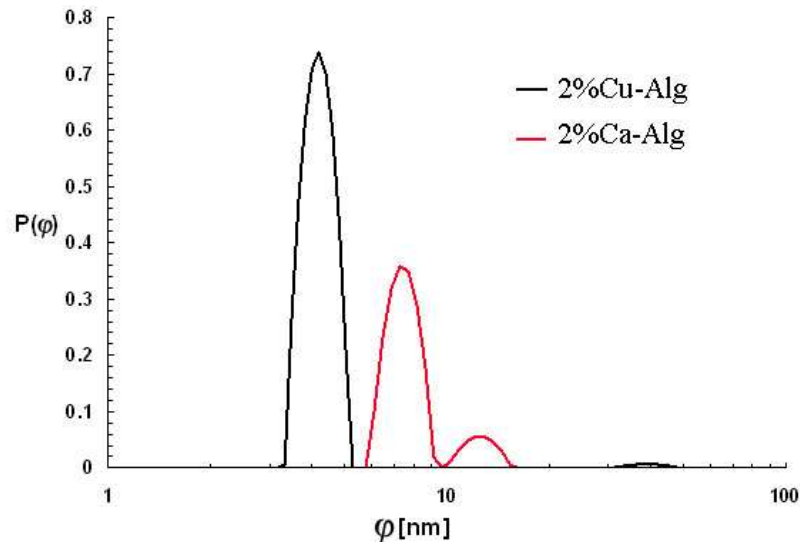


Fig. 6.26: comparison of 2%Ca-Alg and 2%Cu-Alg pores diameter distribution at 25°C.

6.3.2.3 – Cryoporometry structural properties studies on 2% copper alginate

In order to further study system structural conformation, Cryoporometry studies were performed on the 2% alginates reticulated by Cu cations. During the DSC measurements, the water is present only inside the material pores indeed, from the DSC trace the absence of water melting at 0°C can be appreciated (*Fig. 6.27*).

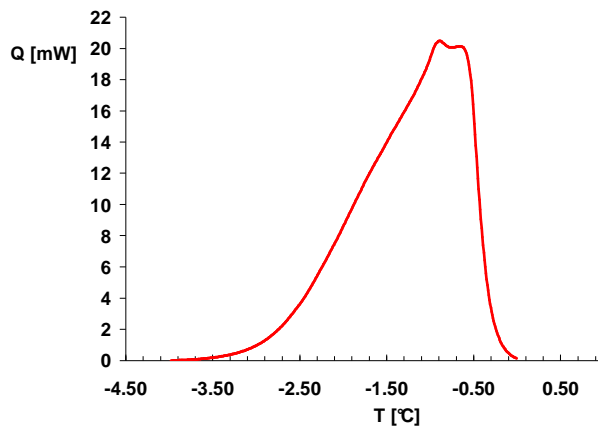


Fig. 6.27: DCS trace of 2%Cu-Alg system.

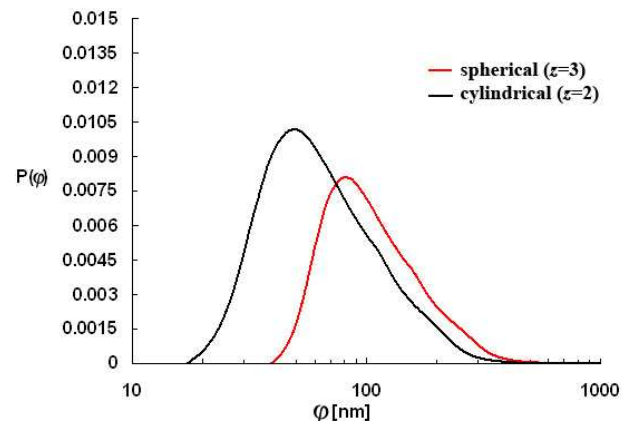


Fig. 6.28: Cryoporometry mesh size distribution on 2%Cu-Alg considering a spherical ($z=3$) and cylindrical ($z=2$) pores geometry.

The DSC procedure consisted in three steps:

4. Cooling from 25°C to -50°C at 10°C/min
5. Hold at -50°C for 1 min.
6. Warming from -50°C to 25°C at 2°C/min.

The pores size distribution was obtained by the elaboration of the DSC traces data by the Fortran software as described in section 4.5.

The procedure considers a cylindrical pores configuration without excess of water ($z=2$) and a spherical pores configuration ($z=3$). The resulting pores size distributions are compared in *figure 6.28*. The non-freezable water layer thickness (β) was calculated as 0,12 nm considering a cylindrical geometry and 0,24 nm considering a spherical geometry. Both the resulting pores size distributions are asymmetrical and the most probable pores have a diameter of 50 nm or 80 nm respectively considering a cylindrical or spherical geometry. The NMR-rheology and Cryoporometry results are compared in *figure 6.29*.

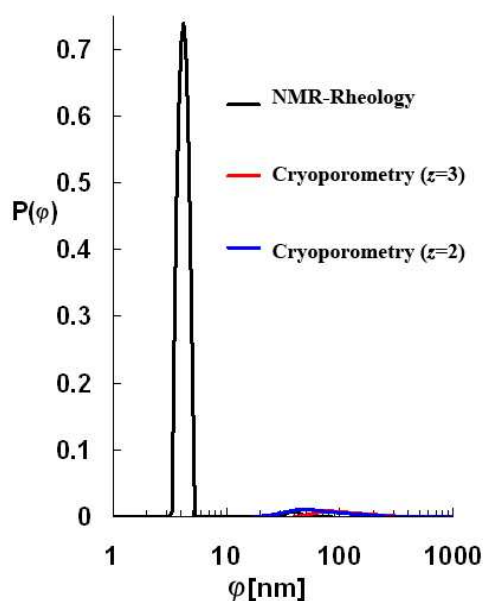


Fig. 6.29: comparison between pores size distribution according to NMR-rheology and Cryoporometry spherical ($z=3$) and cylindrical ($z=2$) geometries.

These differences can be explained by several factors:

- the hydrogels are not stable solids as zeolites and present strong viscoelastic properties (as demonstrated by mechanical spectra). Water solidification can cause mesh enlargement or even, network destructuring due to water volume increase.
- The heating and cooling speed can influence the hydrogel structure.

Figures 6.30 and *6.31*, report the calculated reduction of water melting temperature and enthalpy with mesh diameter in the case of spherical and cylindrical pores.

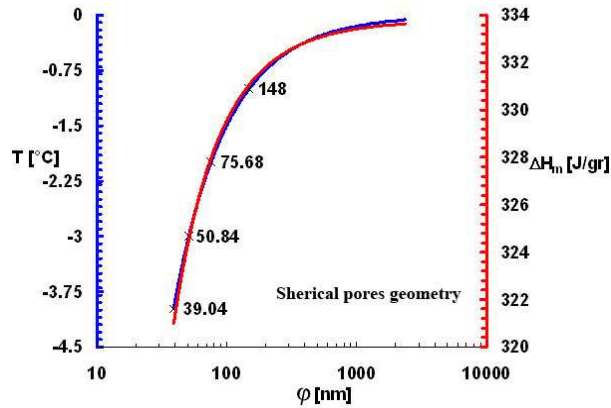


Fig. 6.30: variation of melting temperature (T) and enthalpy (ΔH_m) of water entrapped inside spherical pores versus pores diameter.

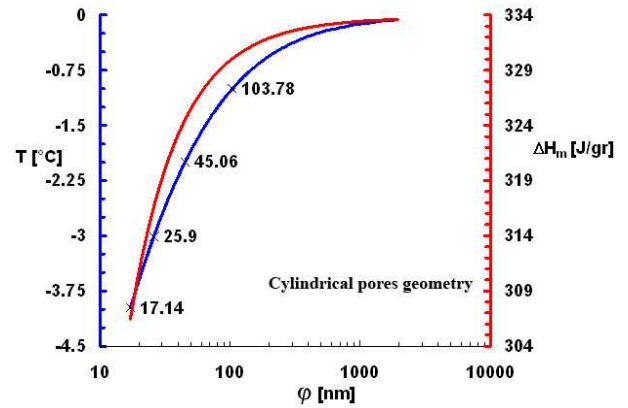


Fig. 6.31: variation of melting temperature (T) and enthalpy (ΔH_m) of water entrapped inside cylindrical pores versus pores diameter.

6.3.3 – 3% alginate hydrogels

This section deals with the characterization of alginate (Protanal™ LF10/60) crosslinked in a 3% aqueous solution containing calcium or copper cations (3%Ca-Alg and 3%Cu-Alg). In particular, the 3%Ca-Alg characterization is important because this gel was used also in the preparation of alginate-dextran methacrylate polymeric blend systems described in the following sections.

6.3.3.1 – Macroscopic characterizations by rheological studies

For both systems SS test prove that the linear viscoelastic (25°C) region spans up to a critical stress around 10 Pa, corresponding to a critical deformation of 0,04% (graph not shown). Accordingly frequency sweep tests were performed at a constant stress of 3 Pa and 25°C. From the storage G' and loss G'' moduli trends versus pulsation ω (Fig. 6.32). It is possible infer strong gel behaviour for both systems.

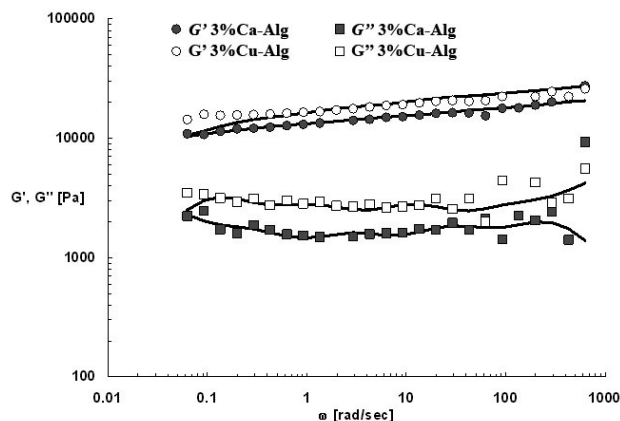


Fig. 6.32: 3%Ca-Alg and 3%Cu-Alg mechanical spectra at 25°C. Continue lines represent the generalized Maxwell model best fitting.

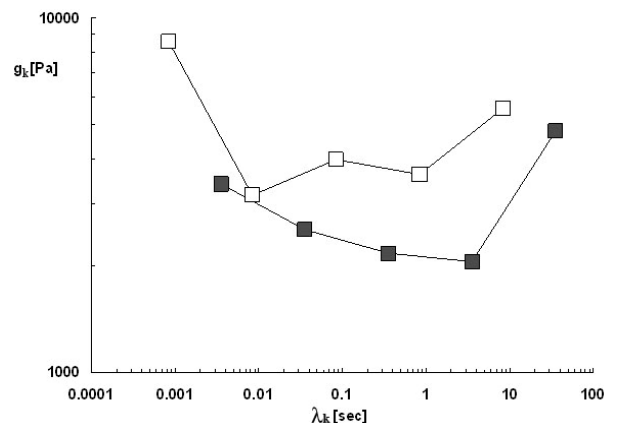


Fig. 6.33: relaxation spectra of 3%Ca-Alg (grey) and 3%Cu-Alg (white) at 25°C obtained by generalized Maxwell model fitting.

The experimental data were satisfactory fitted with the generalized Maxwell model using 5 Maxwell elements. The comparison of the relaxation spectra are shown in *figure 6.33*. From the sum of the elastic contribute of each Maxwell element (g_k), crosslink density ρ_x was calculated. On the basis of Flory and equivalent network theories [1, 5], and ρ_x it was possible estimate the mean mesh size ϕ (*Tab. 6.12*). The 3%Cu-Alg system has a mean mesh diameter slightly lower than 3%Ca-Alg system proof of higher network structuring, as confirmed by the mechanical spectra.

	crosslink density ρ_x (mol/cm ³)	mean mesh size ϕ (nm)
3%Ca-Alg	$8,6 \times 10^{-6}$	7,2
3%Cu-Alg	$1,4 \times 10^{-5}$	6,1

Tab. 6.12.

6.3.3.2 – Characterizations by low field NMR

The T_2 distribution at 25°C demonstrates, for both investigated systems, the presence of three hydrogen aggregation states (*Fig. 6.34* and *6.35* respectively for 3%Ca-Alg and 3%Cu-Alg). The consideration expressed for the previous alginate systems can be extended also to the 3% alginate systems. Therefore, the presence of the three states can be explained as follows: the peak 3 (mean relaxation $T_{2,3}$ and relative peak area A_3), represents the hydrogen of water outside the gel while peaks 1 and 2 ($T_{2,1}$, A_1 ; $T_{2,2}$, A_2), represent hydrogen of the water entrapped into the polymeric network.

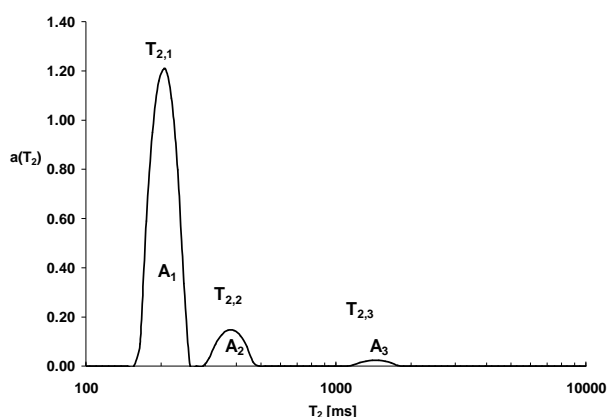


Fig. 6.34: 3%Ca-Alg ¹H proton T_2 spectra obtained by LF-NMR at 25°C.

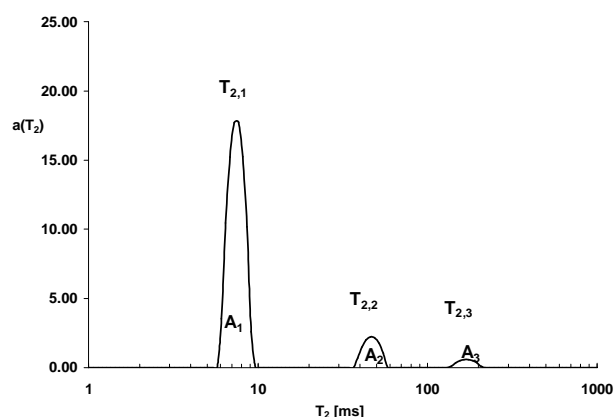


Fig. 6.35: 3%Cu-Alg ¹H proton T_2 spectra obtained by LF-NMR at 25°C.

The first experimental evidence supporting this hypothesis regards the temperature effects on the T_2 distributions. *Figures 6.36* and *6.37*, reports the relative area for each peak (A_i) as function of the peak mean relaxation time ($T_{2,i}$) at different temperatures (10°C, 25°C and 40°C), respectively for 3%Ca-Alg and 3%Cu-Alg. For both systems peaks area are nearly constant in the considered temperature range with the exception of 3%Cu-Alg peak 3 that shows a small decrease

at higher temperatures. While the $T_{2,3}$ (peak 3) has a considerable increase with temperature, $T_{2,1}$ and $T_{2,2}$ (peaks 1 and 2) do not change significantly with temperature increase. Indeed, only for $T_{2,3}$ the variation is significantly bigger than the standard deviation associated to $T_{2,i}$ at 25°C. Also for these two alginate systems, the thermal effects are predominant in the water outside the mesh. In the 3%Cu-Alg gel, peak 3 shows an area decreasing at higher temperature. Contemporary, a small increase can be noticed in the peak 1 and 2.

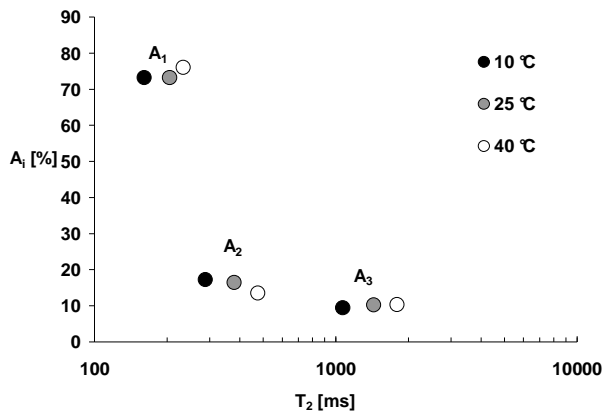


Fig. 6.36: 3%Ca-Alg mean relaxation time $T_{2,i}$ and respective relative area A_i at different temperature.

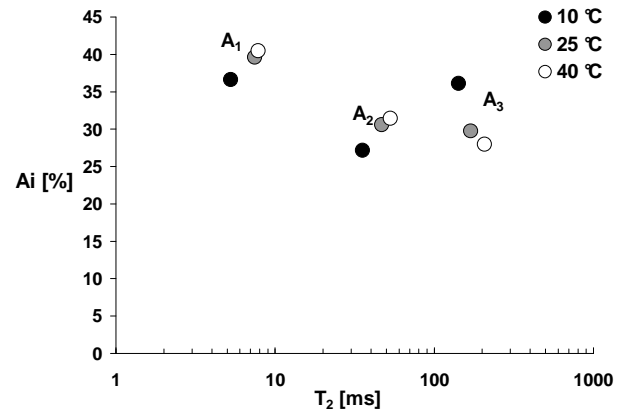


Fig. 6.37: 3%Cu-Alg mean relaxation time $T_{2,i}$ and respective relative area A_i at different temperature.

The fact that peak 1 (that characterized by the lowest T_2) does not represent only ^1H belonging to the polymeric can be explained by the comparison of the theoretical and experimental peaks areas.

Theoretical relative H_2O area = 98,87%

Theoretical relative alginate area = 1,13%

The experimental relative areas A_i and the correspondent mean relaxation time $T_{2,i}$ for the 3%Ca-Alg and 3%Cu-Alg systems at 25°C, are displayed in *tables 6.13* and *6.14*.

Peak	$T_{2,i}$ (ms)	Relative A_i (%)
1	8,2	66,7
2	53,1	21,0
3	276,7	12,3

Tab. 6.13: 3%Ca-Alg hydrogel.

Peak	$T_{2,i}$ (ms)	Relative A_i (%)
1	265,6	65,2
2	449,8	17,2
3	1488,1	17,5

Tab. 6.14: 3%Cu-Alg hydrogel.

Accordingly polymer relaxation cannot be distinguished from that of water entrapped into the mesh. In the Cu-alginate hydrogel, peaks 1 and 2 together represent more than 90% of the total protons, the remaining 10% can be assigned to water leaking from the gel mesh during the sample loading into the measurement system. In the Ca-alginate hydrogel, the structured water into the polymeric mesh is decreased to the 70% (peaks 1 and 2). In both case peak 3, , can be reasonably

assigned to the water outside the polymeric reticule. Due to peak $T_{2,3}$ values this interpretation is also supported by the literature data on similar systems [8].

Based on the peaks meaning, k can be calculated and the conversion of T_2 distribution into mesh size distribution can be achieved (Fig. 6.38) [6-7].

	k (ms/nm)	\bar{T}_2 (ms)
3%Ca-Alg	33,4	240,0
3%Cu-Alg	4,1	24,8

Tab. 6.15.

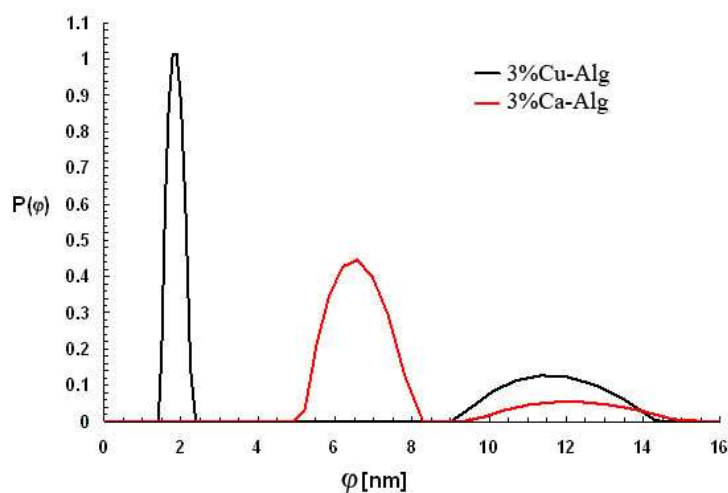


Fig. 6.38: comparison between mesh size distribution of 3%Ca-Alg and 3%Cu-Alg at 25°C, evaluated by NMR-rheology.

Both the systems show a bimodal mesh size distribution. In particular, for the 3%Ca-Alg system, the first peak is centred around 6,5 nm and is extended from 5 nm to 8 nm. The second peak is centred around 11,5 nm and extends from 9 nm to 14 nm. For the 3%Cu-Alg system, the first peak is centred on 2 nm and extends from 1 nm to 3 nm. The second peak is centred on 12 nm and extends from 9,5 nm to 15 nm. The comparison of the first peak from the two systems shows a great difference in mesh size distribution. The Ca-alginate hydrogel present a broad distribution in this area while, the Cu-alginate have a high mesh size developing concentrated in a small diameters range. The second peaks are instead, very similar.

6.3.4 – Concentration effects on alginates hydrogels pores size distribution

In order to better evaluate the effects of the alginate concentration on the polymeric mesh size distribution, the NMR-rheology results obtained at different concentration were plotted together. Figures 6.39 and 6.40 reports the trend of the mesh size distribution in 1%, 2% and 3%

alginate hydrogels crosslinked respectively with Ca cations and Cu cations. All the considered systems show a bimodal distribution.

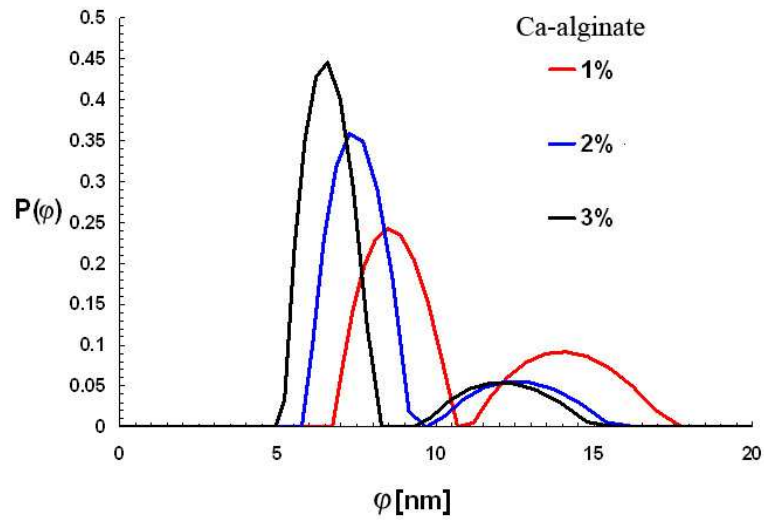


Fig. 6.39: effects of the alginate concentration on the pores diameter distributions of calcium alginate hydrogel (Ca-alginate).

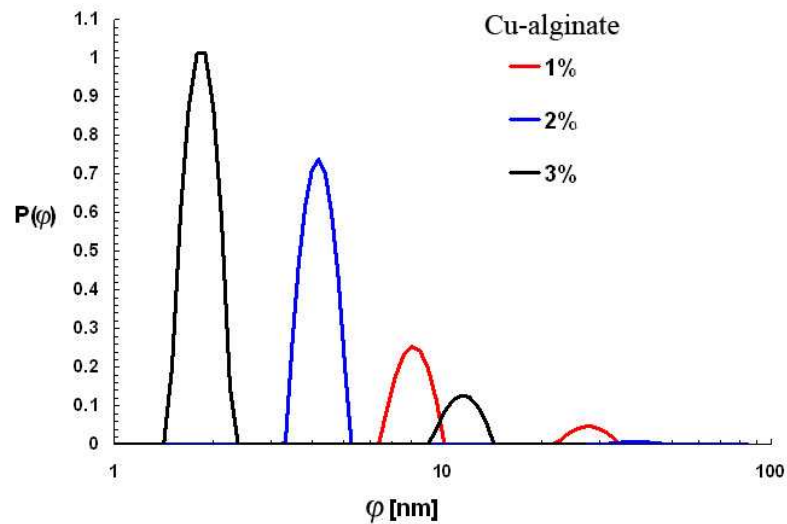


Fig. 6.40: effects of the alginate concentration on the pores diameter distributions of copper alginate hydrogel (Cu-alginate).

As expected, the concentration increase corresponds to a general mesh size decrease and a crosslink density increase. The two salts used as source of cations results in different effect on the final alginate properties. Copper cations are more efficient as crosslinking agent. Interestingly, the ratio between the first peak (lower mesh size) and the second peak (higher mesh size). Increases with the polymer concentration in both Ca-alginates and Cu-alginates. This phenomenon indicates that polymer concentration increase, not only causes an increase of the mesh size, but also a decrease of the relative number of bigger mesh in favour of the smaller ones.

6.4 – Pluronic™ F127 18% hydrogel system

As discussed in the previous section on the general aspects of the Pluronics™ systems, the internal structure of this type of systems is highly dependent on temperature. For this reason, the Pluronics™ characterization was focused on the structural properties dependency on temperature variations. In this studies, Pluronics™ F127 at 18% concentration in water solution was used. In this condition systems gelation occurs around 20°.

6.4.1 – Relaxation time (T_2) measurements by CPMG sequence

The relaxation times T_2 trend of Pluronics™ was studied in a temperature range within 10°C and 40°C (Fig 6.36). The measurements were performed at temperature interval of 1°C in the regions 10-24°C and 24-30°C and 0,5°C in the region 24-30°C.

Figure 6.41 reports T_2 distribution as function of the temperature. The spectra can be divided in two areas on the basis of the different sample behaviour. Within 10°C and 14°C proton relaxation is described by two components: *slow* (free water, $T_2 \approx 1000$ ms) and *medium* (Pluronic™ unimers summed to the interacting water, $T_2 \approx 160$ ms) as shown in figure 6.41. Above 15°C, proton relaxation is described by three components: *slow* (free water), *medium* (Pluronic™ unimers or poor structured Pluronic™) and *fast* (micelles Pluronic™ or high structuring Pluronic™).

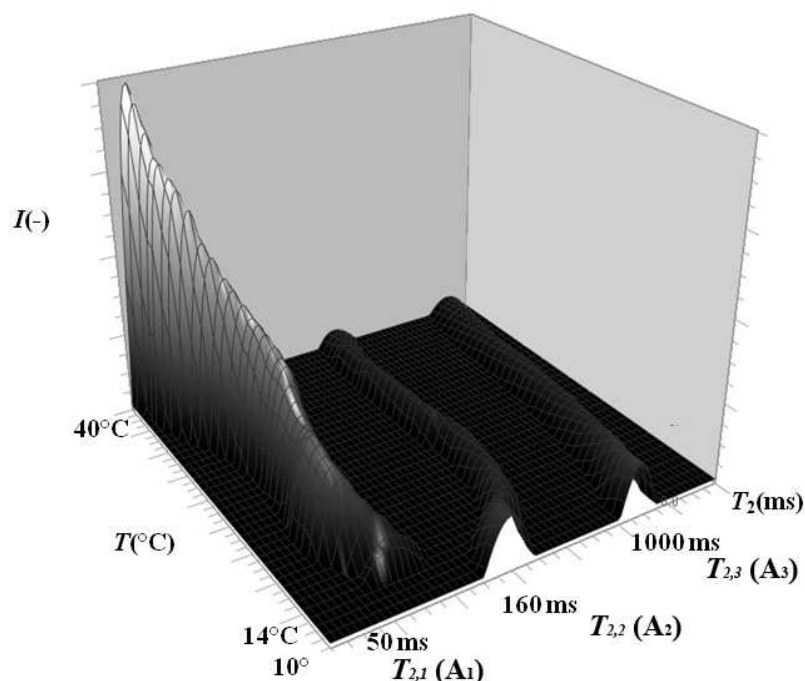


Fig. 6.41: 18% Pluronic™ T_2 evolution versus temperature.

Peaks relative area at low temperature (82,9% and 17,0% respectively for the slow and medium peak), have a good matching with the theoretical areas calculated for the polymer and the water hydrogen as follows:

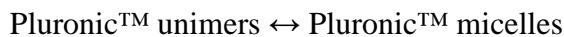
$$\text{Theoretical relative H}_2\text{O area: } 100 \cdot \frac{\frac{We_{H_2O} \cdot N_{H_2O}}{M_{H_2O}}}{\frac{We_{H_2O} \cdot N_{H_2O}}{M_{H_2O}} + \frac{We_{Plu} \cdot N_{Plu}}{M_{Plu}}} = 84,2\%$$

$$\text{Theoretical relative Pluronic}^{\text{TM}} \text{ area: } 100 \cdot \frac{\frac{We_{Plu} \cdot N_{Plu}}{M_{Plu}}}{\frac{We_{H_2O} \cdot N_{H_2O}}{M_{H_2O}} + \frac{We_{Plu} \cdot N_{Plu}}{M_{Plu}}} = 15,7\%$$

where, M_{H_2O} and M_{Plu} are the molecular weight of water and PluronicTM respectively, m_{H_2O} and m_{Plu} are the weight % of water and alginate in the gel, N_{H_2O} and N_{Plu} are the number of protons in the water molecule and polymer chain. In the calculation, it was considered the PluronicTM formula HO-(EO)_n-(PO)_m-(EO)_n-OH where m=65 and n=99 then, considering 4 protons for each EO monomer and 6 for each PO monomer, $N_{Plu}=(4 \cdot 2 \cdot n)+(6 \cdot m)+2=1184$.

As the PluronicTM is responsible for about the 16% of the relative areas, the remaining 1% it is supposed to be the hydrogen of water that interact with the polymer in solution. The hypothesis that the water interacting with the polymer, within 10°C and 14°C, is limited to the 1% it is reasonable because, in this condition, the PluronicTM unimers are prevalent on the PluronicTM micelles where the water can be easily entrapped.

The T_2 and related relative areas evolutions as function of the temperature can gives information about the dynamics of the aggregation phenomena. Normally, temperature increase causes a viscosity reduction with a consequent molecules mobility increase and therefore, a T_2 increase. In the PluronicTM system, molecules mobility increase is reduced and, in some case zeroed, by micelles aggregation. Indeed, it is known that, when temperature is increased, the equilibrium:



moves toward PluronicTM micelles. Therefore, a temperature increase should reflect into a decrease of the unimeric fraction, an increase in the structured fraction, where it is easier the entrapment of water strongly interacting with the polymer [8]. This evidence is better represented in *figure 6.43* where the relative peak area A_3 of the free water as function of the temperature is reported. It is clear that, temperature increase (and therefore micelles number or volume increase)

corresponds to a reduction in the quantity of free water. At the same time, the T_2 of free water increases as consequence of the reduced viscosity and higher protons mobility (*figure 6.42* reports the free water mean relaxation times $T_{2,3}$ as function of the temperature). In this sense it is useful remembering that the pure free water relaxation time, obtained experimentally, is about 2500 ms [9].

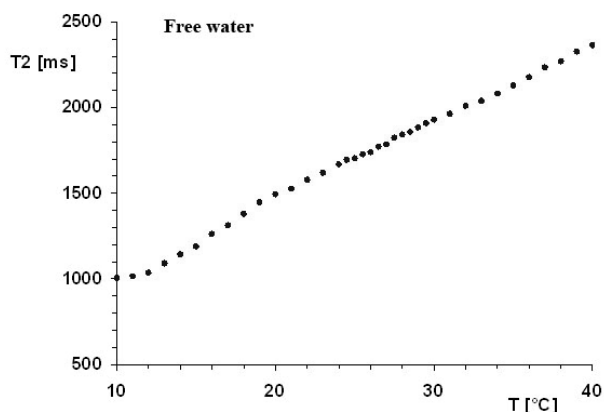


Fig. 6.42: evolution of the free water mean relaxation time ($T_{2,3}$) with temperature in 18% Pluronic™ system.

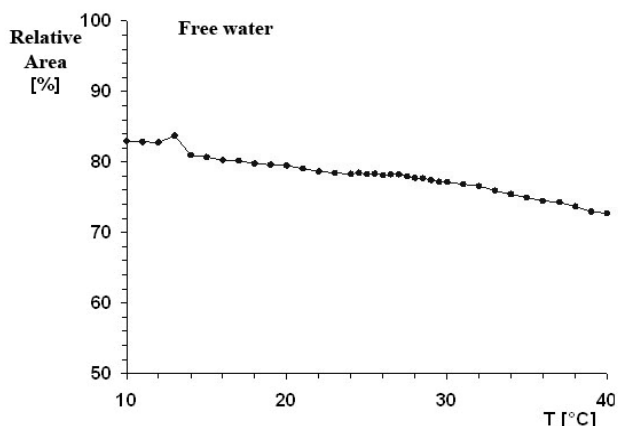


Fig. 6.43: evolution of the free water relative peak area (A_3) with temperature in 18% Pluronic™ system.

For what concerns the medium T_2 values component (160-370 ms), it was assigned to the non-structured Pluronic™ (unimers or small aggregates). In *figure 6.44*, the $T_{2,2}$ trend as function of the temperature is reported. It is possible to distinguish six thermal regions:

- 10°C – 13°C: small relaxation time increasing.
- 13°C – 19°C: the T_2 increase is higher (caused by the reduced viscosity).
- 19°C – 24°C: the curve slope decrease. In this region the T_2 increase with temperature is reduced.
- 24°C – 26°C: inversion of the curve slope. The relaxation time decrease with the temperature. In this region the formation of bigger structure with consequent reduction of the polymeric chain mobility occurs.
- 24°C – 32°C: the T_2 remain constant (structuring region).
- Above 32°C: the temperature effect appearing again resulting in a T_2 increase.

Taking into account peak area (A_2) variation with temperature (*Fig. 6.45*), it is possible to have an estimation of the non-structured Pluronic™ and structured Pluronic™. The peak area trend in *figure 6.45* can be divided in regions analogue to the above T_2 trend:

- 10°C – 14°C: no area variation occurs.
- 14°C – 19°C: a slow decreasing.
- 19°C – 24°C: the area remain constant.
- 24°C – 27°C: a sudden area decreasing.

- Above 27°C: the area remains more or less constant.

The non-structured Pluronic™ fraction decrease follows a two steps process (first step, within 10°C and 24°C and second step from 24°C to 27°C). This behaviour can be described as a two steps polymer chain structuring, according to what suggested in literature [10-11] and as demonstrated by the rheological studies presented in *figure 6.84*. The curve named as P18, shows the gelation process of an 18% Pluronic™ solution. The transition was followed by the storage modulus G' variation as function of the temperature increasing.

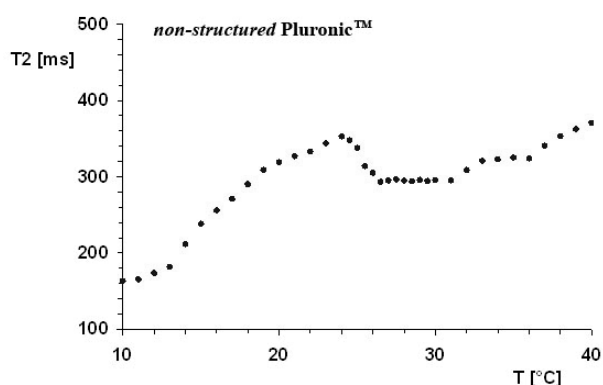


Fig. 6.44: evolution of the *non-structured* Pluronic™ mean relaxation time ($T_{2,2}$) with temperature in 18% Pluronic™ system.

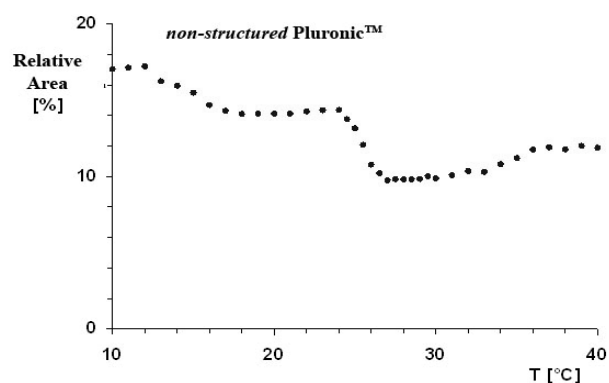


Fig. 6.45: evolution of the *non-structured* Pluronic™ relative peak area (A_2) with temperature in 18% Pluronic™ system.

Finally, the fast component (25-60 ms), appearing only at temperature above 14°C, was assigned to the structured Pluronic™ fraction (rather organized in micelles). In *figure 6.47* it is showed the peak relative area (A_1) as function of the temperature. The trend is nearly symmetrical to the relative area of the medium component (A_2 , *Fig. 6.45*), confirming that the two components represent two aggregation states of the same chemical species: Pluronic™. For the T_2 instead, the trend is different: between 15°C and 20°C, the relaxation time $T_{2,1}$ decreases, confirming the formation of less mobile structures (bigger). From 20°C to 27°C there is no significant $T_{2,1}$ variation, while $T_{2,1}$ decreases for higher temperature (*Fig. 6.46*).

In *figure 6.48*, the relative areas trend as temperature function of fast and medium component (A_1 and A_2 ; respectively structured and non-structured Pluronic™ fractions) are merged for a better comparison. It is clear how the non-structured Pluronic™ decrease is compensated by the structured Pluronic™ increase. The curves crossing point, around 26°C, indicate the substantially completion of the structuring process.

Concluding, the analysis of the T_2 relaxation times of the Pluronic™ 18% in water, allows following the polymeric chain structuration dynamics in micelles complex as the effect of temperature increasing. The presence of at least two discontinuities in the T_2 trend of the fast and

medium component suggests that the phenomenon is not a simple equilibrium within two states (unimer-micelle) but, probably a sequence of events.

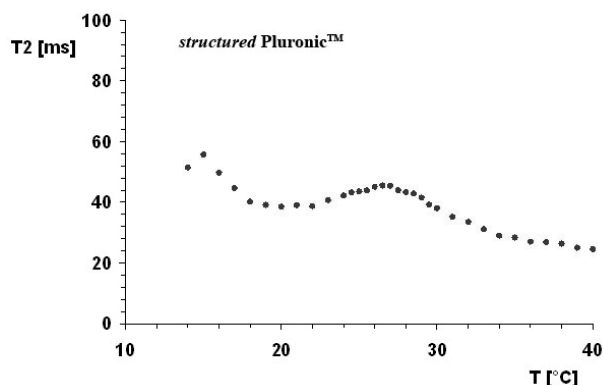


Fig. 6.46: evolution of the *structured Pluronic™* mean relaxation time ($T_{2,1}$) with temperature increase in 18% Pluronic™ system.

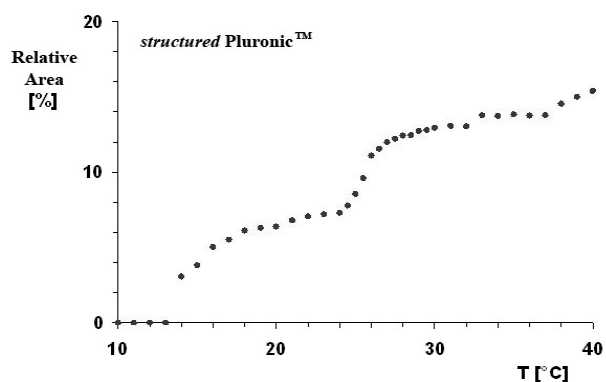


Fig. 6.47: evolution of the *structured Pluronic™* relative peak area (A_1) with temperature increase in 18% Pluronic™ system.

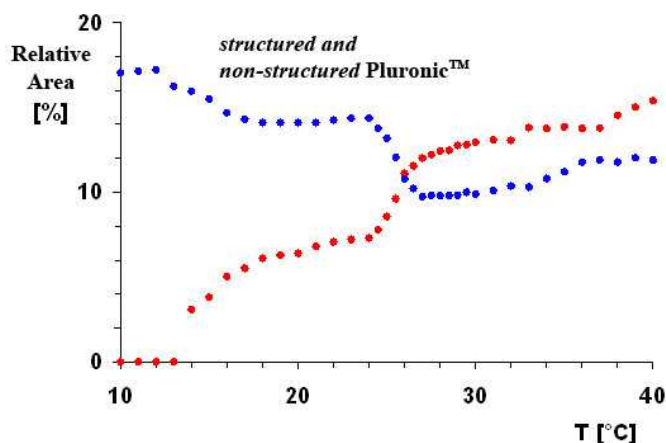


Fig. 6.48: comparison between relative peak areas trend of structured Pluronic™ (A_1 , red dots) and non-structured Pluronic™ (A_2 , blue dots) with temperature increase in 18% Pluronic™ system.

6.5 – Dextran methacrylate hydrogel based systems

This section deals with hydrogel systems based on dextran methacrylate, in particular the D40 and D500 respectively 5% and 30% methacrylate (D40MA5% and D500M30%), both in a 5% water solution.

6.5.1 – Macroscopic characterizations by rheological studies

The two systems differ for the molecular weight and methacrylation degree. The SS tests and FS tests, performed at 25°C, allow determining the viscoelastic properties of the systems. In the mechanical spectra reported in *figure 6.49*, the storage G' and loss G'' moduli are approximately

parallel for both systems. Moreover, G' is one order magnitude higher than G'' mining that, we are dealing with strong gels. Nevertheless D500MA30% stronger than D40MA5%, in virtue of the higher molecular weight and especially, the higher methacrylation degree.

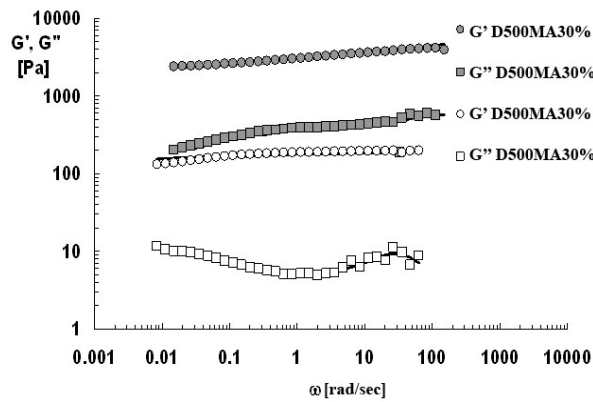


Fig. 6.49: mechanical spectra (FS test) of D40MA5% (white) and D500MA30% (grey).

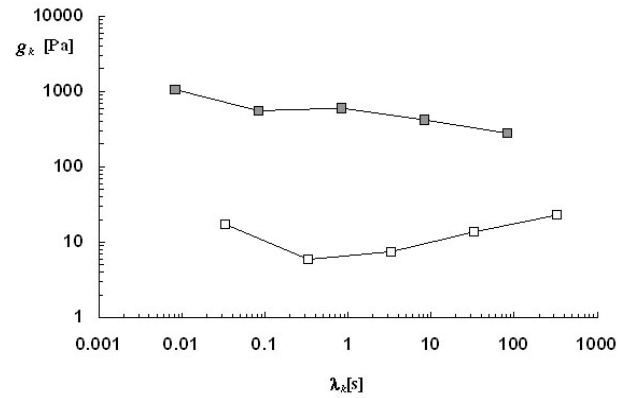


Fig. 6.50: relaxation spectra of D40MA5% (white) and D500MA30% (grey).

Both systems were satisfactory fitted by the generalized Maxwell model with 5 elements (*Fig. 6.49*, continues line). The resulting relaxation spectra (*Fig. 6.50*) differ from each other by, roughly, two orders of magnitude. This phenomenon affects the crosslink density ρ_x that is, exactly, two orders of magnitude lower for D40MA5%.

	crosslink density ρ_x (mol/cm ³)	mean mesh size φ (nm)
D40MA5%	$8,1 \times 10^{-8}$	34,0
D500MA30%	$2,0 \times 10^{-6}$	11,6

Tab. 6.16.

6.5.2 – Cryoporometry structural properties studies

From the DSC traces appears that in the analysed dextrans methacrylate systems water is present only inside the network pores indeed, there is no water melting around 0°C (*Fig. 6.51* and *6.52*).

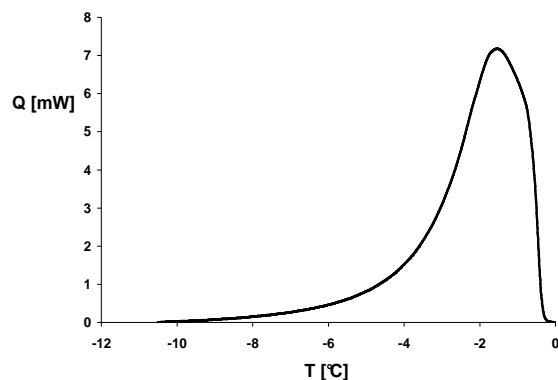


Fig. 6.51: DSC trace of D40MA5%

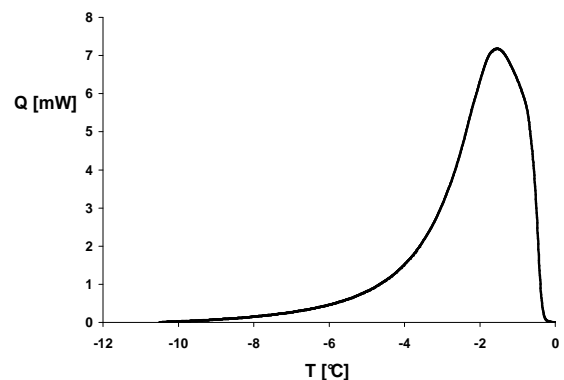


Fig. 6.52: DSC trace of D500MA30%

The thickness of non-freezable water layer into the nanopores (β) is reported in *table 6.17* for D40MA5% and D500MA30% in case of spherical and cylindrical geometry.

	Non-freezable water layer thickness β (nm)	
	Spherical geometry	Cylindrical geometry
D40MA5%	2,3	1,2
D500MA30%	2,8	1,3

Tab. 6.17: non-freezable water layer thickness β for the D40MA5% and D500MA30% systems evaluated considering spherical geometry or cylindrical geometry without excess of water.

The mesh size distributions obtained from the cryoporometric analyses, are reported in *figures 6.53* and *6.54* respectively for D40MA5% and D500MA30%, considering a spherical geometry ($z=3$) and cylindrical geometry ($z=2$). The distribution curves show a maximum probability, for D40MA5%, at 50 nm and 7 nm and for D500MA30%, at 40 nm and 6 nm respectively in spherical and cylindrical geometry.

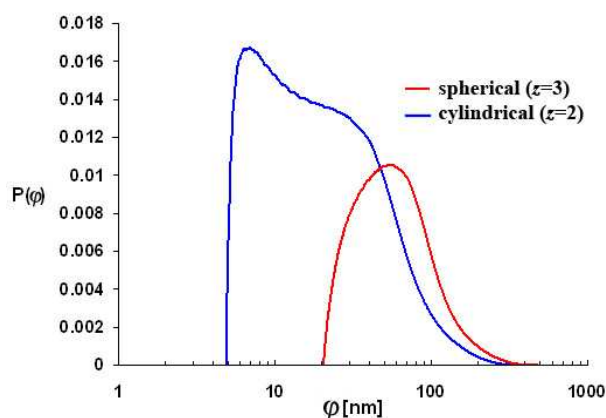


Fig. 6.53: D40MA5% mesh size distribution obtained by Cryoporometry assuming spherical ($z=3$) or cylindrical ($z=2$) pores geometry.

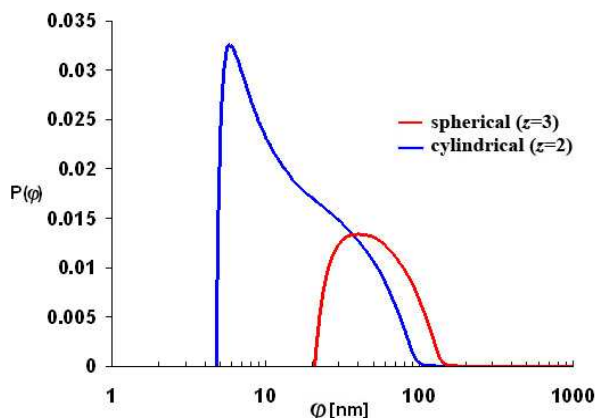


Fig. 6.54: D500MA30% mesh size distribution obtained by Cryoporometry assuming spherical ($z=3$) or cylindrical ($z=2$) pores geometry.

Considering that, from the Rheology studies, the mean mesh size results 34,0 nm and 11,6 nm respectively for D40MA5% and D500MA30%, the best matching between the two techniques occurs for D40MA5% spherical geometry and for D500MA30% cylindrical geometry.

6.6 – Poly-1b hydrogel system

Poly-1b derives from benzofulvene. The detailed preparation is described in the materials preparation section. Before performing the analysis, the dry polymer was swollen in distilled water at 25°C (about 10 hours) obtaining a transparent hydrogel system.

6.6.1 – Macroscopic properties characterizations by rheological studies

The SS test (25°C) collocates the limit of the linear viscoelasticity region at a critical deformation of $\gamma_0=0,9\%$ therefore, the FS test was performed at a constant deformation $\gamma=0,01\%$ and 25°C. The resulting mechanical spectrum is showed in *figure 6.55* (pulsation $\omega=2\pi f$; f = frequency).

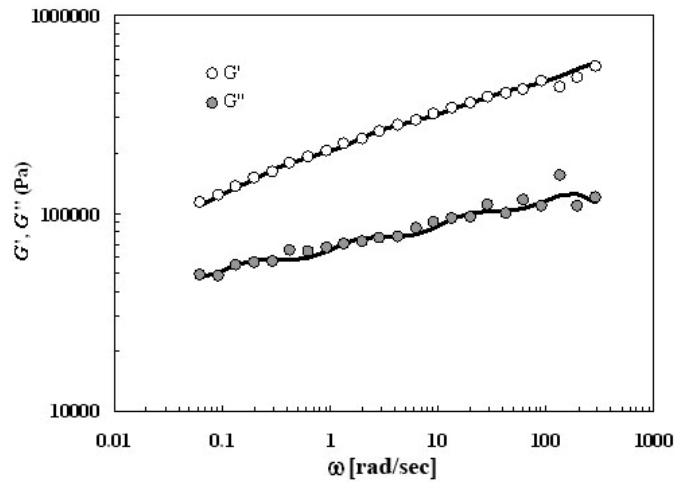


Fig. 6.55: Poly-1b hydrogel mechanical spectra, comparison of storage modulus (G') and loss modulus (G''). The continuous line represents the same values calculated by generalized Maxwell model.

The moduli trends are parallel and moreover, G' is about one order of magnitude higher than G'' therefore, the elastic properties are always predominant, a characteristic of a strong gel. The figure also reports a satisfactory data fitting by the generalized Maxwell model with 5 elements. Based on the Flory and equivalent network [1, 5], the crosslink density ρ_x and mean mesh size φ are:

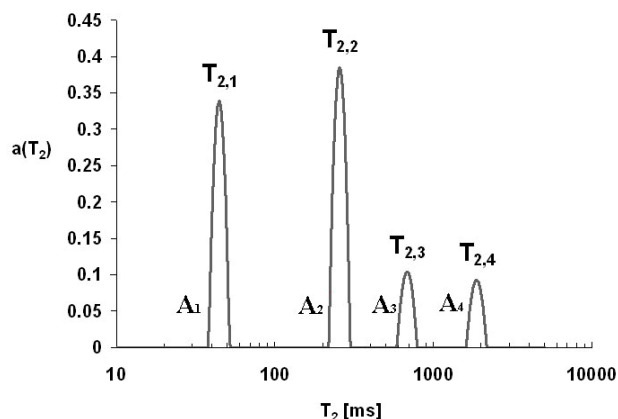
$$\rho_x = 6,6 \times 10^{-5} \text{ mol/cm}^3$$

$$\varphi = 3,6 \text{ nm}$$

6.6.2 – Microscopic characterizations by low field NMR

Low field NMR studies on T_2 (25°C), highlighted the presence of 4 different conditions of the hydrogen atoms in the system (*Fig. 6.56*). Remembering that the system is not perfectly homogeneous (it is similar to a concentrated suspension of particles), the presence of 4 peaks can be explained as follows. Due to its high $T_{2,4}$ value, peak 4 corresponds to the water outside the gel meshes. The third peak ($T_{2,3}$) should correspond to the hydrogen of the water entrapped in the cavities within gel particles while, the second peak ($T_{2,2}$) should correspond to the hydrogen of the water entrapped within the polymeric mesh inside the particles. Finally, the first peak, because of

the low value $T_{2,1}=43$ ms, can be assigned to the polymer hydrogens. *Table 6.18* reports all the $T_{2,i}$ values and the correspondent peak relative area A_i .



Peak	$T_{2,i}$ (ms)	Relative A_i (%)
1	43	4
2	261	23
3	914	18
4	2252	55

Tab. 6.18.

Fig. 6.56: Poly-1b hydrogel T_2 distribution. Four peaks were detected with at $T_{2,i}$ mean relaxation time and A_i relative peak area.

Two experimental evidences confirm the above hypotheses. The first regards the temperature effects on the T_2 distribution. *Figure 6.57* reports the peaks relative area A_i and the mean relaxation time $T_{2,i}$ at different temperature (15°C, 25°C and 40°C). While the relative areas are substantially constant with temperature, the same is not true for the mean relaxation times $T_{2,i}$. Indeed, $T_{2,3}$ and $T_{2,4}$ increase with temperature is significantly bigger than the standard deviation associated to $T_{2,i}$ at 25°C while, $T_{2,2}$ and $T_{2,1}$ are practically constant. This is an indication that, peaks 3 and 4 represent water that is not highly linked with the solid substrate because the thermal energy effects are clearly visible. On the contrary, an increase of the temperature has a negligible effect on the relaxation times of the peaks 1 and 2. Therefore, these peaks represent hydrogen atoms highly structured as the hydrogen of the water entrapped into the polymeric network or polymer chain hydrogens.

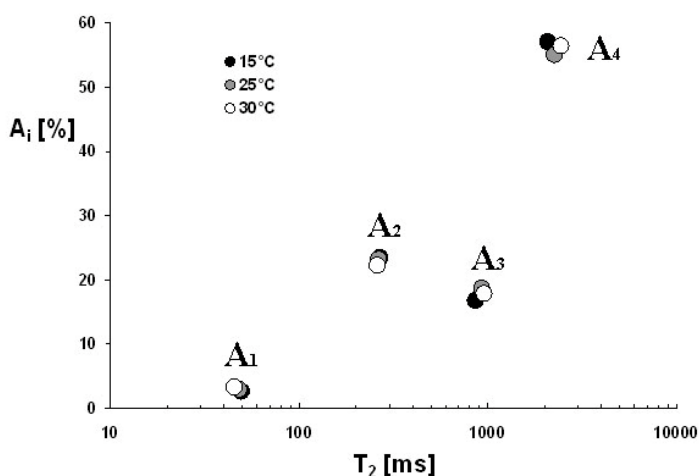


Fig. 6.57: temperature effect on the peaks relaxation times ($T_{2,i}$) and areas (A_i). A temperature increase causes a shifting to higher values of the $T_{2,i}$ corresponding to the peaks 3 and 4. On the contrary it does not influence significantly peaks 1 and 2.

The second experimental evidence supporting the peaks assignment hypothesis, regards the hydrogel swelling ratio S_w defined as the ratio between water mass inside the gel (m_{H_2O}) and the mass of polymer (m_m). Indeed, because as area A_i is proportional to the number of hydrogen atoms relaxing to the mean peak relaxation times $T_{2,i}$, S_w can be written as:

$$S_w = \frac{m_{H_2O}}{m_m} = \frac{N_{H_2O} M_{H_2O}}{N_m M_m} \cdot \frac{A_2}{A_1} \quad (6.2)$$

where N_{H_2O} (=2) and N_m (=52) are respectively the number of hydrogen atoms of the water molecule and polymer monomer; M_{H_2O} (=18) and M_m (=673) are respectively the molecular weight of the water molecule and polymer monomer; A_1 and A_2 are respectively the relative peak area of peak 1 and 2. Notably, the theoretical S_w evaluation according to (6.2) is similar to the experimental value determinate at 25°C by weight increase of the dry polymer swelling in water up to equilibrium.

6.6.3 – Pores size distribution studies

Once recognized that peak 3 represents the water entrapped into the polymeric meshes, it is possible to obtain the mesh size distribution as showed in *figure 6.58* [6-7].

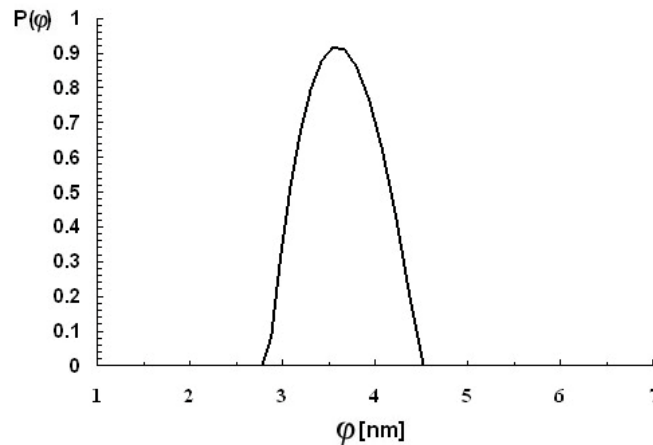


Fig. 6.58: mesh size distribution (pores diameter distribution) of Poly-1b hydrogel obtained by NMR-rheology.

Considering the mesh size, the polymeric system under analysis should be used as matrix for the controlled release of small molecules, characterized by a van der Waals radius (r_{vdW}) lower than 1 nm as, for example, theophylline (0,37 nm) or the vitamin B12 (0,85 nm) [12]. Interestingly, on the basis of the Peppas and Lustig theory [13], it is possible to estimate the reduction of the diffusion coefficient of this molecules in the gel system compared to the water.

$$D_g / D_w \approx \left(1 - \frac{2r_{vdW}}{\phi} \right) e^{-\left(\frac{v_{2p}}{1-v_{2p}} \right)} \quad (6.3)$$

where D_g and D_w are the diffusion coefficient of the molecule respectively in the swollen gel and in water; r_{vdW} is the drug van der Waals radius; v_{2p} is the volumetric fraction of polymer in the gel system ($v_{2p}=0,13$ in this case). For theophylline and vitamin B12, $D_g/D_w= 0,68$ and $0,45$ respectively.

The results obtained from NMR-rheology were compared with the data from Cryoporometry. The asymmetrical DSC trace (*Fig. 6.59*), evidences the non-homogeneity of the system. All the water melts at temperatures lower than 0°C . Melting starts from -10°C with two peaks at $-1,5^\circ\text{C}$ and $-0,5^\circ\text{C}$. *Figure 6.60* reports mesh size distribution. Once again the cylindrical geometry predicts smaller pores. The most probable diameters is 30 nm and 6,5 nm respectively for spherical ($z=3$) and cylindrical ($z=2$) geometry.

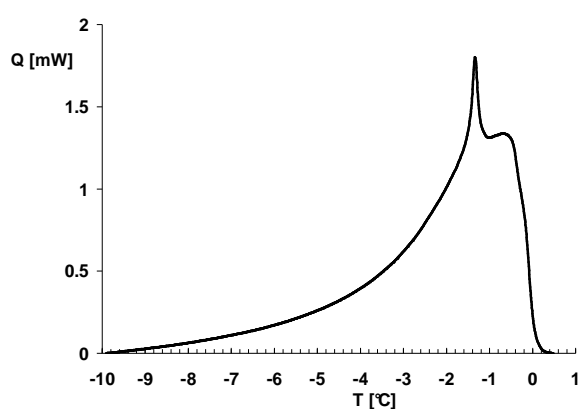


Fig. 6.59: Poly-1b DSC trace.

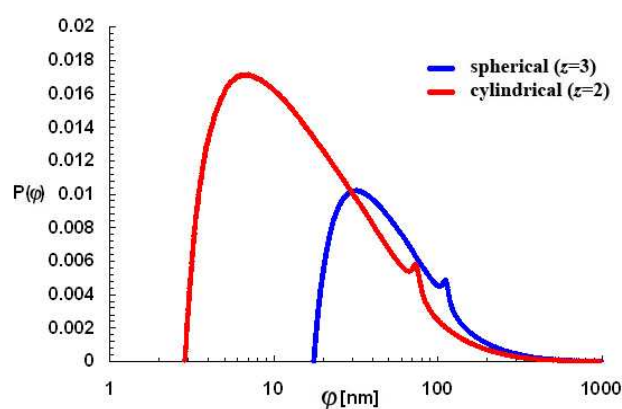


Fig. 6.60: mesh size distribution obtained by Cryoporometry assuming spherical ($z=3$) or cylindrical ($z=2$) pores geometry.

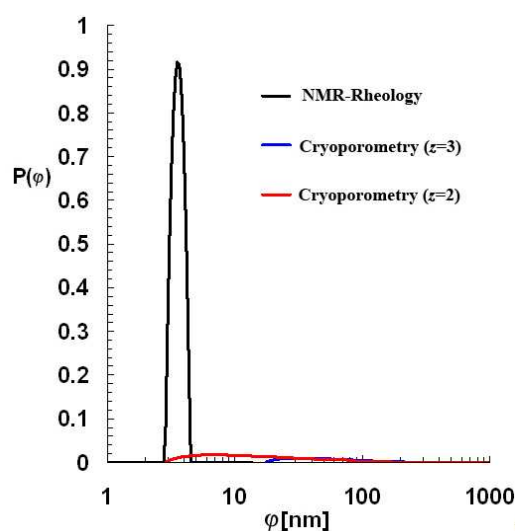


Fig. 6.61: comparison between mesh size distribution obtained by NMR-rheology and Cryoporometry assuming spherical ($z=3$) and cylindrical ($z=2$) pores geometry.

The pores distribution calculated by Cryoporometry and NMR-rheology are compared in *figure 6.61*. The two methodologies give different results in terms of distribution amplitude and position of the most probable diameter. Nevertheless, assuming a cylindrical geometry, the

differences are reduced at least for the most probable diameter, supporting the hypothesis that cylindrical pores are present.

6.7 – Polymeric blends

After the analysis on the single components, the attention was focused on the characterization of polymeric blends, in particular the systems composed by alginate-Pluronic™ (2%-18%) and alginate-dextran methacrylate (3%-5%) were studied.

6.7.1 – Pluronic™-alginate hydrogel system

The Pluronic™-alginate hydrogel consists in a mixture of 2% alginate (Protanal™ LF10/60) crosslinked by Cu cations and 18% Pluronic™ F127.

6.7.1.1 – Structural analysis by NMR-rheology

The SS test was performed at 25°C in order to establish the system linear viscoelastic limit. The limits is represented by a critical shear stress around 40 Pa, corresponding to a critical deformation of 0,07%. On this basis, the FS test was performed at the same temperature using a constant stress of 3 Pa, within the system linear viscoelastic region. *Figure 6.62* reports the mechanical spectra obtained from the FS test. According to Flory and equivalent network theories [1, 5], the crosslink density $\rho_x=2,7 \times 10^{-5}$ (mol/cm³) and the mean mesh size $\phi=4,9$ nm were evaluated.

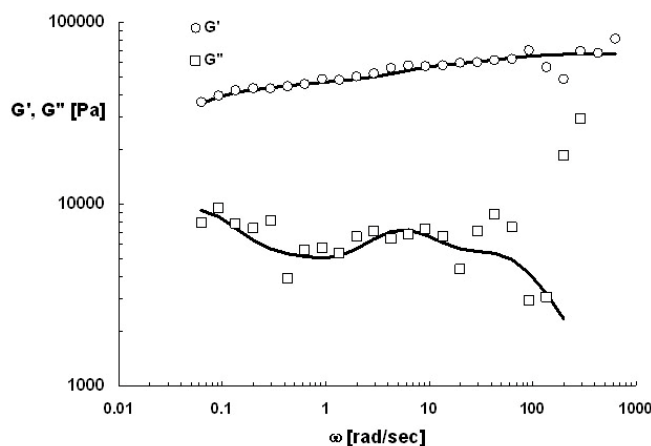
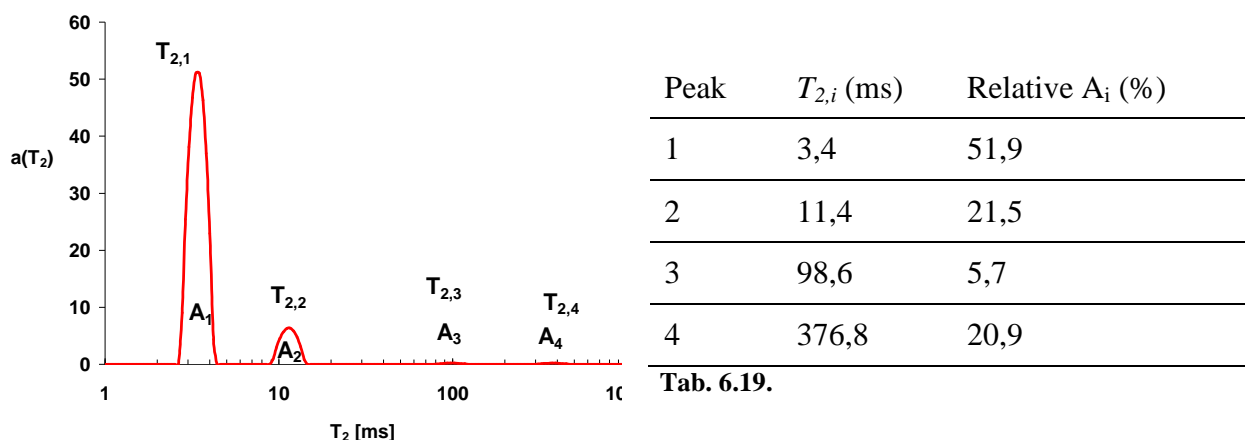


Fig. 6.62: mechanical spectra (FS test) of Pluronic™-alginate hydrogel at 25°C. The continues line represent generalized Maxwell model best fitting.

Figure 6.63, reports the T_2 relaxation spectrum obtained by LF-NMR measurements at 25°C. The presence of 4 proton aggregation states are found. In order to assign a physical meaning

to each peak, the experimental data of peak relative area A_i and mean peak relaxation time $T_{2,i}$ (Tab. 6.19) were compared with the theoretical relative areas calculated considering the hydrogen percentage in the species present in the system.



Tab. 6.19.

Fig. 6.63: Pluronic™-alginate hydrogel T_2 distribution at 25°C. Four peaks were detected.

The calculation was realized as previously described for the single polymer considering that, in this case, there are three species: water, alginate and Pluronic™.

Theoretical relative H₂O area: 83,27 %

Theoretical relative alginate area: 0,77%

Theoretical relative Pluronic™ area: 15,95%

Taking into account this data and the results obtained from alginates and Pluronic™ systems, it is considered that, peak 1 and 2, characterized by the lower relaxation times and corresponding to a relative area of about 75%, can be assigned to the water entrapped into the polymeric mesh. These two components consider also polymer ¹H.

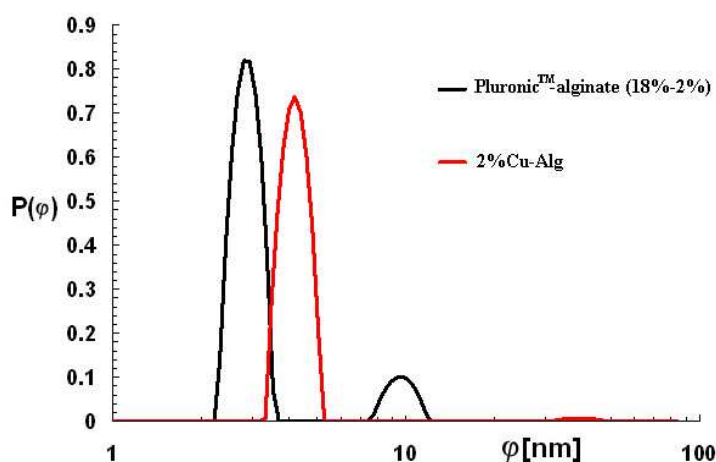


Fig. 6.64: Pluronic™-alginate hydrogel mesh size distribution obtained by NMR-rheology. For comparison, also 2% copper alginate (2%Cu-Alg) is reported.

Once assigned the meaning to each peaks, the system mean relaxation time $\bar{T}_2=5,8$ ms and $k=1,19$ (ms/nm) was calculated. The conversion of the T_2 distribution in mesh size distribution is reported in *figure 6.64*. As evidenced by this figure, the addition of Pluronic™ does not change the bimodal nature of the pores distribution but it causes a general reduction of the mesh size.

6.7.1.2 – Structural analysis by Cryoporometry

The DSC trace shows that all the water is contained within the mesh of the gel because there is no melting peak around 0°C (*Fig. 6.65*).

The mesh size distributions are reported in *figure 6.66* assuming spherical ($z=3$) and the cylindrical ($z=2$) geometry. In both cases the distribution is unimodal. In the spherical geometry, the maximum probability occurs at 80 nm (range within 27 nm - 200 nm) while, in the cylindrical geometry, the maximum probability corresponds to 30 nm (range within 10 nm - 100 nm). The non-freezable water layer is $\beta=0,88$ for the spherical geometry and $\beta=0,66$ for the cylindrical geometry.

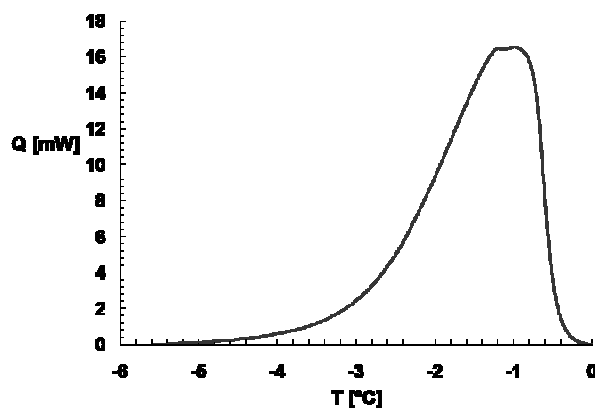


Fig. 6.65: Pluronic™-alginate hydrogel DSC trace.

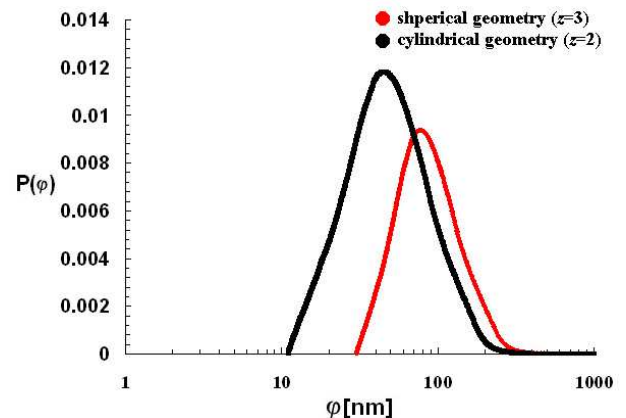


Fig. 6.66: Pluronic™-alginate hydrogel mesh size distribution obtained by Cryoporometry assuming spherical ($z=3$) and cylindrical ($z=2$) pores geometry.

The comparison of mesh size distribution obtained by NMR-rheology and Cryoporometry, reveals big differences for what concern amplitude and position of the most probable diameter (*Fig. 6.67*). The differences could be due to mesh enlargement provoked by water freezing. In addition heating and cooling speed could influence the final result. Nevertheless, assuming a cylindrical pores geometry, the difference between the two methodologies are reduced at least for what concerns the dimension of the most frequent diameter.

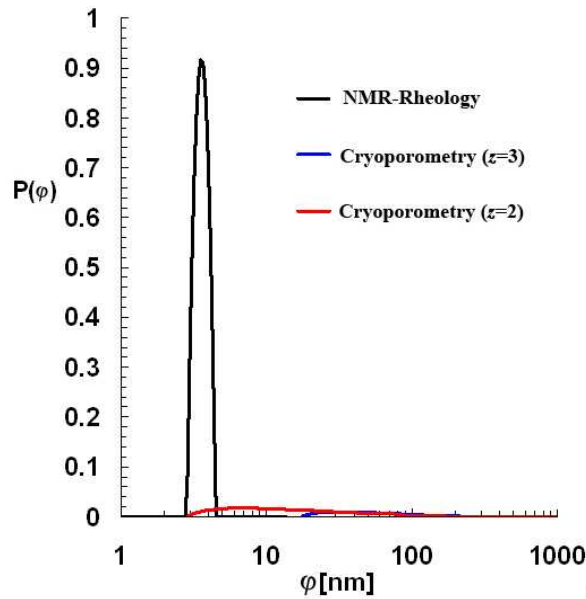


Fig. 6.67: comparison between mesh size distribution by NMR-rheology and Cryoporometry assuming spherical ($z=3$) and cylindrical ($z=2$) pores geometry.

6.7.2 – Alginate-dextran methacrylate hydrogel systems

Two types of alginate-dextran methacrylate hydrogel systems was considered in this studies. The first is composed by 3% alginate (Protanal™ LF10/60) crosslinked by calcium cations with 5% of D40 5% methacrylate (A3D40MA5%). The second is composed by 3% alginate crosslinked by copper cations with 5% of D500 30% methacrylate (A3D500MA30%). Moreover, the systems aging was considered in the T_2 relaxation times distribution characterization.

6.7.2.1 – Macroscopic characterizations by rheological studies

After the preliminary SS tests, the FS tests was performed at 25°C and 3 Pa and the resulting mechanical spectra are showed in *figure 6.68* for A3D40MA5% and A3D500MA30%.

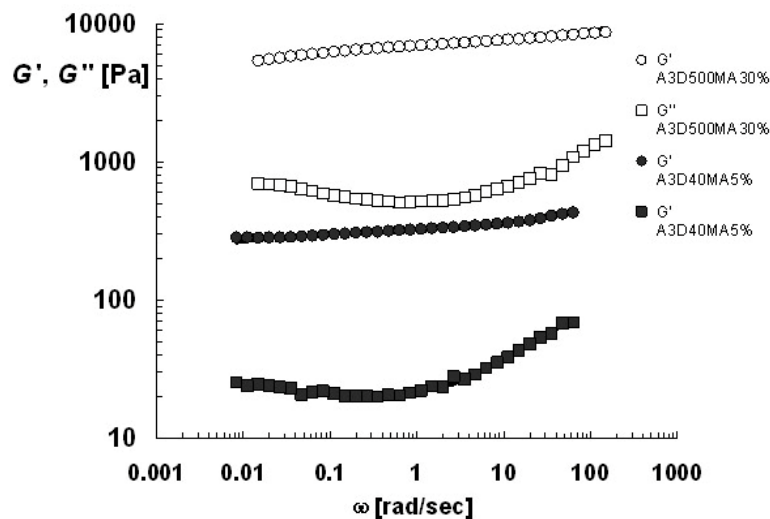


Fig. 6.68: mechanical spectres (FS tests) of alginate-dextran methacrylate hydrogels at 25°C.

On the basis of Flory and equivalent network theories [1, 5], the crosslink density ρ_x and mean mesh size ϕ were calculated; *table 6.20* reports their values.

	crosslink density ρ_x (mol/cm ³)	mean mesh size ϕ (nm)
A3D40MA5%	$2,1 \times 10^{-7}$	24,5
A3D500MA30%	$4,4 \times 10^{-6}$	9,0

Tab. 6.20.

6.7.2.2 – Characterization by low field NMR

The low field NMR analysis was performed on both systems A3D40MA5% and A3D500MA30% comparing the results from freshly made gels or gels stored 15 days at room temperature (aged systems). Moreover, the effect of the temperature was considered analyzing the freshly made systems at 25°C and 37°C and the aged systems at 15°C, 25°C and 37°C. In all the considered situations and systems, the analysis shows the presence of 4 components (4 peaks).

Focusing on the A3D40MA5% aged system, *figure 6.69* reports the variation of the mean relaxation times of each peak ($T_{2,i}$) versus temperature. The peak at $T_{2,4} \approx 900$ ms certainly corresponds to the water outside the gel systems because of its elevated relaxation time and low relative area ($A_4 \approx 0,1\%$). Moreover, the $T_{2,4}$ values have the tendency to increase with the temperature. Indeed, as discussed above, only the free water hydrogens increase its mobility (and therefore the T_2) with the temperature while, the water hydrogen entrapped inside the meshes or the polymer hydrogen do not change significantly with temperature. *Figure 6.69* makes clear that only $T_{2,4}$ significantly increases changing the temperature from 15°C to 37°C while the others remain constant. Indeed only in this case T_2 increase is significantly bigger than the standard deviation associated to $T_{2,1}$ at 25°C. The lower $T_{2,1} \approx 9$ ms, can be reasonably attributed to the polymer hydrogens since the relaxation time value correspond to very low mobility hydrogen and moreover, the experimental relative area ($A_1 \approx 3\%$) is similar to the theoretical relative area calculated for the polymer phase ($\approx 2,5\%$). The others two, $T_{2,2}$ and $T_{2,3}$ (respectively ≈ 20 ms and ≈ 60 ms), probably are related to the hydrogen of the water entrapped into the polymeric meshes. Indeed, the relative areas together represent about the 97% of all the system hydrogens

A similar interpretation can be extended to the A3D500MA30% aged system (*Fig. 6.70*) with the exception of the component with lower relaxation time $T_{2,1}$. In this case, the relative area A_1 is much more evident, corresponding to the 20-30% of the total. Notably, A3D500MA30% system is characterized by relaxation times generally lower than the correspondent T_2 in the A3D40MA5% system. This result, is in agreement with the rheological evidences.

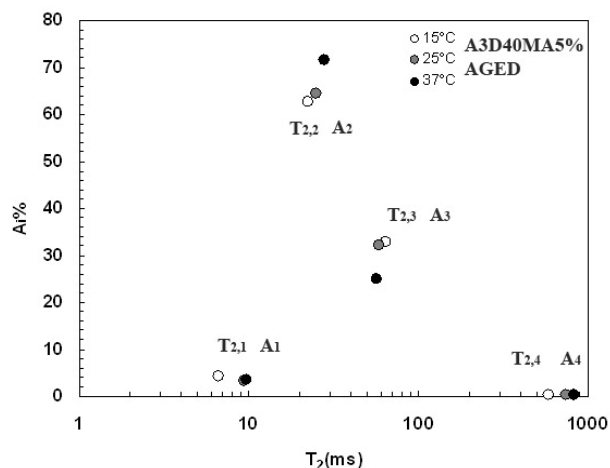


Fig. 6.69: A3D40MA5% aged system. Temperature effect on the peaks mean relaxation times ($T_{2,i}$).

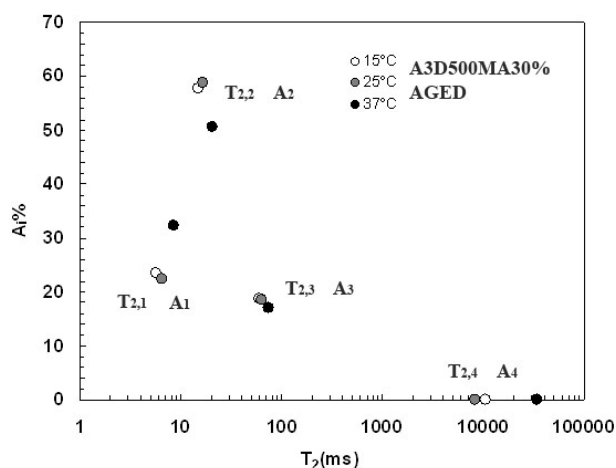


Fig. 6.70: A3D500MA30% aged system. Temperature effect on the peaks mean relaxation times ($T_{2,i}$).

Freshly made systems relaxation times $T_{2,i}$ and relative areas A_i at 25°C are reported in tables 6.21 and 6.22 for A3D40MA5% and A3D500MA30% respectively.

Peak	$T_{2,i}$ (ms)	Relative A_i (%)
1	38	48,4
2	87	20,0
3	363	24,4
4	678	7,2

Tab. 6.21: A3D40MA5% 25°C.

Peak	$T_{2,i}$ (ms)	Relative A_i (%)
1	32	57,4
2	84	30,6
3	351	7,6
4	1013	4,4

Tab. 6.22: A3D500MA30% 25°C.

Both systems have similar $T_{2,i}$ values. Moreover, no relaxation times related to the polymer phase can be detected (theoretical relative area = 3%). The different behavior between freshly made and aged systems is probably related to the water loss by aged hydrogels that causes the shrinking of the polymeric network. Indeed, A_4 is negligible in aged systems.

The temperature influence on the relaxation time $T_{2,i}$ and relative areas A_i of the freshly made systems, can be appreciated in figures 6.71 and 6.72 for A3D40MA5% and A3D500MA30% respectively. All the peaks relative area remain practically constant. Instead, mean relaxation times $T_{2,3}$ (peak 3) and $T_{2,4}$ (peak 4) increase with temperature this indicating the relation of these two peaks with the water outside the network. On the contrary, the temperature does not have significant effects on the $T_{2,1}$ (peak 1) and $T_{2,3}$ (peak 3). Therefore, these components can be assigned to the water entrapped within the polymeric meshes.

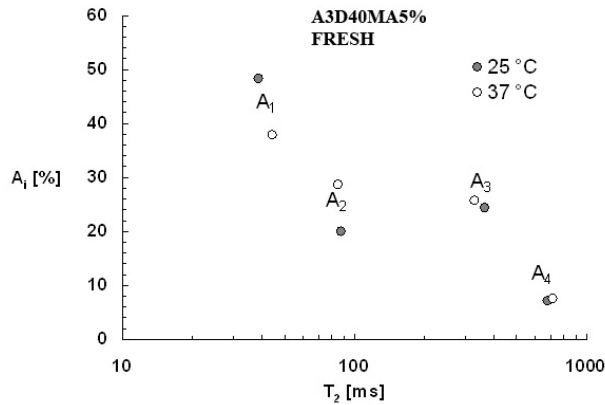


Fig. 6.71: temperature effect on the peaks mean relaxation times ($T_{2,i}$) on freshly made A3D40MA5%.

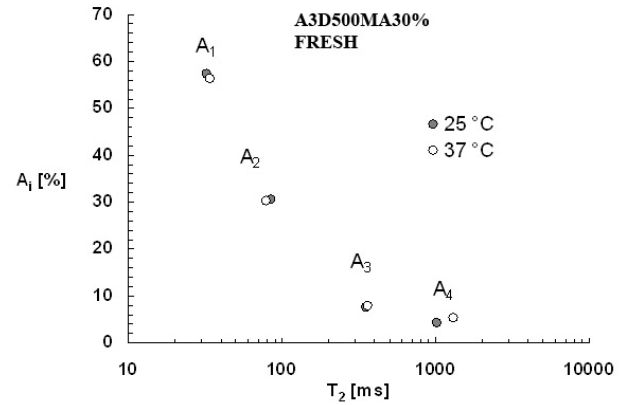


Fig. 6.72: temperature effect on the peaks mean relaxation times ($T_{2,i}$) on freshly made A3D500MA30%.

6.7.2.3 – Pores size distribution studies

Based on the crosslink densities ρ_x and the relaxation times distributions, it is possible to evaluate the mesh size distribution in the considered systems. *Figures 6.73* and *6.74* show the bimodal pores size distribution respectively for A3D40MA5% and A3D500MA30%. In the first case, the peaks (in blue) are centered on 16 nm and 40 nm. In red it is also shown the comparison with the cryoporometric results ($z=3$: spherical geometry) showing a monodisperse distribution matching quite well rheology diameters range. In the second system, the bimodal distribution obtained from NMR-rheology results (in blue) is centered on 7 nm and 16 nm while, the cryoporometric results (in red) is mismatching because it does not change significantly from the previous one.

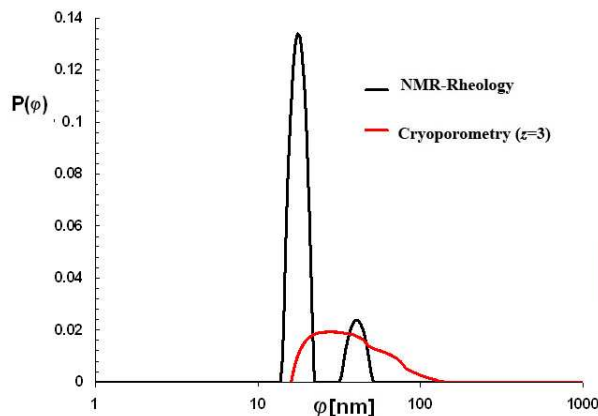


Fig. 6.73: comparison between mesh size probability distribution by NMR-rheology and Cryoporometry assuming spherical ($z=3$) pores geometry for the A3D40MA5% aged system.

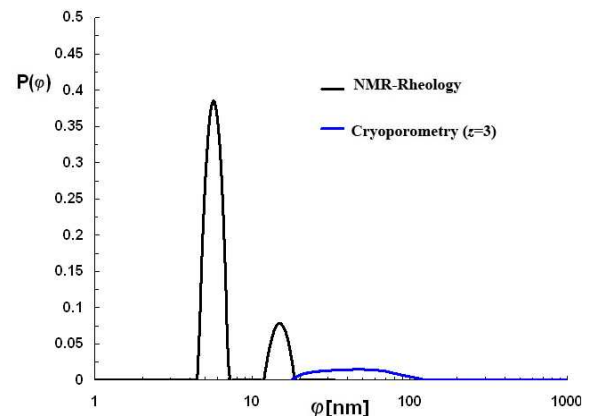


Fig. 6.74: comparison between mesh size probability distribution by NMR-rheology and Cryoporometry assuming spherical ($z=3$) pores geometry for the A3D500MA30% aged system.

6.8 – Biological evaluation of Pluronic™-alginate system for NABDs delivery

6.8.1 – Introduction

In order to evaluate the potential use of the polymeric blends for the NABDs controlled release, a cellular model was selected for testing the release and uptake efficiency of nucleic acids complexes. The polymeric blend was constituted by Pluronic™ F127 18% and 2% alginate (Protanal™ LF10/60) *non-reticulated*. The nucleic acid was represented by a 21 base long siRNA called NAM-R which has demonstrated from previous study an antiproliferative effect [14]. Due to the high synthesis costs of siRNAs, the experiments shown in this work have been performed only in part with the NAM-R siRNA therefore, for the most part it was used the correspondent DNA duplex, here referred as NAM-D, carrying the same sequence as the respective siRNA. The nucleic acids were complexed with liposomes before being embedded into the polymeric blend. The alginate was not crosslinked in the system because, as demonstrated from the above data, the alginate network is too tight for a proper release of big complexes. Therefore, during these studies, the gelation was allowed only for Pluronic™. The cellular model used was represented by two cell lines: vascular smooth muscle cells (VSMC) and human umbilical vein cell (HUVEC).

The basic idea is to realise a system that behaves as a solution in order to be easily injected on the treated area [15]. Then, body temperature causes the gelation of the Pluronic™ portion of the blends and finally, a bivalent cations solution can reinforce the systems creating an outer alginate gelation that shields the system from the blood flow and prevent the siRNA complex loosing into the blood stream [16-17].

6.8.2 – Choice of liposomes

The ideal delivery system for some types of vascular pathology should block the proliferation of VSMC without affecting the proliferation of endothelial cells (EC), here represented by the HUVEC [18]. Uptake studies in VSMC and HUVEC were performed by a FITC-labeled NAM-R complexed with several commercial liposomes. Commercial liposomes were chosen to allow their immediate use in future *in vivo* experiments, thus overcoming synthesis-related problems.

Cellfectin™ and Lipofectin™ (*Fig. 6.75*) complexed with the FITC-labeled NAM-R prepared in serum free medium gave the best results as the two cationic liposomes were efficiently uptaken by VSMC but not EC, fulfilling the above mentioned requirement. Notably, in VSMCs,

uptake efficiencies were not substantially modified preparing the liposome (Cellfectin™/Lipofectin™) and NAM-R complexes in serum free medium, H₂O and PBS (Fig. 6.76).

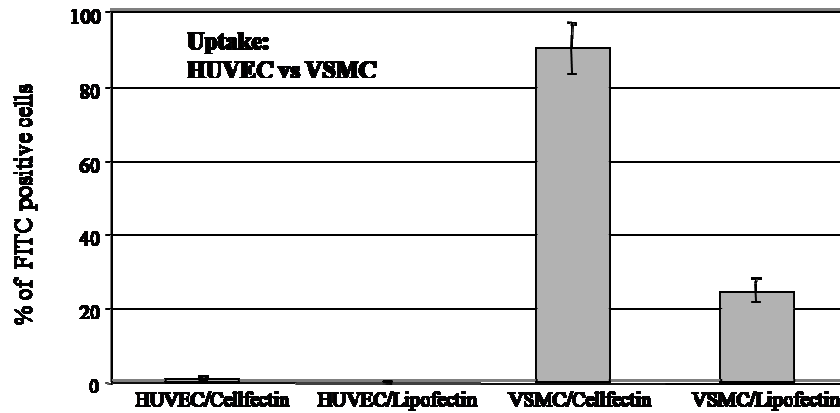


Fig. 6.75: Uptake efficacies in VSMC and HUVEC with either the cationic liposome Cellfectin™ or Lipofectin™ in the presence of serum free medium. The amount of FITC positive cells (reported on the vertical ordinate axis as % of total cell population; means \pm SEM, n=4) were evaluated by flow cytometry. It is evident the much higher transfection efficacy in VSMC compared to HUVEC.

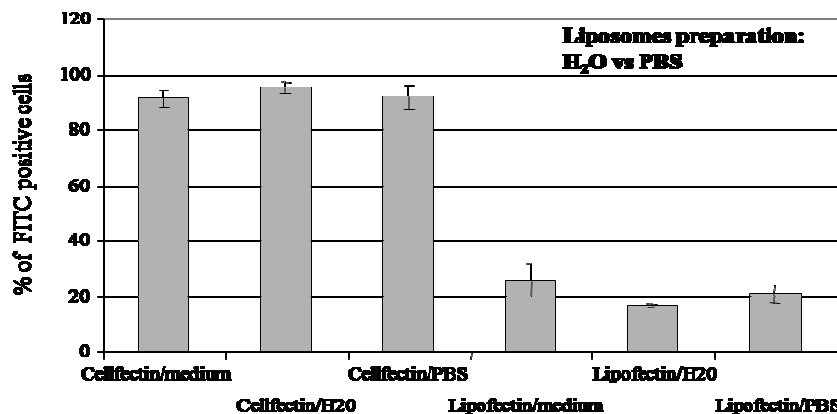


Fig. 6.76: Uptake studies in VSMC conducted preparing liposome/ NAM-R complexes in H₂O and PBS; uptake efficiencies were comparable to those observed preparing liposome/NAM-R complexes in serum free medium (means \pm SEM, n=4).

6.8.3 – Characterization of liposomes particle size

Based on the above reported uptake studies, liposomes Cellfectin™ and Lipofectin™ were undertaken for further analysis. To determine a possible relation between particle size and the Pluronic™ structuring process, complex dimensions were determined both in the presence (PBS) and absence (H₂O) of salts. Figure 6.77 reveals that whereas Lipofectin™ particles, 20 minutes after preparation, are bigger in PBS than in H₂O (P<0.05), the same is not evident for Cellfectin™ liposomes (P>0.05). The addition of NAM-D to Cellfectin™ (P<0.05), but not to Lipofectin™, leads to a reduction in the complex diameters, both in the presence of H₂O and PBS. The polydispersity index, ranging from 0.1 to 0.35, suggests that diameter variations are representative

for the vast majority of the particles. Finally, Lipofectin™ liposomes, regardless of the presence/absence of NAM-D, tend to be smaller in size compared to Cellfectin™ liposomes, especially when H₂O is used for the preparation of the complexes.

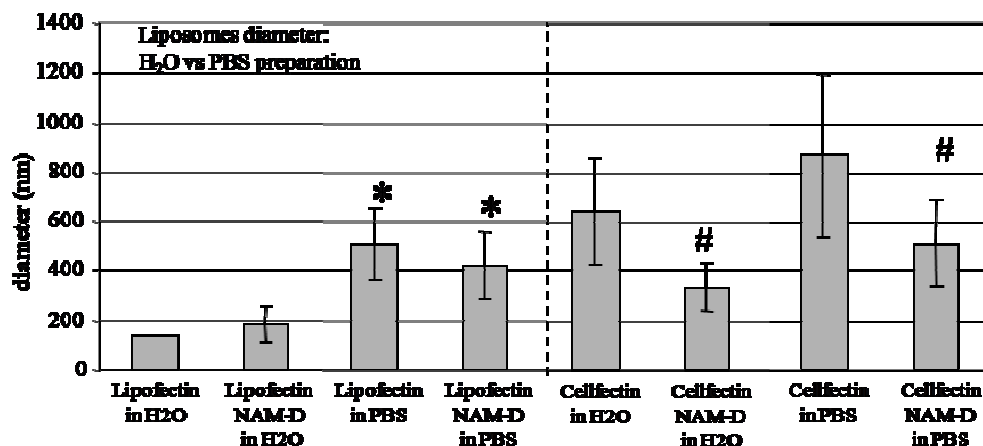


Fig. 6.77: Liposomes diameter determination (d_m) in H₂O and PBS either in the presence or in the absence of NAM-D. Diameters were measured 20 minutes after liposomes preparation. * $P < 0.05$ diameters increase of Lipofectin™ complexes in PBS vs H₂O; # $P < 0.05$ diameter reduction of Cellfectin™ NAM-D vs Cellfectin™ alone (means \pm SEM, $n=4$).

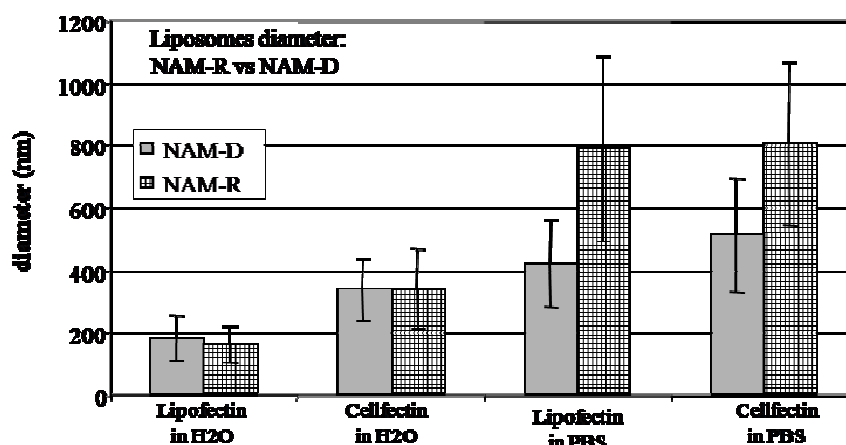


Fig. 6.78: comparison between liposomes diameters evaluated in the presence of either NAM-D or NAM-R; in H₂O no differences were detectable; in the presence of PBS, complexes containing NAM-R just showed the tendency to display an increased diameter (means \pm SEM, $n=4$).

The same sequence and the chemical similarity between NAM-D and NAM-R should guarantee a similar behavior with regard to the effects on liposome diameter. The data reported in figure 6.78 indicate that no significant differences were induced by NAM-R or NAM-D on liposome diameter in H₂O. In the presence of PBS, NAM-R determined the tendency to an increase in the diameter, a variation which, however, was not significantly different from that induced by NAM-D ($P > 0.05$).

6.8.4 – Zeta potential determination

As it is known that charged particles can affect the process of Pluronic™ structuring [19] and that liposomes are charged components, the superficial electric charge zeta-potential of the liposomes was measured. To evaluate the possible influences of salts, the measurements were evaluated in H₂O, KCl and PBS. For both liposomes under investigation, the particle surface is positively charged and the charge does not substantially depend on the salt environment (*Fig. 6.79*). The addition of NAM-D, negatively charged molecules, induces a neatly inversion of global charge polarity.

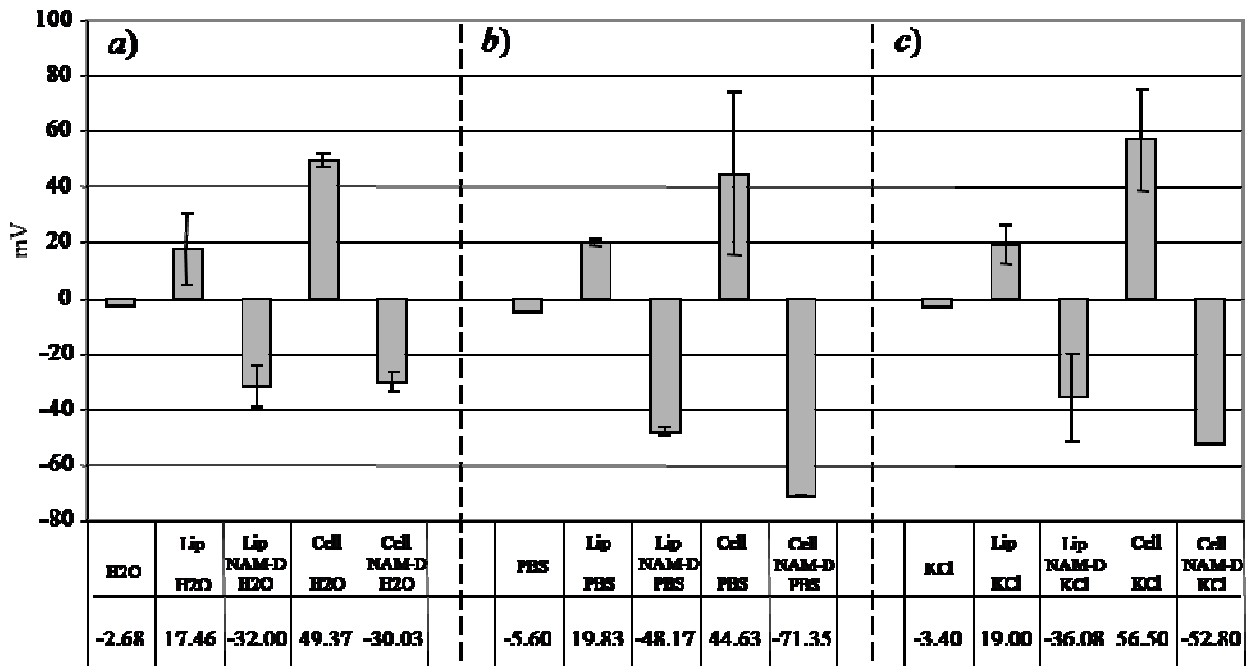


Fig. 6.79: Liposomes Zeta potential (mV) was evaluated in H₂O (*a*), in PBS (*b*) and KCl (*c*) either in the presence or absence of NAM-D. For both kinds of liposomes, regardless of the salt environment in which they have been prepared, particles surface display a positive charge; the addition of NAM-D, induces a neatly inversion of charge sign both for Lipofectin and Cellfectin complexes, regardless of the external medium considered. Data are expressed as means \pm SEM (n=9). R/D = NAM-R/NAM-D

These data indicate that at least part of the negatively charged NAM-D molecules lies on the liposome surface, a fact confirmed by the visualization of NAM-D on the surface of Lipofectin™ liposome (*Fig. 6.80a*), as evidenced by Osmio staining (dark zones). Similar results were obtained preparing the complexes in PBS, using Cellfectin™ liposomes and NAM-R (data not shown). It should be noted that the distribution of NAM-D on liposome surface is not uniform. This implies that negatively and positively charged areas co-exists on liposome surface. Thus, given the difficulties of negatively charged molecules to cross cellular membranes [20], it is reasonable to assume that the liposome complexes interacts with VSMC membranes by the positively charged spots allowing the transfer of NAM into the cells. The fact that this process occurs efficiently in

VSMC but not in EC, reflects the differences in cell membrane composition and charge. NAM-D may be also seen on the liposome particle (*Fig. 6.80b*) a fact observed for other DNA/liposome complexes [21].

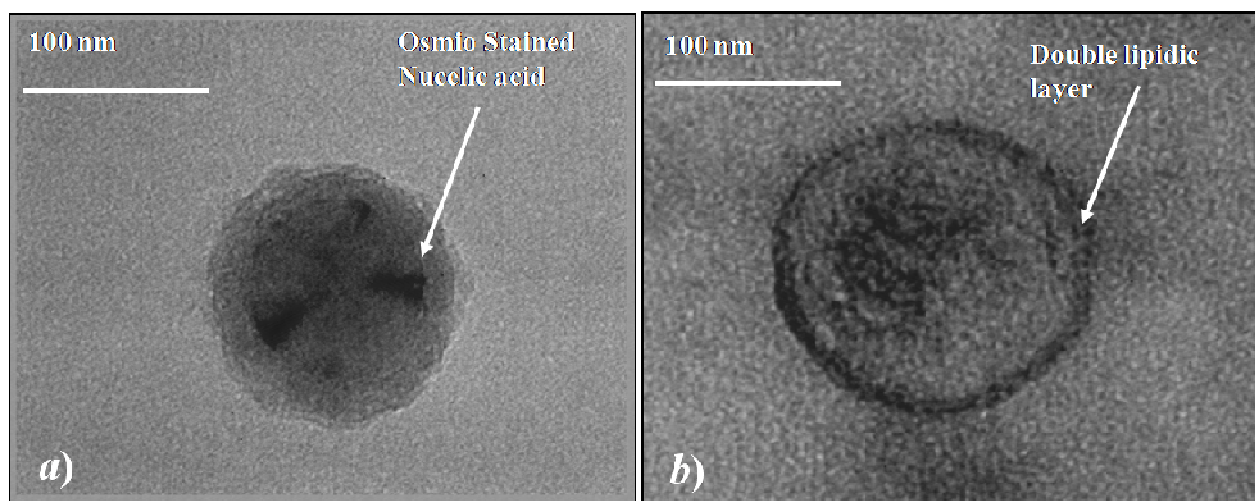


Fig. 6.80: Electronic microscopy images of Lipofectin-NAM-D. *a)* Lipofectin/NAM-D (180.000x) image was taken after preparing the complexes in H₂O and exposing them to osmio vapor. It is evident the grossly rounded shape of the particle with the black areas on the surface of the particles representing the osmio stained NAM-D molecules. *b)* As in *a)* except that osmio staining was omitted and the complexes allowed to dry; it is evident the spherical lipid bi-layer of the particle.

6.8.5 – Rheological characterization

After the evaluation of the structural properties of the alginate and Pluronic™ alone and blended together in an hydrogel system, the attention was focused on the effects induced by liposomes complexes (prepared in water) on the blend rheological properties. *Figure 6.81* reports the trend of the complex modulus G^* as function of the deformation γ (37°C; 1 Hz), relative to Pluronic™-18% (P18), Pluronic™-alginate-18%-2% (P18-A2), Pluronic™-alginate-18%-2%+Lipofectin™ (P18-A2-L) and Pluronic™-alginate-18%-2%+Cellfectin™ (P18-A2-C) systems. The stress sweep curves do not substantially differ from each other and, consequently, the linear viscoelastic range, similar for all the shown systems, extends up to a critical deformation $\gamma_0 \approx 0.002$. Accordingly, as $G^* \approx 1.5 \times 10^4$ Pa, the critical stress is $\tau_c \approx 30$ Pa. *Figure 6.83* shows the difference in the G' trend as function of the temperature during the gelation process relative to P18, P18-A2, P18-A2-L and P18-A2-C systems (1 Pa, 1 Hz, 37°C). In particular for the P18 curve, it turns out that the structuring process occurs according to the two steps mechanism suggested in literature [10-11]. Indeed, up to approximately 22°C, the system behaves as a viscous liquid, since its elastic component G' , is always very small. In these conditions, the system can be seen as a diluted Pluronic™ micelles suspension whose continuous phase is made up by Pluronic™ aqueous solution. A modest temperature increment leads to important interactions between individual

micelles so that the suspension becomes sufficiently concentrated and every micelle begins to be caged by its neighbours. This is the reason why G' undergoes in a sudden increase. Further heating produces an additional increase of micelles phase volume and, correspondingly, also the micelle caging can undergo rearrangements as demonstrated by the curves slope variation.

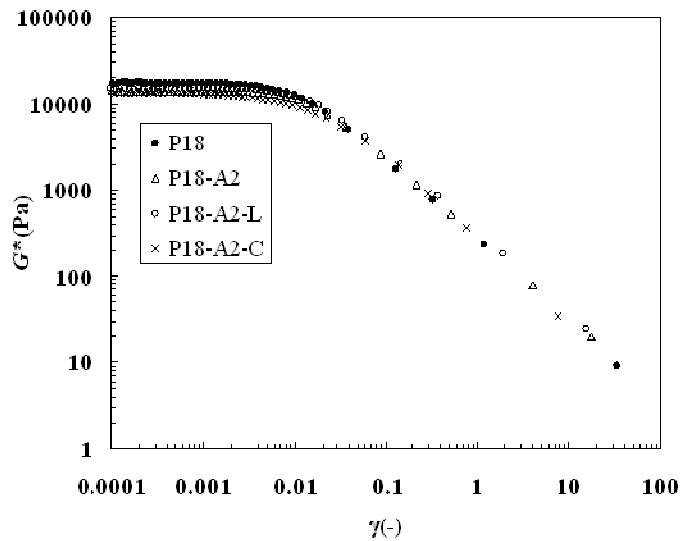


Fig. 6.81: stress sweep curves (1 Hz, 37°C) relative to the Pluronic™-18% (P18), Pluronic™-alginate-18%-2% (P18-A2), Pluronic™-alginate-18%-2%+Lipofectin™ (P18-A2-L) and Pluronic™-alginate-18%-2%+Cellfectin™ (P18-A2-C) systems. G^* is the complex modulus (Pa), while γ is deformation.

According to literature evidence [19, 22-23], the addition of the alginate, a sodium salt, leads to a T_{st} decrease. In particular, in the considered system, this reduction is around 2 °C (Fig. 6.82). Finally, liposomes addition ($70\mu\text{g}/\text{cm}^3$) further anticipates the system structuring transition enlarging the width of the transition zone. If initially the liposomes favour the structuring, then, they would hinder the development of the entire process as their presence makes the rearrangements of Pluronic™ micelles more critical. Indeed, liposomes represent discontinuity elements and, when temperature effects prevail, a complete structuring cannot occur until they find a stable position inside the network. Notably, the structuring zone enlargement induced by Cellfectin™ is more pronounced than that corresponding to Lipofectin™. Assuming that the presence of Pluronic™ and alginate do not sensibly alter the liposome dimensions and surface charges measured (Fig. 6.77 and 6.79), the difference in diameter and zeta potential above discussed are reasonably, at the basis of the different temperature sweep curves (Fig. 6.82). Diameter and superficial charge factors could contribute both to the differences observed in temperature sweep curves [24].

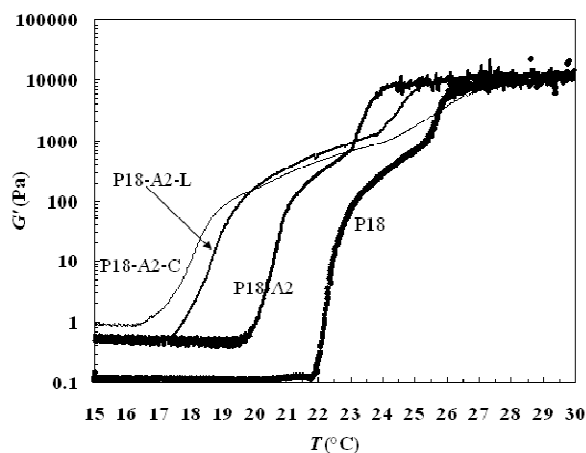


Fig. 6.82: G' temperature sweep curves ($\tau=1$ Pa, 1 Hz, 37°C) relative to the Pluronic™-18% (P18), Pluronic™-alginate-18%-2% (P18-A2), Pluronic™-alginate-18%-2%+Lipofectin™ (P18-A2-L) and Pluronic™-alginate-18%-2%+Cellfectin™ (P18-A2-C) systems.

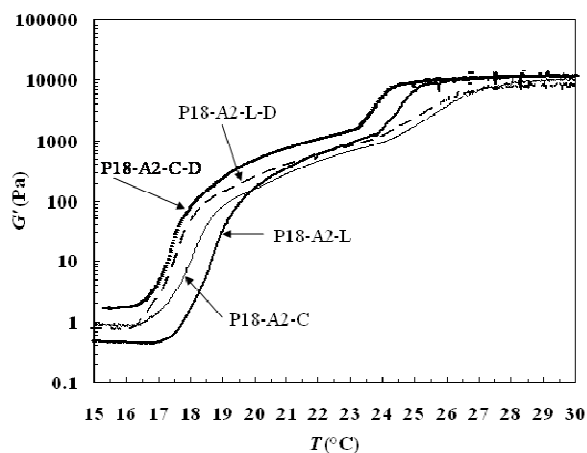


Fig. 6.83: G' temperature sweep curves ($\tau=1$ Pa, 1 Hz, 37°C) relative to Pluronic™-alginate-18%-2%+Lipofectin™ (P18-A2-L), Pluronic™-alginate-18%-2%+Cellfectin™ (P18-A2-C), Pluronic™-alginate-18%-2%+Lipofectin™-NAM-D (P18-A2-L-D) and Pluronic™-alginate-18%-2%+Cellfectin™-NAM-D (P18-A2-C-D) systems. Complexes were prepared in H₂O.

A possible alternative interpretation was offered by the results obtained after the addition of the NAM-D to both liposomes. *Figure 6.83* shows the G' trend ($\tau=1$ Pa, 1 Hz, 37°C) as function of the temperature for the polymeric blend loaded by Lipofectin™ (P18-A2-L), Cellfectin™ (P18-A2-C), NAM-D-Lipofectin™ (P18-A2-L-D) and NAM-D-Cellfectin™ (P18-A2-C-D) complexes. From this figure it is possible to infer that, in absence of NAM-D, Lipofectin™ and Cellfectin™ differ in terms of dimensions (*Fig. 6.77*, H₂O systems), surface charge (*Fig. 6.79*, H₂O) and respective G' vs T curves (*Fig. 6.83*, P18-A2-L and P18-A2-C). In contrast, when liposomes-NAM-D complexes are considered, the Lipofectin™-NAM-D and Cellfectin™-NAM-D are characterised by a very similar negative surface charge (*Fig. 6.79*, H₂O) but different dimensions (*Fig. 6.78*, H₂O systems). In this case, the differences in the G' vs T curve relative to P18-A2-L-D and P18-A2-C-D systems, although present, are less evident than in the previous case, in particular at $T < 20$ °C. This hypothesis is in agreement with the anticipation of gelation caused by charged compounds [19, 22-23]. Notably, no significant effects on gelation kinetic were noted in the presence of NAM-D alone (data not shown). *Figure 6.83* shows also that, the addition of NAM-D to liposome, regardless of the liposome used, determines a decrease of the structuring temperature T_{st} with Cellfectin™-NAM-D being again characterized by an anticipation of the structuring, compared to Lipofectin™-NAM-D. Considering the *in vivo* applications, this aspect would favour Lipofectin™ as we need that the beginning of the structuring process occurs at a temperature as close as possible to physiological conditions in order to minimize any pre-occurring structuring during the *in situ* positioning of the polymeric blend.

6.8.6 – Release and uptake studies from the PluronicTM-alginate blend

In order to evaluate the release and uptake efficiency of the siRNA liposome complex from the PluronicTM-alginate blend, transfection experiments were performed on VSMCs cell line using a NAM-R siRNA tagged with FITC fluorescence dye (FITC-NAM-R). The lack of an organized tissue structure *in vitro* limits the VSMC viability compared to the *in vivo* condition. Thus, the transfer of the FITC-NAM-R by liposomes has to be limited to a defined short time period. For VSMCs was found in literature 2-4 hours [14] to be the optimal and maximal release time. Due to the limited release time, we decided to study the transfer of FITC-NAM-R complexed with CellfectinTM, which gave higher transfer rates compared to LipofectinTM.

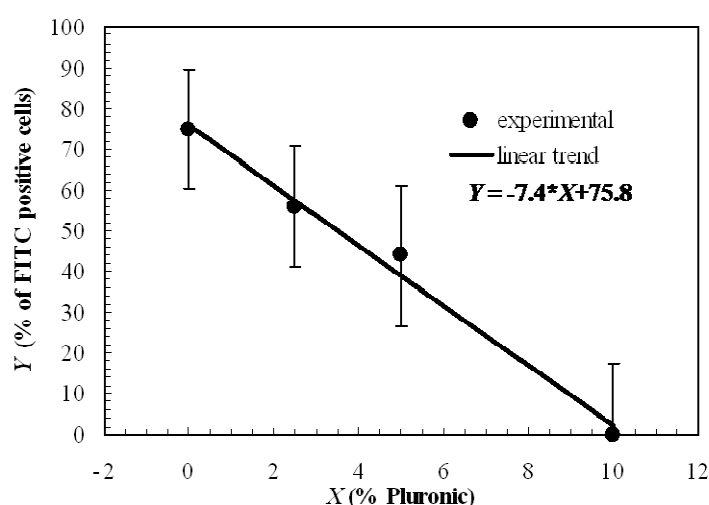


Fig. 6.84: NAM-R/CellfectinTM release from the PluronicTM-alginate gel. VSMCs were over-laid with FITC-NAM-R/CellfectinTM embedded into the PluronicTM-alginate gel prepared at different concentrations; after removing the gel, green fluorescent cells were fixed and counted by a fluorescence microscope. Positive cell were considered those with at least one clear spot of green fluorescence within the cytoplasm. A clear linear decrease in the number of green fluorescent cells is evident when the FITC-NAM-R/CellfectinTM is released from increasing concentrations of PluronicTM. Data are shown as mean \pm SEM, (n = 3).

To study the release of the complexes FITC-NAM-R/CellfectinTM from the PluronicTM-alginate blend, the complexes were mixed with increasing concentrations of the polymeric blend (from 0% to 20% of PluronicTM and 2% alginate). VSMC uptake was evaluated counting the number of green fluorescence positive cells (FITC positive) and observing the concentration of green fluorescence per cell four hours after PluronicTM overlay. As reported in *figure 6.84*, an inverse linear relation between the amount of green fluorescent cells and the % of PluronicTM used is evident. At 20% of PluronicTM, the amount of green fluorescent cells was vanishing. In addition to the decrease in the number of green fluorescent cells in the presence of PluronicTM, it was observed a reduction in the amount of green fluorescence per cell compared to cells receiving the complexes without the polymeric blend (compare *figures 6,85b* with *d* and *f*).

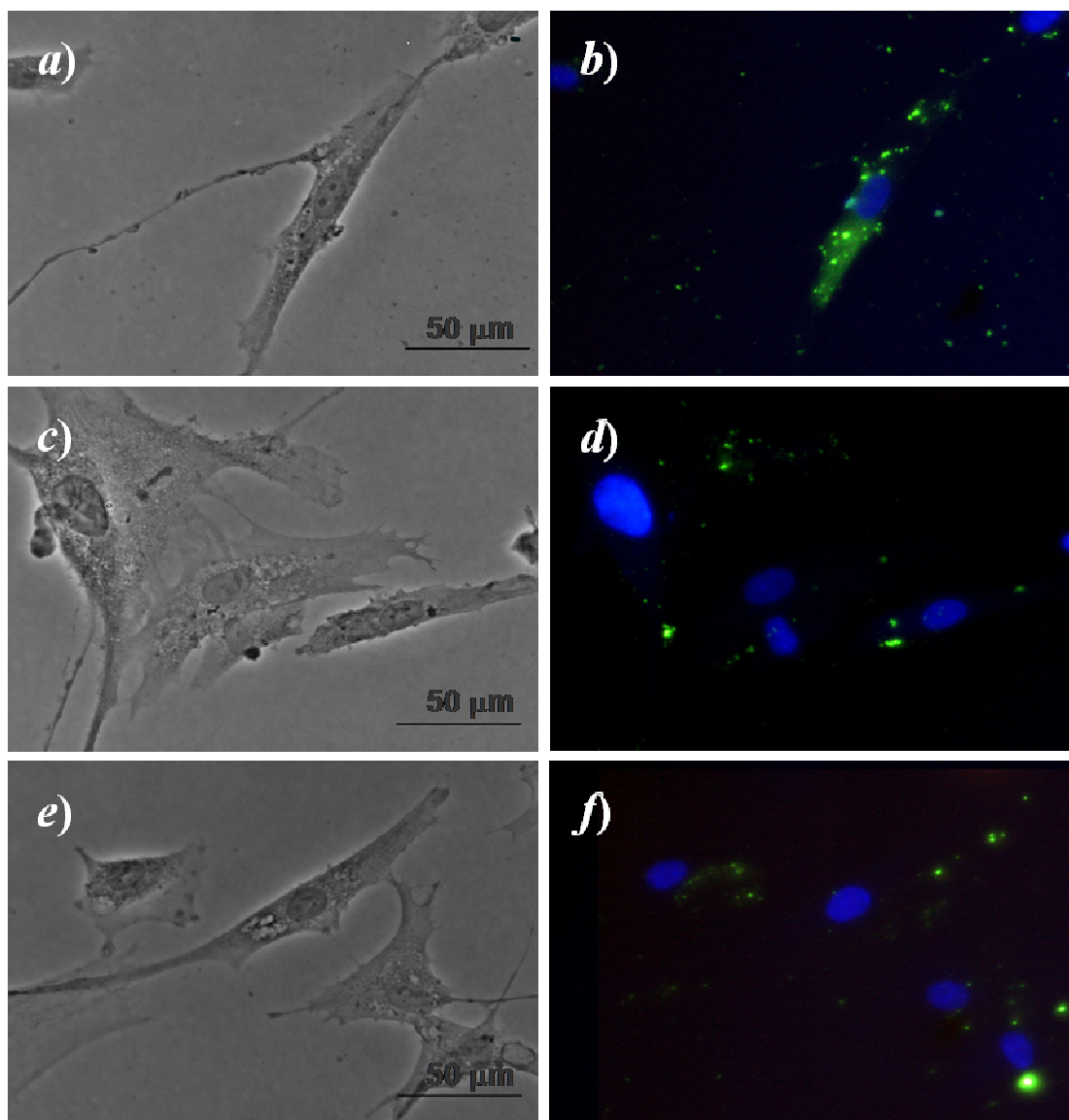


Fig. 6.85: NAM-R/Cellfectin™ release from the Pluronic™-alginate gel. Pictures of the fixed cells are shown at 40x magnification; in *a-b*, *c-d* and *e-f* are shown picture of VSMCs trasduced by FITC-NAM-R/Cellfectin™ without, with 2,5% and 5% of Pluronic™, respectively; *a,c,e*: phase contrast imagines; *b,d,f*: corresponding fluorescence imagines (green; FITC-NAM-R, blue: DAPI stained cellular nuclei).

The data presented clearly indicate that the presence of the polymeric blend, also at low concentration, profoundly retards the release of the FITC-NAM-R/Cellfectin™ complexes, a fact which is evidenced not only by the reduction in the number of green fluorescence cells but also in the reduction of quantity of FITC-NAM-R per cell. This phenomenon is clearly dependent on Pluronic™ concentration, implicating that it is possible to modulate complexes release kinetics on the base of polymeric blend concentration allowing to find optimal release kinetics for the purposed applications.

6.8.7 – Polyplexes transfection experiments

Modelling studies have been demonstrated that the size of the NABD-complexes is a crucial property in release speed from gel systems. A small NABD-complex results in a high release. Accordingly, a release system embedding small NABD-complex turns out to be effective in the first stage of restenosis (see *figure 6.86*) but it is useless for the last stage of the process (late coronary remodeling). On the contrary, systems embedding a big NABD-complex will be effective only for the last part of restenosis process (late remodeling + inflammation). Thus, in order to render the delivery system effective for all the restenosis stages, it could be useful to incorporate both small and big NABD-complex. *Figure 6.86* reports the simulation results of a delivery system embedding both small and big NABD-complex in a ratio R_{bs} ranging from 0,25 to 0,75 [2].

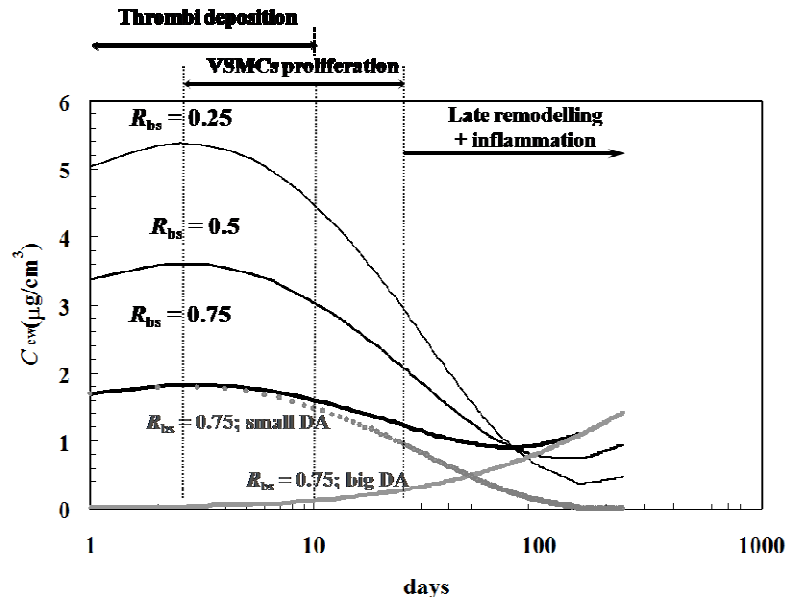


Fig. 6.86: simulation studies of the NABD-complex (or delivery agent, DA) concentration (C_{cw}) temporary evolution, in the coronary wall after the release from gel system. The simulations consider the release of a mixture of big-DA and small-DA embedded into the gel at different initial ratio (total amount of $70 \mu\text{g}/\text{cm}^3$ of DA). R_{bs} is the percentage of the big-DA in the gel: 0,25=25% big (75%small); 0,5=50% big (50%small); 0,75=75% big (25%small). In gray the contributions of big-DA and small-DA respectively, in the case of $R_{bs}=0,75$ are represented.

While liposomes giving origin to big NABD-complex, polymer can give much smaller complex. For example, PHEA ([α,β-poly\(N-2-hydroxyethyl\) D,L-aspartamide](#)) is a synthetic polymer highly water soluble particularly interesting for its biocompatibility. PHAE himself is neutral but can be modified by addition of positively charged side groups in order to obtain cationic polymers that are able to interact with negatively charged nucleic acids and forming polyplexes [25-26]. In order to test smaller NABD-complexes for the siRNA release from 18%Pluronic™-2%alginate hydrogels systems, FITC-GL2 (control siRNA targeting luciferase conjugated with fluorescent dye) was complexed cationic PHAE derivatives and the cellular uptake was evaluated on VSMC cells. Four PHEA derivatives were used: PHEA-spermine (Phea-Sp), PHEA-spermine-butyric

acid (Phea-Sp-C4), PHEA-diethylenetriamine (Phea-Deta) and PHEA-2-aminoethylcarbamate (Phea-Eda) (Fig. 6.87).

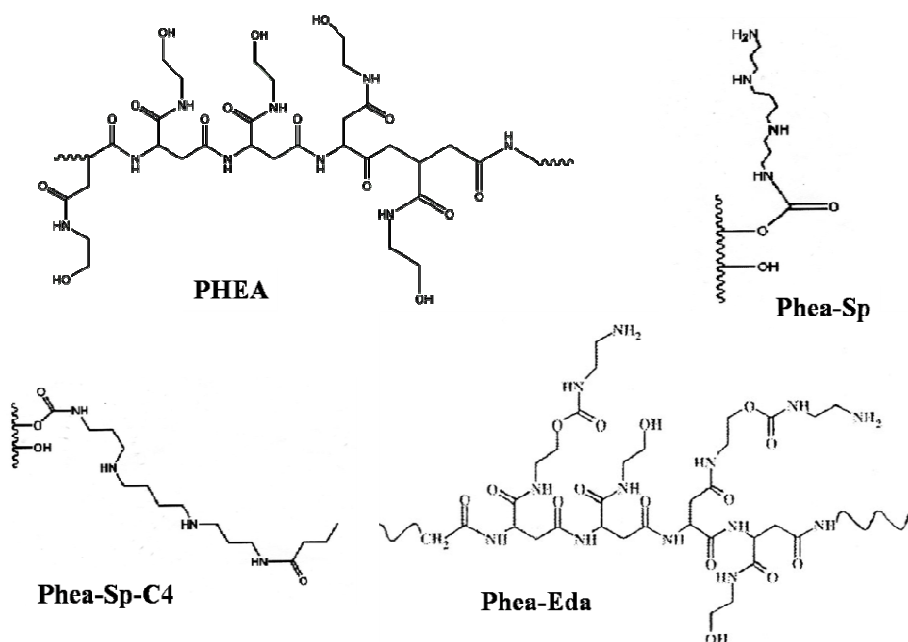


Fig. 6.87: PHEA derivatives

Figure 6.88 shows the results as percentage of FITC positive cells in comparison with the FITC-GL2/Cellfectin™ complex. Unfortunately, even if in the polyplexes formation a high ratio of nucleic acid was used compared to the polymers, only the Phea-Sp polyplexes showed a certain uptake capability but was not sufficient for the purposed applications. The others PHEA derivate polyplexes do not demonstrate any significant transfection properties on VSMC cells. Further studies are required in order to realize a more efficient polyplex to embed in the hydrogels siRNA delivery systems.

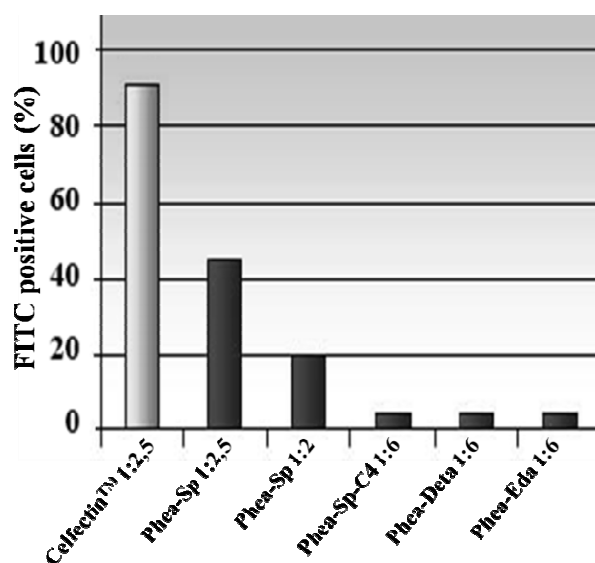


Fig. 9.88: percentage of FITC positive cells in up-take studies on VSMC cells of different PHAE derivatives polyplexes: FITC-GL2/polymer ratio is also showed. In grey the results of FITC-GL2/Cellfectin™ 1:2,5 is also showed.

References

1. Schurz, J., *Rheology of polymer solutions of the network type*. J Prog Polym Sci, 1991. **16**(1): p. 1-53.
2. Davia, L., et al., *Mathematical modelling of NABD release from endoluminal gel paved stent*. Comput Biol Chem, 2009. **33**(1): p. 33-40.
3. Mohrman, D.E. and L.J. Heller, *Cardiovascular physiology*. 4th ed. 1997, New York: McGraw-Hill.
4. Schwinn, D.A., *New Advances in Vascular Biology and Molecular Cardiovascular Medicine* 1998, Baltimore: Williams & Wilkins.
5. Flory, P.J., *Principles of Polymer Chemistry*. 1953, Ithaca, New York: Cornell University Press.
6. Halperin, W.P., et al., *Magnetic Resonance Relaxation Analysis of Porous Media*, in *Molecular Dynamics in Restricted Geometries*, J. Klafter and J.M. Drake, Editors. 1989, John Wiley and Sons: New York. p. 311.
7. Brownstein, K.R. and C.E. Tarr, *Importance of classical diffusion in NMR studies of water in biological cells*. Physical Review A, 1979. **19**: p. 2446-2452.
8. Britton, M.M., R.G. Graham, and K.J. Packer, *NMR relaxation and pulsed field gradient study of alginate bead porous media*. J Magnetic Resonance, 2004. **169**(1): p. 203-14.
9. Vanhamme, L., et al., *MR spectroscopy quantitation: a review of time-domain methods*. NMR in Biomedicine, 2001. **14**(4): p. 233-46.
10. Alexandridis, P. and T.A. Hatton, *Poly(ethylene oxide)-poly(propylene oxide)-poly(ethylene oxide) block copolymer surfactants in aqueous solutions and at interfaces: thermodynamics, structure, dynamics, and modeling*. Colloids Surf A, 1995. **96**: p. 1-46.
11. Lau, B.K., et al., *Micellization to gelation of a triblock copolymer in water: Thermoreversibility and scaling*. J. Polym. Sci. Part B, 2004. **42**: p. 2014-25.
12. Coviello, T., et al., *Structural and rheological characterization of Scleroglucan/borax hydrogel for drug delivery*. Int J Biol Macromol, 2003. **32**(3-5): p. 83-92.
13. Lustig, S.R. and N.A. Peppas, *Solute diffusion in swollen membranes. IX. Scaling laws for solute diffusion in gels*. J Appl Polym Sci, 1988. **36**: p. 735-47.
14. Grassi, G., et al., *Hammerhead ribozymes targeted against cyclin E and E2F1 cooperate to down-regulate coronary smooth muscle cell proliferation*. J Gene Med, 2005. **7**(9): p. 1223-34.
15. Bhargawa, B., et al., *New approaches to preventing restenosis*. British Med J, 2003. **327**: p. 274-9.
16. Blandino, A., M. Macias, and D. Cantero, *Formation of calcium alginate gel capsules: influence of sodium alginate and CaCl₂ concentration on gelation kinetics*. J Biosci Bioeng, 1999. **88**(6): p. 686-9.
17. Liu, X., et al., *Rheology characterization of sol-gel transition in aqueous alginate solutions induced by calcium through in situ release*. Polymer, 2003. **44**: p. 407-12.
18. Imanishi, T., et al., *Sirolimus accelerates senescence of endothelial progenitor cells through telomerase inactivation*. Atherosclerosis, 2006. **189**(2): p. 288-96.
19. Pandit, N.K. and J. Kisaka, *Loss of gelation ability of Pluronic® F127 in the presence of some salts*. Int J Pharm, 1996. **145**: p. 129-36.
20. Zuhorn, I.S. and D. Hoekstra, *On the mechanism of cationic amphiphile-mediated transfection. To fuse or not to fuse: is that the question?* J Membr Biol, 2002. **189**(3): p. 167-79.
21. Zhang, C., et al., *siRNA-containing liposomes modified with polyarginine effectively silence the targeted gene*. J Control Release, 2006. **112**(2): p. 229-39.

22. Su, Y.L., X.F. Wei, and H.Z. Liu, *Effect of sodium chloride on association behaviour of poly(ethylene oxide)–poly(propylene oxide)–poly(ethylene oxide) block copolymer in aqueous solutions*. J Colloid Interface Sci, 2003. **264**: p. 526-31.
23. Anderson, B.C., et al., *The effect of salts on the micellization temperature of aqueous poly(ethylene oxide)-b-poly(propylene oxide)-b-poly(ethylene oxide) solutions and the dissolution rate and water diffusion coefficient in their corresponding gels*. J Pharm Sci, 2002. **91**(1): p. 180-8.
24. Grassi, G., et al., *Characterization of nucleic acid molecule/liposome complex and rheological effects on pluronic/alginate matrices*. Journal of Drug Delivery Science and Technology, 2007. **17**.
25. Giammona, G., B. Carlisi, and S. Palazzo, *Reaction of α,β -poly(*N*-2-hydroxyethyl)-*D,L*-aspartamide with derivatives of carboxy acids*. Journal of Polymer Science Part A: Polymer Chemistry, 1987. **25**(10): p. 2813-2818.
26. Mendichi, R., et al., *Molecular characterization of α, β -poly[(*N*-hydroxyethyl)-*DL*-aspartamide] by light scattering and viscometry studies*. Polymer, 2000. **41**(24): p. 8649-57

7 – Conclusions

Despite the great therapeutics potentiality demonstrated *in vitro* by NABDs, the application on real clinical case resulted much more difficult. The lacking of an efficient delivery system can invalidate the efficacy demonstrated by this class of molecules during the laboratory experiments. For this reasons, great number of studies were performed with both, private and public, investments. The aim of this project was to demonstrate the feasibility of polymeric hydrogel systems as drug delivery device for NABDs. Polymeric hydrogels were analyzed from different point of view: compositions, mechanical properties, thermal stability, network mesh size and, finally, *in vivo* performances.

7.1 – Systems characterization

From the structural point of view, the rheological analysis demonstrates a clear preponderance of the elastic component in all the systems under examination, typical of strong gel behavior. Focusing on the pure alginate hydrogels, the elastic and loss modulus increase with the increasing of the polymer concentration. Gel strength increases with polymer concentration for systems Crosslinked by Ca^{2+} and Cu^{2+} . This effect was more evident in the case of Cu. Indeed, while the 1%Cu-alginate mechanical properties were lower than 1%Ca-alginate, the 2% gel behavior was similar and even higher for Cu-alginate at 3% concentration. The explanations of the Cu-alginate properties are related to the better efficiency of the Cu^{2+} to be caged between the alginate egg-boxes. The reason of the half salt concentration used for the CuSO_4 solution was the fast gelation speed. We hypothesize the use of Ca cations may lead to aggregates formation that locally precipitate causing a network destabilization. On the other side, in the 1%Cu-alginate, the salt and polysaccharide concentration is too low to have a full gelation and the Cu structuring capacity became evident only when concentration is increased.

Another aspect that reinforces this hypothesis is constituted by the mechanical spectra trends as function of the temperature (10°C, 25°C and 40°C). The results have evidenced the strong stability of the Cu-alginate hydrogel while, the Ca-alginate presented a reduction of the mechanical

modulus with the temperature increasing, demonstrating the lower mechanical properties. Crosslink density ρ_x and the mean mesh size φ obtained by the fittings of the generalized Maxwell model increases, decreases, respectively with the polymer concentration increase.

From the microscopic point of view, low field NMR, shows the presence of three aggregation states (or three peaks), except for the 1%Cu-alginate that had 4 peaks. The relaxation times (T_2) of the Cu-alginate hydrogels were clearly lower than the relaxation times of the Ca-alginate, another indication of the stronger interaction between water and the polymeric structure in the systems reticulated by Cu cations. On the contrary, in the Ca-alginate hydrogels, water was less vincolated, this meaning a lower interaction with polymer chains. Based on the temperature effects on the relaxation time distribution and comparing the theoretical peaks areas with the experimental areas, it was shown that is not possible to distinguish the peak correspondent to the polymer protons because of the low concentration. Therefore, the first two peaks, which resulted in an area of more than 70%, were assigned to the water entrapped into the polymeric reticule.

Coupling the results obtained from Rheology and NMR, a bimodal mesh size probability distribution was obtained for all the alginate samples. The concentration increase resulted in a reduction of the mesh size, especially in the Cu-alginate case. The Cu-alginate hydrogels present mesh slightly smaller than the Ca-alginate

In the case of the Pluronic™ F127 solution temperature increase triggers great change in the system structure resulting in the gelation process. The analysis of the T_2 relaxation time allowed following chain structuring dynamics from solution to complex micelles systems promoted by the temperature. The data treatment separated the contribution of a “non-structured” polymer phase, a “structured” polymer phase and a water phase. Indeed, at lower temperatures (10°C – 14°C), the system was described by two components: the slow, assigned to the free water, and the medium, assigned to the Pluronic™. The experimental peaks areas (82,9% and 17,0% respectively for the slow and medium) were in good agreement with the theoretical areas. Within 14°C – 40°C, the system was described by three components: slow (free water), medium (unimeric or low structured Pluronic™) and fast (structured or micelles Pluronic™). These peaks assignments was confirmed by the lower mobility of the micelles compared to the low structured Pluronic™. Normally a higher temperature results in a generalized T_2 increasing because the lower system viscosity and consequent increase of the molecules mobility. Instead, in the Pluronic™ system, the mobility increasing is compensate and overcome by the micelles aggregates formations that results in a system structuring. The presence of at least two discontinuities in the T_2 trend of the medium and fast components is an indication that, the structuring process is not a simple equilibrium within two states (unimers-micelles), but it is a sequence of phases.

The results obtained on the polymeric blend of 2%Cu-alginate-18%Pluronic™ were interpreted on the base of the hypothesis formulated on the single components characterization. The FS test reported mechanical modules for the polymeric blend one order of magnitude higher than the 2%Cu-alginate alone. This result affected in a similar manner also the crosslink density ρ_x and the mean mesh size φ . The analysis of the T_2 relaxation spectra at 25°C had shown the presence of 4 aggregation states (peaks) of the ^1H protons. The peak assignment resulted difficult because of the complexity of the system. The comparison with the relaxation time distribution of the pure alginate hydrogels, allowed to assign the first two peaks to the polymeric mesh and, therefore, to a bimodal distribution of mesh size. Even if not so high, the different within this polymeric blend and the pure alginate system can be justified supposing an influence on the alginate join caused by the presence of the high concentrated Pluronic™.

Regarding the systems made with dextran methacrylate and its polymeric blends (D40 5% methacrylate and D500 30% methacrylate pure in solution at 5% called respectively D40MA5% and D500MA30%, or blended with 3% alginate called respectively A3D40MA5% and A3D500MA30%), an increase of crosslink density ρ_x and reduction of the mean mesh size φ were seen with polymer molecular weight and methacrylation degree increase. As demonstrated by the comparison of the respective mechanical spectra, the addition of alginate crosslinked by Ca cations to the systems constitute by pure dextran methacrylate, contributes to increase the system structuring. The NMR spectra of A3D40MA5% and A3D500MA30%, demonstrated a similar hydrogels behavior when the systems were freshly made. The different composition could be appreciated after 15 days aging when part of the water was evaporated with shrinkage of the polymeric matrix. Indeed, lowering the quantity of water, allowed an easier distinction of the polymeric phase contribution in the relaxation time spectra. On the other side, the observed relaxation time of the water entrapped into the polymeric network were considerable reduced by aging, demonstrating a higher polymer concentration and different interaction with water.

Poly-1b is the only one system not crosslinked in solution but obtained by swelling from the dry state. Considering mechanical characteristics, this systems demonstrated the higher absolute mechanical modules and, this result was reflected in the higher crosslink density ρ_x . The T_2 relaxation times distribution showed 4 peaks corresponding to 4 ^1H protons aggregation states. Comparing the theoretical and the experimental swelling ratio estimations and from the analysis of the temperature effect on the relaxation times distribution, it was possible to hypothesize the assignment of the first two peaks to the polymer phase and to the water entrapped into the mesh respectively.

7.2 – Cryoporometry studies

The cryoporometric analysis allowed the evaluation of the mesh size distribution through the study of water melting inside the polymeric network, assuming spherical or cylindrical pores geometry. Cryoporometric analysis performed on zeolites samples are in good agreement with the results obtained on the same samples by the BET analysis. Therefore, Cryoporometry can be considered a reliable methodology for the materials porosity studies.

Cryoporometric analyses were performed on the polymeric blends, on the dextran methacrylate hydrogels (D40MA5 and D500MA30) and on the 2%Cu-alginate hydrogel. In the resulting DSC traces, it was showed that the lower the pores dimension (equal to a higher systems structuring), lower the temperature at which water melting starts. For examples, in the dextran methacrylate-alginate hydrogels, the water melting starts even at -16°C while in *poly-Ib* start at -10°C . Anyhow, in all the considered systems, water melting starts at temperatures lower than 0°C , this meaning that the polymeric structure forces the water into the nanopores where it freezes in small nanocrystal.

The mesh size distributions obtained by Cryoporometry were different considering spherical or cylindrical geometry. In particular, assuming the cylindrical geometry the estimation results in smaller mesh. On the contrary, observing the trends of the melting enthalpy and the melting temperature of the water into the pores, it was possible to distinguish three characteristic regions. In the first, for both the curves, there was a high slope meaning a strong dependency from pores diameter. The second region represents a transition zone where ΔH and T dependency on pores diameter were gradually reduced. Finally, in the third region, the curves gets a plateau where ΔH and T were independent from pores diameter. Because in this region, a pore diameter increasing does not change significantly the melting temperature and enthalpy, it represents an approximation of the ideal crystal of infinite dimension ($\Delta H=333,7 \text{ J/g}$).

Nevertheless, Cryoporometry estimated higher mesh size than NMR-rheology. This can be explained considering that:

1. The polymeric network could be damaged by water volume increase due to the freezing process.
2. The viscoelastic properties of the network requires a very slow variation of boundary conditions in order to behave nearly to the equilibrium.

Both these factors could influence, in some ways, hydrogels internal structural change. Indeed, Cryoporometric and NMR-rheology analysis are closer for stronger gels as the systems made by dextran methacrylate-alginate, where the interaction within chains is at least partially

covalent (within dextran chains) and thus, stronger. A possible way to overcome this problem is to change Cryoporometry procedure by performing the warming by a *step scan mode* that consists in an temperature increase of an established ΔT followed by a time interval that allows the system to equilibrate before the next increase. By this methodology, warming proceeds through a series of equilibrium states and the final response should be improved. As demonstrated before, for traditional porous systems such as the zeolites, this methodology is not necessary because of the much higher stability of the network.

7.3 – Biological evaluations

In order to prove the usefulness of hydrogels systems for the delivery of NABDs, biological studies were performed on VSMC and HUVEC cells culture as model for a particular case of siRNA delivery: an injectable anti-restenosis stent coating. Based on previous studies, the polymeric blend constituted by 18% Pluronic™ and 2% non crosslinked alginate had been chosen at this purpose. The basic idea is to realise a system that behaves as a solution when injected on the treated area than it undergoes a crosslinking process due to body temperature (gelation of the Pluronic™ portion of the blends). Finally, a bivalent cations solution can reinforce the systems creating an outer alginate gelation that shields the system from the blood flow and prevent the siRNA complex loosing into the blood.

Cellfectin™ and Lipofectin™ were chosen as carrier and were complexed by siRNA. The complexes were then characterized. The rheological analysis showed that these complexes do not affect the gel final properties, even if they affect the structuring process. In particular, Cellfectin™ induces a certain anticipation of the structuring process compared to Lipofectin™, a phenomenon probably connected to the superficial charge of the particles rather than to their sizes. These observations together with the different efficiency in NAM-R uptake into VSMC, suggest that Cellfectin™ is preferable to Lipofectin™ as it can transfer more efficiently the therapeutic NAM-R into VSMC. However, Lipofectin™ is preferable to Cellfectin™ as, in its presence, the structuring process occurs at a slightly higher temperature. This feature can prolong the liquid status of the polymeric blend thus reducing the risk of polymeric blend gelation during application by endo-vascular catheter. Moreover, *in vitro* release tests indicate that, at least in the case of Cellfectin™, complexes release is feasible and depends on the polymeric blend concentration. This would allow finding optimal release kinetics for endo-arterial application.

In addition, the transfection efficiency of smaller siRNA carrier systems was evaluated with the aim to improve the release kinetics. FITC-GL2 fluorescent siRNA was complexed with PHEA

derivates in order to obtain polyplexes for the VSMC up-take evaluation. Unfortunately, these systems resulted into insufficient transfection efficiency on this cell line and further studies are required in order to find a better polyplex system.

Whereas the final choice between the two liposomes tested will also require the evaluation of the delivery kinetic from the considered polymeric blend *in vivo*, we have now identified a polymeric system which is compatible with the presence of specific liposomes and of complexes liposomes/siRNA. These findings open the way for further analysis of our system, aimed at the delivery of NAM-R to diseased vessel wall and, more in general, prove the capability of hydrogels to be applied as delivery systems for NABDs release.

Symbols and Abbreviations

Δc_p	$c_{p_l} - c_{p_s}$
ΔE	Energy difference
ΔG^0	Free energy variation caused by micellation
ΔG_f	Melting free energy
Δh	Standard melting enthalpy (melting enthalpy per mass unit)
ΔH	Melting enthalpy
$\Delta h(T_0)$	Standard melting enthalpy of the ice that melting at $T_0=0^\circ\text{C}$
ΔH^0	Micellation enthalpy
ΔH_I	Standard enthalpy in the I^{st} integration
ΔH_f	Molar melting enthalpy
ΔH_i	Standard enthalpy in the i integration
ΔS^0	Micellation entropy
ΔS_I	Standard entropy in the I^{st} integration
ΔS_f	Molar melting entropy
ΔS_i	Standard entropy in the i integration
Δx	Critical displacement (or maximum displacement)
$^\circ\text{C}$	Celsius temperature degree
$^\circ\text{K}$	Kelvin temperature degree
12-LOX	Platelet-type 12-LipOXygenase
2'-F	Nucleotides fluorination on position 2' of the sugar moiety
2'-FANA	2'-deoxy-2'-fluoro β -D-arabinonucleic acids, a nucleotides modification
2'-O-Me	Nucleotides methylation on position 2' of the sugar moiety
2'-O-MOE	Nucleotides methoxyethyl modification on position 2' of the sugar moiety
4'-S	Nucleotides modification by substitution of 4' oxygen by a sulphur atom
a	Importance factor (weight)
A	Equation parameters
\AA	Amstrong (10^{-10} m)
AAV	Adeno-Asociated Virus
abl	Proto-oncogene
ADV	Adenovirus
a_i	Drug dose
a_i	Importance factor (weight) of the i element
A_{ij}	Contact area between i and j phases
a_i^n	Importance factor (weight) of the i element during the iterative test n
A_k	Pre-exponential factor of the k component
A_l	Interfacial area of liquid phase
A_{lv}	Contact area between liquid and vapor (or gas) phases
AMI	Acute Myocardial Infarction
AP	Anionic Polymerization
AP-1	Activator Protein 1
A_s	Interfacial area of solid phase
A_{sl}	Contact area between solid and liquid phases
ASO	AntiSense Oligonucleotide

Symbols and Abbreviations

AT1	Angiotensin II receptor antagonists
AtuFECT01	b-L-arginyl-2,3-L-diaminopropionic acid-N-palmityl-N-oleyl-amide trihydrochloride
A_v	Interfacial area of vapor (or gas) phase
A_{vs}	Contact area between vapor (or gas) and solid phases
B	Equation parameters
B_0	External magnetic field
B1	A cyclin's family protein
B_1	External rotating magnetic field
b2a2	Oncogene derived from bcr-abl L6 translocation
bcl-2	Oncogene
Bcl-x	Proto-oncogene
bcr	Proto-oncogene
bcr-abl	Oncogene
BF1	A benzofulvene derivate
BH ₃	Boranophosphate nucleotides modification
BHK	Cell line
BV	Baculovirus
c	Light speed BET constant (Gas porosimetry)
C33A	Tumor Cell line
CAC	Critical Aggregation Concentration
CBA	Cystamine bis-acrylamide
CBS	Carbosilane dendrimers
C_{cw}	NABD-complex concentration in the coronary wall
CD	Cyclodextrin
CD4	Proto-oncogene
cdc2	A regulatory kinase protein
c-erb-2	Proto-oncogene
c-fos	Proto-oncogene
CGT	Critical Gelation Temperature
c-jun	Proto-oncogene
CMC	Critical Micellation Concentration
cMET	Mesenchymal-Epithelial Transition factor, a proto-oncogene
CML	Chronic Myelogenous Leukaemia
CMT	Critical Micellation Temperature
CMV	Cytomegalovirus
c-myc	Proto-oncogene
COS7	Cell line
cp	specific heat capacity
cp_l	liquid specific heat capacity
CPMG	Carr-Purcell-Meiboom-Gill pulse sequence
CPP	Cell Penetrating Peptide
cp_s	solid specific heat capacity
d	Gap between rheometer plates
Da	Dalton
DA	Delivery Agent
DAH	1,6-diaminohexane
DAPI	Fluorescent staining for cells nuclei
DDS	Drug Delivery System

<i>De</i>	Number of Deborah
D_g	Diffusion coefficient of molecules in gel
DMA	Di-methyl-acetamide
DMAP	4-di-methyl-amino-pyridine
DMF	Di-methyl-formamide
DMSO	Di-methyl-sulfoxide
DNA	DeoxyriboNucleic Acid
DNase	Deoxyribonuclease
DOPE	dioleoyl-1-a-phosphatidylethanolamine
DOSPA	2,3-dioleyloxy-N-[2(spermincarboxamido)ethyl]-N,Ndimethyl-1-propanaminium trifluoroacetate
DOTMA	N-[1-(2,3-dioleyloxy)propyl]-N,N,N-trimethylammonium chloride
DPhyPE	1,2-diphytanoyl-sn-glycero-3-phosphoethanolamine
DPL	dendritic α -(poly(L-lysine))
DSC	Differential Scanning Calorimetry
DSPE-PEG	N-(carbonyl-methoxypolyethyleneglycol-2000)-1,2-distearoyl-sn-glycero-3-phosphoethanol-amine sodium salt
dsRNA	Double strand RNA
dTTP	Deoxythymidine tri-phosphate
D_w	Diffusion coefficient of molecules in water
DZ2	Prostate cancer cell line
<i>e</i>	Charge
<i>E</i>	Young modulus
<i>E</i>	Equation parameters
E1	A cyclin's family protein
E_1	Adsorption enthalpy of the first layer
E2F	Transcription factor family (include E2F1, E2F2 and E2F3)
E6	human papilloma virus oncogene
EDC	1-ethyl-3-(3-dimethylaminopropyl) carbodiimide
eEF1A	Peptide Elongation Factor 1A
EGTA	Ethylene-glycol-tetraacetic-acid
E_L	Layer adsorption enthalpy (except the first layer)
emt	A zeolite variant of FAU
EO	Ethylene Oxide
<i>Ep</i>	Autovalues
erg-1	Gene encoding early growth response 1, a growth factor
<i>f</i>	Frequency
<i>F</i>	Equation parameters
Fas	Receptor for TNF
FAU	Faujasite, a zeolite
FCS	Fetal Calf Serum
FDA	Food and Drug Administration (USA)
FID	Free Induction Decay
FITC	Fluorescent dye labeling
Flt-1	Gene encoding FLT1 receptor
FLT1	Human VEGF receptor
f_r	Recall elastic force
FS	Frequency sweep
FT	Fourier Transformation
<i>g</i>	Grams (weight)

Symbols and Abbreviations

	Spring constant
G	α -L-gulonate, one of the monomers of alginate copolymer
G	Gibbs free energy Shear modulus (Rheology)
G^*	Complex modulus
G'	Storage modulus (or elastic)
G'_e	Pure elastic component
G''	Loss modulus (or viscous)
gag	HIV-1 gene encoding a viral core protein
GDL	D-glucono- δ -lacton
g_k	Constant of k spring
GL2	Control siRNA targeting luciferase
GMA	Glycidyl-methacrylate
GMF/CSF	Granulocytic-Monocytic colony forming unit activator, a growth factor
g_N	g nuclear factor
h	Plank constant
H1	DNA Polymerase type III promoter
HA	Hyaluronic Acid
HCC	Hepatocellular Cancer
HCT-116	Colon cancer cell line
HCV	Hepatitis C Virus
HeLa	Cell line
HER2/neu	Human Epidermal growth factor Receptor 2 (CD340), a membrane growth factor receptor
HIV-1	Human Immunodeficiency Virus variant 1
h-ras	Oncogene
HRz	Hammerhead ribozyme
HSV	Herpes Simplex Virus
HUVEC	Human Umbelical Vein Cell
HXB2	HIV-1 gene
Hz	Hertz (cycle sec^{-1})
i	Intercept on x -axe
I	Nuclear spin quantum number
$I(\bar{t})$	Intensity at instant \bar{t}
ICAM-1	Inter-Cellular Adhesion Molecule 1 (CD54), an adhesion protein
IGF-1R	Insulin-like Growth Factor Receptor tyrosine kinase
$I_j(\bar{t})_j$	Intensity at instant \bar{t} of the j component
IKK	κ B-kinase, a protein activator
IPN	Interpenetrating Polymer network
ISR	In-Stent Restenosis
J	Joule
JL-1	Leukaemia-specific antigen 1
k	A constant parameter in general
Kg	Kilograms
Ki-67	RNA synthesis factor
k-ras	Oncogene
LF-NMR	Low Field NMR
LNA	Locked Nucleotide, a nucleotides modification
LTA	Zeolite-A
lv	Liquid-vapor (or liquid-gas) interface

LV	Lentivirus
m	Meters
M	Mass (in general) Molarity (moles concentration) Also used for β -D-mannuronate, one of the monomers of alginate copolymer
M	Magnetization (in general)
M_{Alg}	Water molecular weight
MB	Microbubble
MCP-1	Monocyte Chemotactic Protein 1, a chemotactic signal
mdr1	Gene encoding Multi Drug Resistance 1, a membrane transporter
MEND	Means of an envelope-type nano device
m_{H_2O}	Water mass inside the gel
M_{H_2O}	Alginate monomer molecular weight
m_l	Magnetic Quantum number
MI	Mechanical Index
miRNA	Micro RNA
m_m	Mass of polymer in the gel
M_m	Polymer monomer molecular weight
Mn	Mean molecular weight
M_o	Equilibrium net magnetization
MOEG	Methyl PEG oligomers
mol	Moles
MoMLV	Moloney Murine Leukaemia Virus
M_{Plu}	Pluronic™ monomer molecular weight
mRNA	Messenger RNA
ms	Milliseconds
Mw	Molecular weight
M_x	x axe magnetization component
M_{xy}	xy plane magnetization component
M_y	y axe magnetization component
M_z	z axe magnetization component
N	Newton
N or n	In general used to represent the number of elements (systems nuclei, exponentials, moles, nanopores, unimers as aggregation number, etc.)
N2A	Neuroblastoma cell line
N_A	Avogadro's number ($6,22 \times 10^{23} \text{ mol}^{-1}$)
NABD	Nucleic Acid Based Drugs
N_{Alg}	Number of protons in the alginate monomer
NAM-D	DNA duplex carrying the same sequence of NAM-R
NAM-R	siRNA targeting cyclin E1
NF- κ B	Nuclear Factor-kappa B (transcription factor)
N_{H_2O}	Number of protons in the water molecule
n_i	Number of moles of I component
N_i	Number of i data
NIH3T3	Cell line
n_l	Number of moles of the liquid phase
nm	Nanometers (10^{-9} m)
N_m	Number of protons in polymer monomer
NMR	Nuclear Magnetic Resonance
NP	Nanoparticle

Symbols and Abbreviations

N_{Plu}	Number of protons in the Pluronic™ monomer
n-ras	Oncogene
n_s	Number of moles of the solid phase
n_v	Number of moles of the vapor (or gas) phase
ODN	OligoDeoxyNucleotide
OEG	Oligo(ethylene glycol)
OEGMA	Oligo(ethylene glycol methacrylate)
P	Pressure Angular moment (NMR) P-value: statistical significance parameter
$P(\varphi)$	Occurrence probability of the pore with φ diameter
$P(\varphi_i)$	Occurrence probability of the pores with φ_i diameter
p53	Proto-oncogene
Pa	Pascal
PAMAM	poly(amidoamine)
PBS	Phosphate Buffer Solution
PC	Phosphorylcholine
PC3	Prostate cancer cell line
PCNA	Proliferating Cell Nuclear Antigen, a replication factor
PDGF-A	Platelet-Derived Growth Factor subunit A
PEG	poly(ethylene glycol), also referred as poly(ethylene oxide) (PEO)
PEG	Poly(ethylene glycol)
PEG-L	Poly(ethylene glycol) modified liposome
PEI	poly(ethylenimine)
PEO	poly(ethylene oxide), also referred as poly(ethylene glycol) (PEG)
PGA	poly(glycolic acid)
PGE2	Prostaglandin E2
PHEA	α,β -poly(N-2-hydroxyethyl) D,L-aspartamide
Phea-Deta	PHEA-diethylenetriamine
Phea-Eta	PHEA-2-aminoethylcarbamate
Phea-Sp	PHEA-spermine
Phea-Sp-C4	PHEA-spermine-butiric acid
pHPMA	poly(N-2-hydroxypropyl-methacrylamide)
PIC	Nucleoprotein pre-integration complex
P_l	Pressure of the liquid phase
PLA	Poly(lactic acid)
PLL	poly(L-Lysine)
PMO	Phosphorodiamidate Morpholino Oligonucleotide
PNA	Peptide Nucleic Acid
PO	Propylene Oxide
Pol II	DNA Polymerase type II
Pol III	DNA Polymerase type III
PPI	poly(propylenimine)
PPO	Poly(propylene oxide)
P_s	Pressure of the solid phase
PS	Phosphorothioate nucleotides modification
PTSA	p-toluensulphonic monohydrate
P_v	Vapor pressure of the gas phase
P_v^0	Vapor pressure in pore of radius ∞ (saturation vapor pressure)
PVA	Poly(vinyl-alcohol)

P_z	Angular moment component belong z axes
P_α or P_β	Nuclei population deviation (+ or -) from $N/2$ between two state
Q	Volumetric swelling ratio
\dot{Q}	DSC trace power
r	Radius of the water solid crystal into a nanopore
R	Parallel plates sensor radius
R	Universal gas constant ($8.31447.. JK^{-1}mol^{-1}$)
rad	Radiant
raf	A regulatory kinase protein
ras	Proto-oncogene family
R_{bs}	Big/small delivery agent ratio
R_{HI}	Micelles hydrophobic core radius
RISC	RNA Interfering Silencing Complex
R_{lv}	Curve radius of liquid-vapor (or liquid-gas) interface
R_m	Micelles hydrodynamic radius
RNA	RiboNucleic Acid
RNAi	RNA interfering
RNase	Ribonuclease
RNase-H	Ribonuclease that cut double strand RNA
r_p	Radius of liquid-gas interface into a pore
R_p	Pore radius
R_{pi}	Pore radius in the i integration
$R_{pi,Crio}$	Pores radius obtained by cryoporimetry method
$R_{pi,N2}$	Pores radius obtained by BET gas porimetry method
R_{sl}	Curve radius of solid-liquid interface
R_{sv}	Curve radius of solid-vapor (or solid-gas) interface
runx1-cbfa2t1	Oncogene
RV	Retrovirus
r_{vdW}	van der Waals radius
s	Linear function slope
S	Entropy
SANS	Small-Angle Neutron Scattering
<i>sec</i>	Seconds
SFV	Semliki Forest Virus
s_i	Molar entropy with $i=s, l, v$ for solid, liquid and vapor (or gas) respectively
siRNA	small interfering RNA
sl	Solid-liquid interface
S_l	Entropy of the liquid phase
SP	Spontaneous Polymerization
SRF	Serum Responsive Factor
S_s	Entropy of the solid phase
S_s	Specific surface
SS	Stress sweep
STAT3	Signal Transducer and Activator of Transcription 3 (transcription factor)
sv	Solid-vapor (or solid-gas) interface
S_v	Entropy of the vapor (or gas) phase
Sw	Swelling ratio
SWCN	Single Walled Carbon Nanotube
t	Time

Symbols and Abbreviations

\bar{t}	Instant time
T	Tesla (magnetic field) Temperature
\mathbf{T}	Torque moment
T_0	Melting temperature of crystal with ∞ radius (0°C for water)
T_1	Longitudinal relaxation time (spin-lattice)
T_1	Temperature in the I^{st} integration
T_2	Transversal relaxation time (spin-spin)
\bar{T}_2	Mean relaxation time (in general)
$T_{2,i}$	Mean relaxation time of the i peak
T_2^i	Relaxation time of the i element ($i=1$ to N)
T_2^k	Relaxation time of the k component ($k=1$ to N)
T_l	Temperature of the liquid phase
T_s	Temperature of the solid phase
T_v	Temperature of the vapor phase
TAT/Rev	HIV-1 regulatory protein
tel-aml1	Oncogene
TF	Transcription Factor
TFO	Triplex Forming Oligonucleotide
TGF β -1	Transforming Growth Factor beta-1
THF	Tetra-hydrofuran
T_i	Temperature in the i integration
T_l	Temperature of the liquid phase
TMPK	Thymidylate kinase
TNF- α	Tumor Necrosis Factor alpha, a cytokine
t_p	B_1 (RF) pulse application time
TP-10	A cell penetrating peptides
t_r	Repetition time between RF pulse
T_s	Temperature of the solid phase
T_{st}	Structuring temperature
T_v	Temperature of the vapor (or gas) phase
U2OS	Tumor Cell line
U6	DNA Polymerase type III promoter
U937	Cell line
v	Heating speed Number of crosslink's moles
\bar{v}	Specific volume (volume/mass)
V	Volume (sometimes also used to define the final volume)
V_0	Initial volume
v_2	Polymeric volume fraction of the full swelled gel
v_{2p}	Polymer volumetric fraction in the gel
v_{2r}	Polymeric volume fraction at the crosslinked time (not full swelled)
v_a	Absorbed vapor quantity
v_e	Number of crosslink's
VEGF	Vascular Endothelial Growth Factor
vegf-a	Gene encoding VEGF-A
v_f	Volume of water crystal into a nanopore (<i>freezable</i> water)
V_f	Total volume of <i>freezable</i> water (nanocrystal volume)
v_i	Molar volume with $i=s, l, v$ for solid, liquid and vapor (or gas) respectively

V_j	Volume j phase
V_l	Volume liquid phase
v_m	Quantity of vapor adsorbed as a monolayer
v_{nf}	Volume of <i>non-freezable</i> water into a nanopore
V_{nf}	Total volume of <i>non-freezable</i> water
v_p	Nanopore volume
V_p	Total nanopores volume
$V_{p,calc}$	Total nanopores volume calculated during iterative evaluation of β
V_s	Volume solid phase
VSMC	Vascular Smooth Muscle Cell, a cell line
VSV-G	Vesicular Stomatitis Virus Glycoprotein
V_v	Volume vapor (or gas) phase
We_{Alg}	Weight of alginate in gel system
We_{H_2O}	Weight of water in gel system
We_{Plu}	Weight of Pluronic™ in gel system
W_f	Mass of freezable water inside the pores
W_{H_2O}	Mass of water melting at 0°C
W_{nf}	Mass of non-freezable water inside the pores
W_t	Total water mass inside and outside the system
z	Pores geometry parameter (2=cylindrical, 3=cubic/spherical)
ZK-4	A zeolite
ZSM-11	Socony-Mobil 11 Zeolite
ZSM-5	Socony-Mobil 5 Zeolite
α	Extension ratio
α_x	Extension ratio in x axe
α_y	Extension ratio in y axe
α_z	Extension ratio in z axe
β	Thickness of <i>non-freezable</i> water layer into a nanopores
γ	Giromagnetic ratio (NMR) Deformation, in particular identify the shear deformation (Rheology) Surface tension (Cryoporimetry)
$\dot{\gamma}$	Deformation speed
γ_0	Critical deformation
$\dot{\gamma}_0$	Critical deformation speed
γ_H	Proton giromagnetic moment
γ_{lv}	Surface tension liquid water-vapor (or liquid-gas)
γ_{lv}	Surface tension liquid-vapor (or liquid-gas)
γ_{sl}	Surface tension ice-liquid water (or solid-liquid)
γ_{sv}	Surface tension solid-vapor (or solid-gas)
γ_{vs}	Surface tension ice-vapor (or solid-gas)
δ	Excess of nuclei in higher energy state compared to the lower (NMR) Loss angle, phase displacement between $\dot{\gamma}$ and τ (Rheology)
δP_i	i component pressure infinitesimal variation
δT	temperature infinitesimal variation
$\delta \mu_i$	i component chemical potential infinitesimal variation
ϵ	Tolerance Deformation, in particular identify the deformation to normal stress (Rheology)
η	Viscosity (in general)
η_k	Viscosity of the k component

Symbols and Abbreviations

θ	Angle between B_I and M_0
ϑ_{lv}	Contact angle between liquid and vapor (or gas) phase
ϑ_{lw}	Contact angle between liquid and pore wall
ϑ_{sl}	Contact angle between solid and liquid phase
κ	Boltzman constant
λ	Wave length (NMR) Relaxation time (Rheology)
Λ	Applied deformation process time
λ_k	Mechanical relaxation time of the k component (Rheology)
μ	Magnetic moment (NMR) Chemical potential (Cryoporimetry)
μ_l	Chemical potential of the liquid phase
μ_N	Magneton (μ measure units)
μ_s	Chemical potential of the solid phase
μ_v	Chemical potential of the vapor (or gas) phase
μ_z	Magnetic moment component belong z axes
ν_0	Larmor precession frequency in Hertz, see also ω_0
ν_{RF}	B_I rotation frequency
π	Pi constant = 3,14159...
ρ	Density
ρ_{ice}	Ice density at temperature T
$\rho_{ice}(0^\circ C)$	Ice density at temperature $T_0=0^\circ C$
ρ_l	Liquid density
ρ_s	Solid density
ρ_x	Crosslink density
σ	Deviation
τ	Pulse sequence interval (NMR) Shear stress (Rheology)
τ_0	Critical stress
φ	Mean mesh size (or mean mesh diameters)
ϕ	Probability to have a pore of radius R in the system
φ_i	Single pores diameters into a mesh size distribution
χ^2	Sum of square difference
ω	Angular frequency or pulsation (Rheology)
Ω	Rotational speed
ω_0	Larmor precession frequency in (rad sec^{-1}), see also ν_0
ω_I	Angular frequency between B_I and M_0

Acknowledgements/Ringraziamenti

First of all I would like to thank my tutor Prof. Mario Grassi for the trust and patience in explaining some mathematical treatment that are not really my favorite subject. Moreover, I would like to thank Prof. Gabriele Grassi for the *in vivo* tests. Also thanks go to colleagues: Antonella, Claudia, Constanza, Daniela, Flavio, Francesca, Guadalupe, Riccardo and the “youngest” of all, Riaz. Special thanks to Aroul, Cristiano, Massimo and Susanna, who have always been available with a precious help. I cannot forget, “pure energy” Erminio that has the only defect to be an Inter supporter, and Diego which, from time to time, offer a good coffee and a talk. Another thanks goes to Mr. Pietro Ferrero, the inventor of Nutella, a fantastic anti-depressant that, in the last months has contributed to “increase” my abdominal looks (sob!).

More than any others I thank my parents, Franca and Roberto, and my grandparents, far in terms of distance but always close in heart.

This thesis is dedicated to all the people mentioned above and those that I forgot to mention, even if I wanted to do but, in particular I would like to dedicate it to my “puppy” Sara who has accepted living with a noisy “boar.”

Also, a dedication is addressed to all those who believed in me but, more importantly, to those (hopefully few) who have not believed. MVFC!

Innanzitutto vorrei ringraziare il mio tutore Prof. Mario Grassi per la fiducia dimostrata e per la pazienza avuta nello spiegarmi alcune trattazioni matematiche che non sono proprio la mia materia preferita. Inoltre vorrei ringraziare il Prof. Gabriele Grassi per quanto riguarda la parte delle prove *in vivo*. Un doveroso ringraziamento va anche ai colleghi di lavoro: Antonella, Claudia, Constanza, Daniela, Flavio, Francesca, Guadalupe, Riccardo e il più “giovane” di tutti, Riaz. Un ringraziamento speciale ad Aroul, Cristiano, Massimo e Susanna che sono sempre stati disponibili con un aiuto prezioso. Non posso poi dimenticare “energia pura” Erminio che ha l’unico difetto di essere Interista e Diego cui di tanto in tanto scroccavo un buon caffè e quattro chiacchiere. Altro ringraziamento va al Sig. Pietro Ferrero, l’inventore della Nutella, un fantastico anti depressivo che, negli ultimi mesi, ha contribuito ad “aumentare” la mia prestanza addominale (sob!).

Più di ogni altri ringrazio i miei genitori, Franca e Roberto, ed i miei nonni che anche se lontani in quanto a distanza sono sempre vicini nel cuore.

Questa tesi è dedicata a tutte le persone sopra menzionate e a quelle che mi sono scordato di menzionare, anche se avrei voluto farlo. In particolare, però, la vorrei dedicare al mio “cucciolo” Sara che con amore ha accettato la convivenza con un rumoroso “cinghiale”.

Inoltre, una dedica è rivolta a tutti colori che hanno creduto in me ma, soprattutto, a quelli (spero pochi) che non hanno creduto. MVFC!